Advanced User-centric Modeling for Future Wireless Communication Networks: Performance Analysis and Optimization

Khaled Humadi

A Thesis

In

The Department of

Electrical and Computer Engineering

Presented in Partial Fulfillment of the Requirements

For the Degree of

Doctor of Philosophy (Electrical and Computer Engineering)

Concordia University

Montréal, Québec, Canada

August, 2022

Concordia University

School of Graduate Studies

This is to certify that the thesis prepared

By: **Khaled Humadi**

Entitled: **Advanced User-centric Modeling for Future Wireless Communication Networks: Performance Analysis and Optimization**

and submitted in partial fulfillment of the requirements for the degree of

Doctor of Philosophy (Electrical and Computer Engineering)

complies with the regulations of this University and meets the accepted standards with respect to originality and quality.

Signed by the final examining commitee:

Dr. Ahmed Soliman	Chair
Dr. Long Le	External Examiner
Dr. Arash Mohammadi	External to Program
Dr. Jun Cai	Examiner
Dr. Dongyu Qiu	Examiner
Dr. Wei-Ping Zhu	Supervisor
Dr. Wessam Ajib	Co-Supervisor

Approved by _____

Dr. Jun Cai, Graduate Program Director

August 25, 2022 _____

Dr. Mourad Debbabi, Dean

Gina Cody School of Engineering and Computer Science

Abstract

Advanced User-centric Modeling for Future Wireless Communication Networks: Performance Analysis and Optimization

Khaled Humadi, Ph.D.
Concordia University, 2022

Due to the increasingly growing demand for high data rates and a massive number of connected devices, future wireless communication networks are required to provide much more resources than the current networks can do. As an emerging solution for future cellular networks, dense deployment of small cell base stations (BSs) has received a great deal of attention both in academia and industry. A major challenge in dense cellular networks is the interference experienced by the user from its neighboring active BSs. The effect of such interference is more deleterious at cell-edge users which limits the density of deployed BSs.

An effective promising solution is to move from a cell-centric to a user-centric paradigm which allows each user to be connected to a set (cluster) of BSs instead of being associated with a single one. This will mitigate the interference effect and remove the cell boundaries, i.e, no cell-edge users. In this thesis, we develop novel BS clustering models to enable a user-centric BS cooperation for future wireless networks. Unlike the existing clustering models, where a user is served by a cluster of BSs with fixed size (either a fixed number of BSs or fixed cluster radius), our proposed models adapt the cluster of each user dynamically based on its channel condition and quality-of-service (QoS) requirements.

To design user-centric networks, we focus on several technologies introduced for future wireless wireless communication systems such as millimeter wave (mmWave) and terahertz (THz) networks, unmanned aerial vehicle (UAV)-assisted networks, hybrid multi-tier networks, and energy harvesting networks. We first investigate the performance of a user-centric mmWave network under the proposed dynamic BS clustering model using tools from stochastic geometry. To maximize the system spectral efficiency, an optimization framework for the user's serving cluster is developed. Then, a user-centric THz system is designed to compensate for the high pathloss and hence improve the coverage of THz networks. Both dynamic and static clustering approaches are considered, based on which we study the coverage probability of the user-centric THz network by using stochastic geometry. Then, to design an energy-efficient and reliable air-to-air connection in UAV networks, we design a 3D user-centric clustering model where a set of UAV transmitters spatially distributed in a 3D space in the sky are carefully selected to serve another UAV receiver. Analytical expressions for the spectral efficiency and energy efficiency of this user-centric UAV network are provided and an efficient and tractable optimization framework to maximize its energy efficiency is developed.

In this thesis, we also implement a user-centric BS clustering for hybrid networks where THz, mmWave, and sub6-GHz BSs coexist. In this system, a user can be associated with the best BS cluster, from either a sub6-GHz, mmWave or THz tier based on either the maximum SINR criterion or the maximum rate criterion. Thus, with carefully planned networks, enabling hybrid user-centric wireless systems can provide ultra-high rates while maintaining sufficient coverage in future multi-tier networks. Furthermore, we adopt the proposed user-centric clustering model to enhance the joint rate and energy coverage of cellular networks with simultaneous wireless information and power transfer (SWIPT). For this setup, we aim to insure that the user can harvest sufficient energy in a given time slot and receive the required minimum data from a given serving cluster. Then, a mathematical optimization model for the time switching coefficient is developed to maximize the system joint rate and energy coverage performance. All analytical results are vali-

dated by simulation with comparison to some of the existing works, demonstrating that the proposed analytical frameworks are accurate and efficient in the design and deployment of future user-centric wireless networks.

Acknowledgements

First of all, I bow down before God the Almighty for his blessings on me throughout the last 4 years of my life as a Ph.D. researcher in particular and throughout my life in general. I would like to express my deepest gratitude to my parents to whom this work is dedicated. It is always your love and prays that raise me up again when I get weary.

I would also like to express my genuine appreciation and gratitude to my supervisors, Dr. Wei-Ping Zhu and, Dr. Wessam Ajib, from UQAM, who have provided constant support, guidance, and encouragement throughout my Ph.D. work. Their valuable advice, constructive feedback, and careful proofreading and editing contributed enormously to the preparation of this thesis and to the publications we accomplished together.

I sincerely appreciate my committee members Dr. Arash Mohammadi, Dr. Jun Cai, and Dr. Dongyu Qiu for their time, valuable feedback, and constructive comments. I would also like to extend my appreciation to Dr. Long Le for accepting to serve as my external examiner.

I also wish to mention 3 people who have lived this Ph.D. journey with me, through all its stages. I thank my wife, Eng. Khawla Al-Sabri, and my two daughters, Amal and Joodi. Thank you, Khawla, for your love, patience, and constant support. Thank you for being my muse during difficult times and, most of all, thank you for being my best friend. I owe you everything and I am blessed to have you in my life. Thank you, my two princesses, Amal and Joodi. You have made me better, stronger, and happier than I ever believed possible. For as far as the eye can see, I adore you.

I would also like to thank Dr. Imene Trigui, the brilliant research that I got the chance to work with during the course of this thesis.

To my sisters, my brothers, and to my entire family, nothing is more valuable than having you in my life. I am also grateful to all my friends and colleagues who supported me, advised me when I needed it the most, laughed with me, and made unforgettable memories.

Finally, I would like to thank Concordia University and FRQNT for their financial support which made this work possible.

Contents

List of Figures

List of Tables

List of Acronyms

1D	One-Dimensional
2D	Two-Dimensional
3D	Three-Dimensional
3GPP	3rd Generation Partnership Project
5G	5th Generation
6G	6th Generation
ABS	Aerial Base Station
AoA	Angles of Arrivals
ASE	Average Spectral Efficiency
AUE	Aerial User Equipment
B5G	Beyond 5th Generation
bps	bits/second
BS	Base Station
CDF	Cumulative Distribution Function
CCDF	Complimentary Cumulative Distribution Function
CLT	Central Limit Theorem

CoMP	Coordinated Multipoint
CRAN	Cloud Radio Access network
CU	Control Unit
D2D	Devise-to-Device
DCC	Dynamic Cooperation clustering
EE	Energy Efficiency
eMBB	Enhanced Mobile Broadband
GHz	Gigahertz
HAP	High-Altitude Platform
HetNet	Heterogeneous Network
i.i.d	independent and identical distributed
IoT	Internet-of-Things
ITU	International Telecommunication Union
JT	Joint Transmission
LOS	Line-of-Sight
LTE-A	Long Term Evaluation Advanced
MBS	Millimeter Wave Base Station
MIMO	Multiple-Input-Multiple-Output
mmWave	Millimeter wave
MRCS	Maximum Rate Cluster Selection
MSCS	Maximum SINR Cluster Selection

NC	Non-cooperative
NLOS	None-Line-of-Sight
NOMA	None-Orthogonal Multiple Access
OBS	Optimal Base Station Selection
OPS	Optimal Point Selection
p.g.fl.	probability generating functional
PDF	Probability Density Function
PMF	Probability Mass Function
PPP	Poisson Point Process
QoS	Quality of Service
r.v	Random Variable
RF	Radio Frequency
RIS	Reconfigurable Intelligent Surface
SBS	sub-6GHz Base Station
SCC	Static Cooperation Clustering
SE	Spectral Efficiency
SINR	Signal-to-Interference-Plus-Noise Ratio
SWIPT	Simultaneous Wireless Information and Power Transfer
TBS	Terahertz Base Station
THz	Terahertz
Tbps	Terabits-per-Second

UAV	Unmanned Aerial Vehicle
UE	User Equipment
UMa	Urban macrocell
UMi	Urban microcell
URLLC	Ultra-Reliable Low Latency Communications

Chapter 1

Introduction

1.1 Looking Forward to Future Wireless Networks

Every ten years or so, wireless communication networks go through a new generation. However, the period between two successive generations is decreasing [1]. For example, wireless communication technologies beyond fifth-generation (B5G), referred to as the sixth generation (6G) technologies, are attracting a significant interest both in academia and industry, while the 5G technologies just already become a commercial reality. In fact, this rapid development of wireless communication networks is necessary to meet the fast growth of mobile users demands. Over the last few years, mobile data traffic has increased significantly. According to the recent statistics provided by International Telecommunication Union (ITU), global user wireless data traffic is predicted to hit 607 Exabytes for each month by 2025 and 5016 Exabytes for each month by 2030 [2]. Additionally, by 2025, nearly two-thirds of the population is expected to have a mobile service subscription [3].

The predicted proliferation of internet of things (IoT) applications in a variety of fields, including industry, medicine, transportation, and agriculture, will result in an explosion in the number of IoT devices. As such, massive wireless connectivity is required to enable such massive number of IoT devices to connect, interact, and exchange data at anytime and anywhere [4]. At the moment, IoT devices communicate with various wireless networks primarily through low-cost technologies such as

Bluetooth [5] and WiFi [6]. However, such technologies can only be considered as an intermediate solution for connecting a small number of IoT devices, but clearly will become inefficient for supporting reliable connections when the number of IoT devices significantly increases. Therefore, wireless networks are required to support an efficient multiple access techniques to enable massive connections. These techniques can be classified into two types [7]. The first type is the massive orthogonal access which includes the massive multiple-input multiple-output (MIMO) systems [8], [9] and radio frequency resources with a huge bandwidths such as millimeter wave and terahertz. The second type is the massive non-orthogonal access such as power-domain and code-domain non-orthogonal multiple access (NOMA) [10], [11]. The above mentioned massive access techniques, however, necessitate the use of sophisticated transmitters and receivers in order to work properly. Given the high-dimensionality of the channel in systems with massive connectivity as a result of the deployment of large number of transmitting and receiving nodes, the computational complexity at the transmitters and receivers increases dramatically. As a result, future research and industry should focus on the design and implementation of simple yet effective multiple access schemes.

Future wireless communication networks are expected to facilitate and support extensive developments in fields like those demanding extremely high data rates. Nowadays, video is rapidly becoming the preferred means of communication. As a result, the capability of video resolution is rapidly improving. For example, 4k video requires a per user data rate of 15.4 Mb/s [12]. Furthermore, end-user watching time is expanding to the point that shall allow users to watch entire television shows, live sporting activities and virtual reality etc [1]. For example, the COVID-19 pandemic demonstrates how video communication enabled educational institutions, such as schools and universities, to keep working remotely. Also, health provider remained connected with patients, governments were able to deliver services to citizens, individuals kept in touch with friends and family members without the need for travel. Until this time, major conferences and seminars are being held remotely via live video platforms. It is anticipate that many of these virtual events will continue to

operate even after the pandemic period. Therefore, to provide a high-fidelity holographic capability, a new communication system with extremely high data rate is needed.

As mentioned above, with the new emerging wireless communication technologies, cellular networks will connect a huge or vast number of IoT nodes that are mainly low-power devices. They are often powered by low-capacity batteries [13]. To extend the life of these devices and to ensure the sustainability of wireless services, several attempts have been made to develop self-sustainable communication systems with effective energy harvesting techniques, while maintaining the end-user QoS requirements. In fact, energy harvesting is a technique that involves gathering and converting unused or insignificant energy such as heat, sound, and RF signals into useful electricity. In comparison to currently existing batteries, the ambient environment provides high-quality energy sources [14]. Because of the irregular and unpredictable nature of ambient sources, energy harvesting employing natural sources were not as effective as intended. Additionally, major energy harvesting approaches are environment-specific [15]. Wireless power transfer is one of the energy harvesting techniques that overcome the aforementioned restrictions, as it relies on the RF signals to collect energy in order to power the nodes in the communications network. Green energy can be harvested using two methods in the WPT, either from the random ambient electromagnetic signals or from a dedicated fully controlled wireless power source such as a BS [14]. With the fast developments of wireless transmitters and receivers, they are going to have a very small size and to be more energy efficient. This motivates researchers to investigate the possibility of combining the aspects of both data and energy transmission, namely, simultaneous wireless information and power transfer (SWIPT). The SWIPT approach is used as a flexible power source [16] and its primary benefit is guaranteeing the amount of energy that can be gathered from RF signals rather than from expensive traditional power sources. As a result, SWIPT has been identified as a possible method for increasing the energy efficiency of current wireless communication networks. In [17], it was showed that using BS cooperation can enhance the energy harvested at the

user as well as the achievable throughput.

One of the major issues of future communications is the transmission reliability. In the existing 5G networks, machine-type communication (MTC) and ultra-reliable low latency communication (URLLC) techniques are supported. However, such techniques provide a limited reliability and high latency in the 5G networks. In the 6G networks, it is predicted to provide massive MTC (mMTC) and massive URLLC (mURLLC) scenarios with extremely enhanced performances in terms of reliability and latency [3]. In general, there are two methods to meet the URLLC requirements: either improving the reliability of a single transmission or reducing the latency between data retransmissions [18]. One efficient solution is to employ or adopt a BS cooperation. In particular, for a BS cooperation with joint transmission, a user can receive multiple versions of the intended data symbols. This can increase the strength of the useful signal power while mitigating the unwanted interfering signals, enabling the communication system to reach a targeted reliability. Furthermore, receiving multiple versions of the user's data can help in minimising the required number of retransmissions and hence mitigating the latency limitations. The issues mentioned above can be addressed by adopting an efficient user-centric cooperation among various BSs in the network.

1.2 User-Centric Network Architecture

It is known that cellular networks are composed of semi-autonomous cells. It is fundamentally a strategy for network operation, in which each cell becomes semi-independent and radio resource reuse among cells need to be planned well in advance. This network layout was established in the 1950s and had a critical role in the widespread development of wireless communication networks. However, as mobile user's data has surpassed voice calls as the primary mode of traffic, the cellular network architecture's flaws have become abundantly clear. Although modern networks provide high peak data speeds, user-guaranteed rates are extremely low. This is because of the severe pathloss fluctuations and inter-cell interference inher-

ent in the cellular network architecture [19]. A promising approach to resolving these challenges is to abandon the cellular architecture and turn to a new network paradigm devoid of cells. This idea is referred to as cell-free massive MIMO [20]. In fact, cell-free massive MIMO is a technology that essentially encompasses three fundamental technologies:

1) Large-scale (or massive) MIMO system, where serving nodes can be considered as a spatially distributed antenna. Indeed, it is envisioned that cell-free BS cooperation will lead to substantial shift of wireless system/network designs, from the existing massive-MIMO system without BS clustering to the new BS clustering-aided small/moderate MIMO systems. In fact, when properly designed, cell-free networking can compensate for the lack of multiple transmit and/or receive antennas, thereby reducing the hardware cost and energy consumption without compromising the users' QoS.

2) Network densification where many access points are deployed within a small geographical area. To enable a cell-free massive MIMO network, the number of transmitting nodes are supposed to be larger than the number of users. This guarantees that each user is surrounded by multiple access points not the inverse; and

3) Joint transmission and reception from and to spatially distributed access points. This has been already investigated under multiple techniques including coordinated multipoint (CoMP) transmission.

Interestingly, the researches in [20]–[24], have disclosed that applying cell-free massive MIMO techniques results in significant enhancement in in the system performance (in particular, 95% spectral efficiency improvement) when compared to conventional wireless networks in a variety of scenarios. For example, the authors of [20] show that cell-free can provide tenfold and fivefold improvements over a small-cell networks under correlated and uncorrelated shadow fading, respectively.

The technology of cell-free massive MIMO means full cooperation among access points where all users are served by all BSs or each BS can serve all users [20],

[25]. This implementation may result in some system inefficiencies as the size of the deployment area of the considered network increases. Indeed, it is very inefficient to waste power and time/frequency resources at a BS to process signals received from users located very far from the BS and with a very low SINR. This makes the cell-free concept more suitable only for small-scale networks, i.e, a network with small and finite number of BSs and users. As such, a user-centric BS cooperation is introduced to be adopted for large-scale networks. Unlike cell-free networks in which the user can be served by all BSs, in user-centric networks only a limited number of BSs can cooperatively serve a user which reduces the backhauling network complexity [25]. In [26], the authors showed that in addition to reducing the system complexity compared to the fully cooperative cell-free networks, a user-centric approach would lead to higher spectral and energy efficiencies.

In the user-centric technique, each user gets connected to a number of nearby transmitters, effectively removing cell boundaries and, as a consequence, the traditional concepts of a cell-edge user who experiences the worst performance disappear [27]. As a result, unlike conventional wireless cellular systems, cells have no bearing on the access channel. This significantly improves the network performance [28], making user-centric communication a promising solution for future wireless networks [29]. To summarize, the main benefits of this technique are as follows:

- Eliminating the cell-edge effect: in cell-centric networks where the user may be located at the cell boundary and hence receiving a weak useful signal power which is comparable to those received from neighbor interferers, and hence degrading the communication link QoS. This cell-edge effect is completely eliminated in the user-centric network since strong interferning signals are transformed to a useful signal [30] as shown in Figure 1.1.

- SINR and rate coverage enhancements: to increase the capacity of wireless communication systems, network operators can be carried out using one of, or a combination, of three primary technologies: 1) network densification; 2) increasing the system bandwidth (e.g. moving to higher frequency bands such as millimeter wave or terahertz bands); and 3) making the spectrum more

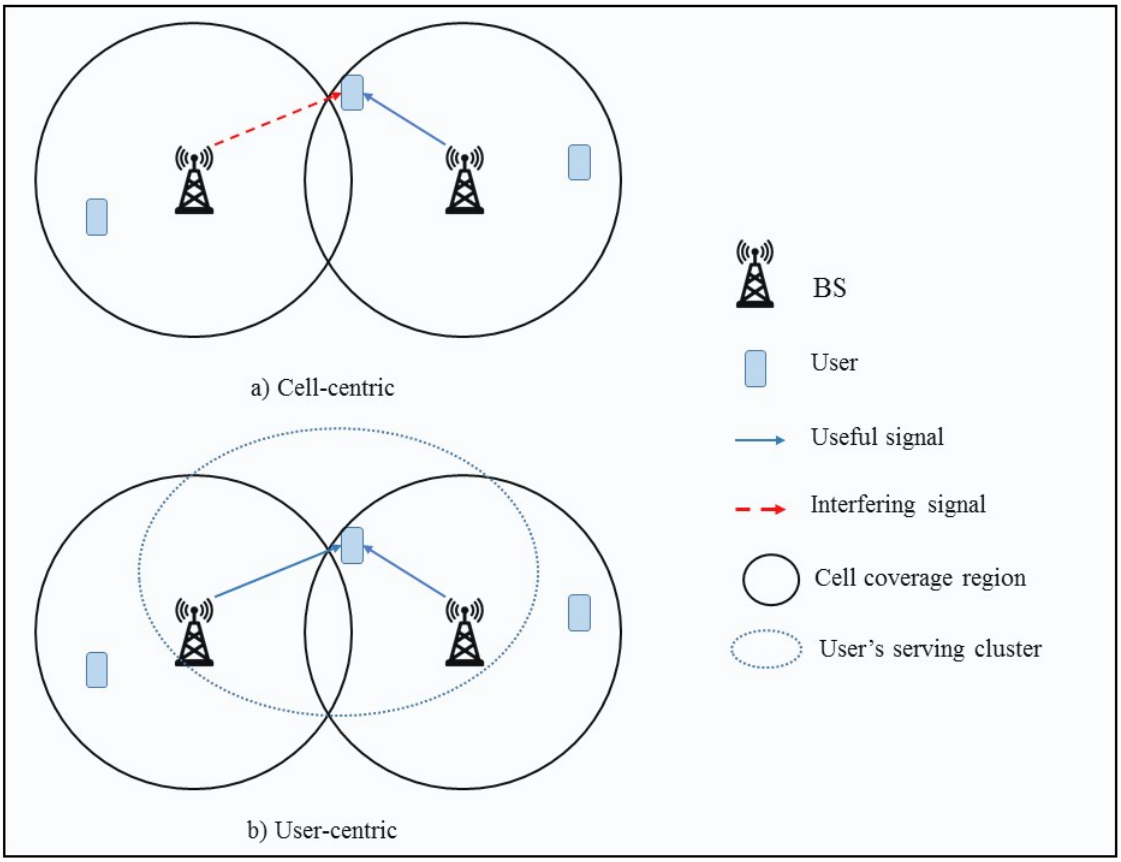

Figure 1.1: User-centric network versus cell-centric network

efficient (e.g. using massive MIMO system or advanced coding schemes). For network densification, a large number of access points are spatially deployed within a small geographical area, where the main idea behind this is to get the access points as close as possible to the end users [31]. Moreover, network densification can significantly increase the available communication resources. Unfortunately, many challenges arise from increasing the BSs density, where high inter-cell interference is the primary issue. This limits the maximum number of deployed BSs without compromising the system performance. Under user-centric cooperation, interferers with dominant and strong received power are transformed to a useful signal as shown in Figure 1.1. This enhances the signal strength and mitigates the interference effect. As such, the received SINR and hence data rate are significantly improved under user-centric cooperation.

- Reliability enhancement: this is achieved from the diversity due to distinct characteristics of links between a user and all serving transmitters. Moreover, since the user is connected to multiple access points, if one of the links is blocked or suffer from a deep fading, the user keep connected and receiving service from the other transmitters in its serving cluster.

- Energy efficiency improvement: this gain in the energy efficiency results from the relative proximity of the user to its serving cluster. According to [32], compared to single-cell (non-cooperative) massive MIMO systems, this technology can provide more than double the energy efficiency and at the same time significantly improve the per user data rate in suburban and rural environments, while in urban scenarios, the enhancement in the energy efficiency is moderate at less than 50% with the same per user date rate improvement as in suburban and rural scenarios.

Therefore, the user-centric communication systems are considered as a shift from the BS centric cellular design to the concept of a network serving the user. This implies that the entire network optimization process, including resource management, will now be carried out on an individual basis to improve the user performance. This transition from the idea of a network controls the user to a network serves the user entails the disconnection of local and network services. This can be accomplished through the separation of the user serving units and control units, where low-dense large range macro cells work as the control units and highly-dense deployed small cells acting as a data provider for users [33]. Figure 1.2 shows the architecture of the user-centric network in which a cellular user is cooperatively served by a set of BSs, where all BSs are connected to a CU using a backhauling system.

1.3 Objectives and Contributions

The main objective of this thesis is to design advanced dynamic user-centric models for future 5G/beyond 5G (B5G) networks to improve their performances in terms of coverage probability, SE, and EE. In particular, to enable an efficient user-centric

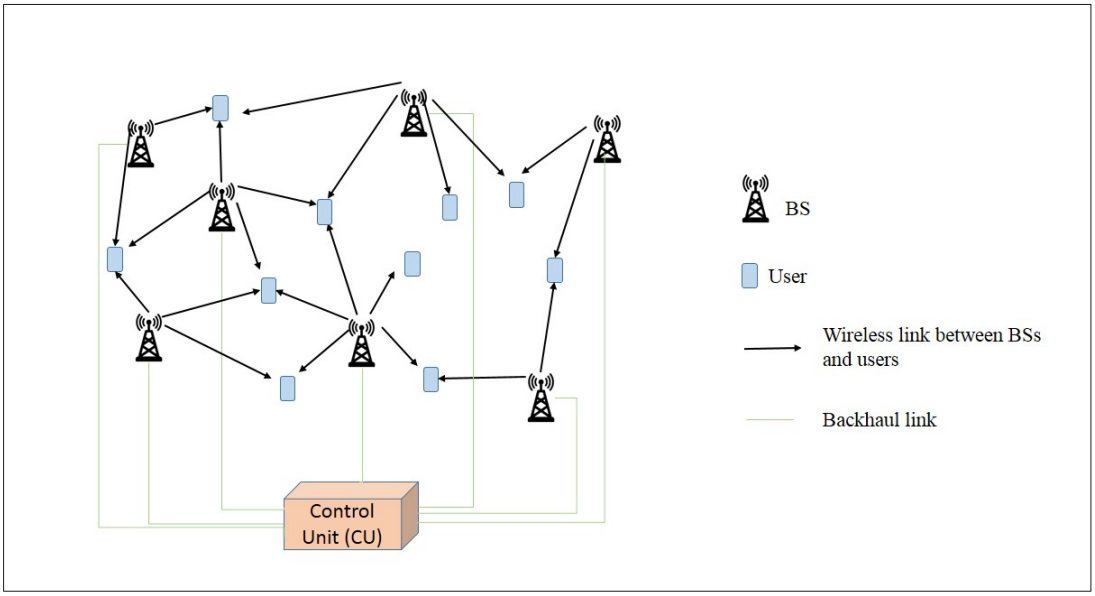

Figure 1.2: User-centric network architecture.

network, we focus in this thesis on the design of dynamic BS clustering models, where a user selects a set of serving BSs based on the channel condition and QoS requirements, with taking into account the network loading capability and spectrum resources constraints. In the existing literature, very limited research has focused on the design of dynamic user-centric technique for future wireless networks. To the best of our knowledge, this is the first work which investigates the implementation of dynamic user-centric clustering for the new promising wireless networks such as mmWave and THz networks, UAV-assisted networks, and energy harvesting networks under the considerations of BS-load and spectrum resources limitation.

While each subsequent cheaper presents a detailed description of an independent contribution, the general contributions of this thesis are listed as follow:

- First, 2D and 3D clustering models are proposed for the design and implementation of user-centric wireless networks under dynamic BS selection in which the user serving cluster is dynamically adapted to its environment and QoS requirement. Unlike a fixed-distance cluster, where the user is served by all BSs within a predetermined cluster of fixed radius, and a fixed-number cluster where the user is cooperatively served by a fixed number of surrounding BSs,

the proposed clustering schemes allow a dynamic selection of serving BSs. This implies that different users can form their own serving clusters with different sizes.

- The proposed dynamic BSs clustering models are used to enable user-centric BS cooperation for networks operating in high frequency bands such as mmWave and THz bands. As a matter of fact, compared to microwave frequencies, dynamic user-centric technique is much more important for networks operating in higher frequency bands. This is because the dynamic clustering can compensate for the high penetration loss in mmWave and THz bands that significantly degrades the link quality and causes the received power from different BSs to be highly changing. Moreover, as communication links in these bands are more sensitive to blockages, the user may easily become in outage due to moving objects. To tackle these problems in future networks operating in mmWave and/or THz frequencies, a user-centric BS cooperation with dynamic clustering is investigated in this thesis.

- We implement user-centric modeling with adaptive cluster size for UAV-enabled wireless networks. Although most of the studies in literature focused on the communication between UAVs and ground BSs or users, there are many applications that require direct connections between UAVs such as exchanging data to avoid collisions between flying elements, enabling UAVs to do joint tasks, offering UAV-to-UAV relays, and forwarding data to terrestrial users. In light of this, we adopt the implementation of user-centric cooperation for UAV networks to provide energy efficient and reliable air-to-air data transmission. Taking into consideration the dynamic locations of flying elements in UAV networks, dynamic cooperative transmissions/receptions is used to mitigate the interference and improve their massive connectivity and coverage capabilities.

- In future architectures of wireless networks, a heterogeneous network (HetNet) is expected to comprise different tiers of BSs such as sub-6 GHz macrocells

and mmWave and THz small cell BSs. Therefore, to design a hybrid user-centric network in this thesis, we propose a hybrid clustering model for a multi-tier network comprising sub-6 GHz, mmWave and THz BSs. In this hybrid user-centric system, each user is associated with the best BS cluster, from either a sub-6 GHz, mmWave or THz tier based on the maximum signal-to-interference-plus-noise-ratio (SINR) criterion or the maximum rate criterion.

- We integrate mmWave and user-centric BS cooperation to enhance the performance of wireless networks with simultaneous wireless information and power transfer (SWIPT) . Due to its large bandwidth, the mmWave communication is leveraged to meet the high data transmission requirement. Moreover, it is shown in [34] that wireless power transfer at mmWave outperforms that at lower frequency bands. This implies that SWIPT-enabled mmWave systems are feasible and suitable for energy efficient communication networks. Furthermore, in addition to improving the downlink data rate, user-centric BS cooperation in mmWave networks is expected to further enhance the wireless power transfer due to the fact that the mmWave transmitters/receivers are equipped with highly directive antennas, and thus the amount of energy that can be harvested from a useful signal is larger than that harvested from the interfering signal.

- By exploiting tools from stochastic geometry, we investigate the performance of the proposed clustering models in terms of SINR and rate coverage probabilities and spectral and energy efficiencies. Since the received signal power and hence the received SINR depend on the distance and nature of the wireless transmission medium, the spatial distribution of transmitting and receiving nodes has a significant impact on the performance of cellular networks. Therefore, a powerful tool is needed to capture this impact of random network geometry. Stochastic geometry is a highly effective mathematical and statistical tool which can be used for modelling, analyzing, and designing wireless networks with unpredictable layouts [35].

- BS clustering optimization frameworks to achieve maximum system performance in terms of spectral efficiency and/or energy efficiency are developed in this thesis by taking into consideration the user distribution and overall network configuration. Such optimization frameworks can provide useful tools for network designers to better characterize and fine-tune the performance of future wireless networks.

1.4 Thesis Organization

The rest of this thesis is organized as follows. Chapter 2 proposes a 2D dynamic BS clustering model to enable user-centric BS cooperation for networks operating in millimeter wave bands, analyze network performances, and provide an optimization framework to maximize the system SE. In Chapter 3, both dynamic and static BS clustering models are presented for user-centric THz networks and their performance is analyzed. The 2D BS clustering model in Chapter 2 is extended to 3D in Chapter 4 and adopted for air-to-air communication networks, where the system model is analytically studied and an optimization problem is formulated to provide maximum system EE. In Chapter 5, the performance of user-centric hybrid sub-6 GH-mmWave-THz network is investigated under dynamic BS clustering. In Chapter 6, we investigate the performance of SWIPT-enabled mmWave system under user-centric BS cooperation. Finally, in Chapter 7, we summarize the contributions of this thesis and suggest future research directions.

Note that throughout the thesis, notations in each chapter are used independently. As such, some notations may appear in two or more chapters while serving different purposes.

Chapter 2

Dynamic Base Station Clustering in User-Centric Millimeter Wave Networks

2.1 Introduction

To meet the fast increasing demands for ubiquitous network services, large capacity, high data rate, massive connectivity, and low latency, and to overcome the shortage of the available spectrum at microwave bands, researchers and engineers have been motivated to make use of the much larger millimeter wave (mmWave) bandwidth (30 - 300 GHz) in mobile networks [36].

Due to large penetration loss and high sensitivity to blockages at mmWave bands, the coverage areas of base stations (BSs) are generally small. This motivates the densification of the network [37] where a large number of BSs are deployed in a small geographical area, making the number of BSs comparable to or even greater than the number of simultaneously served users [38]. However, increasing the BS density will also increase the interference received by a user from the neighboring BSs, which limits the maximum number of BSs to be deployed. To mitigate this interference, a user can be connected to multiple BSs through BS cooperation [39].

In BS cooperation with full joint transmission [40]–[42], all BSs within a given

set (named serving cluster) transmit the same data to the user. This cooperative transmission improves the communication reliability and reduces the amount of interference. In BS cooperation with coordinated beamforming [43], [44], a user coordinates with a cluster of BSs and communicates with only one of the BSs in the cluster without receiving interference from the other in-cluster BSs. To avoid the cell-edge effect and provide a boundaryless communication, a new BS cooperation scheme, namely, user-centric clustering, is introduced where the serving clusters may overlap [45], [46]. This scheme can provide better performance in terms of user throughput [47], which motivates us to investigate the user-centric clustering-based BS cooperation in this chapter.

2.1.1 Background and Related Works

The performance of user-centric networks using microwave frequency communications was investigated in [48]–[51] based on the concepts of stochastic geometry. In [48], the user at the center/origin is served by all BSs within a circle of a predetermined radius. The authors of [49] studied the spectral efficiency of heterogeneous networks under non-coherent joint transmission BS cooperation. In [50], the authors proposed a user-centric power control strategy, where the user is served only by one BS with the largest power while the other BSs in the cluster make use of power control coefficients to mitigate the strong interfering signals. The authors of [51] investigated two user-centric clustering schemes: number-based cooperation that uses a fixed number of serving BSs and distance-based cooperation that fixes the radius of the user's serving cluster, i.e, the radius of the circle centered at the user and contains all serving BSs, and then studied the tradeoff between handoff cost and data rate of the cell-edge users. The area spectral and energy efficiencies of a user-centric cloud radio access network (C-RAN) are investigated in [52] by implementing an iterative clustering algorithm to search for the best serving BS within a cluster of a given radius.

The performance of BS cooperation in mmWave has been studied in the literature [53]–[57]. In [53], a BS clustering scheme where a user is connected to a fixed

number of BSs is proposed. The authors addressed the effect of different network and system parameters, such as blockages, BS density, and antenna arrays, on the coverage probability performance. Numerical results in [53], interestingly, show that BS cooperation provides minimal performance improvements in sparse mmWave networks, i.e. with low BS density and high blockage. In [54], a BS selection scheme based on a two-level procedure is proposed for multi-tier networks. In the first-level a set of candidate BSs, which belong to different tiers, is pre-selected while in the second-level, the user selects from the pre-selected set the BS with the highest signal-to-interference-plus-noise ratio (SINR). The authors of [55], [56] used stochastic geometry tools to develop analytical expressions for the coverage probability and the ergodic capacity of mmWave user-centric networks. In [57], two schemes of BS cooperation, namely, fixed-number BS cooperation and fixed-region BS cooperation, were proposed to reduce the outage probability and enhance the downlink rate.

The aforementioned works studied the performance of user-centric networks under static clustering, where either the number of serving BSs or the radius of the cluster is fixed. Although user-centric techniques with static clustering do not incur significant costs in terms of implementation complexity and network overhead compared to dynamic clustering, they often achieve poorer performance [58]. Indeed, in static clustering, using a large cluster size may result in redundant connections and hence waste the network resources. On the other hand, small cluster sizes may cause some users to be in outage. Therefore, the dynamic clustering policy in which the cluster size, namely, the number of serving BSs or the radius of the user's serving cluster, is selected according to the user requirements and network configurations is seen as a promising solution.

Dynamic clustering approaches for microwave frequencies were proposed in [58]–[61]. The authors of [58] presented three different approaches of dynamic and adaptive clustering to determine the set of serving or nulling BSs in a user-centric network and evaluated the performance of their approaches by simulation. In [59], dynamic clustering algorithms are proposed to enhance the overall downlink system perfor-

mance. In [60], a dynamic user-centric clustering algorithm for uplink cooperation is implemented to improve the cell-edge user achievable data rate. A joint dynamic user-centric clustering and frequency allocation algorithm is proposed in [61] to maximize the coverage probability of ultra-dense networks. Generally speaking, these algorithms suffer from relatively high complexity which increases with the density of deployed BSs, the number of BS antennas, and the user density. The authors of [58]–[61] evaluated their approaches by simulation only. More importantly, they focused on microwave frequency bands, where some inherent issues of mmWave networks (such as the channel characteristics, the sensitivity to blockages, and the antenna directional beamforming) have not been addressed.

2.1.2 Motivations and Contributions

The above observations unveiled the advantages of user-centric dynamic BS clustering techniques. The performance evaluation for the user-centric networks in mmWave bands is still an open issue. In fact, compared to microwave frequencies, user-centric clustering is more important for networks operating in mmWave bands because it can compensate for the high penetration loss in such bands. Moreover, as mmWave links are more sensitive to blockages, the user may easily fall in outage due to moving objects and hence a joint transmission scheme with dynamic clustering is strongly recommended. Motivated by these observations, in this chapter, the performance of mmWave user-centric networks with dynamic clustering is analytically studied using stochastic geometry theory. Our main contributions are summarized as follows:

- We propose a dynamic clustering model to enable user-centric BS cooperation in mmWave networks. Our model is based on the path loss between the user and the BSs while the size of the serving cluster is controlled using a single clustering parameter.

- Unlike [56], where the serving cluster has a fixed radius, and [55] where the number of serving BSs is fixed, our clustering model allows a dynamic selection

of BSs. This implies that different users can form their own serving clusters with different sizes.

- With the aid of stochastic geometry, we investigate the coverage probability and average spectral efficiency using the proposed dynamic clustering model under the BS-load and resources limitation considerations.

- We develop an optimization framework for computing the clustering parameter to maximize the system performance in terms of average spectral efficiency.

- Numerical and simulation results are provided to show the performance of our proposed clustering model and to validate our theoretical analysis.

To the best of our knowledge, this chapter provides for the first time analytical expressions for the coverage probability and spectral efficiency of the user-centric mmWave network under dynamic BS clustering. From a complexity standpoint, our clustering model only requires to optimize a single parameter to be used by all the users. It is worth-mentioning that the dynamic clustering schemes existing in literature [59]–[61], are implemented through iterative greedy algorithms in which the optimization complexity increases with the the number of BSs and users. In contrast, our clustering approach is optimized offline through the efficient analytical framework.

The rest of this chapter is organized as follows. The system model is described in Section 2.2. Section 2.3 is devoted to the coverage probability analysis. In Section 2.4, we develop an analytical expression for the average spectral efficiency and propose an optimization framework for the clustering parameter. Numerical and simulation results along with necessary discussions are provided in Section 2.5. Finally, we conclude the chapter in Section 2.6.

Notations: $\Gamma(a,x)=\int_a^\infty t^{x-1}e^{-t}dt$ denotes the incomplete gamma function [62] and $\Gamma(x)=\Gamma(0,x)$. ${}_pF_q(.)$ is the generalized hypergeometric function [62]. $\mathrm{P}(A)$ represents the probability of event A. $\Delta_X(s)$ and $\Xi_Z(s)$ are the Laplace transform of the random variable X and that of the sum of random variables Z, respectively,

and $\mathbb{E}_X[\cdot]$ is the expectation over X. Other commonly used symbols are summarized in Table 2.1.

Table 2.1: Table of Notations

Symbol	Description
Φ_b, λ_b	BS PPP and density.
Φ_u, λ_u	User PPP and density.
Φ_b^L, Φ_b^N	LOS and NLOS BS PPPs.
α_L, α_N	Path loss exponent for the LOS and NLOS links.
δ	System clustering parameter.
τ	Minimum path loss
Φ_b^S	Typical user's serving cluster.
$\lvert\zeta_k\rvert^2$, $\lvert\zeta_j\rvert^2$	Channel gain of the k-th serving link and j-th interfering link.
m_L,m_N	Nakagami channel parameter for the LOS and NLOS links.
r_k, r_j	Distance to the k-th serving BS and to the j-th interfering BS.
G_M,G_S	Main-lobe and side-lobe gains of the BS antenna arrays.
θ_w	Beamwidth of the BS antenna arrays.
σ^2	Thermal noise power normalized by the BS transmitted power.
A_L, R_L	Average LOS area of the typical user and its average radius.
ψ	Maximum load or number of available resources.
T	SINR threshold.
κ	Selection probability of the typical user.
ρ	BS-user density ratio.
$\bar{c}, \bar{G}$	Maximum and average total gain between the typical user and a BS.
r	Distance from the typical user to the closest LOS BS.
S	Sum of useful signal powers received by the typical user.
I	Sum of interfering signal powers received by the typical user.
n_b	Average number of BSs in A_L.
n_u	Average number of users in A_L.

2.2 System Model

In this section, we discus in detail the system model that is proposed in this chapter.

2.2.1 Network and Channel Models

We consider the downlink of an outdoor dense mmWave network where users and BSs are modeled as two independent homogeneous Poisson point processes (PPPs) $\Phi_u = \{x_i\} \in \mathbb{R}^2$ and $\Phi_b = \{y_k\} \in \mathbb{R}^2$ with densities λ_u and λ_b, respectively, x_i and y_k being the coordinates of the i-th user and the k-th BS. Each user is served by a cluster of cooperative BSs that jointly transmit the same data. By using the Slivnyak theorem [63], without loss of generality, a typical user can be assumed to be located at the origin $(0, 0) \in \mathbb{R}^2$.

Denote the small-scale channel coefficient of the link between the typical user and the k-th BS by ξ_k, which is assumed to follow Nakagami-m distribution where m indicates the degree of fading severity. In mmWave line-of-sight (LOS) links, the number of scatterers is relatively small and hence, the fading is less severe or the value of m is relatively larger and is typically modeled by a Rice fading [64], which can be well approximated by the Nakagami-m model with parameter $m = \frac{(K+1)^2}{2K+1}$, where K is the Rician factor [65]. Conversely, the parameter m for the non-LOS (NLOS) link is smaller [66]. Therefore, several works (e.g. [55], [66], [37]) have suggested Nakagami-m fading, a general yet tractable model for mmWave bands. Although there are some other accurate cluster-based channel models, e.g., [67], yet they are found to be mathematically intractable. Under the Nakagami-m fading assumption, the small-scale channel gain $|\zeta_k|^2$ is a normalized independent and identically distributed (i.i.d.) Gamma random variable (r.v.) with $|\zeta_k|^2 \sim \Gamma(m_v, 1/m_v)$, where $m_v, v \in \{L, N\}$, are the Nakagami-m parameters for LOS and NLOS links. Then, the probability density function (PDF) of the power fading $|\zeta_k|^2$ is expressed as

$$f_{|\zeta_k|^2}(x) = \frac{m_v^{m_v}}{\Gamma(m_v)} x^{m_v-1} e^{-m_v x}, \quad x > 0 \tag{2.1}$$

where $\Gamma(\cdot)$ is the Gamma function.

2.2.2 Directional Beamforming

To compensate for the high path loss and to reduce the effect of co-channel interference in mmWave frequency bands, all BSs are equipped with highly directional beamforming antenna array. In this chapter, we consider a sectored antenna model to mathematically define the antenna array patterns of the BS. This model is widely used in the literature (e.g. [68], [69]) due to its analysis tractability. It describes the antenna array pattern using two constant values, G_M and G_S, for the main-lobe and all back and side-lobes, respectively. Therefore, the antenna gain G in an arbitrary direction is expressed as

$$G = \begin{cases} G_M, & |\theta| \leq \frac{\theta_w}{2} \\ G_S, & \text{otherwise} \end{cases} \tag{2.2}$$

where θ denotes the angle of the boresight direction which is modeled as a random variable uniformly distributed in $[-\pi,\ \pi]$ and θ_w is the antenna beamwidth. The user is equipped with a single omnidirctional antenna with unity gain and thus is able to receive multiple beams from different BSs. As such, the total antenna gain of an arbitrary link between the user and a BS is modeled as a discrete random variable $G = \{G_M,\ G_S\}$ with probability $p_G = \{\frac{\theta_w}{2\pi},\ \frac{2\pi-\theta_w}{2\pi}\}$. We assume that all BSs can perfectly estimate the channel fading and the angles of arrivals (AoA) and are capable of adjusting accordingly their antenna steering orientations to provide the maximum directivity gain [56], [66], [70].

2.2.3 Dynamic BS Clustering Model

Here we propose a new paradigm of dynamic BS clustering. To enable user-centric BS clustering, the typical user uses the lowest average path loss $\tau = \min_{k \in \Phi_b} \mathrm{PL}(r_k)$ as a user-side information, where $\mathrm{PL}(r_k)$ is the path loss of the k-th BS and $r_k = \| y_k \|$ is its distance to the typical user. Using τ, the user forms its serving cluster as defined by

$$\Phi_b^S = \{y_k \in \Phi_b,\ \tau \leq \mathrm{PL}(r_k) \leq \frac{\tau}{\delta}\}, \tag{2.3}$$

where $\delta \in [0, 1]$ is the system clustering parameter which can be tuned for optimizing the system performance. Without loss of generality, we assume that for the typical

user, the path loss function is $\mathrm{PL}(r_k) = r_k^{\alpha}$, where α is the path loss exponent. This clustering policy ensures that all BSs with sufficiently small path loss are assigned into the serving cluster. As shown in Fig. 2.1, a user is connected to all the BSs

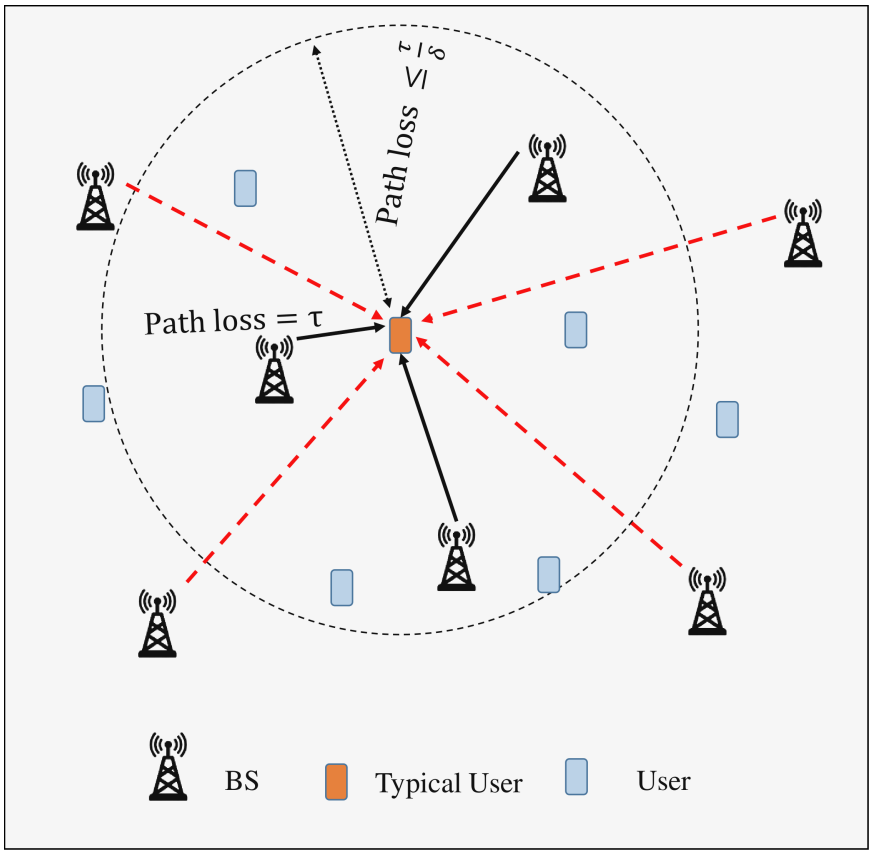

Figure 2.1: System model

with path loss $\leq \frac{\tau}{\delta}$ (black solid arrows) while all other BSs with path loss $> \frac{\tau}{\delta}$ (red dashed arrows) represent the interferers. In contrast to the static clustering approaches reported in [55], [56], (2.3) enables dynamic and adaptive selection of BSs according to network configurations and the user's channel condition (i.e., path loss). Indeed, as will be discussed in Section 2.4, δ can be tuned according to the system status such as users' and BSs' densities, path loss exponents, and maximum load. Optimally choosing δ to achieve maximum performance under the BS-load and resource limitation considerations is a crucial issue for the proposed user-centric network, and constitutes one of the main contributions of this chapter.

All signals are transmitted using the mmWave bands and hence the blockages

cause substantial differences in LOS and NLOS path loss characteristics. For a given user, BSs can be divided into two independent non-homogenous PPPs based on their propagation paths to the user. We have a set of LOS BSs denoted by Φ_b^L with density function $\lambda_b P_{\text{LOS}}$ and a set of NLOS BSs denoted by Φ_b^N with density function $\lambda_b(1 - P_{\text{LOS}})$, where P_{LOS} is the probability of having a LOS propagation path. For the k-th BS, the two normalized path losses for LOS and NLOS propagation paths can be, respectively, written as [71]

$$\text{PL}^L(r_k) = r_k^{\alpha_L} \tag{2.4}$$

and

$$\text{PL}^N(r_k) = r_k^{\alpha_N}, \tag{2.5}$$

where α_L and α_N denote the LOS and NLOS path loss exponents, respectively. In fact, increasing the BS density will decrease the distances to serving BSs and in turn increases the probability of the serving BS being LOS. Recall that based on (2.3), the user is connected to BSs with low path loss and that in mmWave bands the path loss of NLOS links is very high compared to that of LOS links. Therefore, with dense BS deployment in mmWave networks, it is reasonable to assume that the links between serving BSs and the user are LOS [37], [66]. This assumption will be justified in Section 2.5, based on the probability mass function (PMF) of the number of BSs within the typical user's serving cluster as shown in Fig. 2.2. Accordingly, in dense mmWave networks, the user-centric clustering model in (2.3) becomes

$$\Phi_b^S = \{y_k \in \Phi_b^L, \tau \leq \text{PL}^L(y_k) \leq \frac{\tau}{\delta}\}. \tag{2.6}$$

Hereafter, for the sake of tractability, we simplify the analysis by approximating a general LOS probability function by a step function [66]. Essentially, the LOS probability of the link is taken to be one within a certain fixed radius R_L and zero outside. This blockage model is shown to be flexible and tractable yet accurate enough to capture the features of the blockage effects in mmWave bands by the field measurements [37], [72].

From (2.6), it is clear that given the nearest LOS BS which provides the lowest path loss at a distance $r \in [0, R_L]$ from the typical user, the maximum distance to the

farthest serving BS, i.e. the serving cluster radius, is $r\delta^{\frac{-1}{\alpha_L}}$ for $r \in \mathcal{R}_1 = [0, R_L\delta^{\frac{1}{\alpha_L}}]$ or R_L for $r \in \mathcal{R}_2 = [R_L\delta^{\frac{1}{\alpha_L}}, R_L]$. Accordingly, we can define two cases of the serving cluster Φ_b^S as follows:

Case 1, $\Phi_b^S \subsetneq \Phi_b^L$

it means only a subset of LOS BSs can serve the user while the other LOS BSs are considered as interferers. This case may dominate when the network is deployed with high BS density and/or with small average cluster size (i.e., small average number of serving BSs).

Case 2, $\Phi_b^S = \Phi_b^L$

it implies that all LOS BSs can jointly serve the user. This is the extreme case which unlikely happens where the serving cluster becomes saturated and static. This may occur in low density networks and/or large average cluster size.

2.3 System Performance Analysis

In this section, the coverage probability performance of user-centric mmWave network using the proposed clustering model is studied under the consideration of BS loading and random user distribution. To proceed, we first develop theoretical expressions for the selection probability and the received SINR of a typical user as well as the Laplace transforms of the signal and interference components. We then derive the coverage probability expression under the proposed dynamic clustering model.

2.3.1 Typical User Selection Probability

Considering that the users are randomly distributed and the selection of serving BSs for a user depends on the user's channel condition, the serving clusters of different users may overlap, i.e. a BS may join two or more clusters. Therefore, the interference a typical user experiences can be a sum of: 1) interference received

from BSs outside the user's serving cluster and 2) interference received from BSs within the user's serving cluster that arises when a BS simultaneously serve other users using the same non-orthogonal resources. In order to avoid the interference from BSs within the user's serving cluster, we assume that the overlapped clusters are assigned different orthogonal resources [73] and thus the maximum number of clusters a BS can join depends on the available orthogonal resources. To this end, efficient resource allocation is needed to mediate the computational complexity and network performances [73]. However, the resource allocation issue is beyond the scope of this chapter.

According to our clustering model, a user sends serving request to all BSs satisfying (2.6) but not all BSs may accept to serve the user. In general, increasing the cluster size allows more BSs to join the user's serving cluster, yet it also increases the load of each BS that is simultaneously serving multiple users in the network. Therefore, due to the limited available resources, a BS may not accept all requests from users. Indeed, if a BS is fully-loaded, it will deny the requests. To address this issue, we introduce a parameter, κ, named *selection probability* which determines the probability of a user being selected/accepted by a BS. With all users having an equal probability to receive services (or having an equal share of resources), we can obtain the following lemma for the selection probability of the typical user when all users, distributed as Φ_u with density λ_u, request service.

Lemma 2.3.1 *With PPP-modeled users, the selection probability of the typical user is given by*

$$\kappa = \begin{cases} \frac{\Gamma\left(\psi, \frac{1}{\rho}\delta^{\frac{-2}{\alpha_L}}\right)}{(\psi-1)!}, & \Phi_b^S \subsetneq \Phi_b^L \\ \frac{\Gamma\left(\psi, \pi R_L^2 \lambda_u\right)}{(\psi-1)!}, & \Phi_b^S = \Phi_b^L \end{cases} \tag{2.7}$$

where ρ denotes the BS-user density ratio and ψ is an integer number representing the maximum load (i. e., the maximum number of users that can be simultaneously served) of the BS.

Proof: see Appendix 2.7.1.

The first expression in (2.7) shows that the selection probability is a function of both δ and ρ, which is the normal clustering case. Intuitively, a small value of δ allows more BSs to join the user's serving cluster implying that more resources are allocated to the user, but meanwhile it allows more users to be connected to each BS which will reduce the user selection probability. Therefore, from a network perspective, there exists an optimal δ for the proposed user-centric BS clustering that maximizes the system performance. The second expression in (2.7) refers to an extreme clustering scenario where all LOS BSs are selected to form the serving cluster.

2.3.2 Received SINR at a Typical User

In this chapter, we consider a non-coherent joint transmission, where a user's signal is sent by a set of cooperating BSs without requiring a phase correction or strict synchronization among BSs. At the user side, an opportunistic power gain is obtained by combining the received signals non-coherently [41], [57]. According to [41], [74], non-coherent JT outperforms its coherent counterpart by providing some important features for future heterogeneous cellular networks such as its lower design complexity for both the backhaul and channel feedback and its capability to perform load balancing. The instantaneous SINR at the typical user is given by

$$\text{SINR} = \frac{\sum_{k\in\widetilde{\Phi}_b^S} G_k|\zeta_k|^2\text{PL}^L(r_k)}{\sum_{i\in\Phi_b^L\setminus\widetilde{\Phi}_b^S} G_i|\zeta_i|^2\text{PL}^L(r_i)+\sum_{j\in\Phi_b^N} G_j|\zeta_j|^2\text{PL}^N(r_j)+\sigma^2}, \tag{2.8}$$

where $\widetilde{\Phi}_b^S$ is a thinned process of Φ_b^S with density $\kappa\lambda_b$ which contains all BSs that jointly transmit signals to the user whereas the BSs in $\Phi_b\setminus\widetilde{\Phi}_b^S = \Phi_b^N \bigcup\{\Phi_b^L \setminus \widetilde{\Phi}_b^S\}$ are treated as external interfering source. Moreover, r_k denotes the Euclidian distance from the k-th serving BS located at y_k in Φ_b to the user, G_k is the total antenna gain of the k-th BS. In the denominator, the first and second terms represent the LOS and NLOS interferences, respectively, while σ^2 is the thermal noise power normalized by the BS transmitted power.

2.3.3 Laplace Transform Analysis

Before conducting the coverage probability analysis, we first provide the Laplace transform expressions for the signal and interference parts. Let the SINR expression in (2.8) be rewritten as $SINR = \frac{S}{I+\sigma^2}$, where S and I denote the aggregated signal and interference, respectively. Then, conditioned on the existence of BSs in $B(0, R_L)$ with the nearest LOS BS at a distance r from the typical user, S and I and their Laplace transforms for the two cases of the user's serving cluster are given as follows.

Case 1, $\Phi_b^S \subsetneq \Phi_b^L$

The aggregated signal in this case can be defined as $S = F + U$, where $F = G|\zeta|^2 \mathrm{PL}^L(r)$ is the signal power received from the closest BS, and $U = \sum_{k \in \widetilde{\Phi}_b^S \setminus B(0,r)} G_k|\zeta_k|^2 \mathrm{PL}^L(r_k)$ represents the aggregated signal powers received from the other BSs in $\widetilde{\Phi}_b^S$. On the other hand, the aggregated interference is $I = I_L + I_N$, where $I_L = \sum_{i \in \Phi_b^S \setminus \widetilde{\Phi}_b^S} G_i|\zeta_i|^2 \mathrm{PL}^L(r_i) + \sum_{j \in \Phi_b^L \setminus \Phi_b^S} G_j|\zeta_j|^2 \mathrm{PL}^L(r_j)$ is the LOS interference, and $I_N = \sum_{j \in \Phi_b^N} G_j|\zeta_j|^2 \mathrm{PL}^N(r_j)$ is the NLOS interference. Note that the LOS interference in this case results from the BSs within Φ_b^S that denied to serve the user and also from all LOS BSs outside Φ_b^S. The Laplace transform expressions for the signal and interference components are then provided in the following Lemma.

Lemma 2.3.2 *Given $\Phi_b^S \subsetneq \Phi_b^L$ with the closest BS at a distance r, the Laplace transforms of F, U, I_L, and I_N denoted by $\Delta_{F|r}(s)$, $\Xi_{U|r}(s)$, $\Xi_{I_L|r}$, and $\Xi_{I_N|r}(s)$, respectively, are given by*

$$\Delta_{F|r}(s) = \left(1 + \frac{s\bar{c}r^{-\alpha_L}}{m_L}\right)^{-m_L}, \tag{2.9}$$

$$\Xi_{U|r}(s) = \exp\left(-\frac{2\pi\kappa\lambda_b s\bar{c}}{r^{\alpha_L-2}(\alpha_L-2)}\left(\mathcal{F}_L\left(-\frac{s\bar{c}r^{-\alpha_L}}{m_L}\right) - \frac{\mathcal{F}_L\left(-\frac{s\bar{c}\delta r^{-\alpha_L}}{m_L}\right)}{\delta^{\frac{-\alpha_L+2}{\alpha_L}}}\right)\right), \tag{2.10}$$

$$\Xi_{I_L|r}(s) = \exp\Bigg\{ -\frac{2\pi s\lambda_b}{\alpha_L-2}\sum_G p_G G\Bigg(\frac{(1-\kappa)\mathcal{F}_L\Big(-\frac{sG}{r^{\alpha_L}m_L}\Big)}{r^{\alpha_L-2}} + \frac{\kappa\mathcal{F}_L\Big(-\frac{sG\delta r^{-\alpha_L}}{m_L}\Big)}{\delta^{\frac{-\alpha_L+2}{\alpha_L}} r^{\alpha_L-2}} - \frac{\mathcal{F}_L\Big(-\frac{sGR_L^{-\alpha_L}}{m_L}\Big)}{R_L^{\alpha_L-2}}\Bigg)\Bigg\}, \tag{2.11}$$

and

$$\Xi_{I_N|r}(s) = \exp\left(-\frac{2\pi\lambda_b s}{\alpha_N-2}\sum_{k=1}^{4} p_G G\frac{\mathcal{F}_N\Big(-\frac{sGR_L^{-\alpha_L}}{m_N}\Big)}{R_L^{\alpha_N-2}}\right), \tag{2.12}$$

where

$$\mathcal{F}_v(z) = {}_3F_2\left(m_v+1, 1, 1-\frac{2}{\alpha_v}; 2, 2-\frac{2}{\alpha_v}; z\right), \tag{2.13}$$

with $v \in \{L, N\}$ *and* ${}_3F_2(.)$ *standing for the hypergeometric function [62].*

Proof: See Appendix 2.7.2.

Case 2, $\Phi_b^S = \Phi_b^L$

In this case, the aggregated signal and interference can be expressed as $S = F + \widetilde{U}$ and $I = \widetilde{I}_L + I_N$, respectively, where F and I_N are defined as in Case 1, $\widetilde{U} = \sum_{k\in\Phi_b^L\cap\widetilde{\Phi}_b^S\setminus B(0,r)} G_k|\zeta_k|^2\mathrm{PL}^L(r_k)$ is the sum of signal powers received from all LOS BSs (except the closest one) that accept to serve the user and $\widetilde{I}_L = \sum_{i\in\Phi_b^S\setminus\widetilde{\Phi}_b^S} G_i|\zeta_i|^2\mathrm{PL}^L(r_i)$ is the sum of interfering signal powers received from all LOS BSs within Φ_b^S that denied to serve the user. The Laplace transforms of F and I_N in this case are the same as that expressed in (2.9) and (2.12), respectively, while the Laplace transforms of $\widetilde{U}$ and $\widetilde{I}_L$ are obtained from the following lemma.

Lemma 2.3.3 *Given* $\Phi_b^S = \Phi_b^L$ *with the closest BS at a distance* r*, the Laplace transforms of* $\widetilde{U}$ *and* $\widetilde{I}_L$*, respectively denoted as* $\Xi_{\widetilde{U}|r}(s)$ *and* $\Xi_{\widetilde{I}_L r}(s)$*, are given by*

$$\Xi_{\widetilde{U}|r}(s) = \exp\Bigg\{ -\frac{2\pi\kappa\lambda_b s\bar{c}}{\alpha_L-2}\Bigg(\frac{\mathcal{F}_L\Big(-\frac{s\bar{c}r^{-\alpha_L}}{m_L}\Big)}{r^{\alpha_L-2}} - \frac{\mathcal{F}_L\Big(-\frac{s\bar{c}R_L^{-\alpha_L}}{m_L}\Big)}{R_L^{\alpha_L-2}}\Bigg)\Bigg\}. \tag{2.14}$$

and

$$\Xi_{\widetilde{I}_L|r}(s) = \exp\left\{-\frac{2\pi s(1-\kappa)\lambda_b}{\alpha_L-2}\sum_G p_G G\left(\frac{\mathcal{F}_L\left(-\frac{sGr^{-\alpha_L}}{m_L}\right)}{r^{\alpha_L-2}} - \frac{\mathcal{F}_L\left(-\frac{sGR_L^{-\alpha_L}}{m_L}\right)}{R_L^{\alpha_L-2}}\right)\right\}. \tag{2.15}$$

Proof: See Appendix 2.7.3.

Recalling that BSs are assumed to be capable of adjusting their antenna steering as desired, the total gain of the link between the typical user and the k-th serving BS $G_k = \bar{c}$ is maximum such that $\bar{c} = G_M$.

2.3.4 Coverage Probability

In this subsection, we provide mathematical expressions for the coverage probability of two BS cooperation schemes, using the dynamic clustering model in (2.6), named dynamic joint transmission (JT) and dynamic optimal point selection (OPT) as well as the coverage probability of a non-cooperative transmission scheme called single-BS selection scheme. Mathematically, given an SINR threshold at a typical user, say T, the coverage probability is defined as

$$P_{\text{cov}}(T) \triangleq \mathbb{P}\left(\text{SINR} \geq T\right), \tag{2.16}$$

To proceed, we need to find the distribution of the distance r to the nearest serving BS for the two cases of the user's serving cluster. Given the user's serving cluster is in Case i, $i \in \{1,\ 2\}$, the distribution of the distance r between the user and its closest LOS BS is

$$f_i(r) = \frac{2\pi\lambda_b r}{\chi_i} e^{-\pi\lambda_b r^2}, \tag{2.17}$$

where χ_i is the probability that the user's serving cluster is in Case i, as given by

$$\chi_i = \begin{cases} \chi_1 = 1 - \exp\left(-\pi\lambda_b R_L^2 \delta^{\frac{2}{\alpha_L}}\right), & r \in \mathcal{R}_1; \\ \chi_2 = \exp\left(-\pi\lambda_b R_L^2 \delta^{\frac{2}{\alpha_L}}\right) - \exp\left(-\pi\lambda_b R_L^2\right), & r \in \mathcal{R}_2, \end{cases} \tag{2.18}$$

Dynamic JT

Under this scheme, all BSs within $\widetilde{\Phi}_b^S$ jointly send the same data to the user. To calculate the coverage probability of this scheme, we need to consider the two cases of clustering as follows:

Case 1, $\Phi_b^S \subsetneq \Phi_b^L$

The coverage probability in Case 1 denoted as $\mathcal{P}_1(T)$, is expressed as

$$\begin{aligned}\mathcal{P}_1(T) &= \int_{r\in\mathcal{R}_1}\int_{-\infty}^{\infty}\frac{\Delta_{F|r}(-ws)\Xi_{U|r}(-ws)-1}{ws} \\ &\quad\times\Xi_{I_N|r}(Tws)\Xi_{I_L|r}(Tws)e^{-Tws\sigma^2}f_1(r)dsdr, \end{aligned} \tag{2.19}$$

where $w = 2\sqrt{-1}\pi$ and $\Delta_{F|r}(s)$, $\Xi_{U|r}(s)$, $\Xi_{I_L|r}(s)$, $\Xi_{I_N|r}(s)$, and $f_1(r)$ are given in (2.9), (2.10), (2.11), (2.12), and (2.17), respectively.

Case 2, $\Phi_b^S = \Phi_b^L$

In this case, the coverage probability is given as

$$\begin{aligned}\mathcal{P}_2(T) &= \int_{r\in\mathcal{R}_2}\int_{-\infty}^{\infty}\frac{\Delta(-ws)\Xi_{\widetilde{U}|r}(-ws)-1}{ws} \\ &\quad\times\Xi_{I_N|r}(Tws)\Xi_{\widetilde{I}_L|r}(Tws)e^{-Tws\sigma^2}f_2(r)dsdr, \end{aligned} \tag{2.20}$$

where $\Xi_{\widetilde{U}|r}(s)$, $\Xi_{\widetilde{I_L}|r}(s)$, and $f_2(r)$ are given in (2.14), (2.15), and (2.17), respectively. Now, we are in a position to formalize the coverage probability of a typical user as presented in the following Proposition.

Proposition 2.3.1 *The coverage probability of mmWave networks using the proposed user-centric BS clustering is given by*

$$P_{cov}(T) = \Lambda\Big(\chi_1\mathcal{P}_1(T) + \chi_2\mathcal{P}_2(T)\Big), \tag{2.21}$$

where χ_i and $\mathcal{P}_i(T)$, $i \in \{1,2\}$, are given in (2.18), (2.19), and (2.20), respectively, and Λ is the probability of having at least one LOS BS within $B(0,R_L)$, which is obtained as

$$\Lambda = \mathrm{P}(\Phi_b^L \cap B(0,R_L) \neq \varnothing) = 1 - e^{-\pi\lambda_b R_L^2} \tag{2.22}$$

Proof: Once $\mathcal{P}_i(T)$, $i \in \{1,2\}$ are obtained, calculating the coverage probability $\mathcal{P}_{cov}(T)$ is straightforward with using the law of total probability.

Remark 2.3.1 *Since $\mathcal{F}_v(\delta z)$ in (2.13) increases with δ, $\mathcal{P}_1(T)$ is a strictly monotonically decreasing function of δ. However, the clustering parameter δ cannot be arbitrarily small since the BS load would be unrealistically large according to Lemma 2.3.1. Thus, there exists a tradeoff between coverage probability and BS load.*

Optimal Point Selection (OPS)

In this scheme, only one BS in the serving cluster transmits data to the user while others keep silent. This scheme incurs lower coordination costs than BS cooperation through JT [42]. It is worth-mentioning that our OPS scheme corresponds to an extension of the OPS scheme in [42] where the serving cluster is fixed to three nearest BSs and only one of them serves the user while the other two keep silent. Here, in our scheme, both the serving BS and the cluster size are dynamically adapted according to the user's channel condition. Therefore, given that the OPS scheme is applied to the serving cluster Φ_b^S of the typical user with a prescribed coverage probability threshold T, the coverage probability can be calculated as a special case of the JT schemes. This can be obtained from letting $\Xi_{U|x}(s) = 1$ and $\Xi_{\widetilde{U}|r}(s) = 1$ in (2.19) and (2.20), respectively, and then substitute the results in (2.21). Therefore, we write the coverage probability under dynamic OPS as

$$\widehat{P}_{cov}(T) = P_{cov}(T)_{\left(\Xi_{U|x}(s)\leftarrow 1, \Xi_{\widetilde{U}|r}(s)\leftarrow 1\right)}. \tag{2.23}$$

Single-BS Selection

The coverage probability under single-serving BS selection, where only the LOS BS closest to the user is selected to transmit data, has been previously addressed in [37], [66], for mmWave networks. Exploiting the general expression for the coverage probability under JT scheme developed in this chapter, the coverage probability of the single-BS selection scheme can be easily obtained by letting $\delta = 1$ in (2.10), (2.11) and (2.17) and accordingly computing (2.19) and (2.20) and then substituting

the results into (2.21). Therefore we can write the coverage probability under single-BS selection scheme as

$$\widetilde{P}_{\text{cov}}(T) = \mathcal{P}(T)_{(\delta \leftarrow 1)}, \tag{2.24}$$

where in dense networks, short distances between BSs and users result in their serving (nearest) BSs with $f_1(r) = 2\pi\lambda_b r e^{-\pi\lambda_b r^2}$. Therefore, (2.24) can be simplified to $\widetilde{P}_{\text{cov}}(T) = \mathcal{P}_1(T)_{(\delta \leftarrow 1)}$.

2.4 Average Spectral Efficiency Analysis and Optimization

In this section, we first provide analytical expression of the average spectral efficiency and then optimize the system energy efficiency performance.

2.4.1 Average Spectral Efficiency

This subsection derives a general Average Spectral Efficiency (ASE) expression of the dynamic user-centric BS clustering for the typical user. Given the user's actual serving cluster $\widetilde{\Phi}_b^S$, we can write the ASE as

$$\mathcal{E} = \mathbb{E}_{\Phi_b,|\zeta|^2}\left(\ln\left(1+\frac{\sum_{k\in\widetilde{\Phi}_b^S} G_k|\zeta_k|^2 \text{PL}^L(r_k)}{\sum_{j\in\Phi_b^L\setminus\widetilde{\Phi}_b^S} G_j|\zeta_j|^2\text{PL}^L(r_j)+\sum_{j\in\Phi_b} G_j|\zeta_j|^2\text{PL}^L(r_j)+\sigma^2}\right)\right). \tag{2.25}$$

Note that the ASE can be found by averaging (2.25) over all channel realizations and network configurations. To derive the spectral efficiency, we use the lemma reported in [75], which reads as

$$\ln\left(1+\frac{X}{Y}\right) = \int_0^\infty \frac{e^{-zY}}{z}\left(1-e^{-zX}\right)dz. \tag{2.26}$$

For X and Y are independent random variables satisfying $X \geq 0$ and $Y > 0$, then, we can write

$$\mathbb{E}_{X,Y}\left(\ln\left(1+\frac{X}{Y}\right)\right) = \int_{z>0} \frac{1-\Xi_X(z)}{z}\Xi_Y(z)dz, \tag{2.27}$$

where $\Xi_X(z)$ and $\Xi_Y(z)$ are the Laplace transforms of X and Y, respectively.

Proposition 2.4.1 *The ASE of the user-centric mmWave networks under the proposed BS clustering model in (2.6) is obtained as*

$$\mathcal{E} = \frac{\Lambda}{\ln(2)} \left(\chi_1 \mathcal{E}_1 + \chi_2 \mathcal{E}_2\right), \tag{2.28}$$

in bps/Hz, where $\mathcal{E}_1$ and $\mathcal{E}_2$ are the ASE given the user's serving cluster in Case 1 and 2 , respectively, and are expressed as

$$\mathcal{E}_1 = \int_{r\in\mathcal{R}_1} \int_0^\infty \frac{1-\Delta_{F|r}(s)\Xi_{U|r}(s)}{s} \Xi_{I_N|r}(s)\Xi_{I_L|r}(s) e^{-s\sigma^2} f_1(r) ds dr. \tag{2.29}$$

and

$$\mathcal{E}_2 = \int_{r\in\mathcal{R}_2} \int_0^\infty \frac{1-\Delta_{F|r}(s)\Xi_{\widetilde{U}|r}(s)}{s} \Xi_{I_N|r}(s)\Xi_{\widetilde{I_L}|r}(s) e^{-s\sigma^2} f_2(r) ds dr, \tag{2.30}$$

Proof: Recalling that r is the distance to the nearest BS in Φ_L^S, given the user's serving cluster in Cases 1 and 2, the ASEs can be written as $\mathcal{E}_1|_r = \mathbb{E}_{F,U,I_L,I_N}\big(\ln\big(1+\frac{F+U}{I_L+I_N+\sigma^2}\big)\big)$ and $\mathcal{E}_2|_r = \mathbb{E}_{F,\widetilde{U},\widetilde{I}_L,I_N}\big(\ln\big(1+\frac{F+\widetilde{U}}{\widetilde{I}_L+I_N+\sigma^2}\big)\big)$, respectively. Then, using (2.27) and averaging over the PDF of r, $\mathcal{E}_1$ and $\mathcal{E}_2$ can be, respectively, expressed as in (2.29) and (2.30), where $\Delta_{F|r}(s)$, $\Xi_{U|r}(s)$, $\Xi_{I_L|r}(s)$, $\Xi_{I_N|r}(s)$, $\Xi_{\widetilde{U}|r}(s)$ and $\Xi_{\widetilde{I_L}|r}(s)$ are already obtained in (2.9), (2.10), (2.11), (2.12), (2.14), and (2.15), respectively. Finally, taking the mean of $\mathcal{E}_1$ and $\mathcal{E}_2$, the ASE can be obtained as given by (2.28).

Likewise, the ASE of the user-centric network under dynamic OPS can be written as

$$\widehat{\mathcal{E}} = \mathcal{E}_{\left(\Xi_{U|x}(s)\leftarrow 1, \Xi_{\widetilde{U}|r}(s)\leftarrow 1\right)}, \tag{2.31}$$

while the ASE of a single-BS selection network is obtained from (2.28) as

$$\widetilde{\mathcal{E}} = \mathcal{E}_{(\delta\leftarrow 1)}, \tag{2.32}$$

2.4.2 Average Spectral Efficiency Maximization

In this sub-section, we introduce an analytical framework to determine the optimal δ which maximizes $\mathcal{E}$ in (2.28). To simplify the analysis, we then resort to an analytically tractable upperbound of $\mathcal{E}$. In Section 2.5, it will be shown through numerical study that this upperbound is tight and efficient enough to be used for

the maximization problem as it yields the same optimum values of the clustering parameter as those provided by exact ASE expression. Since the BS density will be large in future mmWave networks, we can consider only Case 1 of the users' serving cluster by ignoring the noise and the NLOS interference and focusing only on the LOS interference-limited regime. Accordingly, the aggregated signal and interference components are, respectively, expressed as $S = \sum_{k\in\widetilde{\Phi}_b^S} \bar{c}|\zeta_k|^2 \mathrm{PL}^L(r_k)$ and $I = \sum_{j\in\Phi_b\setminus\widetilde{\Phi}_b^S} G_j|\zeta_j|^2\mathrm{PL}^L(r_j)$. Given the distance r to the nearest BS, S and I are independent. Since $\mathcal{E}$ in (2.28) is a concave function with respect to δ, by applying the Jensens's inequality, we obtain the following upperbound of $\mathcal{E}$

$$\mathcal{E} \leq \mathbb{E}_r\left[\ln\left(1+\mathbb{E}_{\widetilde{\Phi}_b^S,|\zeta|}\left[\frac{S}{I}\right]\right)\right] \approx \mathbb{E}_r\left[\ln\left(1+\frac{\overline{S}_r}{\overline{I}_r}\right)\right]. \tag{2.33}$$

where $\overline{S}_r = \mathbb{E}_{\widetilde{\Phi}_b^S,|\zeta|}\big[S|r\big]$ and $\overline{I}_r = \mathbb{E}_{\Phi_b\setminus\widetilde{\Phi}_b^S,|\zeta|}\big[I|r\big]$ are, respectively, the means of the aggregated signal and interference for a given r. This implies that decreasing the value of δ is desired from the ASE viewpoint as $\overline{S}_r$ increases and $\overline{I}_r$ decreases with decreasing δ. In fact, this is not always the case since a very small δ will reduce the user selection probability and hence decreasing its ASE. To resolve this dilemma, we formulate the problem below

$$\begin{aligned}\delta_{\mathrm{opt}} = \max_{\delta} \quad & C(\delta) = \frac{\overline{S}_r}{\overline{I}_r} \\ s.t. \quad & 0 \leq \delta \leq 1.\end{aligned} \tag{2.34}$$

For PPP $\widetilde{\Phi}_b^S$ with density $\kappa\lambda_b$ in a 2-dimensional plane, the mean of the total signal power, $\overline{S}_r$, is given by

$$\begin{aligned}\overline{S}_r &= \mathbb{E}_{\widetilde{\Phi}_b^S,|\zeta_k|^2}\Bigg[\sum_{k\in\widetilde{\Phi}_b^S}\bar{c}|\zeta_k|^2\mathrm{PL}^L(r_k)\Bigg] \\ &\overset{(a)}{=} \mathbb{E}_{|\zeta|^2}\Bigg[\bar{c}|\zeta|^2 r^{-\alpha_L} + 2\pi\lambda_b\kappa\bar{c}\int_{t\in\left[r,\, r\delta^{-\frac{1}{\alpha_L}}\right]}|\zeta|^2 t^{-\alpha_L+1}dt\Bigg] \\ &\overset{(b)}{=} \bar{c}r^{-\alpha_L} + \frac{\pi\lambda_b\kappa\bar{c}}{\alpha_L-2}\big(1-\delta^{\frac{\alpha_L-2}{\alpha_L}}\big)r^{-\alpha_L+2},\end{aligned} \tag{2.35}$$

where (a) follows from applying the Campbell theorem [76], and (b) results from using $\mathbb{E}\big[|\zeta|^2\big]=1$. Similarly $\overline{I}_r$ is calculated as

$$\begin{aligned}
\overline{I}_r &= \mathbb{E}_{\Phi^b\setminus\widetilde{\Phi}_b^S}\Bigg[\sum_{j\in\Phi_b^L\setminus\widetilde{\Phi}_b^S} G_j|\zeta_j|^2\mathrm{PL}^L(r_j)\Bigg] \\
&= \mathbb{E}_{|\zeta|^2}\Bigg[2\pi\lambda_b(1-\kappa)\bar{G}\int_{t\in\left[r,\, r\delta^{-\frac{1}{\alpha_L}}\right]}|\zeta|^2 t^{-\alpha_L+1}dt + 2\pi\lambda_b\bar{G} \\
&\quad\times\int_{t\in\left[r\delta^{-\frac{1}{\alpha_L}},\,\infty\right]}|\zeta|^2 t^{-\alpha_L+1}dt\Bigg] \\
&= \frac{2\pi\lambda_b\bar{G}}{\alpha_L-2}\Bigg((1-\kappa)\big(1-\delta^{\frac{\alpha_L-2}{\alpha_L}}\big)+\delta^{\frac{\alpha_L-2}{\alpha_L}}\Bigg)r^{-\alpha_L+2}, \qquad (2.36)
\end{aligned}$$

where $\bar{G}$ denotes the average gain and κ is the selection probability of the typical user obtained in (2.7). By plugging (2.35) and (2.36) into (2.34) and using $\kappa=\frac{\Gamma\left(\psi,\,\frac{1}{\rho}\delta^{\frac{-2}{\alpha_L}}\right)}{(\psi-1)!}$, the optimal solution δ_{opt} can be computed by maximizing $C(\delta)$ below

$$C(\delta) = \frac{\bar{c}r^{-2}+\frac{\pi\lambda_b\bar{c}}{\alpha_L-2}\frac{\Gamma\left(\psi,\,\frac{1}{\rho}\delta^{\frac{-2}{\alpha_L}}\right)}{(\psi-1)!}\big(1-\delta^{\frac{\alpha_L-2}{\alpha_L}}\big)}{\frac{2\pi\lambda_b\bar{G}}{\alpha_L-2}\Bigg(\Bigg(1-\frac{\Gamma\left(\psi,\,\frac{1}{\rho}\delta^{\frac{-2}{\alpha_L}}\right)}{(\psi-1)!}\Bigg)\big(1-\delta^{\frac{\alpha_L-2}{\alpha_L}}\big)+\delta^{\frac{\alpha_L-2}{\alpha_L}}\Bigg)}, \qquad (2.37)$$

Recall that decreasing δ would enlarge the user's serving cluster cardinality and at the same time decrease its selection probability. Considering this and using (2.37), the optimization problem in (2.34) can be simplified as

$$\begin{aligned}
\delta_{\mathrm{opt}} &= \max_{\delta} \quad \widetilde{C}(\delta) \\
&\quad s.t. \quad 0\le\delta\le 1. \qquad (2.38)
\end{aligned}$$

where

$$\widetilde{C}(\delta)=\frac{\Gamma\left(\psi,\,\frac{1}{\rho}\delta^{\frac{-2}{\alpha_L}}\right)}{(\psi-1)!}\big(1-\delta^{\frac{\alpha_L-2}{\alpha_L}}\big). \qquad (2.39)$$

From (2.38), it can be observed that in dense mmWave networks, the computation of optimal δ depends on three system parameters, namely, BS-user density ratio ρ, BS maximum load ψ, and path loss exponent α_L.

Special Case 1): when $\rho\to\infty$, i.e, $\lambda_b\gg\lambda_u$, we have $\delta_{\mathrm{opt}}\to 0$, which implies that when the BS density is extremely high compared to the user density, more resources are available for each user while with a small probability of cluster overlapping.

Special Case 2): when $\rho \to 0$, i.e, $\lambda_b \ll \lambda_u$, then, $\delta_{\text{opt}} \to 1$. In this case, no BS cooperation may occur, indicating that user-centric clustering is not suitable for networks with very low BS density.

Special Case 3): $\psi = 1$. In this case, we have $\kappa = \exp(-\frac{1}{\rho}\delta^{\frac{-2}{\alpha_L}})$ according to (2.7). Then, for $\alpha_L = 3$, the exact optimum value of δ, obtained from maximizing (2.39), is given in closed-form as

$$\delta_{\text{ opt}} = 2\left(\frac{1}{\rho} - \frac{2}{D(\rho)} + \frac{D(\rho)}{3\rho^3}\right), \tag{2.40}$$

where

$$D(\rho) = \left(\rho^{\frac{9}{2}}\sqrt{27(8+27\rho)} - 27\rho^5\right)^{\frac{1}{3}}. \tag{2.41}$$

Clearly, (2.40) demonstrates that δ_{opt} decrease as ρ increases and vice-versa. This is expected since the available resources per user increase with ρ. In such a case, more BSs may join the user's serving cluster. For general values of ρ, ψ, and α_L, the optimal value of δ can be determined through an offline numerical maximization of $\widetilde{C}(\delta)$ in (2.39).

Remark 2.4.1 *Being focused on an analytical method of determining δ_{opt} and optimizing dense networks performances, our approach is therefore much more practically appealing comparing to some existing clustering schemes using iterative algorithms like [59]–[61], which are more complex and computationally heavy. The optimal cluster parameter δ_{opt} can be easily calculated offline given an apriori knowledge of the BS load, ratio of BSs and users densities, and pathloss exponents. Since these parameters are not varying very fast with time, δ_{opt} can still easily be updated online, thereby reducing system overhead and computational complexity compared to the existing iterative algorithms. Furthermore, the mechanism required for the implementation of the proposed clustering scheme is simple. The network broadcasts the value of δ_{opt} which is calculated using the proposed analytical expressions for the given system parameters. Then the user selects its serving BSs based on δ_{opt} and informs the network.*

Remark 2.4.2 *In practical scenarios, the tradeoff between spectral efficiency and energy efficiency is of tremendous importance as driven by the rise of green cellular networks. In this respect, based on the analytical result of the ASE in Proposition 2.4.1, determining the optimal value of the clustering parameter which minimizes the area power consumption while satisfying the minimum required spectral efficiency is more important in reality and will be left for future investigation.*

2.5 Numerical Results and Discussion

In this section, numerical and simulation results are shown to validate our analytical framework proposed in this chapter. Unless otherwise specified, the system parameters are listed in Table 2.2. Here, we use A_L to denote the user's average LOS area which can be calculated as $A_L = \pi R_L^2$. Therefore, if the average number of BSs or users in A_L is $n_a, a \in \{b, u\}$, then the corresponding BS or user density is n_a/A_L.

Table 2.2: System Parameters

Parameters	Values
Operating frequency	28GHz
Bandwidth	100MHz
Nakagami parameters ($m_L,\ m_N$)	(3, 2)
LOS and NLOS path loss exponents ($\alpha_L,\ \alpha_N$)	(2.2, 4)
Average LOS range, R_L	200m
BS antenna arrays parameters ($G_M,\ G_S,\ \theta_w$)	(20dB, 0dB, 45^o)
BS transmit power	30 dBm
Noise power	-94 dBm

First of all, to justify the proposed BS clustering model in (2.6), we compute the PMF of the number of serving BSs (the serving cluster size) of the typical user in dense mmWave network in Fig. 2.2. Two cases are assumed: when the user can connect to both LOS and NLOS BSs and when only LOS BSs are connected. The

results are obtained by Monte Carlo simulation using 10^5 network realizations. In this figure, we use the rectangle Boolean scheme to model the blockage effect [77] with blockage parameter $\beta = 0.0071$. The figure shows that in dense millimetre wave networks, with high probability, there is always at least one LOS BS serving the user and that considering NLOS BSs has no effect on the PMF of the number of BSs within the user's serving cluster.

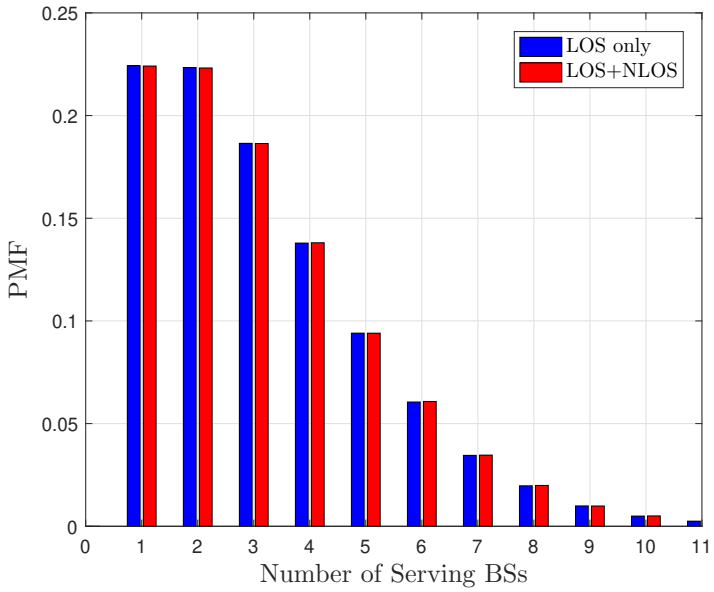

Figure 2.2: PMF of the number of BSs cooperatively serving the typical user in user-centric mmWave network with BS density $\lambda_b = 6.36 \times 10^{-5}$ (corresponding to the minimum BS density used in the this section) and clustering parameter $\delta = 0.15$.

Fig. 2.3 plots the coverage probability performance of the typical user achieved by the proposed user-centric clustering model in (2.6). For comparison purposes, the coverage probabilities of three different transmission schemes, namely, dynamic JT (using (2.21)), dynamic OPS (using (2.23)), and single-serving BS (using (2.24)) are plotted. With dynamic clustering for $\delta = 0.25$, the SINR achieved by the typical user exceeds 25 dB with probabilities 0.58 and 0.49 for JT and OPS, respectively, while for the single-serving BS selection the typical user exceeds the same SINR level with probability 0.25. This proves the efficiency of the proposed clustering model and highlights the dramatic performance improvements it may provide. Again from the

clustering model in (2.6), it can be seen that the coverage probability increases with mean cooperative range $\left[r, r\delta^{\frac{-1}{\alpha_L}}\right]$ which decreases with δ. Indeed, larger cluster size leads to higher useful signal strength and lower interference. However, this figure also shows that the coverage probability for $\delta = 0.25$ is better than that for $\delta = 0.15$. This is because a very small value of δ also means a large number of users sending serving requests to a BS which reduces the probability of accepting the typical user request by the BS.

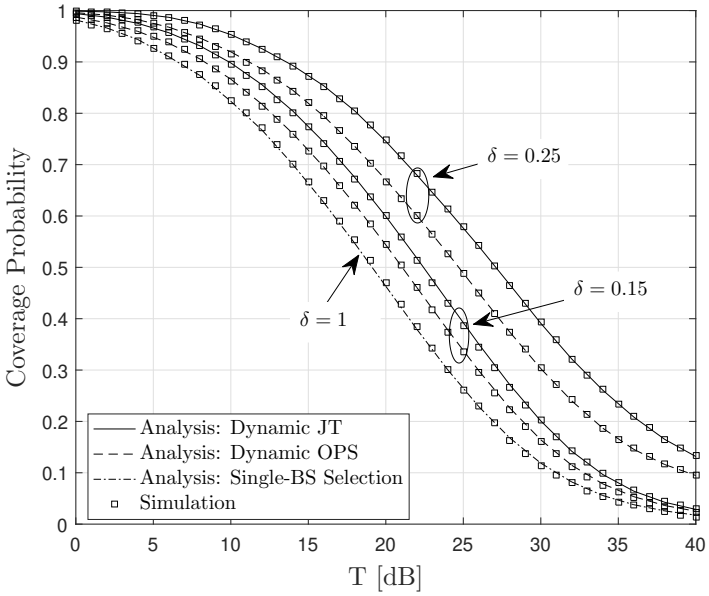

Figure 2.3: Coverage probability versus the SINR threshold T for dynamic JT, dynamic OPS, single-BS selection network for different values of δ with $\rho = 0.33$ and $n_b = 8$.

In order to elucidate the network performance as a function of the clustering parameter δ, we compute the ASE for the dynamic JT according to (2.28) and for the dynamic OPS according to (2.31). Fig. 2.4 shows the effect of δ on the ASE for different values of the BS-user density ratio, ρ. It can be seen that for a fixed ρ, there exists an optimal value δ_{opt} which maximizes the ASE. Meanwhile, this optimal value δ_{opt} decreases with increasing ρ. This is because as ρ increases more BSs may join the typical user's serving cluster, thereby decreasing δ_{opt} or increasing the serving cluster radius. Recall that the value of δ cannot be too small, otherwise, more

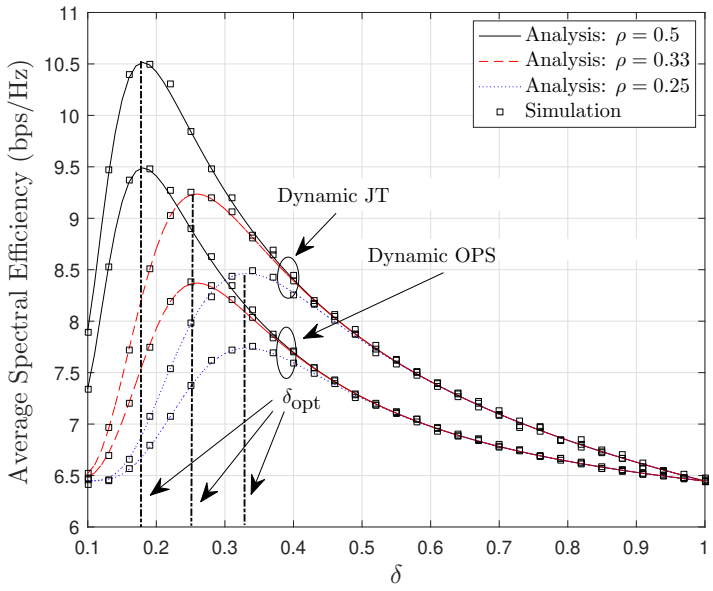

Figure 2.4: ASE versus the clustering parameter δ for the dynamic JT and OPS user-centric network for different values of ρ. with $n_b = 8$

.

users would request BS services, thereby degrading the system ASE performance. This result gives us an insight in determining appropriate δ from the perspective of ASE. Fig. 2.4 also shows that the dynamic JT approach always outperforms the dynamic OPS approach in terms of the ASE as well. Interestingly, according to Fig. 2.4, the performance variations around δ_{opt} are small especially for small values of ρ. Hence, small deviations from δ_{opt} due to quantization errors or environmental changes results in a negligible loss in the performance, which entails the practical feasibility of our clustering method.

Fig. 2.5 shows the coverage probability performances of the dynamic JT and OPS cooperative schemes with comparison to the non-cooperative scheme, i.e. single-selection, for different values of R_L, with $\delta = 0.4$ and $\psi = 10$. In this figure, to insure the BS density is high enough to benefit from using the proposed user-centric clustering schemes, we use $n_b = 8$ for $R_L = 200$ which leads to $n_b \approx 4$ for $R_L = 140$. This figure demonstrates that with dense BS deployments, a decrease in R_L would increase the coverage probability performance. This can be simply interpreted as

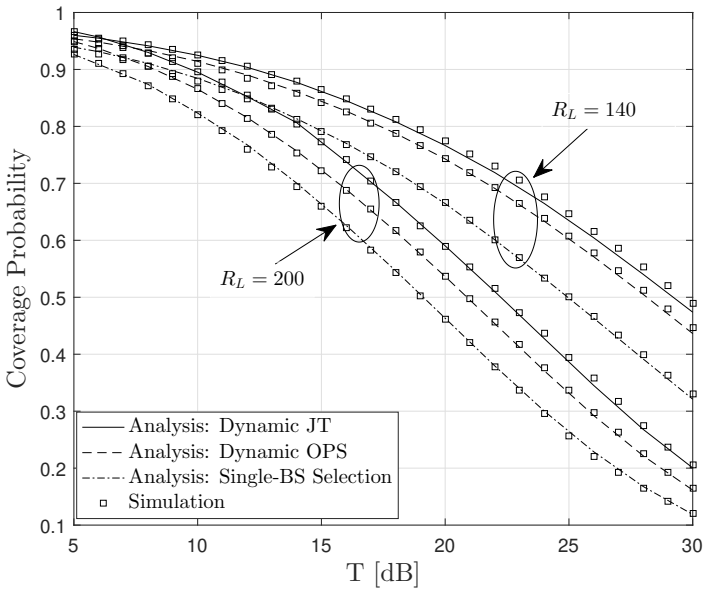

Figure 2.5: Coverage probability versus the SINR threshold T for dynamic JT, dynamic OPS, and single-BS selection network for different values of R_L with $\rho = 0.25$ and $\delta = 0.4$.

follows: shorter R_L results in smaller number of LOS interfering links.

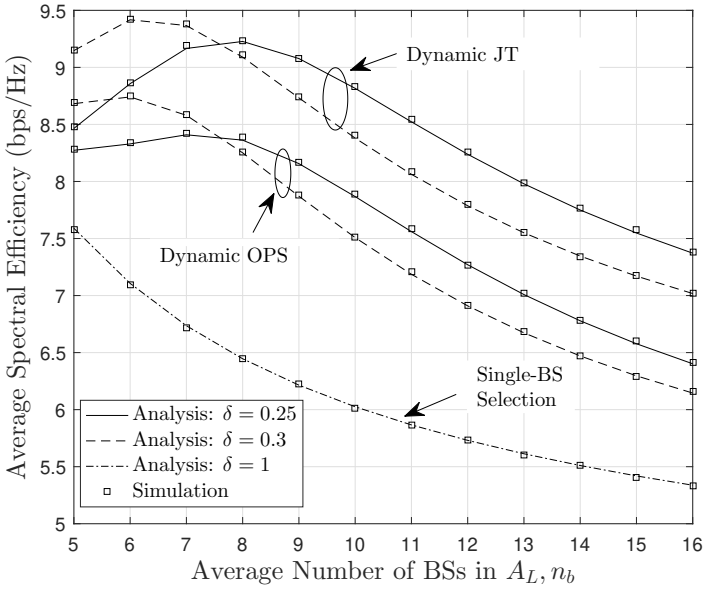

Figure 2.6: ASE against the BS density for the dynamic JT, dynamic OPS, and single-BS selection for different values of the clustering parameter δ with $n_u = 24$.

Fig. 2.6 reports the ASE versus the BS density under dynamic JT, dynamic OPS and single-BS selection. First, as shown, the dynamic clustering schemes outperform the single-BS selection. The figures also show that there is an optimum BS density (termed "critical density" in [37]) after which the system performance starts degrading. It is also clear from this figure that increasing the BS density would degrade the performances of the single BS selection scheme due to the fact that only one BS serves the user while other BSs create interference.

For the sake of mathematical tractability, we have used the power-law path loss model. However, we have investigated here two 3GPP models, namely, urban macrocell (UMa) and urban microcell (UMi) models [78, Table 7.4.1-1], and obtained, via Monte Carlo simulations, the performances of the proposed dynamic clustering scheme under the two 3GPP models, which are shown in Figures 2.7 and 2.8 with the corresponding power-law model performances. It is found that the 3GPP models lead to similar coverage probability and ASE performances as that provided by the power-law model. This could justify the feasibility of the power-law model. It is worth-mentioning that incorporating the 3GPP models or other path loss models such as bounded single slope, the bounded multi-slope, and the stretched exponential into theoretical analysis will not lead to tractable or closed form results.

To illustrate the advantage of using dynamic clustering, we compare our method with two static clustering schemes. The first static clustering scheme is adopted in [53], called here Clustering Scheme 1, where the serving cluster contains a fixed number of BSs. This fixed number is set to the average number of serving BSs in the proposed dynamic clustering. The second scheme is similar to the one investigated in [49], called here Clustering Scheme 2, where the serving cluster has a fixed radius. For fair comparison, this fixed radius for the static clustering is set to the mean radius of the dynamic clustering, which is computed by $(1/\sqrt{2\lambda_b})\delta^{(-1/\alpha_L)}\chi_1 + R_L\chi_2$. Fig. 2.9 depicts the coverage probability versus the threshold T at $\delta = 0.2$ and 0.4 and $\rho = 0.4$ for the proposed dynamic JT scheme, the two static clustering schemes, and the single-BS selection scheme. In Fig. 2.10, we show the ASE versus δ for the proposed dynamic JT and OPS and compare it with that for the static

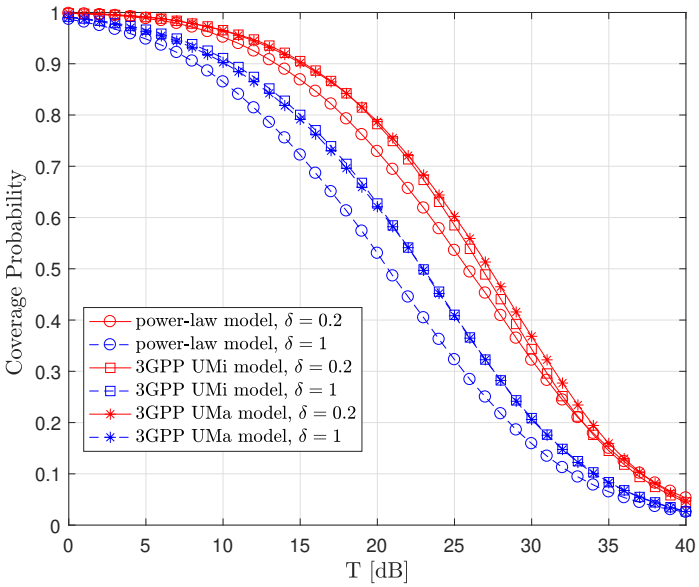

Figure 2.7: Coverage probability of the user-centric millimeter wave networks under different path loss models.

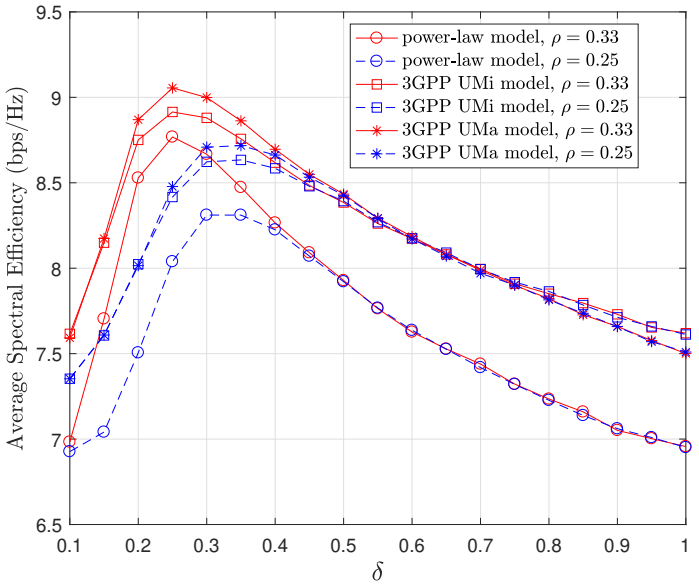

Figure 2.8: ASE vs the clustering parameter δ of the user-centric millimeter wave networks under different path loss models.

clustering under fixed cluster radius [49] at $\rho = 0.4$ and 0.3. It can be seen that the proposed dynamic JT scheme outperforms the static clustering schemes both

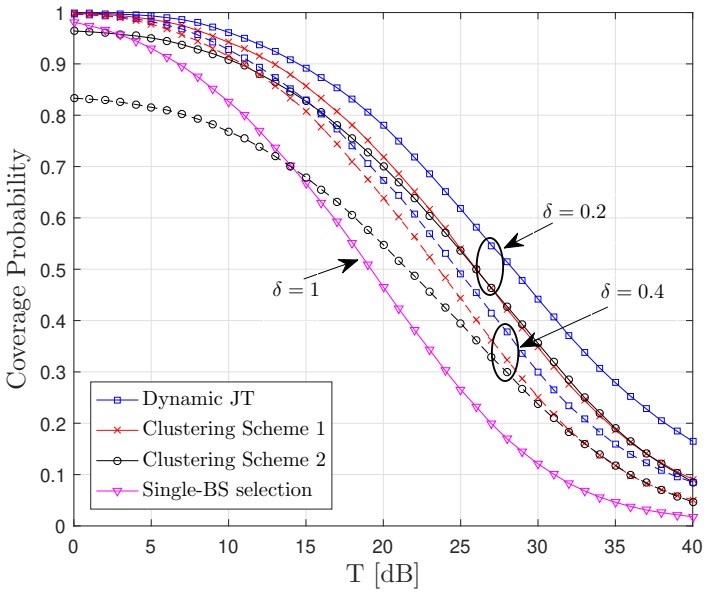

Figure 2.9: Comparison of the coverage probability of several clustering techniques when $\delta = 0.2$ and 0.4, $\rho = 0.4$ and $n_b = 8$.

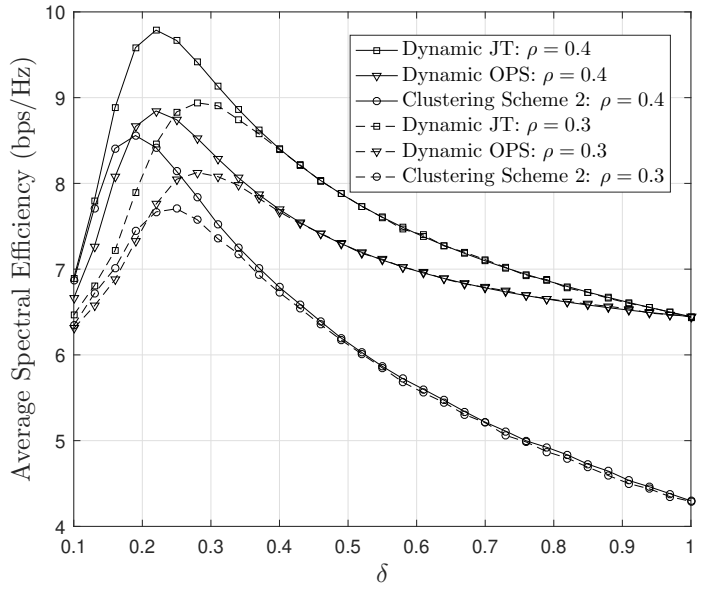

Figure 2.10: Comparison of the ASE of several clustering techniques when $\rho = 0.4$ and 0.3 and $n_b = 8$.

with fixed cluster radius and with fixed number of serving BSs. This is because in static clustering, all users form their own serving clusters with the same size which

increases the number of serving requests a BS may receive and hence reduces the typical user selection probability.

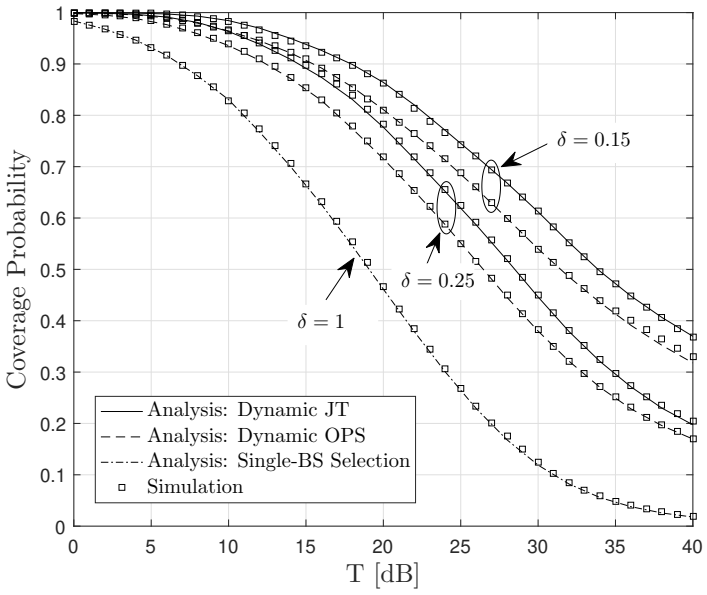

Figure 2.11: Coverage probability versus the SINR threshold T for dynamic JT, dynamic OPS, and single-BS selection schemes when $\psi \to \infty$ (i.e. $\kappa = 1$) with $\rho = 0.33$ and $n_b = 8$.

Fig. 2.11 illustrates the coverage probability of the user-centric BS clustering under dynamic JT and OPS at $\delta = 0.15$ and 0.25 with comparison to the single-BS selection when there is no BS-load constraint, i.e, $\psi \to \infty$ (or $\psi \gg A_L \lambda_u$). Unlike the results shown in Fig. 2.3, this figure shows that the coverage probability always increases with decreasing δ, particularly at high SINR thresholds. This is expected since, as $\psi \to \infty$, then $\kappa = 1$, and hence each BS can accept all users serving requests, thereby increasing the number of BSs joining the user's serving cluster.

Fig. 2.12 shows the ASE for $\rho = 0.5$, along with the upperbound calculated using (2.33), as a function of the clustering parameter δ. It can be seen that the exact ASE and its upperbound show a similar behavior and moreover, there is a unique δ_{opt} for which the two curves attain their maximums. Therefore, the ASE upperbound in (2.33) is highly effective and can be used for optimizing the clustering parameter δ without compromising the system performance.

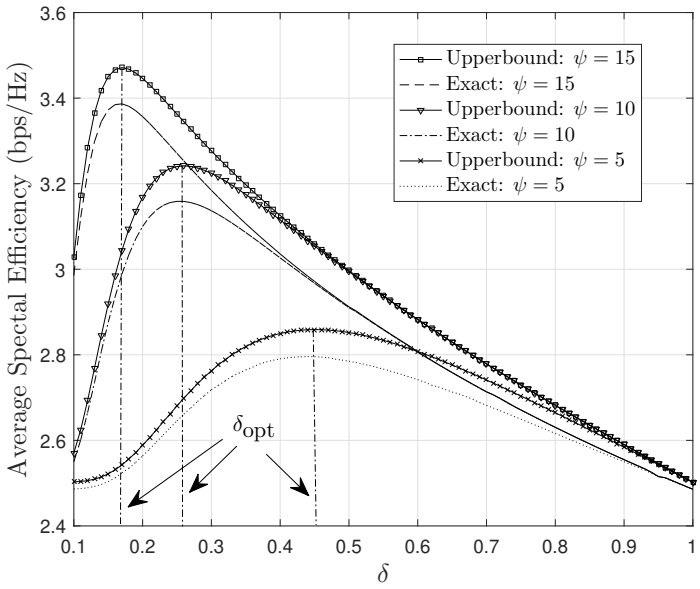

Figure 2.12: Comparison of exact ASE and its upperbound versus the clustering parameter δ for different number of available resources ψ with BS-user density ratio $\rho = 0.5$ and $n_b = 16$.

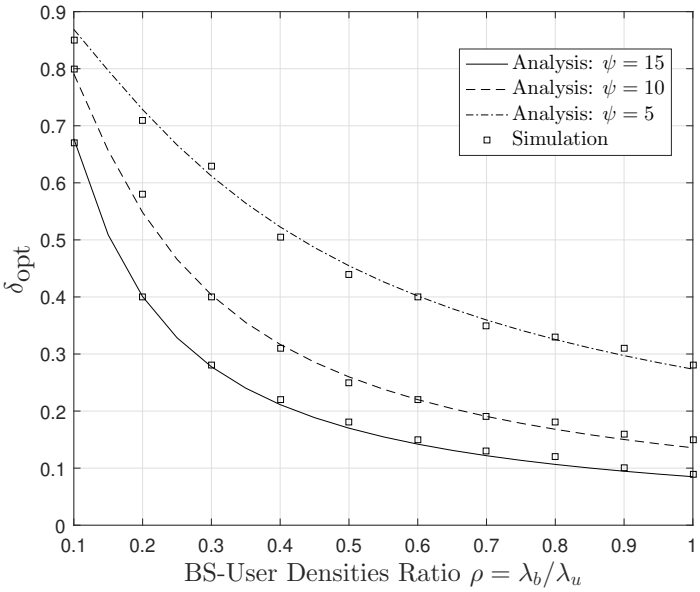

Figure 2.13: Optimum clustering parameter δ_{opt} as a function of the BS-user density ratio ρ for different values of ψ with $n_b = 16$.

Fig. 2.13 shows the optimal value of the clustering parameter as a function of the BS-user density ratio for several values of ψ (corresponding to the available resources to accommodate multiple users). We can see that the results of δ_{opt} obtained from (2.38) match well with the simulation results, which confirms the effectiveness of using the ASE upperbound as a computationally inexpensive alternative. Fig. 2.13 further corroborates the trends of Fig. 2.4 in that δ_{opt} increases as user density grows, thereby providing a sustainable solution to massive connectivity challenge.

2.6 Summary

In this chapter, we have proposed a dynamic user-centric BS clustering model for mmWave networks and analyzed its performance under PPP-based modeling of BSs and users. Our analysis exploits the results from stochastic geometry for the computation of the coverage probability and ASE performances. The proposed user-centric clustering selects BSs carefully and dynamically based on network configurations and user's channel condition. The performance of the new clustering model is studied under two different BS cooperation schemes namely dynamic JT and dynamic OPS and compared with that of the static clustering and single-BS selection schemes. In addition, we proposed an optimization framework for the clustering parameter to provide maximum performance in terms of ASE. The analytical results which are validated by simulation showed that the new dynamic clustering can enhance the system coverage probability and ASE performances which makes it a highly attractive solution for future mmWave networks.

2.7 Appendices

2.7.1 Proof of Lemma 2.3.1

Under the proposed clustering model, the average association area of each BS is given by

$$\mathbb{A} = \begin{cases} \frac{1}{\lambda_b}\delta^{\frac{-2}{\alpha_L}}, & \Phi_b^S \subsetneq \Phi_b^L \\ \pi R_L^2, & \Phi_b^S = \Phi_b^L. \end{cases} \tag{2.42}$$

Further, the users are PPP distributed with density λ_u, thus the average number of users associated to a BS is $\lambda_u \mathbb{A}$. The probability that a BS accepts the user's serving request is equivalent to the probability that the number of users within the BS association area is less than the maximum load, ψ. Let $\mathcal{N}(\lambda_u|A|)$ be the number of users with density λ_u in a geographical area $|A|$. Then, κ can be calculated as follows

$$\begin{aligned} \kappa &= \mathbb{P}(\mathcal{N}(\lambda_u|A|) < \psi) \\ &= \sum_{n=0}^{\psi-1} \Pr[\mathcal{N}(\lambda_u|\mathbb{A}| = n)] \\ &\overset{(a)}{=} \sum_{n=0}^{\psi-1} \frac{(\lambda_u|\mathbb{A}|)^n}{n!} e^{-\lambda_u|\mathbb{A}|} \end{aligned} \tag{2.43}$$

where (a) follows from the PMF of a PPP. Hence, substituting (2.42) into (2.43) yields

$$\kappa = \sum_{n=0}^{\psi-1} \frac{(\frac{\lambda_u}{\lambda_b}\delta^{\frac{-2}{\alpha_L}})^n}{n!} e^{-\frac{\lambda_u}{\lambda_b}\delta^{\frac{-2}{\alpha_L}}} = \frac{\Gamma\left(\psi, \frac{\lambda_u}{\lambda_b}\delta^{\frac{-2}{\alpha_L}}\right)}{(\psi-1)!}, \tag{2.44}$$

if $\Phi_b^S \subsetneq \Phi_b^L$, and

$$\kappa = \sum_{n=0}^{\psi-1} \frac{(\pi\lambda_u R_L^2)^n}{n!} e^{-\pi\lambda_u R_L^2} = \frac{\Gamma\left(\psi, \pi R_L^2 \lambda_u\right)}{(\psi-1)!}, \tag{2.45}$$

if $\Phi_b^S = \Phi_b^L$, which completes the proof.

2.7.2 Proof of Lemma 2.3.2

Conditioned on the distance r between the typical user and its nearest serving BS, $\Delta_{F|r}(s)$ is obtained as

$$\begin{aligned}\Delta_{F|r}(s) &= \mathbb{E}_{|\zeta|^2}\left[e^{-s\bar{c}|\zeta|^2 r^{-\alpha_L}}\right] \\ &\overset{(a)}{=} \frac{1}{\left(1+\frac{s\bar{c}r^{-\alpha_L}}{m_L}\right)^{m_L}},\end{aligned} \tag{2.46}$$

where (a) results from applying the moment generation function of the normalized Gamma distributed random variable $|\zeta|^2$ with parameter m_L. The aggregate power from the other BSs in the serving cluster $\widetilde{\Phi}_b^S$ is characterized through its Laplace transform which follows from the probability generating functional (p.g.fl.)[79] of a PPP $\widetilde{\Phi}_b^S$ with density $\kappa\lambda_b$, giving

$$\begin{aligned}\Xi_{U|r}(s) &= \mathbb{E}_{|\zeta|}\left(\exp\left(-s\sum_{k\in\widetilde{\Phi}_b^S\setminus B(0,r)}\bar{c}|\zeta_k|^2 r_k^{-\alpha_L}\right)\right) \\ &\overset{(a)}{=} \exp\left(-2\pi\kappa\lambda_b\mathbb{E}_{|\zeta|^2}\left(\int_r^{\delta^{\frac{-1}{\alpha_L}}r}\left(1-e^{-s\bar{c}|\zeta|^2 t^{-\alpha_L}}\right)tdt\right)\right),\end{aligned} \tag{2.47}$$

where (a) results from applying the Campbell's theorem. Recognizing that $1-e^{-x} = xe^{-x}{}_1\mathrm{F}_1(1,2;x)$ in (2.47) and applying

$$\int x^{\alpha-1}e^{-cx}{}_1\mathrm{F}_1(a,b;cx)dx = \frac{x^\alpha}{\alpha}{}_2\mathrm{F}_2(b-a,\alpha,b,\alpha+1;-cx), \tag{2.48}$$

we obtain

$$\Xi_{U|r}(s) = \exp\left(-\frac{2\pi\lambda_b s\bar{c}}{\alpha_L-1}\left\{\Omega\big(s,r\big)-\Omega\big(s,\delta^{-\frac{1}{\alpha_L}}r\big)\right\}\right), \tag{2.49}$$

where $\Omega\big(s,r\big) = \mathbb{E}_{|\zeta|^2}\left[\frac{|\zeta|^2}{r^{\alpha_l-2}}{}_2\mathrm{F}_2\left(1,1-\frac{2}{\alpha_\mathrm{L}};2,2-\frac{2}{\alpha_\mathrm{L}};-\mathrm{s\bar{c}}|\zeta|^2\mathrm{r}^{-\alpha_\mathrm{L}}\right)\right]$. Averaging over the Gamma distribution of $|\zeta|^2$ with the aid of [80] and [81], we obtain

$$\Omega\big(s,r\big) = r^{2-\alpha_L}{}_3\mathrm{F}_2\left(m_L+1,1,1-\frac{2}{\alpha_L};2,2-\frac{2}{\alpha_L};-\frac{s\bar{c}r^{-\alpha_L}}{m_L}\right). \tag{2.50}$$

Finally, substituting (2.50) into (2.49) completes the proof of $\Xi_{U|r}(s)$ as shown in (2.10).

In case 1, the Laplace transform of the aggregate interference received at a typical user from LOS BSs is

$$\Xi_{I_L|r}(s) = \mathbb{E}_{G,|\zeta|}\Bigg[\left(\exp\left(-s\sum_{j\in\Phi_b^S\setminus\widetilde{\Phi}_b^S} G_j|\zeta_j|^2 r_j^{-\alpha_L}\right)\right) + \left(\exp\left(-s\sum_{j\in\Phi_b^L\setminus\Phi_b^S} G_j|\zeta_j|^2 r_j^{-\alpha_L}\right)\right)\Bigg], \tag{2.51}$$

where Φ_b^S is a thinning process of Φ_b^L with density $\kappa\lambda_b$. With $|\zeta_j|$ being i.i.d. for all $j \in \Phi_b^L \setminus \Phi_b^S$ and based on the probability generating functional of the underlying PPP interference, $\Xi_{I_L|r}(s)$ is obtained as

$$\Xi_{I_L|r}(s) = \exp\Bigg(-2\pi\lambda_b\mathbb{E}_{|\zeta|^2,G}\Bigg((1-\kappa)\int_r^{\delta^{\frac{-1}{\alpha_L}}r}\left(1-e^{-sG|\zeta|^2t^{-\alpha_L}}\right)tdt + \int_{\delta^{\frac{-1}{\alpha_L}}r}^{R_L}\left(1-e^{-sG|\zeta|^2t^{-\alpha_L}}\right)tdt\Bigg)\Bigg). \tag{2.52}$$

Following the steps in obtaining (2.48) to (2.50) and averaging over G, the Laplace transform of the LOS interference $\Xi_{I_L|r}(s)$ is obtained as in (2.11). Likewise, the NLOS interference Laplace transform $\Xi_{I_N|r}(s)$ is obtained by following the same steps for the BSs in Φ_b^N.

Now, with the obtained interference and signal characterization in $\Delta_{F|r}(s)$, $\Xi_{U|r}(s)$, $\Xi_{I_N|r}(s)$, and $\Xi_{I_L|r}$, the coverage probability of a typical user in Case 1 can be analyzed by resorting to [82, Proposition 2.2]

2.7.3 Proof of Lemma 2.3.3

As far as Case 2 is concerned, the typical user is at a distance r with $R_L\delta^{\frac{1}{\alpha_L}} \leq r \leq R_L$ from its nearest BS. This implies that $r\delta^{\frac{-1}{\alpha_L}}$ will be outside the LOS ball $B(0, R_L)$. In this case, the signal Laplace transform is given by

$$\Xi_{\widetilde{U}|r}(s) = \exp\left\{-2\pi\kappa\lambda_b\mathbb{E}_{|\zeta|^2}\left(\int_r^{R_L}\left(1-e^{-s\bar{c}|\zeta|^2t^{-\alpha_L}}\right)tdt\right)\right\}, \tag{2.53}$$

which follows the same line of (2.49) after some manipulations, as shown in (2.14). The LOS interference in Case 2 stems from BSs in $\Phi_b^S = \Phi_b^L$ that have denied the

typical user serving requests, while serving other users in their proximity. In this case, the LOS interference Laplace transform is given by

$$\Xi_{\widetilde{I_L}|r}(s) \;=\; \exp\left\{-2\pi\lambda_b\mathbb{E}_{|\zeta|^2,G}(1-\kappa)\int_r^{R_L}\left(1-e^{-sG|\zeta|^2t^{-\alpha_L}}\right)tdt\right\}. \quad (2.54)$$

Then, $\Xi_{\widetilde{I_L}|x}$ in (2.15) is obtained from (2.54) by following the steps in obtaining (2.48) to (2.50) when $\Phi_b^S = \Phi_b^L$ and averaging over G.

Chapter 3

Coverage Analysis of User-Centric Dense Terahertz Networks

3.1 Introduction

With the tremendous growth of wireless services, next generation networks are required to support ultra-broadband communication with a data rate of multiple terabits-per-second (Tbps) [83]. However, it is not feasible to achieve such a high data rate with the current sub-6 GHz networks, or even the forthcoming millimeter wave (mmWave) networks. Therefore, the terahertz (THz) frequency band (0.1-10 THz) is recommended for future beyond 5th-generation networks as a long-term key technology capable of meeting the extremely high-speed data requirements [84]. Since THz signal experiences a very high loss mainly due to molecular absorption resulting from water vapors or oxygen molecules, ultra-dense deployments are expected for THz networks. This, however, will dramatically increase the interference at the user which eventually limits the network density. As such, user-centric base station (BS) cooperation is regarded as a promising solution to mitigate the interference in dense THz networks.

Recently, a handful of works studied the performance of wireless networks operating in THz band under the assumption of conventional single-BS, i.e. non-cooperative (NC), association [85]–[88]. For instance, the authors in [85] investi-

gated the mean interference power for arbitrary dimensional propagation space and accordingly, derived an expression for the outage probability. In [86], a stochastic model for multi-user interference in pulse-based THz-band communication networks is developed and experimentally validated. In [87], the statistics of the interference and coverage probability of a typical user in a THz network coexisting with a radio frequency (RF) network are characterized. Also a statistical THz channel model is investigated in [88] to characterize the THz indoor propagation.

However, it is noticed that none of the existing studies has provided an analytical framework to characterize the performance of THz networks under user-centric BSs cooperation. In this chapter, with the aim to reduce the interference in THz networks and enhance user's coverage performance, we integrate user-centric BS clustering into THz networks. To this end, we consider both dynamic and static clustering schemes to form user's serving BS cluster. Although both schemes have been investigated for mmWave and sub-6 GHz networks such as in [57], [89], the performance of user-centric THz networks remains unexplored yet. It is worthy to mention that the analytical approaches proposed in literature for user-centric mmWave/sub-6 GHz networks are not applicable to user-centric networks operating in THz bands. This is because the THz propagation model is different due to the fact that the transmitted signal power in THz band suffers from a severe attenuation caused by the molecular absorption. In this chapter, using stochastic geometry, we first characterize the distribution of the aggregated interference in dense THz networks by leveraging the central limit theorem (CLT). Then, we propose an analytically tractable framework to study the coverage probability of user-centric THz networks under both static and dynamic clustering.

3.2 System Model

3.2.1 Network Model and Antenna Arrays

We consider the downlink of a dense THz network in which both users and BSs are modeled as independent homogeneous Poisson point processes (PPPs) represented

by $\Phi_u = \{x_i\} \in \mathbb{R}^2$ and $\Phi_b = \{y_k\} \in \mathbb{R}^2$ with densities λ_u and λ_b, respectively, where x_i is the location of the i-th user and y_k is that of the k-th BS.

To compensate for the high propagation loss in THz bands, all BSs are assumed to be equipped with highly directional beamforming antenna array. In this chapter, we model the antenna gain using a sectored antenna model [85], [87]. Therefore, the antenna gain G in an arbitrary direction is expressed as

$$G = \begin{cases} G_M, & |\theta| \leq \frac{\theta_w}{2} \\ G_S, & \text{otherwise}, \end{cases} \tag{3.1}$$

where G_M and G_S, are the gain of antenna main-lobe and that of all back and side-lobes, respectively, θ denotes the angle of the boresight direction which is modeled as a random variable uniformly distributed in $[-\pi,\ \pi]$ and θ_w is the antenna beamwidth. As a result, the antenna gain of a link between the user and a BS is modeled as a discrete random variable taking the form of $G = \{G_M,\ G_S\}$ with corresponding probability $p_G = \{\frac{\theta_w}{2\pi},\ \frac{2\pi-\theta_w}{2\pi}\}$. We assume that all BSs are capable of adjusting their antenna steering orientations to achieve the maximum directivity gain [66].

3.2.2 Propagation Model

Due to the high molecular absorption and ultra dense deployment of BSs in THz networks, the line-of-sight (LOS) links are dominant. Without loss of generality, we study the performance of a user located at the origin $(0, 0) \in \mathbb{R}^2$ called a typical user [63]. According to [86], [87], [90], the LOS channel between the typical user and a BS at distance y is given by

$$\xi(y) = \frac{c^2}{(4\pi f)^2} y^{-\alpha} \exp\big(-k_a(f)y\big), \tag{3.2}$$

where f is the operating frequency, c is the speed of light, α is the path loss exponent, and $k_a(f)$ is the molecular absorption coefficient which is a function of the operating frequency. As such, the received signal power is given by $P_R(x) = P_T G_M \xi(x)$, where P_T is the BS transmit power.

3.3 Base Station Clustering Models

Under a user-centric modeling, a cell-free network allows each user to be served by a selected subset of BSs (called serving cluster). Here, we consider two BS clustering models.

3.3.1 Dynamic Cooperation Clustering

Let $P_R(r_k)$ denote the average received power from the k-th BS at a distance $r_k = || y_k ||$ and $\tau = \max_{k \in \Phi_b} P_R(r_k)$ be the largest power received by a typical user. We define the dynamic cooperation clustering (DCC) model as

$$\Phi_b^S = \{y_k \in \Phi_b,\ r \leq || y_k || \leq \frac{r}{\delta}\}, \tag{3.3}$$

where $\delta \in [0, 1]$ is called dynamic clustering parameter, which determines the cluster size, and r is the distance to the BS offering the maximum received power and is computed as

$$r = \frac{\alpha\ \text{LambertW}_0\Big(\frac{k_a(f)\big(\frac{\tau}{C_T G_M}\big)^{\frac{-1}{\alpha}}}{\alpha}\Big)}{k_a(f)}, \tag{3.4}$$

where $C_T = \frac{P_T c^2}{(4\pi f)^2}$ and $\text{LambertW}_0(.)$ is the Lambert W_0 function defined as the inverse of the function $f(w) = we^w$. According to (3.3), different users form their serving clusters with different sizes. Also, if a user changes its location, both the cluster size and serving BSs may change.

3.3.2 Static Cooperation Clustering

In the static cooperation clustering (SCC) model, Φ_b^S contains the N_s closest BSs, i.e, the user is connected to a fixed number of BSs. Thus, the SCC is defined as

$$\Phi_b^S = \{y_k \in \Phi_b,\ || y_k || = r_i,\ i = 1, 2, ...N_s\}, \tag{3.5}$$

where r_i is the distance to the i-th nearest BS. This means that, all users form their own clusters with the same sizes and if a user changes its location, the cluster size will not change even though the BSs in the cluster may be updated. Therefore this scheme is referred to as static clustering.

Note that when $\delta \to 0$, or $N_s \to \infty$, a user can connect to all BSs, or equivalently a BS serves all users. This case corresponds to a cell-free network [20], which is suitable for small-scale networks. On the other hand, for large-scale networks, the clustering parameters can be selected according to some network constraints such as maximum BS load and network backhauling complexity. Considering such constraints is beyond the scope of this chapter. In this chapter, we focus on the design of clustering approaches to enable a user-centric BS cooperation under the assumption that a BS is capable of serving all associated users.

3.4 System Coverage Analysis

In this section, the coverage probability of a typical user is investigated considering DCC and SCC. To this end, we first develop theoretical expressions for the signal-to-interference-plus-noise ratio (SINR) and the interference distribution.

3.4.1 Received SINR at a Typical User

The instantaneous SINR at the typical user is given by

$$\text{SINR} = \frac{\sum_{k\in\Phi_b^S} G_M C_T r_k^{-\alpha} \exp\big(-k_a(f) r_k\big)}{\sum_{j\in\Phi_b\setminus\Phi_b^S} G_j C_T r_j^{-\alpha} \exp\big(-k_a(f) r_j\big) + \sigma^2}, \tag{3.6}$$

where r_k and r_j denote the Euclidian distances from the user to the k-th serving BS located at $y_k \in \Phi_b^s$ and to the j-th interfering BS located at $y_j \in \Phi_b \backslash \Phi_b^S$, respectively, G_j is the total antenna gain of the j-th interfering link which is a random variable, and σ^2 is the thermal noise power. It is clear that the distance between BSs is very short in ultra-dense deployments. Therefore we assume that all serving BSs are in LOS with respect to the user. In addition, since the LOS links are dominant in dense THz networks, we consider only LOS interferes. In this chapter, both DCC and SCC schemes select BSs based on the average power received by the typical user. Therefore, to simplify the analysis, we used the propagation model in [86], [87], [90] which ignored the channel small-scale fading. Actually, according to [66], the small scale fading, at higher frequency bands, has only minor effect on the coverage

performance when BSs are densely deployed and equipped with highly directional antennas. To incorporate the effect of blockages on the interfering signals, we use the Boolean blockage model [66] in which a BS at a distance y is considered LOS with probability $e^{-\beta y}$, where β is a constant dependant on the blockages sizes and density. To simplify the analysis, we rewrite (3.6) as SINR $= \frac{S_{agg}}{I_{agg}+\sigma^2}$, where $S_{agg} = \sum_{k\in\Phi_b^S} G_M C_T r_k^{-\alpha} \exp\big(-k_a(f)r_k\big)$ and $I_{agg} = \sum_{j\in\Phi_b^L\setminus\Phi_b^S} G_j C_T r_j^{-\alpha} \exp\big(k_a(f)r_j\big)$ are the aggregated signal and interference, respectively, and Φ_b^L is the LOS BSs PPP.

3.4.2 Interference Characterization Using CLT

Hereafter, we consider a unified interference characterization under both DCC and SCC. For this purpose, we introduce the following definition of the serving cluster radius

$$\nu(r) = \begin{cases} r\delta^{-1}, & \text{DCC} \\ r_{N_s}, & \text{SCC.} \end{cases} \tag{3.7}$$

The Laplace transform of the aggregated interference is, then, provided in the following Lemma.

Lemma 3.4.1 *Given the typical user's serving cluster with radius $\nu(r)$, the Laplace transform of the aggregated interference, I_{agg}, denoted by $\Xi_{I_{agg}|\nu(r)}(s)$, is given by*

$$\Xi_{I_{agg}|v(r)}(s) = \exp\Big(-2\pi\lambda_b \sum_G \sum_{n=1}^{\infty} \frac{p_G(-sC_TG)^n \Gamma(2-\alpha n,\ n(k_a(f)+\beta)\nu(r))}{n!(nk_a(f)+n\beta)^{2-\alpha n}}\Big). \tag{3.8}$$

Proof:

Recall that I_{agg}=$\sum_{j\in\Phi_b^L\setminus\Phi_b^S} G_j C_T r_j^{-\alpha} \exp\big(-k_a(f)r_j\big)$, the Laplace transform of the

aggregated interference is given by

$$\begin{aligned}
\Xi_{I_{agg}|v(r)}(s) &= \mathbb{E}_{I_{agg}}\left[e^{-sI_{agg}}\right] \\
&= \mathbb{E}_{G,\Phi_b^S}\left[\exp\left\{-s\sum_{j\in\Phi_b^L\setminus\Phi_b^S} G_j C_T r_j^{-\alpha}\exp\big(-k_a(f)r_j\big)\right\}\right] \\
&\overset{(a)}{=} \exp\left\{-2\pi\lambda_b\sum_G p_G\int_{v(r)}^{\infty}\big(1-\exp\big(-sGC_T t^{-\alpha}e^{-k_a(f)t}\big)te^{-\beta t}dt\big)\right\} \\
&\overset{(b)}{=} \exp\left\{-2\pi\lambda_b\sum_G p_G\int_{v(r)}^{\infty}\sum_{n=1}^{\infty}\frac{(-sGC_T)^n t^{-n\alpha+1}e^{-n(k_a(f)+\beta)t}}{n!}dt\right\} \\
&\overset{(c)}{=} \exp\left\{-2\pi\lambda_b\sum_G\sum_{n=1}^{\infty}\frac{p_G(-sC_TG)^n\Gamma(2-\alpha n, n(k_a(f)+\beta)v(r))}{q!(nk_a(f)+n\beta)^{2-\alpha n}}\right\},
\end{aligned} \tag{3.9}$$

where (a) follows from the probability generating functional of a PPP [63] and from averaging over the gain, (b) results from replacing the inner exponential function by its series expansion, and (c) follows from applying $\int_z^\infty t^{a-1}e^{-t}dt = \Gamma(a,z)$.

Due to the infinite summation in (3.8), it is not tractable to compute the CDF of the aggregated interference using a method relying on the Laplace transform such as Gil-Pelaez inversion theorem [91]. For this reason, we use the central limit theorem to approximate the interference with a normal distribution for a given serving cluster radius. Note that in a user-centric network, the typical user is served by multiple BSs normally in a close proximity from which the user received the most dominant signals. Thus, the serving cluster can be considered as an interference exclusion region. In [92], [93], it is shown that as the exclusion region expands and/or the BS density increases, the aggregated interference tends to approach the Gaussian distribution. As a consequence, the conditional CDF of the interference under a given cluster radius $v(r)$ is obtained by the following proposition.

Proposition 3.4.1 *Given THz BSs densely deployed and distributed according to a PPP, the aggregated interference has the following approximate CDF for cluster*

radius $v(r)$,

$$\begin{aligned} F_{I_{agg}|v(r)}(T) &= Pr\Bigg(\sum_{j\in\Phi_b\setminus\Phi_b^S} C_T G_j r_j^{-\alpha} e^{-k_a(f)r_j} \leq T\Bigg) \\ &\approx \frac{1}{2}\Bigg(1+erf\Bigg(\frac{T-\mu_{I_{agg}}(v(r))}{\sqrt{2var_{I_{agg}}(v(r))}}\Bigg)\Bigg), \end{aligned} \tag{3.10}$$

where $erf(z)=\frac{2}{\sqrt{\pi}}\int_0^z e^{-t^2}dt$ *is the error function [62], and* $\mu_{I_{agg}}(v(r))$ *and* $var_{I_{agg}}(v(r))$ *are the mean and variance of* I_{agg} *for a given* $v(r)$ *which are computed as*

$$\mu_{I_{agg}}(v(r)) = \mathcal{M}^{(1)}(v(r)), \tag{3.11}$$

and

$$var_{I_{agg}}(v(r)) = \mathcal{M}^{(2)}(v(r)) - \big(\mathcal{M}^{(1)}(v(r))\big)^2, \tag{3.12}$$

where $\mathcal{M}^{(1)}(v(r))$ *and* $\mathcal{M}^{(2)}(v(r))$ *are the first and second moments of* $I_{agg|v(r)}$ *that can be obtained by taking the first and second derivatives of the Laplace transform in (3.8), resulting in*

$$\begin{aligned} \mathcal{M}^{(1)}(v(r)) &= -\frac{\partial \Xi_{I_{agg}|v(r)}(s)}{\partial s}\bigg|_{s=0} \\ &= \frac{2\pi\lambda_b C_T G^{(1)}\Gamma\big(2-\alpha,\ (k_a(f)+\beta)v(r)\big)}{(k_a(f)+\beta)^{2-\alpha}}, \end{aligned} \tag{3.13}$$

and

$$\begin{aligned} \mathcal{M}^{(2)}(v(r)) &= \frac{\partial^2 \Xi_{I_{agg}|v(r)}(s)}{\partial s^2}\bigg|_{s=0} \\ &= \frac{\big(2\pi\lambda_b (C_T G^{(2)})\Gamma\big(2-\alpha,\ (k_a(f)+\beta)v(r)\big)\big)^2}{(k_a(f)+\beta)^{4-2\alpha}} \\ &+ \frac{4\pi\lambda_b (C_T G_{avg})^2\Gamma\big(2-2\alpha,\ 2(k_a(f)+\beta)v(r)\big)}{2\big(2(k_a(f)+\beta)\big)^{2-2\alpha}}. \end{aligned} \tag{3.14}$$

In (3.13) and (3.14), $G^{(1)}$ and $G^{(2)}$ are, respectively, the first and second moments of the interferers antenna gain.

3.4.3 Coverage Probability

Given an SINR threshold at a typical user, γ, the coverage probability of the user-centric THz network under the two considered user-centric clustering schemes is stated as follows.

Proposition 3.4.2 *The coverage probability of the user-centric THz network under DCC is expressed as,*

$$P_{cov}^{d}(\gamma) = \int_{0}^{\infty} \frac{1}{2}\Bigg(1+\sum_{q=0}^{\infty}\frac{(\pi\lambda r^2(\delta^{-2}-1))^q}{q!}e^{-\pi\lambda r^2(\delta^{-2}-1)}erf\Bigg(\frac{1}{\gamma\sqrt{2var_{I_{agg}}(r)}}$$

$$\times\Bigg(G_m C_T r^{-\alpha}e^{-k_a(f)r}+2qG_m C_T k_a(f)^{-\alpha+2}r^{-2}(\delta^{-2}-1)^{-1}\Bigg(\Gamma\big(2-\alpha,k_a(f)r\big)$$

$$-\Gamma\big(2-\alpha,k_a(f)r\delta^{-1}\big)\Bigg)-\gamma\big(\sigma^2+\mu_{I_{agg}}(r)\big)\Bigg)\Bigg)f_r(r)dr, \tag{3.15}$$

where $f_r(r)$ is the probability density function (PDF) of the distance to the nearest BS as given by [63]

$$f_r(r)=2\pi\lambda_b r e^{-\pi\lambda_b r^2}, \quad 0<r<\infty. \tag{3.16}$$

Proof:

For the SINR threshold γ, the coverage probability can be expressed as

$$\begin{aligned}
\mathrm{P}_{cov}^{d}(\gamma) &= \Pr(SINR>\gamma)\\
&= \Pr\Bigg(I_{agg}<\frac{S_{agg}-\gamma\sigma^2}{\gamma}\Bigg)\\
&= \mathbb{E}_{S_{agg},r}\Bigg[F_{I_{agg}|r}\Bigg(\frac{S_{agg}-\gamma\sigma^2}{\gamma}\Bigg)\Bigg]\\
&\overset{(a)}{=} \mathbb{E}_{S_{agg},r}\Bigg[\frac{1}{2}\Bigg(1+\mathrm{erf}\Bigg(\frac{\frac{S_{agg}-\gamma\sigma^2}{\gamma}-\mu_{I_{agg}}(r\delta^{-1})}{\sqrt{2\mathrm{var}_{I_{agg}}(r\delta^{-1})}}\Bigg)\Bigg)\Bigg],
\end{aligned} \tag{3.17}$$

where (a) follows from applying (3.10). Given the distance to the nearest BS, r, the aggregated signal can be expressed as $S_{agg}|r = G_M C_T r^{-\alpha}e^{-k_a(f)r}+\sum_{k\in\Phi_b^S\setminus B(0,r)}G_M$

$C_T r_k^{-\alpha} \exp\big(-k_a(f) r_k\big)$, where the k-th distance, r_k, is a random variable uniformly distributed in $[r,\ r\delta^{-1}]$ with a PDF

$$f_{r_k}(t) = \frac{2t}{r^2\delta^{-2} - r^2}, \qquad r < t \leq r\delta^{-1}. \tag{3.18}$$

Given Q BSs in $\Phi_b^S \setminus B(0,r)$, the coverage probability in (3.17) can be written as

$$\mathrm{P}_{cov}^{d}(\gamma) \;=\; \mathbb{E}_{r,\,Q}\left[\frac{1}{2}\left(1 + \mathrm{erf}\left(\frac{S_{agg}|r,Q - \gamma\sigma^2 - \gamma\mu_{I_{agg}}(r\delta^{-1})}{\gamma\sqrt{2\mathrm{var}_{I_{agg}}(r\delta^{-1})}}\right)\right)\right], \tag{3.19}$$

where the conditional aggregated signal power, $S_{agg}|r,Q$, is given by

$$\begin{aligned} S_{agg}|r,Q \;&=\; G_M C_T r^{-\alpha} e^{-k_a(f)r} + QG_M C_T \int_r^{r\delta^{-1}} t^{-\alpha} e^{-k_a(f)t} f_{r_k}(t)dt \\ &= G_M C_T r^{-\alpha} e^{-k_a(f)r} + 2QG_M C_T k_a(f)^{-\alpha+2} r^{-2}(\delta^{-2}-1)^{-1} \\ &\times\Big(\Gamma\big(2-\alpha, k_a(f)r\big) - \Gamma\big(2-\alpha, k_a(f)r\delta^{-1}\big)\Big). \end{aligned} \tag{3.20}$$

Since the BSs are distributed according to a PPP, the random variable Q in (3.19) and (3.20) follows a Poisson distribution with a mean $\pi\lambda_b r^2(\delta^{-2}-1)$ and its probability mass function (PMF) is written as

$$\Pr[Q=q] = \frac{\big(\pi\lambda_b r^2(\delta^{-2}-1)\big)^q}{q!} e^{-\pi\lambda_b r^2(\delta^{-2}-1)}. \tag{3.21}$$

Then, substituting (3.20) into (3.19) and averaging it over Q with (3.21) and r with $f_r(r) = 2\pi\lambda_b r e^{-\pi\lambda_b r^2}$ give the expression in (3.15).

Proposition 3.4.3 *Under the SCC, the coverage probability of the user-centric THz network can be derived as given in (3.22), shown bellow,*

$$\begin{aligned} P_{cov}^{s}(\gamma) \;&=\; \int_{0\leq r_1\leq r_2 \ldots \leq r_N} \ldots \int \frac{1}{2}\left(1 + erf\left(\frac{\sum_{j=1}^{N_s} G_m C_T r_j^{-\alpha} e^{-k_a(f)r_j} - \gamma\big(\sigma^2 + \mu_{I_{agg}}(r_N)\big)}{\sqrt{2var_{I_{agg}}(r_N)}}\right)\right) \\ &\times f_{r_1,r_2,\ldots r_N}(r_1, r_2, ..., r_N)dr, \end{aligned} \tag{3.22}$$

where $f_{r_1,r_2,\ldots r_{N_s}}(r_1, r_2, ..., r_{N_s})$ is the joint PDF of the distances to the N_s serving BSs which is given by [63]

$$\begin{aligned} f_{r_1,r_2,\ldots r_{N_s}}(r_1, r_2, ..., r_{N_s}) = \;& (2\pi\lambda_b)^{N_s} r_1 r_2 \ldots r_{N_s} e^{-\pi\lambda_b r_{N_s}^2}, \\ & 0 < r_1 < r_2 \ldots r_{N_s} < \infty. \end{aligned} \tag{3.23}$$

Proof: Recall that $\mathrm{P}_{\mathrm{cov}}^{s}(\gamma) = \mathbb{E}_{S_{agg},r_1,\ldots r_{N_s}}\left[F_{I_{agg}|r_1,\ldots r_{N_s}}\big(\frac{S_{agg}-\gamma\sigma^2}{\gamma}\big)\right]$, where under SCC, we have $S_{agg} = \sum_{j=1}^{N_s} G_m C_T r_j^{-\alpha} e^{-k_a(f)r_j}$. Then, using (9) and averaging over (3.23), the proposition is proved.

3.5 Numerical Results

This section presents numerical results for the coverage probability of user-centric terahertz networks using DCC and SCC approaches with comparison to the NC scheme in which the user is connected to only one BS. The derived analytical expressions are both numerically computed and verified with Monte Carlo simulations. For the coverage probability of DCC, it is found that the summation in (3.15) converges fast and the first 9 terms are sufficient to provide a close match with the simulation. Unless otherwise specified, the simulation parameters are assumed as follows. The BS antenna parameters are set to $\theta_w = 30^o$, $G_M = 13.8$ dB, $G_s = 0$ dB [85]. The transmit power of all BS is assumed to be $P_T = 30$ dBm, the pathloss exponent is $\alpha = 2.2$, the BS density, when fixed, is $\lambda_b = 0.005$ BSs/m^2, and $\beta = 1/141.4$ [66]. The absorption coefficient, when fixed, is set to 0.03, 0.06 and 0.1 corresponding to an operating frequency of 0.8 THz, 1 THz, and 1.5 THz, respectively, according to the realistic data for water vapor molecules with humidity 36.78% [94].

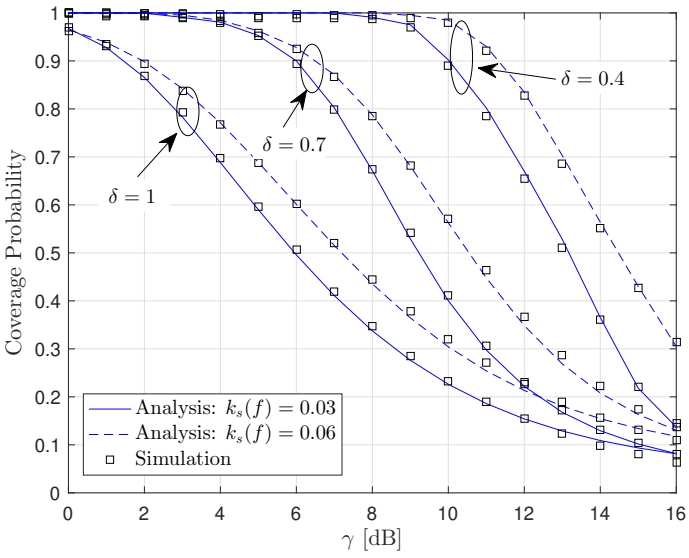

Figure 3.1: Coverage probability versus the SINR threshold γ for DCC with $\delta = 0.7$ and 0.4 compared to the NC scheme, $\delta = 1$.

Fig. 3.1 shows the coverage probability of the user-centric THz network using DCC, for different $\delta = 0.4$ and 0.7 and compares it with that of NC transmission.

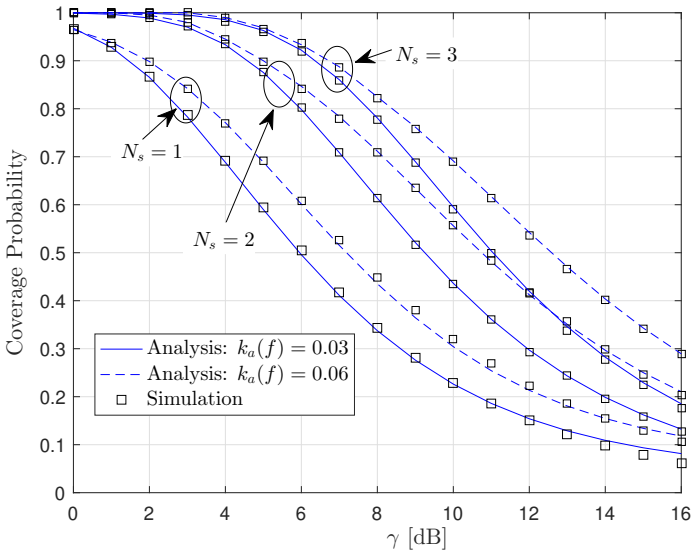

Figure 3.2: Coverage probability versus the SINR threshold γ for the SCC with $N_s = 2$ and 3 compared to the NC scheme, $N_s = 1$.

Similarly, Fig. 3.2 shows the coverage probability under SCC for different cluster sizes, N_s, along with that under the NC transmission for comparison. The results illustrate the performance improvement of the two cooperative transmission schemes over the NC scheme. Figs. 3.1 and 3.2 also demonstrate that the coverage performance is improved with increasing the absorption coefficient. This is mainly because the strength of the interfering signals decreases with $k_a(f)$. Note that, however, this is not always the case as will be shown in the next experiment.

Fig. 3.3 demonstrates the coverage probability as a function of the molecular absorption coefficient, $k_a(f)$, for DCC, SCC, and NC transmission schemes. In this figure we consider the experimental data in [94, Table 4] in which the frequency is fixed at 1.56 THz and $k_a(f)$ varies due to the changes in humidity. It can be seen that the coverage probability increases with $k_a(f)$ to a maximum value and then gradually decreases, which can be interpreted as follows: in dense THz networks, increasing $k_a(f)$ will decrease the strength of the interfering signals relative to the useful signal and hence will improve the received SINR. However, when $k_a(f)$ reaches a certain level, the received signal becomes weaker and the coverage probability starts to decay.

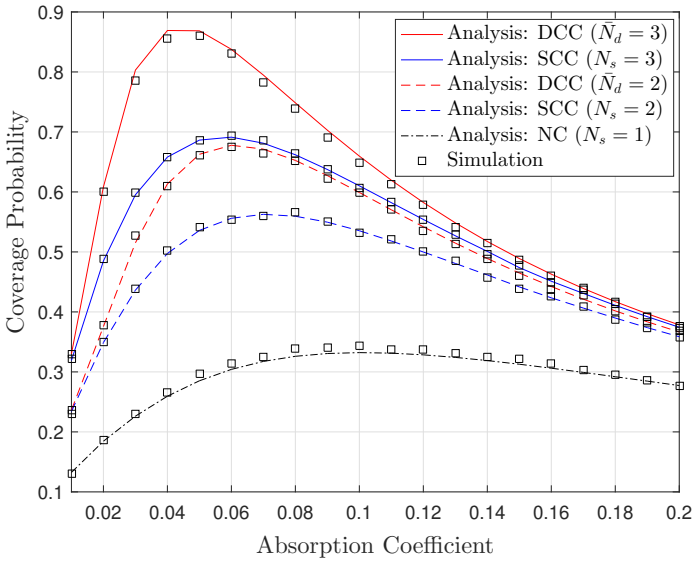

Figure 3.3: Coverage probability versus the absorption coefficient $k_a(f)$ for DCC, SCC, and NC schemes at SINR threshold $\gamma = 10$ dB.

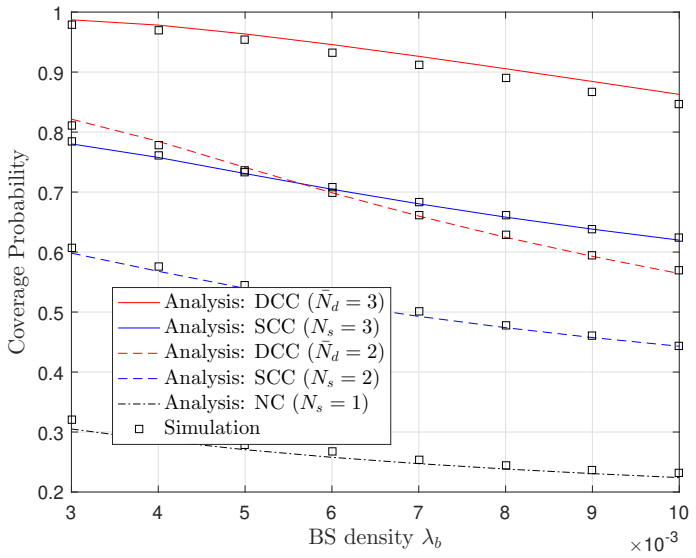

Figure 3.4: Coverage probability versus the BS density, λ_b, for DCC, SCC, and NC schemes at SINR threshold $\gamma = 10$ dB.

In Fig. 3.4, we plot the coverage probability of the two clustering schemes as a function of the BS density. For fair comparison, the dynamic clustering parameter δ is set such that the average number of BSs in the user' serving cluster, $\bar{N}_d$, is equal to the fixed cluster size of SCC, i.e., we choose $\bar{N}_d = 2$ and $\bar{N}_d = 3$ which result

from using $\delta = 0.63$ and $\delta = 0.51$, respectively. This figure shows that the coverage probability decreases with increasing the BS density as a result of increasing the interference level. Furthermore, as shown in the figure, DCC outperforms the SCC. This is because the user's serving cluster, under DCC, is formed according to its channel condition which ensures that the user is connected to all BSs with large received power. On the other hand, SCC fixes the user's serving cluster which causes some BSs with large received power to be outside the cluster and contribute interferences to the user.

3.6 Summary

We have presented a stochastic geometry framework to characterize the coverage performance of user-centric THz networks using both dynamic and static BS clustering schemes. Through a unified characterization of the aggregate interference statistics and the CLT-based approximation of such an interference, we have derived the coverage probability of the considered user-centric THz network. Numerical computation and Monte Carlo simulation with different network configurations, channel conditions, and clustering parameters have been carried out to validate our theoretical finding and demonstrate the superiority of the proposed dynamic as well as static clustering schemes to the single BS association.

Chapter 4

Energy-Efficient Cluster Sizing for User-Centric UAV Networks

4.1 Introduction

Unmanned aerial vehicles (UAVs) have attracted much attention in academia and industry due to their easy deployment and flexible applications [95]. They can be integrated with terrestrial wireless networks to improve spectrum efficiency (SE) and tackle many challenges in future networks by providing seamless and ubiquitous coverage and playing a role of relaying systems. The energy efficiency (EE) of UAV-assisted networks was investigated in [96]–[100]. The authors in [96] optimized the UAV's trajectory to provide maximum EE. In [97], the advantages of both UAVs and backscatter communications are combined to provide an energy-efficient wireless system. In [98], an energy-efficient UAV relaying system is designed to serve a ground user for a given time. The authors in [99] optimized the UAV's hover time in a three-tier heterogeneous network to improve the system EE under a minimum quality-of-service (QoS) requirement. In [100], an energy-efficient UAV system serving ground users is developed by jointly optimizing the UAV trajectory and the UAV to users scheduling. Although most of the studies in literature including [96]–[100] have focused on the communication between UAVs and terrestrial base stations or users, there are many applications that require direct connections between UAVs. These

include exchanging data to avoid collisions between flying elements, enabling UAVs to do joint tasks, offering UAV-to-UAV relays, and forwarding data to terrestrial users [101].

Coordinated transmission, in which a cluster of base stations (BSs) serve one user equipment (UE), is a promising technique that can improve the performance of future wireless networks. The authors of [102], [103] studied the performances of coordinated transmissions in UAV-based networks with a fixed size of serving clusters. While these fixed-size clustering techniques do not incur significant costs in terms of overhead and complexity since their parameters are static and predetermined, they often achieve poor performance in varying environments. Therefore, adaptive clustering, in which the serving cluster size is adapted dynamically according to the network operating conditions, is highly recommended.

In this chapter, we first propose a novel 3D analytical framework for the design of an adaptive user-centric UAV-to-UAV network. In the proposed framework, an aerial UE (AUE) is served by a set of carefully selected aerial BSs (ABSs) forming a serving cluster which is adapted to the network operating conditions. Then, using stochastic geometry tools, we derive analytical expressions for the SE and EE under adaptive clustering. Finally, with reasonable approximations, we derive an efficient and tractable closed-form expression of the optimum clustering parameter that provides maximum EE for dense large-scale spatial UAVs networks.

4.2 System Model and Definitions

We consider a 3D wireless network consisting of two types of UAVs, i.e., AUE and ABS, distributed within a finite ball of radius R above the ground. In particular, we assume that the drones of type ABSs are serving the drones of type AUEs in the downlink scenario[1]. Moreover, both ABSs and AUEs are modeled as two independent homogeneous Poisson Point Processes (PPPs) Φ_b and Φ_u with densities λ_b and λ_u, respectively. To enable user-centric ABS clustering, a reference AUE,

[1]The ABSs are interconnected with the core network via high-altitude platforms (HAPs) and/or terrestrial BSs, while AUEs forward data to their associated terrestrial UEs.

located at the origin [63], uses the signal with maximum average power, i.e, with minimum path loss, as user-side information to form its serving cluster, Φ_b^S, such that

$$\Phi_b^S = \Big\{ x_k \in \Phi_b, \delta P_{\max} \leq \| x_k \|^{-\alpha} \leq P_{\max} \Big\}, \tag{4.1}$$

where $P_{\max} = \max_{k \in \Phi_b} \| x_k \|^{-\alpha}$, with α being the path-loss exponent, is the maximum normalized average power received by the reference AUE, and $\delta \in [0, 1]$ is the clustering parameter that can be used to optimize the system performance.

Assuming joint transmission between the ABSs within the serving cluster, we can express the received signal-to-interference-plus-noise ratio (SINR) at the reference AUE as

$$\text{SINR} \;=\; \frac{\sum_{k \in \widetilde{\Phi}_b^S} h_k r_k^{-\alpha}}{\sum_{j \in \Phi_b \setminus \widetilde{\Phi}_b^S} h_j r_j^{-\alpha_L} + \frac{\sigma^2}{P_t}}, \tag{4.2}$$

where the numerator denotes the aggregate desired powers originating from the cooperating set $\widetilde{\Phi}_b^S$. Here, $\widetilde{\Phi}_b^S$ is a thinned process of Φ_b^S with density $\kappa\lambda_b$, where κ is the selection probability defined as the probability that the ABS within $\widetilde{\Phi}_b^S$ is not fully-loaded and accepts to serve the AUE.

Lemma 4.2.1 *With PPP-modeled AUEs, the selection probability of the reference AUE is given by*

$$\kappa = \frac{\Gamma\big(\psi,\ \rho\delta^{\frac{-3}{\alpha}}\big)}{(\psi - 1)!}, \tag{4.3}$$

where $\rho = \frac{\lambda_u}{\lambda_b}$ is the AUE-ABS density ratio and ψ represents the maximum load (or available resources) of the ABSs.

Proof:

The average volume of the association ball of the clustering approach in (4.1) is $\mathbb{V} = \frac{1}{\lambda_b}\delta^{\frac{-3}{\alpha}}$. In a network with AUEs being PPP distributed with density λ_u, the average number of AUEs associated to an ABS is $\lambda_u \mathbb{V}$. The selection probability, κ, is equivalent to the probability that the number of AUEs within the ABS association volume is less than its maximum load, ψ. Let $\mathcal{N}(\lambda_u|\mathbb{V}|)$ be the number of ABSs with density λ_u in a ball of volume $|\mathbb{V}|$. Then, κ can be calculated by $\kappa = \mathbb{P}(\mathcal{N}(\lambda_u|\mathbb{V}|) <$

$\psi) = \sum_{n=0}^{\psi-1} \Pr[\mathcal{N}(\lambda_u|\mathbb{V}| = n)] = \sum_{n=0}^{\psi-1} \frac{(\lambda_u|\mathbb{V}|)^n}{n!} e^{-\lambda_u|\mathbb{A}|}$. Hence, plugging the expression of $\mathbb{V}$ yields: $\kappa = \sum_{n=0}^{\psi-1} \frac{(\frac{\lambda_u}{\lambda_b}\delta^{\frac{-3}{\alpha}})^n}{n!} e^{-\frac{\lambda_u}{\lambda_b}\delta^{\frac{-2}{\alpha}}} = \frac{\Gamma\left(\psi, \rho\delta^{\frac{-3}{\alpha}}\right)}{(\psi-1)!}$.

In (4.2), r_k denotes the distance from the k-th ABS to the reference AUE, h_k represents the k-th channel gain, σ^2 is the thermal noise power, and the first term of the denominator represents the power of interfering signals. For downlink transmission without power control, the transmit powers of all ABSs are assumed to be identical to P_t.

In this chapter, we focus on large-scale spatial networks, where small-scale fading and/or line-of-sight (LoS) communication links may exist between UAVs. This model gives a reasonable approximation for low-altitude UAVs operating in an urban area. For small-scale fading, we adopt a Nakagami-m model for the channel gain [104]. Hence, the probability density function (PDF) of h is $f_h(x) = \frac{m^m}{\Gamma(m)} x^{m-1} e^{-mx}$, where m indicates the fading severity. For modeling LoS UAV links, Rice fading can be well approximated by the Nakagami-m model with $m = \frac{(K+1)^2}{2K+1}$, where K is the Rician factor [65].

4.3 Performance Characterization of User-Centric UAV Network

4.3.1 System Spectral Efficiency Analysis

This subsection derives a general SE expression of the dynamic user-centric ABS clustering for the reference AUE. According to (4.2), we can write the SE as

$$\mathcal{E} = \mathbb{E}_{\Phi_b,h}\left(\ln\left(1 + \frac{\sum_{k\in\widetilde{\Phi}_b^S} h_k r_k^{-\alpha}}{\sum_{j\in\Phi_b\setminus\widetilde{\Phi}_b^S} h_j r_j^{-\alpha_L} + \frac{\sigma^2}{P_t}}\right)\right). \tag{4.4}$$

Proposition 4.3.1 *The achievable SE of the reference AUE can be calculated as*

$$\mathcal{E} = \mathbb{E}_r\left\{ \int_0^\infty \frac{1 - \Delta_{F|r}(s)\Xi_{U|r}(s)}{s} \Xi_{I|r}(s) e^{-s\frac{\sigma^2}{P_t}} ds \right\}, \tag{4.5}$$

in nats/s/Hz, where $\Delta_{F|r}(s)$, $\Xi_{U|r}(s)$, and $\Xi_{I|r}$ are the Laplace transforms of F, U, and I, respectively, and F, U, and I, represent the signal received from the clos-

est ABS in $\widetilde{\Phi}_b^S$, the sum of the signals received from other ABSs in $\widetilde{\Phi}_b^S$, and the sum of interfering signals received from all ABSs in $\Phi_b \setminus \widetilde{\Phi}_b^S$, respectively. Then, $\Delta_{F|r}(s)$, $\Xi_{U|r}(s)$, and $\Xi_{I|r}$ are given by

$$\Delta_{F|r}(s) = \left(1 + m^{-1} s r^{-\alpha}\right)^{-m}, \tag{4.6}$$

$$\begin{aligned}\Xi_{U|r}(s) &= \exp\Bigg\{ -\frac{4}{3}\pi\kappa\lambda_b \Bigg[r^3\left(\delta^{-\frac{3}{\alpha}} - 1\right) + \frac{3\left(\frac{s}{m}\right)^m r^{3+m\alpha}}{3+m\alpha}\Bigg(\frac{\mathcal{F}\left(-\frac{m\delta^{-1}r^\alpha}{s}\right)}{\delta^{\frac{3+m\alpha}{\alpha}}} \\ &\quad - \mathcal{F}\left(-\frac{m r^\alpha}{s}\right)\Bigg)\Bigg]\Bigg\},\end{aligned} \tag{4.7}$$

and

$$\begin{aligned}\Xi_{I|r}(s) &= \exp\Bigg\{ -\frac{4}{3}\pi\lambda_b \Bigg[R^3 \\ &\quad - \delta^{\frac{-3}{\alpha}} r^3 + \frac{3\left(\frac{s}{m}\right)^m}{3+m\alpha}\left(R^{3+m\alpha}\mathcal{F}\left(-\frac{mR^\alpha}{s}\right) - \frac{r^{3+m\alpha}\mathcal{F}\left(-\frac{m\delta^{-1}r^\alpha}{s}\right)}{\delta^{\frac{3+m\alpha}{\alpha}}}\right) \\ &\quad + (1-\kappa)\left(\delta^{\frac{-3}{\alpha}} r^3 + \frac{3\left(\frac{s}{m}\right)^m}{3+m\alpha}\left(\frac{r^{3+m\alpha}\mathcal{F}\left(-\frac{m\delta^{-1}r^\alpha}{s}\right)}{\delta^{\frac{3+m\alpha}{\alpha}}}\right)\right)\Bigg]\Bigg\},\end{aligned} \tag{4.8}$$

where $\mathcal{F}(z) = {}_2F_1\left(m, m+\frac{3}{\alpha}; 1+m+\frac{3}{\alpha}; z\right)$, with ${}_2F_1(\cdot)$ standing for the Gauss hypergeometric function [62]. Moreover, in (4.5), r is the distance between the reference AUE and its closest ABS, which according to [79] has a PDF given by $f_r(x) = 4\pi\lambda_b x^2 e^{-\frac{4}{3}\pi\lambda_b x^3}$.

Proof:

The SINR in (4.2) can be expressed as

$$SINR = \frac{F+U}{I + \frac{\sigma^2}{P_t}}, \tag{4.9}$$

where $F = hr^{-\alpha}$, $U = \sum_{k\in\widetilde{\Phi}_b^S\setminus B(0,r)} h_k r_k^{-\alpha}$ and $I = \sum_{j\in\Phi_b\setminus\widetilde{\Phi}_b^S} h_j r_j^{-\alpha}$, r being the distance to the nearest ABS. Conditioned on the distance r between the reference AUE and its nearest serving ABS, $\Delta_{F|r}(s)$ is obtained as

$$\Delta_{F|r}(s) = \mathbb{E}_h\left[e^{-shr^{-\alpha}}\right] = \left(1 + \frac{sr^{-\alpha}}{m}\right)^{-m}. \tag{4.10}$$

The aggregate power from the other ABSs in the serving cluster $\widetilde{\Phi}_b^S$ is characterized through its Laplace transform which follows from the probability generating functional (p.g.fl.)[79] of the PPP $\widetilde{\Phi}_b^S$ with density $\kappa\lambda_b$, and is given by

$$\begin{aligned}\Xi_{U|r}(s) &= \mathbb{E}_{\widetilde{\Phi}_b^S, h_k}\left[e^{-s\sum_{k\in\widetilde{\Phi}_b^S\setminus B(0,r)} h_k z_k^{-\alpha}}\right] \\ &= \mathbb{E}_{\mathcal{N}|r}\left[\left(\mathbb{E}_z\left(\left(1+\frac{sz^{-\alpha}}{m}\right)^{-m}\right)\right)^{\mathcal{N}}\right] \\ &= \sum_{n=0}^{\infty}\left(\mathbb{E}_z\left(\left(1+\frac{sz^{-\alpha}}{m}\right)^{-m}\right)\right)^n f_{\mathcal{N}|r}(n), \end{aligned} \tag{4.11}$$

where $f_{\mathcal{N}|r}(n)$ is given by $f_{\mathcal{N}|r}(n) = \mathbb{P}\big[\mathcal{N}\big(B\big(r, r\delta^{-\frac{1}{\alpha}}\big)\big) = n\big] = \frac{\left(-\int_{B(r,r\delta^{-\frac{1}{\alpha}})}\kappa\widetilde{\lambda}_b(x)dx\right)^n}{n!}$ $\exp\big(-\int_{B\left(r,r\delta^{-\frac{1}{\alpha}}\right)}\kappa\widetilde{\lambda}_b(x)dx\big)$. Using the 3D ABS density to 1D mapping, $\widetilde{\lambda}_b(x) = 4\pi\lambda_b x^2$ [63], $f_{\mathcal{N}|r}(n)$ can be expressed as

$$f_{\mathcal{N}|r}(n) = e^{-\frac{4}{3}\pi\kappa\lambda_b r^3\left(\delta^{\frac{-3}{\alpha}}-1\right)}\frac{\left(\frac{4}{3}\pi\kappa\lambda_b r^3\left(\delta^{\frac{-3}{\alpha}}-1\right)\right)^n}{n!}. \tag{4.12}$$

Note that in (4.11), z is the distance from the reference AUE to a random ABS in $[r, r\delta^{\frac{-1}{\alpha}}]$ which has a uniform distribution such that $f'_{Z|r}(z) = \frac{3z^2}{r^3(\delta^{\frac{-3}{\alpha}}-1)}$, $z \in [r,\ r\delta^{\frac{-1}{\alpha}}]$. Therefore, the expectation $\mathbb{E}_z\big((1+\frac{sz^{-\alpha}}{m})^{-m}\big)$, in (4.11), is computed as

$$\begin{aligned}\mathbb{E}_z\left(\frac{1}{\left(1+\frac{sz^{-\alpha}}{m}\right)^m}\right) &= \int_r^{r\delta^{\frac{-1}{\alpha}}}\frac{f'_{Z|r}(z)}{\left(1+\frac{sz^{-\alpha}}{m}\right)^m}dz \\ &= \frac{3r^{m\alpha}\left(\frac{\mathcal{F}\left(-\frac{m\delta^{-1}r^\alpha}{s}\right)}{\delta^{\frac{3+m\alpha}{\alpha}}} - \mathcal{F}\left(-\frac{mr^\alpha}{s}\right)\right)}{\left(\frac{s\bar{c}}{m}\right)^{-m}\big(3+m\alpha\big)\big(\delta^{-\frac{3}{\alpha}}-1\big)}, \end{aligned} \tag{4.13}$$

where $\mathcal{F}(z) = {}_2F_1\left(m, m+\frac{3}{\alpha}; 1+m+\frac{3}{\alpha}; z\right)$. Then, (4.7) is obtained by substituting (4.12) and (4.13) into (4.11) and replacing the summation with its equivalent exponential function. Moreover, by following a similar manner to compute $\Xi_{I|r}(s)$, we can prove (4.8). Finally, resorting to [75]

$$\ln\left(1+\frac{X}{Y}\right) = \int_0^\infty \frac{e^{-zY}}{z}\left(1-e^{-zX}\right)dz. \tag{4.14}$$

and using (4.4) and (4.9), we obatin the SE as shwon in (4.5).

Corollary 4.3.1 *(Special Case: $R, \psi \to \infty$): In large-scale UAV networks with $R \longrightarrow \infty$ and $\psi \to \infty$, the SE in (4.5) reduces to*

$$\mathcal{E} = \int_0^\infty \int_0^\infty \frac{e^{-s\frac{\sigma^2}{P_t}}}{s} \Bigg[\exp\Bigg\{ 4\pi\lambda_b \frac{\left(\frac{s}{m}\right)^{\frac{3}{\alpha}} \mathrm{B}\left(\frac{3}{\alpha}+m, \frac{-3}{\alpha}\right)}{\alpha} \Bigg\} \Bigg(\exp\Bigg\{ -4\pi\lambda_b \times \Bigg(\frac{\left(\frac{s}{m}\right)^{-m} \left(\frac{r}{\delta^{\frac{1}{\alpha}}}\right)^{\alpha m+3}}{3+\alpha m} \mathcal{F}\Big(-\frac{mr^\alpha}{s\delta}\Big) - \frac{\left(r^{-\alpha}\delta\right)^3}{3} \Bigg) \Bigg\} - 1 \Bigg) \Bigg] f_r(r) dr ds, \quad (4.15)$$

where $\mathrm{B}(a,b)$ *denotes the Beta function [62].*

Proof:

For large-scale UAV networks, $(R \to \infty)$, with assuming $\psi \to \infty$, the SE is given by

$$\begin{aligned} \mathcal{E} &\overset{(a)}{=} \mathbb{E}_{\Phi_b,h}\Bigg[\int_0^\infty \frac{1}{s} \Bigg(\exp\Bigg(-s \sum_{j\in\Phi_b\setminus\Phi_b^S} h_j r_j^{-\alpha} \Bigg) - \exp\Bigg(-s \sum_{k\in\Phi_b} h_k r_k^{-\alpha} \Bigg) \Bigg) ds \Bigg] \\ &\overset{(b)}{=} \mathbb{E}_r\Bigg[\int_0^\infty \frac{1}{s} \Bigg(\exp\Bigg(-4\pi\lambda_b \mathbb{E}_h\Bigg[\int_{r\delta^{\frac{-1}{\alpha}}}^\infty (1-e^{-shx^{-\alpha}}) x^2 dx \Bigg] \Bigg) \\ &\quad - \exp\Bigg(-4\pi\lambda_b \mathbb{E}_h\Bigg[\int_0^\infty (1-e^{-shx^{-\alpha}}) x^2 dx \Bigg] \Bigg) \Bigg) ds \Bigg], \end{aligned} \quad (4.16)$$

where (a) follows from (4.4) and (4.14), (b) follows from applying the Campbell theorem [63] in 3D space. Finally, averaging over h and r gives the result in (4.15).

4.3.2 System Energy Efficiency

Now, we study the UAV energy-efficiency by jointly considering the SE and energy consumption. Assuming a very low-mobility (hovering) UAV network[2], the total power consumption can be written as $P_T = P_h + \overline{P}_c$, where P_h is the power consumed by a UAV due to hovering [105] and $\overline{P}_c$ is the average communication power consumption which is given by $\overline{P}_c = \overline{\mathcal{N}}_u P_u$ where P_u is the power required to process and transmit the data of each AUE and $\overline{\mathcal{N}}_u$ is the average number of AUEs

[2]UAVs hovering over a fixed location can provide continuous wireless coverage for certain areas, making them able to assist cellular networks [95].

connected to an ABS which is given by

$$\overline{\mathcal{N}}_u = \min\left\{\psi, \mathbb{E}_r\left(\frac{4}{3}\pi\lambda_u(r\delta^{-\frac{1}{\alpha}})^3\right)\right\} = \min\left\{\psi, \rho\delta^{-\frac{3}{\alpha}}\right\}. \tag{4.17}$$

We define the EE of the proposed 3D user-centric clustering approach as the ratio of the SE per unit volume, $\lambda_u\mathcal{E}$, to the power consumption per unit volume, $\lambda_b P_{\mathrm{T}}$, namely,

$$E_{\text{eff}} = \frac{\lambda_u\mathcal{E}}{\lambda_b P_T} = \frac{\rho\mathcal{E}}{P_h + \overline{P}_c}, \tag{4.18}$$

In dense large-scale UAVs networks, the SE is given in (4.15) which is obviously an increasing function of δ. However, this improvement comes at the expense of energy dissipation. This fact leads to a crucial design problem of how to determine the optimal cluster size of ABSs which maximizes the EE.

4.3.3 Energy Efficiency Optimization

We explore a tractable approximation for the achievable EE in dense large-scale spatial air-to-air networks. The analysis relies on the condition that α is greater than the space dimension, i.e., 3. This condition is particularly suitable for dense large-scale air-to-air communication networks with low-altitude UAVs operating in urban areas where the building height is comparable to UAV altitude and $\alpha > 3$ usually holds.

Proposition 4.3.2 *Assuming that $\psi \to \infty$, the SE in dense large-scale air-to-air networks with ABS clustering is approximated as*

$$\widetilde{\mathcal{E}} \;\approx\; ln\left(\frac{\alpha-3}{3}\Gamma\left(1-\frac{3}{\alpha}\right)^{\frac{\alpha}{3}}\delta^{\frac{3}{\alpha}-1}\right). \tag{4.19}$$

Proof:

Starting from the results in step (b) of (4.16), the asymptotic SE, $\widetilde{\mathcal{E}}$, can be accurately approximated as

$$\widetilde{\mathcal{E}} \;\overset{(a)}{\approx}\; \mathbb{E}_{r,h}\left[\int_0^{\infty}\frac{1}{s}\Big(\exp\big(-A_1(h,r)s\big)-\exp\big(-A_2(h)s^{\frac{3}{\alpha}}\big)\Big)ds\right], \tag{4.20}$$

where (a) follows from using $1-e^{-x}\approx x$ for small x, $A_1(h,r)=\frac{4\pi\lambda_b}{\alpha-3}h\delta^{\frac{\alpha-3}{\alpha}}r^{3-\alpha}$ and $A_2(h)=\frac{4}{3}\pi\lambda_b h^{3/\alpha}\Gamma(\frac{\alpha-3}{\alpha})$. Letting $v=A_1(h,r)s$, $\widetilde{\mathcal{E}}$ is obtained as

$$\begin{aligned}\widetilde{\mathcal{E}} &= \mathbb{E}_{r,h}\Bigg[\int_0^\infty \frac{1}{v}\Big(e^{-v}-e^{-A_2(h)^{\frac{\alpha}{3}}A_1(h,r)^{-1}v}\Big)dv+\\ &\qquad \int_0^\infty \frac{1}{v}\Big(e^{-A_2(h)^{\frac{\alpha}{3}}A_1(h,r)^{-1}v}-e^{-A_2(h)A_1(h,r)^{\frac{-3}{\alpha}}s^{\frac{3}{\alpha}}}\Big)dv\Bigg]\\ &\overset{(b)}{=} \mathbb{E}_{r,h}\left[\ln\Big(A_2(h)^{\frac{\alpha}{3}}A_1(h,r)^{-1}\Big)+\frac{\alpha-3}{3}C\right] \qquad (4.21)\end{aligned}$$

where (b) follows from applying $\ln(x)=\int_0^\infty \frac{1}{s}(e^{-s}-e^{-(1+x)s})ds$ for the first integral in (a) and $\int_0^\infty \frac{1}{s}(e^{-s^a}-e^{-s^b})ds=C\frac{a-b}{ab}$ for the second integral in (a), with C denoting the Euler's Constant. Plugging $A_1(h,r)$ and $A_2(h)$ in the last equation and averaging over r while applying $\mathbb{E}_r\big[\ln(r)\big]=-\frac{1}{3}C-\frac{1}{3}\ln(\frac{4}{3}\pi\lambda_b)$, we attain the desired result.

Recall that, in this case, the average number of AUEs served by an ABS is $\overline{\mathcal{N}}_u=\rho\delta^{-\frac{3}{\alpha}}$. Then, substituting (4.19) together with $\overline{P_c}=\overline{\mathcal{N}}_u P_u=\rho\delta^{-\frac{3}{\alpha}}P_u$ into (4.18), the approximated EE can be expressed in terms of the clustering parameter δ as follows

$$\widetilde{E}_{\text{eff}}(\delta) \approx \frac{\ln\Big(\frac{\alpha-3}{3}\Gamma\big(1-\frac{3}{\alpha}\big)^{\frac{\alpha}{3}}\Big)+\big(\frac{3}{\alpha}-1\big)\ln\delta}{\delta^{\frac{-3}{\alpha}}P_u+\frac{P_h}{\rho}}. \qquad (4.22)$$

Proposition 4.3.3 *The optimal clustering parameter, δ_{opt}^{EE}, that leads to the maximum EE can be obtained by solving the following equation,*

$$\frac{\partial\widetilde{E}_{\mathit{eff}}(\delta)}{\partial\delta}=0, \qquad (4.23)$$

which, after some manipulations, yields

$$\delta_{opt}^{EE} = \left(\frac{P_u\rho}{P_h}\right)^{\frac{\alpha}{3}}\mathcal{W}\left(\frac{P_h}{P_u\rho e}\left(\frac{\alpha-3}{3}\right)^{\frac{3}{\alpha-3}}\Gamma\left(1-\frac{3}{\alpha}\right)^{\frac{\alpha}{\alpha-3}}\right)^{\frac{\alpha}{3}}, \qquad (4.24)$$

where $e=2.218$ and $\mathcal{W}(z)$ is the solution of the equation $z=xe^x$.

4.4 Numerical Results

In this section, we consider a UAV network in which ABSs and AUEs are hovering in a 3D space. Unless otherwise specified, we assume $R = 1$km, the average number of ABSs $\mu_b = 5$ where $\lambda_b = \mu_b/(\frac{4}{3}\pi R^3)$ and $\lambda_u = \mu_b\rho/(\frac{4}{3}\pi R^3)$, $\psi = 20$, $\sigma^2/p_t = -110$dBm, $m = 3$, $\alpha = 2.5$, $P_u = 2W$, and $P_h = 168.5W$. Note that the value of the hovering power P_h is calculated using [105, Eq. (64) and Table I].

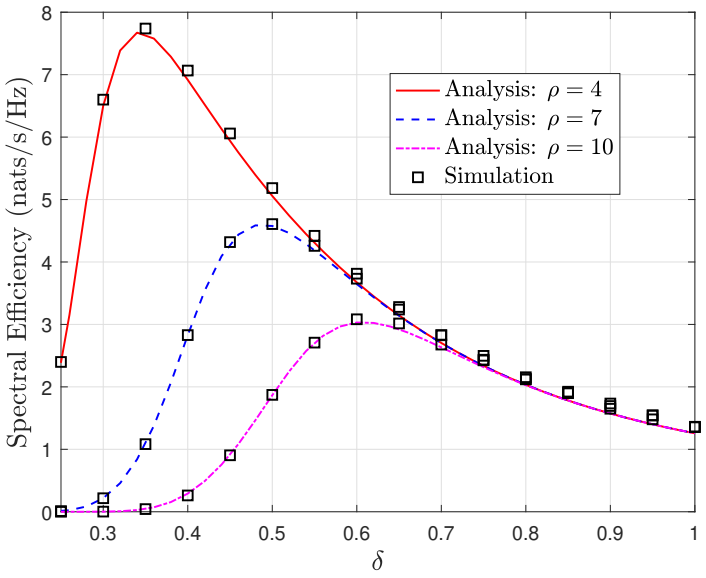

Figure 4.1: SE versus the clustering parameter δ for different values of the user-Bs density ratio ρ.

Fig. 4.1 plots the analytical SE based on (4.5) as well as the corresponding simulation result as a function of the system clustering parameter, δ, for different values of the AUE-ABS density ratio, $\rho = 4, 7$, and 10. It can be seen that for a fixed ρ, there exists an optimum value of δ which maximizes SE. Meanwhile, this optimum value increases with ρ while the corresponding SE deceases. This is because the available resources per AUE decreases with increasing ρ and, hence, more serving requests are denied by ABSs. This figure also shows that the simulation and analytical results agree closely demonstrating the accuracy of the provided analytical expressions.

Fig. 4.2 shows the volume power consumption as a function of δ. We observe

that, for a given ρ, the volume power consumption increases with decreasing δ until reaching a saturation point. This is because decreasing δ increases the number of AUEs associated to the same ABS until it reaches its maximum load. Furthermore, for the same δ, increasing ρ means to increase the number of AUEs served by an ABS and hence increases the amount of consumed power.

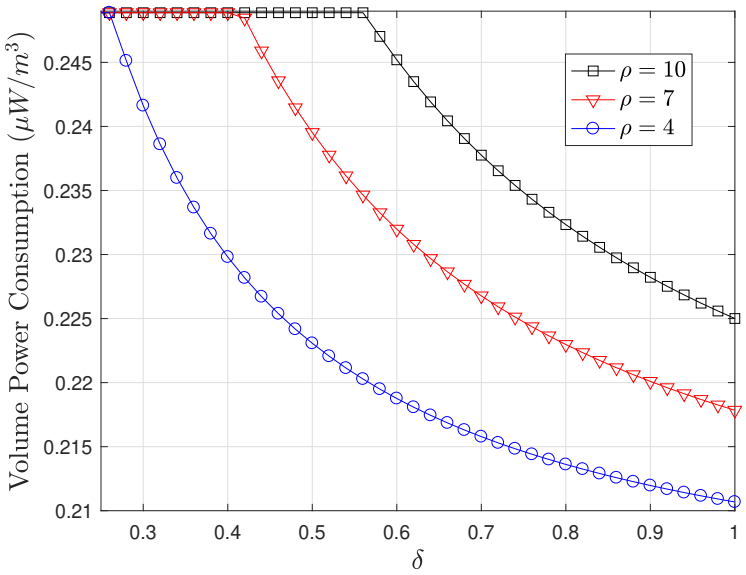

Figure 4.2: Volume power consumption versus the clustering parameter δ for different values of the user-BS density ratio ρ.

Fig. 4.3 depicts the system EE as a function of δ for $\rho = 4$, 7, and 10. Similar to Fig. 4.1, we observe that, for a given ρ, there is an optimum value of δ at which the proposed approach provides maximum EE. It is worth noting that, as the EE depends on the SE and power consumption both of which are a function of δ, the optimum values of δ at which the EE is maximum are not the same as those providing maximum SE as shown in Figs. 4.1 and 4.3. This gives more design flexibility. For example, for systems with limited bands, the optimum δ which maximizes the SE is preferable while systems with limited power can use optimum δ which gives maximum EE.

In Fig. 4.4, we depict the analytical EE for dense large-scale spatial networks with $\rho = 4$, using (4.22), and compare it with the exact EE expression in (4.18). It

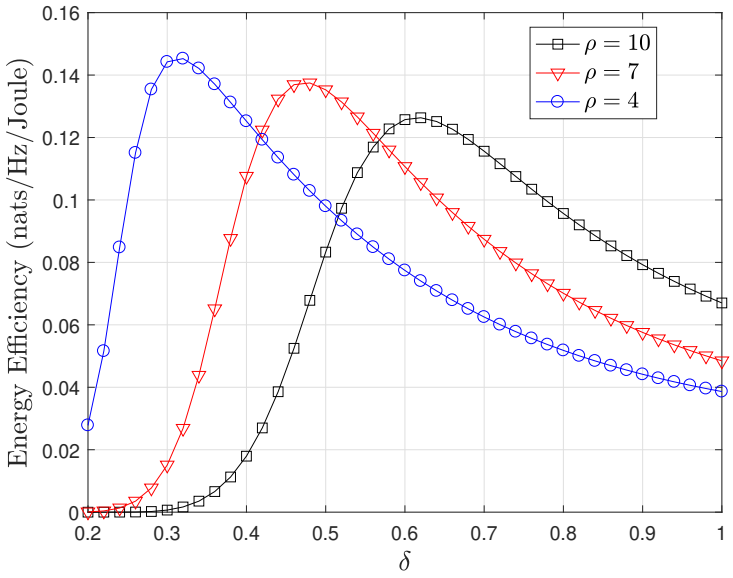

Figure 4.3: System EE versus the clustering parameter δ for different values of the user-BS density ratio ρ.

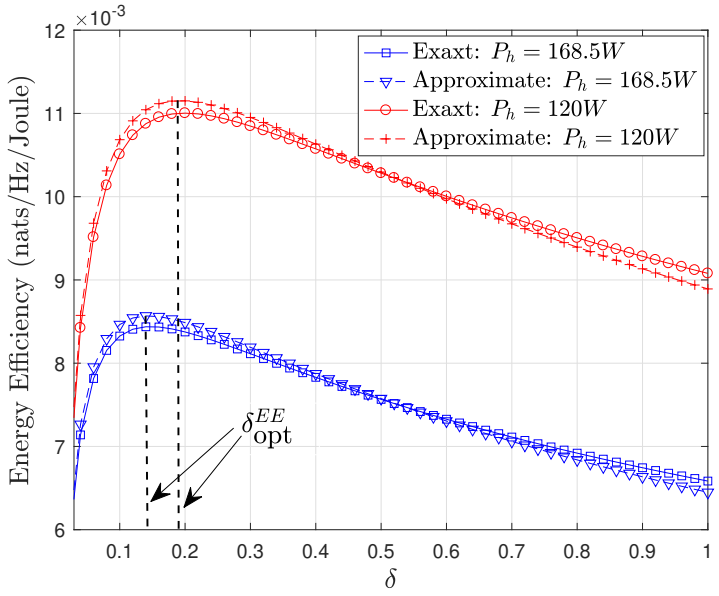

Figure 4.4: EE versus δ for dense large-scale UAV networks with $\psi \to \infty$ ($\kappa = 1$) and $\alpha = 3.3$ for different values of the hovering power P_h.

is clearly observed that (4.22) is a very accurate approximation of the EE. In this figure, we also highlight the values of δ_{opt}^{EE} (as shown by the vertical dashed lines) that maximize the EE for different values of the hovering power consumption, P_h.

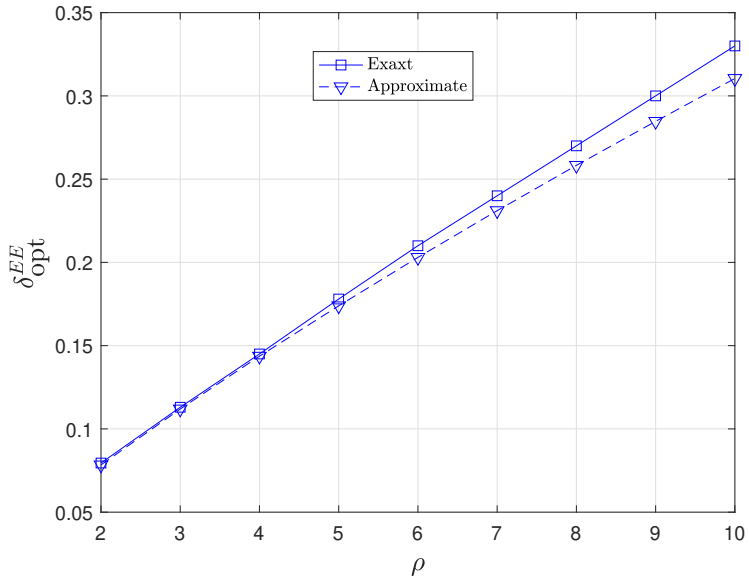

Figure 4.5: Optimum value of the clustering parameter, δ_{opt}^{EE}, versus ρ for dense large-scale spatial UAVs network with $\psi \to \infty$ ($\kappa = 1$) and $\alpha = 3.3$.

The approximate values of δ_{opt}^{EE}, obtained using (4.24), are $\delta_{\text{opt}}^{EE} = 0.143$ and 0.192 for $P_h = 168.5W$ [105] and $120W$, respectively. Interestingly, these values are as accurate as the exact values of δ_{opt}^{EE} shown in Fig. 4.4.

Fig. 4.5 illustrates the δ_{opt}^{EE} in the case of dense large-scale UAV networks as a function of ρ using (4.24), which is obtained by maximizing the approximated EE in (4.22) and compares it with δ_{opt}^{EE} obtained by performing numerical maximization of the exact EE expression in (4.18). Again, Fig. 4.5 shows that our optimization expression in (4.24) is quite accurate for dense UAV networks, i.e, for small values of ρ.

4.5 Summary

In this chapter, we proposed a novel 3D framework for the design of energy efficient user-centric air-to-air networks where an AUE is cooperatively served by a set of carefully selected ABSs according to its operation conditions. With the aid of stochastic geometry tools, we derived analytical expressions for the SE and EE. An-

alytical and simulation results demonstrated that the system clustering parameter can be tuned to obtain maximum system performance. In addition, we showed that the optimum cluster size of serving ABSs can be easily computed by a closed-form expression serving as a useful tool for network designers to better characterize and fine-tune the performance of UAV-based air-to-air networks.

Chapter 5

Hybrid User-Centric Design for Multi-tier Sub-6GHz, mmWave and THz Coexisting Networks

5.1 Introduction

5.1.1 Background and Related Works

Following the birth and successful deployment of commercial millimeter wave (mmWave) technology in the fifth generation (5G) of wireless communications [36], [106], terahertz (THz) waves are currently being considered as a critical enabler for 6G design goals [107]–[109]. Specifically, the THz waves with enormous bandwidth can be used to support applications requiring terabits per second data rates [83]. This along with the existing sub-6 GHz and mmWave bands can help achieving the true potential of many emerging applications. Further, owing to their short wavelength, THz band also provides a remarkable potential for enabling accurate sensing and localization techniques [110].

Although mmWave and THz bands have a huge potential for their usage in future communications, there are significant challenges in their commercial deployments. In particular, communications in these bands suffer from poor propagation character-

istics due to higher penetration and scattering losses, thereby reducing the coverage range [37], [107]. To deal with this issue, a promising technology has emerged, called as network densification. However, the interference increases significantly with the base station (BS) deployment density which is more harmful for the cell-edge users. As such, an effective solutions is to move from a cell-centric to a user-centric network design. Unlike the user-centric concept adopted in [111] and [112] which relies on the correlation between the users and BSs deployments, the user-centric technique in this chapter defines how each user gets connected to a number of nearby BSs which effectively eliminates the cell boundaries, i.e., no cell-edge users. In addition to mitigating the interference, user-centric networking enhances the communication reliability due to the diversity achieved from the distinct characteristics of the different links between a user and all its serving BSs. Furthermore, it is investigated that in addition to reducing the backhauling network complexity compared to the fully cooperative cell-free networks [25], the user-centric technique provides a communication system with higher spectral and energy efficiencies [26]. Therefore, advanced communications and networking techniques, such as network densification and user-centric networking have been advocated [38], [113]. In particular, BS clustering is known to better cope with the hostile propagation environment at high frequencies compared to a co-located system, as the presence of many serving BSs in the user proximity enhances coverage and link reliability. Moreover, keeping some Sub-6 GHz cells can surpass the limited coverage of THz and mmWave communications. As such, integrated user-cenetric Sub-6GHz-mmWave-THz communications can effectively support various emerging applications that require high data rates and/or reliable connections such as enhanced mobile broadband (eMBB) and ultra-reliable low latency communications (URLLC) [114], [115].

Lately, several works have studied the performance of hybrid networks under conventional single-BS association such as [87], [116]–[118], but no one considered the user-centric cooperation for such hybrid networks. For instance, the authors of [116] provided an analytical framework for uplink and downlink cell association in a hybrid sub-6GHz-mmWave cellular network. In [117], the coverage probability

of the mmWave heterogeneous cellular network which comprises multiple tiers of ultra-high-frequency macrocell and small-cell base stations (BSs) and a single tier of mmWave small-cell BSs was investigated. The authors of [87] first characterized the statistics of the downlink interference in a coexisting sub-6GHz-THz network and then studied the user performance in terms of rate coverage probability. In [87], the user is connected either to the nearest BS in the sub-6GHz-THz hybrid network or to the BS with maximum biased received signal power. The work in [118] used tools from stochastic geometry to analyze the performance of a heterogeneous network composed of macro BSs operating on sub-6 GHz, unmanned aerial vehicles (UAVs) and small cells operating on mmWave and THz frequencies.

Many works in literature studied the idea of user-centric BS cooperation for wireless networks [45], [48], [50], [51], [55]–[57], [119], [120]. For example in [48], the performance of a user served by all BSs at a distance less than a given value is evaluated. The authors of [50] proposed a user-centric scheme in which a user first determines its set of serving BSs and then selects only one BS with the largest received power to transmit data while the other BSs are assigned power control coefficients to mitigate the interference. In [51], to enable a user-centric BS cooperation, two schemes of BS clustering are considered, namely, the number-based cooperation which fixes the number of serving BSs, and the distance-based cooperation which uses a fixed cluster radius. It is shown that with the cost of increasing the system complexity, the distance-based cooperation scheme outperforms the number-based cooperation scheme. In [57], BS cooperation in mmWave network was introduced to improve the system performance in terms of the outage probability and downlink rate, where two schemes are proposed, namely, fixed-number BS cooperation and fixed region BS cooperation. In [55] and [56], tools from stochastic geometry are used to analyze the user-centric dense mmWave network and to provide analytical expressions for the system coverage probability and for the ergodic capacity. It is worth mentioning that to enable the the user-centric clustering, the works [48], [50], [51], [55]–[57], used a fixed clustering schemes where either the number of serving BSs or the cluster radius are predetermined. To enhance the BS cooperation effi-

ciency, adaptive clustering schemes are investigated in [45], [119], [120]. Specifically in [119], it is shown that in dense network deployment, interference-aware BS cooperation outperforms both fixed-number and fixed-radius clustering sachems in terms of the coverage performance. The authors of [120] proposed a novel dynamic clustering scheme for mmWave networks and used stochastic geometry tools to evaluate its performance in terms of coverage probability and spectral efficiency. Although, heterogeneous wireless networks are to be deployed for future communication to meet the ever-increasing user traffic demand, the above works studied the the user-centric cooperation only in a single-tier networks.

Recently, BS cooperation in heterogeneous wireless networks have attracted a lot of research interest. For instant, [121] studied the meta distribution of the signal-to-interference ratio (SIR) of a multi-tier heterogeneous network under BS cooperation, where two types of users are considered: the worst-case user which receives data from a single-tier and the general user which can be connected to BSs from different tiers. In [122], BS cooperation based on users' location is enabled for multi-tier networks. It is shown that a moderate level of BS cooperation is optimal for improving the link quality without compromising users' throughput. In [123], a multi-tier heterogeneous wireless network with macro BSs, modeled as a homogeneous Poisson point process (PPP), and users and mmWave small BSs, modeled as a Poisson cluster processes, is analysed. Both fractional frequency reuse and coordinated multi-point transmission are integrated to limit the co-tier interference and improve the coverage and capacity of the network. However, the the works in [121], [122] did not investigate the case when different tiers use different radio spectrum while the work in [123] which analysed a heterogeneous network composed of sub-6 GHz macro BSs and mmWave small BSs, did not study the coverage-rate trade-off in such networks due to different bandwidths provided in different tiers.

5.1.2 Contributions

In [124], we considered a hybrid network composed of only mmWave and THz tiers and investigated the SINR-based user association scheme that leads to maximum

SINR coverage. In the present chapter, we consider a three-tier network, namely, Sub-6 GHz, mmWave and THz, coexist in the network. More importantly, we analyze the coverage performance of the hybrid network by considering both SINR-based and rate-based user association schemes. The reason to adopt the rate-based association is that the maximum SINR coverage may reduce the end-user data rate as will be shown in this work. In fact, for a hybrid network comprising multiple tiers each with a different available spectrum bandwidth, the SINR coverage and link rate behaviours are different and the user association scheme that maximizes the SINR coverage may be unable to maximize the link rate and vice versa. Furthermore, several other enhancements are applied in the system model including the blockage effect consideration and a practical antenna beamforming model with its parameters related to the antenna array size. Finally, this chapter provides several new theoretical findings and numerical results, validating our comprehensive analysis with the aid of Monte Carlo simulations. The main contributions of this chapter can be described as follows:

- We investigate the user-centric BS cooperation in multi-band networks consisting of independently distributed sub-6GHz macrocells and mmWave and THz small cells to improve the network performance. The user is associated with the BSs in each tier based on either maximum SINR or maximum rate criterion while the serving BS cluster within each band is dynamically adapted to the user's channel conditions.

- Using stochastic geometry, we develop a new framework that is leveraged to derive exact expressions for band-specific serving distance distribution, SINR coverage probability, and rate coverage probability, and further simplify the above expressions by considering dominant line-of-sight (LOS) signals scenario in mmWave and THz propagation.

- We provide numerical and simulation results to validate the derived expressions and reveal the impact of different system parameters on the network performance. Such parameters include SINR and rate reliability thresholds,

the cluster size in each band, the molecular absorption loss, which significantly affects the THz propagation. The obtained results entail a coverage/rate trade-off imposed by the network densification with THz and mmWave BSs and provide useful insight to the hybrid network design.

- Our analytical work reveals that the achievable performance of the considered user-centric network heavily depends on the cluster radius, i.e., the distance within which the user is cooperatively served by the BSs in each band. Moreover, despite the substantial performance improvement achieved by the BS cooperation, under both cluster selection strategies, the coverage/rate trade-off due to bandwidth discrepancies among the three tiers is worth further studying.

The rest of this chapter is organized as follows. In Section II, we present the system model. Section III provides analytical expressions for the SINR and rate coverage performances of the proposed user-centric hybrid system. In Section IV, numerical and simulation results are provided to validate the performance characterization of the considered system. Finally, the work in this chapter is concluded in Section V.

5.2 Hybrid System Model

5.2.1 Spatial Model and Assumptions

We consider a three-tier downlink network composed of THz BSs (TBSs), mmWave BSs (MBSs), and sub-6GHz BSs (SBSs) that are distributed uniformly in $\mathbb{R}^2$ according to three independent homogeneous PPPs, Φ_T, Φ_M, and Φ_S, with densities λ_T, λ_M, and λ_S, respectively. It is also assumed that users are distributed uniformly in $\mathbb{R}^2$ according to another independent homogeneous PPP, Φ_u with density λ_u. Each user is served by a cluster of BSs, belonging to one of the three tiers, that cooperate to transmit data to the user. This serving BS cluster is formed based on a dynamic clustering approach as will be discussed later in this section. The analysis

is undertaken for a user located at the origin, $(0,0) \in \mathbb{R}^2$, referred to as a typical user, which, according to the Slivnyak theorem [63], exhibits the same statistical properties as other users at different locations in the network.

We assume that all SBSs are equipped with a single omindirection antenna with unit gain. On the other hand, both TBSs and MBSs are assumed to be supplied with highly directional beamforming antenna arrays to increase the gain in the direction of the intended user [37]. This can compensate for the high path loss and can reduce the effect of the interference in mmWave and THz bands since TBSs and MBSs are expected to be deployed with high densities. To model the radiation patterns of the antenna arrays in all BSs we consider a sectored model which is widely used in literature [66], [68], [69]. As such, the gain in any arbitrary direction can be expressed as

$$G_v = \begin{cases} G_v^{max}, & |\theta| \leq \frac{\theta_v}{2} \\ G_v^{min}, & \text{otherwise,} \end{cases} \tag{5.1}$$

where $v \in \{T,\ M,\ S\}$ refers to the THz, mmWave, and sub-6GHz tiers, G_v^{max} and G_v^{min} are the maximum and minimum antenna array gains corresponding to the gain in the directions of the main-lobe and that of the back and side-lobes, respectively, $\theta \in [-\pi,\ \pi]$ is the angle of the boresight direction and θ_v is the beamwidth of the main-lobe in tier v.

According to [125], [126], the antenna arrays parameter of tier v, i.e, G_v^{max}, G_v^{min}, and θ_v, are related to the number of elements in the array and the array geometry. For a uniform linear antenna array with space between elements equal to half the operating wavelength, G_v^{max}, G_v^{min}, and θ_v are given as

$$G_v^{max} = \frac{2\pi N_v^2 \sin\left(\frac{3\pi}{2N_v}\right)}{\theta_v N_v^2 \sin\left(\frac{3\pi}{2N_v}\right) + (2\pi - \theta_v)}, \tag{5.2}$$

$$G_v^{min} = \frac{2\pi}{\theta_v N_v^2 \sin\left(\frac{3\pi}{2N_v}\right) + (2\pi - \theta_v)}, \tag{5.3}$$

and

$$\theta_v = 2 \arcsin\left(\frac{2.782}{\pi N_v}\right). \tag{5.4}$$

where N_v is the number of elements in the corresponding array. Note that in systems with beamforming antenna directivity, to serve multiple users, BSs are equipped with large antenna arrays which consist of subsets of smaller antenna arrays known as subarrays. These subarrays can direct different beams to multiple users at different locations. In this case, N_v is the number of elements per subarray. All users are assumed to be equipped with omnidirctional antennas with unity gain. This enables each user to receive multiple beams from different BSs and avoid the high power consumption at the user side. Therefore, the total link gain between the user and an arbitrary interferer in tier v is modeled as a discrete random variable $G_v = \{G_v^{max}, G_v^{min}\}$ with probability $p_{G_v} = \{\frac{\theta_v}{2\pi}, \frac{2\pi-\theta_v}{2\pi}\}$. When the array size is $N_v = 1$, then $G_v^{max} = G_v^{min} = 1$ and $\theta_v = 2\pi$, i.e., the antenna arrays are omnidirectional, which is the case for all SBSs. We also assume that all TBSs and MBSs are able to make their antennas orientations in the direction of maximum gain with respect to the served user [37], [100].

5.2.2 Multi-tier Propagation Models

In this work, we consider dense deployments of TBSs and MBSs. This implies that a user can observe a large number of TBSs and MBSs in its LOS range. Furthermore, due to the high penetration and absorption losses at THz and mmWave bands, the power signal received from non-LOS (NLOS) BSs is very weak compared to that received from the LOS BSs. As such, LOS transmissions become dominant over the NLOS transmissions [37], [87], [88]. Moreover, in [66, Fig. 8], it is shown that NLOS links have negligible effect on the system coverage performance in dense mmWave networks. Therefore, to simplify the analysis in this chapter, only the LOS links are taken into account. According to [86], [87], [90], the LOS channel between the i-th TBS located at distance r_i and the the typical user is given by

$$\xi_T(r_i) = \frac{c^2}{(4\pi f_T)^2} r_i^{-\alpha_T} \exp\big(-k_a(f_T) r_i\big), \tag{5.5}$$

where α_T is the path loss exponent, c is the speed of light in free space, f_T denotes the THz operating frequency, and $k_a(f_T)$ represents the molecular absorption coefficient

which depends on the network operating frequency, f_T. For the mmWave tier, the LOS communication channel to the i-th MBSs located at a distance r_i is expressed as [36], [37]

$$\xi_M(r_i) = \frac{c^2}{(4\pi f_M^2)} h_M r_i^{-\alpha_M}, \tag{5.6}$$

where f_M denotes the operating frequency of mmWave tier, α_M is the path loss exponent of the mmWave path, and h_M defines the small-scale fading channel gain. We assume that the small-scale fading follows Nakagami-m distribution [37]. Therefore, h_M is a Gamma random variable with $h_M \sim \Gamma(m, 1/m)$, where m is the Nakagami parameter. Then, the probability density function (PDF) of h_M is given as

$$f_{h_M}(t) = \frac{m^m}{\Gamma(m)} t^{m-1} e^{-mt}. \quad t > 0 \tag{5.7}$$

For the sub-6GHz links, the propagation channel is similar to (5.6), i.e, $\xi_S(r_i) = \frac{c^2}{(4\pi f_S^2)} h_S r_i^{-\alpha_S}$, where α_S and f_S are the pathloss exponent and the operating frequency of the sub-6GHz tier, respectively, and h_S is the channel fading gain which is assumed to follow the Rayleigh distribution. As such, the power received by the typical user from the i-th serving BS in tier v located at a distance r_i from the origin is given as

$$P_v(r_i) = P_{t,v} G_v^{max} \xi_v(r_i), \tag{5.8}$$

where $P_{t,v}$, $v \in \{T,\ M,\ S\}$ denotes the BS transmit power in tier v which is assumed the same for all BSs in the same tier.

Due to the high penetration loss in mmWave and THz communications, the signal may be interrupted when an obstacle blocks the signal paths. The blockage effect can be properly incorporated such that the probability that the i-th BS at a distance r_i from the typical user is LOS (not blocked) can be modeled as $P_{\text{LOS}}(r_i) = e^{-\beta r_i}$, where β is a parameter dependent on the sizes and density of blockages. For the sake of tractability, we use the LOS ball model proposed in [66] which defines the LOS probability function $P_{\text{LOS}}(r_i)$ as one for $r_i \leq R_L$ and zero otherwise, where R_L is the LOS range. This model is proved to be accurate enough to account for the effect of blockage when R_L is carefully determined. To achieve accurate results, the LOS range is computed such that $R_L = \sqrt{2}/\beta$, according to [66].

5.3 Hybrid Clustering and User Association Models

In the user-centric BS cooperation, each user can be served by a carefully selected cluster of BSs. In this chapter, we consider a hybrid network composed of three tiers with different RF resources, where the typical user first forms three candidate clusters, each containing BSs from the same tier, and then selects only one of these three candidate clusters to transmit the data. Fig. 5.1 depicts an example of the considered hybrid network where TBSs, MBSs and SBSs are denoted by the red circles, blue triangles, and green squares, respectively. Since the analysis is conducted for the typical user, only this user is illustrated in the figure as denoted by the black star. Three candidate clusters are shown in Fig. 5.1, where for a given tier, the BSs with black arrows toward the user represent the candidate serving cluster from this tier. In the following we will illustrate how the user determines the three candidate clusters and how one of these clusters is selected to serve the user. Let $\bar{P}_{r,v}(y_k)$ be the average power received from the k-th BS in tier v which is located at a distance r_k from the typical user and let τ_v be the maximum average power received by the typical user from tier v, i.e, it is defined as

$$\tau_v = \max_{k \in \Phi_v} \bar{P}_v(r_k) \tag{5.9}$$

Then, τ_v is used as a reference to build the three candidate serving clusters. Given the distance r_v between the typical user and the BS with the maximum average received power τ_v, the user forms the three candidate serving clusters as,

$$\widetilde{\Phi}_v = \left\{ y_k \in \Phi_v, \ || \ y_k \ || \leq a_v \right\}, \quad v \in \{T, M, S\} \tag{5.10}$$

where $\widetilde{\Phi}_v$ is the candidate serving cluster for tier v and $a_v = \delta_v^{-1} r_v$ is the cluster radius with $0 < \delta_v \leq 1$ being the dynamic clustering parameter in tier v, which controls the cluster size. From (5.9), τ_v can be redefined as $\tau_v = \bar{P}_v(r_v)$. Then,

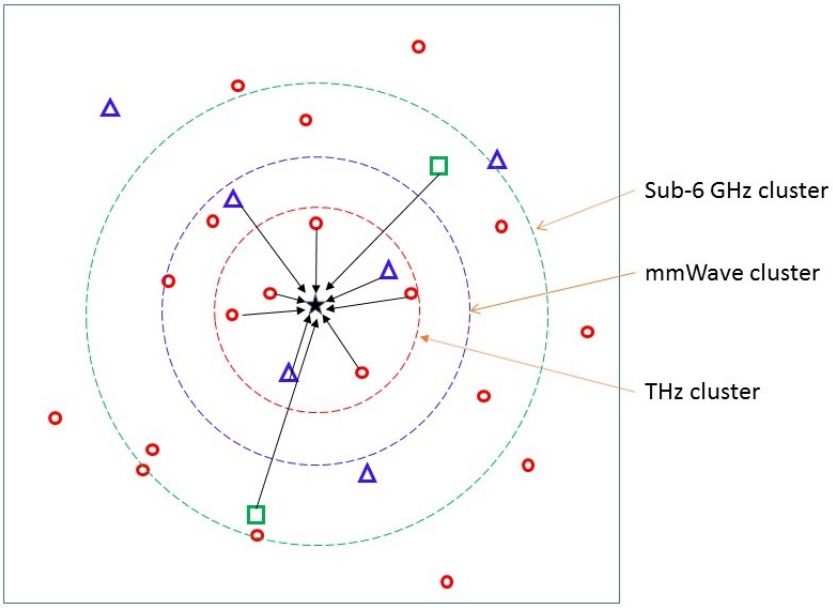

Figure 5.1: An illustration of the system model for a three-tier hybrid network. The typical user at the origin is denoted by the black star mark, while TBSs, MBSs and SBSs are denoted by the red circles, blue triangles, and green squares, respectively.

using (5.5)-(5.8), for the typical user, a_v, can be computed as follows

$$a_v = \begin{cases} \dfrac{\text{LambertW}_0\left(\dfrac{k_a(f_T)\left(\frac{\tau_T}{C_T G_{max}^T}\right)^{\frac{-1}{\alpha_T}}}{\alpha_T}\right)}{\delta_T k_a(f)}, & \text{for } \widetilde{\Phi}_T, \\ \frac{1}{\delta_M}\left(\frac{\tau_M}{P_M C_M G_M^{max}}\right)^{\frac{-1}{\alpha_M}}, & \text{for } \widetilde{\Phi}_M \\ \frac{1}{\delta_S}\left(\frac{\tau_R}{P_S C_S}\right)^{\frac{-1}{\alpha_S}}, & \text{for } \widetilde{\Phi}_S \end{cases} \tag{5.11}$$

where $C_v = \frac{c^2}{(4\pi f_v)^2}$, $v \in \{T,\ M,\ S\}$ and $\text{LambertW}_0(.)$ is the Lambert W_0 function defined as the inverse of the function $f(w) = we^{-w}$. Fig. 5.2 illustrates a scenario, where for a given tier v, the maximum received power τ_v is first calculated and then used to determine the cluster radius according to (5.11). If this cluster is selected to serve the user, all BSs within the cluster can cooperatively send data to the user while those outside the cluster from the same tier are considered as interferers. Since r_v is the distance to the BS with the maximum average received power τ_v, defined in (5.9), it is clear that r_v is the distance to the closest BS in tier v. As such, because BSs from the three tiers are distributed according to three independent PPPs, the

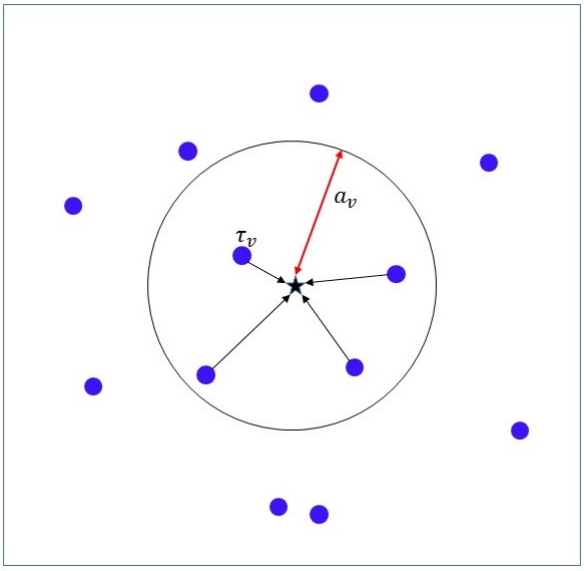

Figure 5.2: Building a candidate serving cluster from a given tier $v \in \{T, M, S\}$. The typical user at the origin is denoted by the black star, while the blue dots represent BSs from tier v. The cluster radius is determined by the red double-headed arrow which is determined based on τ_v according to (5.11).

distribution of the cluster radius a_v is written as [63]

$$f_{a_v}(t) = 2\pi\lambda_v t e^{-\pi\lambda_v \delta_v^{-2} t^2}/\mathcal{B}, \quad 0 \leq t < \delta_v R_L \tag{5.12}$$

where $\mathcal{B} = 1 - e^{-\pi\lambda_v R_L^2}$ is the probability that at least one BS from tier v exists at a distance less than R_L from the typical user, where in dense network deployments, $\mathcal{B} \approx 1$. Once the three candidate clusters are determined, only one of them is selected to serve the user. In the following, two schemes are proposed to select the user's serving cluster, namely, maximum SINR cluster selection (MSCS) and maximum rate cluster selection (MRCS) schemes.

5.3.1 Maximum SINR Cluster Selection

In the maximum SINR cluster selection (MSCS) scheme, the serving cluster is selected from the three candidates clusters based on the maximum SINR as follows

$$\phi = \left\{ \widetilde{\Phi}_v, v = \arg \max_{v \in \{T,\, M,\, U\}} \{\Upsilon_v\} \right\}, \tag{5.13}$$

where Υ_v is the received SINR given the user is connected to tiers v.

5.3.2 Maximum Rate Cluster Selection

In the maximum rate cluster selection (MRCS) scheme, the user selects the candidate cluster which provides the maximum downlink rate as given by

$$\phi = \left\{ \widetilde{\Phi}_v, v = \arg \max_{v \in \{T,\, M,\, U\}} \{\mathcal{R}_v\} \right\}, \tag{5.14}$$

where $\mathcal{R}_v$ is the achievable rate when the user is connected to tier v, which can be expressed as

$$\mathcal{R}_v = B_v \log_2\big(1 + \Upsilon_v\big), \quad v \in \{T,\ M,\ S\} \tag{5.15}$$

bit/second (bps), where B_v is the per user bandwidth provided by tier v. Let B_{max} is the maximum bandwidth among the three tiers, which practically be the THz bandwidth. We can normalize the rate as $\overline{\mathcal{R}}_v = \overline{b}_v \log_2\big(1 + \Upsilon_v\big) = \log_2\big(1 + \Upsilon_v\big)^{\overline{b}_v}$, where $\overline{b}_v = \frac{B_v}{B_{\max}}$ is the normalized bandwidth of tier v. As a result, the serving cluster selection in (5.14) is redefined as

$$\phi = \left\{ \widetilde{\Phi}_v, v = \arg \max_{v \in \{T,\, M,\, S\}} \left\{ \big(1 + \Upsilon_v\big)^{\overline{b}_v} \right\} \right\} \tag{5.16}$$

From (5.13) and (5.16), it is clear that in hybrid networks with different bandwidth for each tier, no clustering scheme can maximize the rate and SINR coverage performances at the same time. This means that there should be a trade-off between the received SINR and the link rate as will be discussed in details in Section IV. On the other hand, (5.13) and (5.16) indicate that MSCS and MRCS schemes are exactly the same when the three tiers provide the same bandwidths. Moreover, according to the proposed clustering model and the two cluster selection schemes, different users may be associated to different tiers with different cluster sizes. Furthermore, if the user's location is changed, its serving tier and cluster size may change. As such, (5.13)- (5.16) provide a dynamic BS clustering and tier association model.

5.4 System Performance Analysis

In this section, we investigate the SINR and rate coverage probabilities of a typical user which is cooperatively served by a set of BSs in tier v, under MSCS and MRCS schemes, respectively. Let Υ denote the instantaneous received SINR at the user, then using (5.1)-(5.10), Υ can be written as

$$\Upsilon = \Big\{\Upsilon_v,\ \phi = \widetilde{\Phi}_v\Big\}, \quad v \in \{T,\ M,\ S\}, \tag{5.17}$$

with Υ_v being given by

$$\Upsilon_v = \begin{cases} \dfrac{\sum_{k\in\widetilde{\Phi}_T} P_T G_{T,k} C_T r_k^{-\alpha_T} e^{-k_a(f_T)r_k}}{\sum_{j\in\Phi_T\setminus\widetilde{\Phi}_T} P_T G_{T,j} C_T r_j^{-\alpha_T} e^{-k_a(f_T)r_j} + \sigma_T^2}, & v = T \\ \dfrac{\sum_{k\in\widetilde{\Phi}_M} P_M G_{M,k} C_M h_{M,k} r_k^{-\alpha_M}}{\sum_{j\in\Phi_M\setminus\widetilde{\Phi}_M} P_M C_M G_{M,j} h_{M,j} r_j^{-\alpha_M} + \sigma_M^2}, & v = M \\ \dfrac{\sum_{k\in\widetilde{\Phi}_S} P_S C_S h_{S,k} r_k^{-\alpha_S}}{\sum_{j\in\Phi_S\setminus\widetilde{\Phi}_S} P_S C_S h_{S,j} r_j^{-\alpha_S} + \sigma_S^2}, & v = S \end{cases} \tag{5.18}$$

where r_k is the Euclidian distance between the typical user and the k-th BS in its serving cluster while r_j denotes the distance to the j-th interfering BS from the same tier as the serving BS, and $\sigma_v^2, v \in \{M,\ T,\ S\}$ represents the noise power for band v. The SINR and rate coverage probabilities are provided in the following theorem.

Theorem 5.4.1 *For a given SINR threshold, γ_{th}, and a given rate threshold, $\mathcal{R}_{th}$, the SINR coverage probabilities, denoted as $\mathcal{P}_\Upsilon\big(\gamma_{th}\big)$, and the rate coverage probability, denoted as $\mathcal{P}_\mathcal{R}\big(\mathcal{R}_{th}\big)$, of the considered hybrid user-centric network under the MSCS and MRCS schemes are, respectively, given as*

$$\mathcal{P}_\Upsilon\big(\gamma_{th}\big) = 1 - \prod_{v\in\{T,M,S\}} \Big(1 - \mathcal{F}_v\big(\gamma_{th}\big)\Big), \tag{5.19}$$

and

$$\mathcal{P}_\mathcal{R}\big(\mathcal{R}_{th}\big) = 1 - \prod_{v\in\{T,M,S\}} \Big(1 - \mathcal{F}_v\Big(2^{\frac{R_{th}}{\bar{b}_v B_{max}}} - 1\Big)\Big), \tag{5.20}$$

where $\mathcal{F}_v(x)$ is the conditional SINR CCDF at a threshold x given that the user is served by a cluster of BSs from tier v.

Proof: From (5.13) and (5.16), it is clear that both the received SINR under the MSCS scheme and the rate under the MRSC scheme are random variables reflecting the maximum of three independent random variables. Therefore, the CCDFs of the received SINR, Υ, and the rate, $\mathcal{R}$, of the considered hybrid user-centric network are given as in (5.19) and (5.20), respectively.

In the following subsections, we provide analytical expressions for the conditional CCDFs of SINR.

5.4.1 SINR Distribution given $\phi = \widetilde{\Phi}_T$

First, we derive the received SINR CCDF when $\phi = \widetilde{\Phi}_T$, i.e, the SINR coverage probability given the user served by a set of dynamically selected TBSs. Let's rewrite the SINR received from the THz tier as $\Upsilon_T = \frac{S_T^{agg}}{I_T^{agg}+\sigma_T^2}$, where $S_T^{agg} = \sum_{k\in\widetilde{\Phi}_T} P_T G_T^{max} C_T r_k^{-\alpha_T} \exp\big(-k_a(f_T)r_k\big)$ is the sum of signal powers received from all TBSs in the user's serving cluster, i.e., from BSs in $\widetilde{\Phi}_T$, and $I_T^{agg} = \sum_{j\in\Phi_T\setminus\widetilde{\Phi}_T} P_T$ $G_{T,j} C_T r_j^{-\alpha_T} \exp\big(-k_a(f_T)r_j\big)$ is the aggregated interference received from all TBS in $\{\Phi_T \setminus \widetilde{\Phi}_T\}$. Then, for a threshold x, the SINR CCDF given $\phi = \widetilde{\Phi}_T$, $\mathcal{F}_T(x)$, is defined as

$$\begin{aligned}\mathcal{F}_T(x) &= \Pr\big[\Upsilon_T > x\big] = \Pr\left[\frac{S_T^{agg}}{I_T^{agg}+\sigma_T^2} > x\right] \\ &= \Pr\left[I_T^{agg} < \frac{S_T^{agg}}{x} - \sigma_T^2\right] \\ &= \widetilde{\mathcal{F}}_{I_T^{agg}}\left(\frac{S_T^{agg}}{x} - \sigma_T^2\right), \end{aligned} \tag{5.21}$$

where $\Pr[A]$ defines the probability of event A, $\widetilde{\mathcal{F}}_{I_T^{agg}}(\widetilde{x})$ is the CDF of the aggregated interference I_T^{agg} for a threshold $\widetilde{x}$. which may be calculated by resorting to the Gil–Pelaez inversion theorem [91], [127] as $\widetilde{\mathcal{F}}_{I_T^{agg}}(\widetilde{x}) = \frac{1}{2} - \frac{1}{\pi}\int_0^\infty \frac{\mathrm{Im}\left\{\exp(-j\omega\widetilde{x})\Lambda_{I_T^{agg}}(j\omega)\right\}}{\omega}$ $d\omega$, where $\Lambda_{I_T^{agg}}(j\omega)$ denotes the characteristic function of I_T^{agg}, and $\mathrm{Im}\{.\}$ is a function that returns the imaginary part of its argument. The expression of the characteristic function of I_T^{agg} is provided using the following lemma.

Lemma 5.4.1 *Suppose the typical user is served by a cluster of TBSs, i.e,* $\phi = \widetilde{\Phi}_T$*, and* a_T *is the cluster radius, then the characteristic function of the aggregated interference* I_T^{agg}*,* $\Lambda_{I_T^{agg}|a_T}(j\omega)$*, is given by*

$$\Lambda_{I_T^{agg}|a_T}(j\omega) = \exp\Bigg\{ -2\pi\lambda_T \sum_{G_T} \sum_{n=1}^{\infty} \frac{p_{G_T}(-j\omega C_T G_T)^n}{n!(nk_a(f_T))^{2-n\alpha_T}} \times \Big(\Gamma(2-\alpha_T n,\ nk_a(f_T)a_T) - \Gamma(2-\alpha_T n,\ nk_a(f_T)R_L)\Big)\Bigg\}. \quad (5.22)$$

Proof: See Appendix 5.7.1.

Note that the infinite summation in (5.22) results from the existence of the molecular absorption term in the THz propagation channel. Due to the infinite summation in (5.22), using the Gil-Pelaez inversion theorem to compute the CDF of the THz interference, $\widetilde{\mathcal{F}}_{I_T^{agg}}$, is intractable. Therefore, we apply the central limit theorem to approximate the interference with a normal distribution. As a result, the CDF of the aggregated THz interference for a given cluster radius a_T is obtained by the following proposition.

Proposition 5.4.1 *For a given threshold* $\widetilde{x}$*, the CDF of the aggregated interference in a user-centric dense THz networks with a serving cluster radius* a_T*, can be approximated as,*

$$\widetilde{F}_{I_T^{agg}|a_T}(\widetilde{x}) \approx \frac{1}{2}\left(1 + erf\left(\frac{\widetilde{x} - \mu_{I_T^{agg}}(a_T)}{\sqrt{2\mathcal{V}_{I_T^{agg}}(a_T)}}\right)\right), \quad (5.23)$$

where $erf(z) = \frac{2}{\sqrt{\pi}} \int_0^z e^{-t^2} dt$ *is the error function [62], and* $\mu_{I_T^{agg}}(a_T)$ *and* $\mathcal{V}_{I_T^{agg}}(a_T)$ *are the mean and variance of the aggregated interference,* I_T^{agg}*, which can be computed as*

$$\mu_{I_T^{agg}}(a_T) = \mathcal{M}'(a_T), \quad (5.24)$$

and

$$\mathcal{V}_{I_T^{agg}}(a_T)) = \mathcal{M}''(a_T) - \Big(\mathcal{M}'(a_T)\Big)^2, \quad (5.25)$$

where $\mathcal{M}'\big(a_T\big)$ *and* $\mathcal{M}''\big(a_T\big)$ *are the first and second moments of the random variable* I_T^{agg} *that can be obtained from its characteristic function in (5.22) as*

$$\mathcal{M}'\big(a_T\big) = \frac{1}{j^{-1}}\frac{\partial \Lambda_{I_T^{agg}|a_T}(j\omega)}{\partial \omega}\bigg|_{\omega=0} = \frac{2\pi\lambda_T P_T C_T G_T^{(1)}}{k_a(f_T)^{2-\alpha_T}} \times\bigg(\Gamma\Big(2-\alpha_T,\ k_a(f_T)a_T\Big) - \Gamma\Big(2-\alpha_T,\ k_a(f_T)R_L\Big)\bigg) \tag{5.26}$$

and

$$\begin{aligned}\mathcal{M}''\big(a_T\big) &= \frac{1}{j^{-2}}\frac{\partial^2 \Lambda_{I_{agg}|a_T}(j\omega)}{\partial \omega^2}\bigg|_{\omega=0} = \bigg(\frac{2\pi\lambda_T P_T C_T G_T^{(2)}}{k_a(f_T)^{4-2\alpha_T}} \\ &\times\bigg(\Gamma\Big(2-\alpha_T,\ k_a(f_T)a_T\Big) - \Gamma\Big(2-\alpha_T,\ k_a(f_T)R_L\Big)\bigg)\bigg)^2 \\ &+\frac{4\pi\lambda_T (P_T C_T G_T^{(1)})^2}{2\big(2k_a(f_T)\big)^{2-2\alpha_T}}\bigg(\Gamma\Big(2-2\alpha_T,\ 2k_a(f_T)a_T\Big) \\ &-\Gamma\Big(2-2\alpha_T,\ 2k_a(f_T)R_L\Big)\bigg),\end{aligned} \tag{5.27}$$

where $G^{(1)}$ *and* $G^{(2)}$ *are the first and second moments of* G_T*, respectively.*

From (5.23)-(5.27), it is clear that the interference distribution is approximated as a normal distribution, i.e, $I_T^{agg} \sim \mathcal{N}\Big(\mu_{I_T^{agg}}(a_T), \mathcal{V}_{I_T^{agg}}(a_T)\Big)$, for a given cluster radius a_T. Moreover, according to [92], [93], this approximation becomes more efficient if the interferers with dominant power are excluded and/or when the network is deployed with high BS density. For a given exclusion region, the authors of [92] used Kolmogorov–Smirnov bound and the authors of [93] used Berry–Esseen bound to compares the aggregated interference CDF with the Gaussian CDF. It is proved that, as the exclusion region and/or the BS density increase, the distribution of the aggregated interference matches well the Gaussian distribution (see [92, Fig. 8] and [93, Fig. 2]). It is worth noting that for the case of the proposed user-centric BS cooperation, the user's serving cluster represents an interference exclusion region and also THz networks are expected to be deployed with ultra-density. This results in the aggregate interference being a sum of a large number of independent random

variables with comparable variances which justify the applicability of central limit theorem. Using (5.21) and (5.23), the SINR CCDF for a user served the THz tier is obtained from the following proposition.

Proposition 5.4.2 *Given that the user is connected to the THz tier, i.e, $\phi = \widetilde{\Phi}_T$, the received SINR CCDF at the typical user under the proposed dynamic clustering scheme is given as*

$$\begin{aligned}\mathcal{F}_T(x) &= \int_0^{\infty} \frac{1}{2}\Bigg(1+\sum_{\widetilde{n}=0}^{\infty}\frac{(\pi\lambda(t\delta_T)^2(\delta_T^{-2}-1))^{\widetilde{n}}}{\widetilde{n}!}e^{-\pi\lambda_T(t\delta_T)^2(\delta_T^{-2}-1)}\mathrm{erf}\Bigg(\frac{1}{x\sqrt{2\mathcal{V}_{I_T^{agg}}(t)}}\\
&\times\Bigg(P_T G_T^{max} C_T (t\delta_T)^{-\alpha_T} e^{-k_a(f_T)t\delta_T} + 2\widetilde{n} G_T^{max} P_T C_T k_a(f_T)^{-\alpha_T+2}(t\delta_T)^{-2}\\
&\times(\delta_T^{-2}-1)^{-1}\Big(\Gamma\big(2-\alpha_T, k_a(f_T)t\delta_T\big) - \Gamma\big(2-\alpha_T, k_a(f_T)t\big)\Big)\\
&-x\big(\sigma_T^2 + \mu_{I_T^{agg}}(t)\big)\Bigg)\Bigg) f_{a_T}(t)dt, \end{aligned} \tag{5.28}$$

Proof: See Appendix 5.7.2.

5.4.2 SINR Distribution given $\phi = \widetilde{\Phi}_M$

When the user is served by a cluster of MBSs, the SINR expression in (5.18) can be rewritten as $\Upsilon_M = \frac{S_M^{agg}}{I_M^{agg}+\sigma_M^2}$, where $S_M^{agg} = \sum_{k\in\widetilde{\Phi}_M} P_M G_M^{max} C_M h_{M,k} r_k^{-\alpha_M}$ and $I_M^{agg} = \sum_{j\in\Phi_b^M\setminus\widetilde{\Phi}_M} P_M G_{M,j} h_{M,j} r_j^{-\alpha_M}$ are the aggregated mmWave signal and aggregated mmWave interference, respectively. Then, using the Gil–Pelaez inversion theorem [91], [127], the SINR CCDF, $\mathcal{F}_M(x)$, can be obtained from the following proposition.

Proposition 5.4.3 *Given $\phi = \Phi_M^S$, the CCDF of the received SINR at the typical user for the considered dynamic user-centric network is given by*

$$\begin{aligned}\mathcal{F}_M(x) &= \frac{1}{2} + \int_0^{\infty}\int_0^{\infty}\frac{1}{\omega} Im\Big\{\Lambda_{S_M^{agg}|t}(-j\omega)\Lambda_{I_M^{agg}|t}(j\omega x)e^{-j\omega\sigma^2 x}\Big\}\\
&\times f_{a_M}(t)d\omega dt, \end{aligned} \tag{5.29}$$

where $\Lambda_{S_M^{agg}|t}(j\omega)$ *and* $\Lambda_{I_M^{agg}|t}(j\omega)$ *are, respectively, the characteristic functions of the aggregated signal,* S_M^{agg}*, and the aggregated interference* I_M^{agg}*, for a given culster radius* $a_M = t$*.*

The following lemma provides theoretical expressions for both $\Lambda_{S_M^{agg}|t}(j\omega)$ and $\Lambda_{I_M^{agg}|t}(j\omega)$.

Lemma 5.4.2 *Suppose the user is served by a cluster of MBSs, i,e.* $\phi = \widetilde{\Phi}_M$*, the characteristic functions of* S_M^{agg}*, and* I_M^{agg} *for a given cluster radius* $a_M = t$ *are expressed, respectively, as*

$$\begin{aligned}\Lambda_{S_M^{agg}|t}(j\omega) &= \Big(1+\frac{j\omega P_M G_M^{max} C_M (\delta_M t)^{-\alpha_M}}{m}\Big)^{-m} \exp\Bigg(-\frac{j2\pi\lambda_M \omega P_M C_M G_M^{max}}{t^{\alpha_M-2}(\alpha_M-2)} \\ &\times\Bigg(\frac{\Gamma\Big(2-\frac{2}{\alpha_M}\Big)\Gamma(2)}{\Gamma(m+1)\Gamma(1-\frac{2}{\alpha_M})} G_{1,3}^{3,3}\left[\frac{j\omega G_M^{max} P_M C_M t^{-\alpha_M}}{m}\middle| \begin{matrix} m, 0, \frac{2}{\alpha_M} \\ 0, -1, \frac{2}{\alpha_M}-1 \end{matrix}\right] \\ &-\frac{\delta_M^{\alpha_M-2}\Gamma\Big(2-\frac{2}{\alpha_M}\Big)\Gamma(2)}{\Gamma(m+1)\Gamma(1-\frac{2}{\alpha_M})} G_{1,3}^{3,3}\left[\frac{j\omega P_M G_M^{max} C_M \delta_M^{\alpha_M} t^{-\alpha_M}}{m}\middle| \begin{matrix} m, 0, \frac{2}{\alpha_M} \\ 0, -1, \frac{2}{\alpha_M}-1 \end{matrix}\right]\Bigg)\Bigg)\end{aligned} \tag{5.30}$$

and

$$\begin{aligned}\Lambda_{I_M^{agg}|t}(j\omega) &= \exp\Bigg(-\frac{j2\pi\lambda_M\omega C_M}{t^{\alpha_M-2}(\alpha_M-2)}\sum_{G_M} P_{G_M}\frac{G_M \delta_M^{\alpha_M-2}\Gamma\Big(2-\frac{2}{\alpha_M}\Big)\Gamma(2)}{\Gamma(m+1)\Gamma(1-\frac{2}{\alpha_M})} \\ &\times\Bigg(G_{1,3}^{3,3}\left[\frac{j\omega G_M C_M \delta_M^{\alpha_M} t^{-\alpha_M}}{m}\middle| \begin{matrix} m, 0, \frac{2}{\alpha_M} \\ 0, -1, \frac{2}{\alpha_M}-1 \end{matrix}\right] \\ &-G_{1,3}^{3,3}\left[\frac{j\omega G_M C_M R_L^{-\alpha_M}}{m}\middle| \begin{matrix} m, 0, \frac{2}{\alpha_M} \\ 0, -1, \frac{2}{\alpha_M}-1 \end{matrix}\right]\Bigg)\Bigg),\end{aligned} \tag{5.31}$$

where $\mathrm{G}_{p,q}^{m,n}(\cdot)$ *is the Meijer's G function [62, Eq.(9.301)].*

Proof: See Appendix 5.7.3.

5.4.3 SINR Distribution given $\phi = \widetilde{\Phi}_S$

Similarly, for $\phi = \widetilde{\Phi}_S$, we have $\Upsilon_S = \frac{S_S^{agg}}{I_S^{agg}+\sigma_S^2}$, where $S_S^{agg} = \sum_{k\in\widetilde{\Phi}_S} P_S C_S h_{S,k} r_k^{-\alpha_S}$ and $I_S^{agg} = \sum_{j\in\Phi_b^S\setminus\widetilde{\Phi}_S} P_S G_{S,j} h_{S,j} r_j^{-\alpha_S}$ are the aggregated sub-6 GHz signal and aggregated interference, respectively. In this case, the SINR CCDF, $\mathcal{F}_S(x)$, is provided as follows.

Proposition 5.4.4 *Given $\phi = \widetilde{\Phi}_S$, the CCDF of the received SINR at the typical user for the considered dynamic user-centric network is given by*

$$\begin{aligned}\mathcal{F}_S(x) &= \frac{1}{2} + \int_0^\infty \int_0^\infty \frac{1}{\omega} Im\Big\{\Lambda_{S_S^{agg}|t}(-j\omega)\Lambda_{I_S^{agg}|t}(j\omega x)e^{-j\omega\sigma^2 x}\Big\} \\ &\quad \times f_{a_S}(t)d\omega dt, \end{aligned} \tag{5.32}$$

where $\Lambda_{S_S^{agg}|t}(j\omega)$ and $\Lambda_{I_S^{agg}|t}(j\omega)$ are, respectively, the characteristic functions of S_S^{agg} and I_S^{agg}, which for $a_S = t$ can be obtained from the following lemma.

Lemma 5.4.3 *For $\phi = \widetilde{\Phi}_S$, the characteristic functions of S_S^{agg} and I_S^{agg} for a given cluster radius $a_S = t$ are, respectively, expressed as*

$$\begin{aligned}\Lambda_{S_S^{agg}|t}(j\omega) &= \frac{1}{1+j\omega P_S G_S^{max} C_S t^{-\alpha_S}} \exp\Bigg(- \frac{2\pi\lambda_R j\omega P_S C_S}{t^{\alpha_S-2}(\alpha_S-2)} \Bigg(\frac{\Gamma\Big(2-\frac{2}{\alpha_S}\Big)}{\Gamma(1-\frac{2}{\alpha_S})} \\ &\quad \times G_{1,3}^{3,3}\Bigg[j\omega P_S C_S t^{-\alpha_S} \Bigg| \begin{matrix} 1, 0, \frac{2}{\alpha_S} \\ 0, -1, \frac{2}{\alpha_S}-1 \end{matrix} \Bigg] - \frac{\delta_S^{\alpha_S-2}\Gamma\Big(2-\frac{2}{\alpha_S}\Big)}{\Gamma(1-\frac{2}{\alpha_S})} \\ &\quad \times G_{1,3}^{3,3}\Bigg[j\omega P_S C_S \delta_S^{\alpha_S} t^{-\alpha_S} \Bigg| \begin{matrix} 1, 0, \frac{2}{\alpha_S} \\ 0, -1, \frac{2}{\alpha_S}-1 \end{matrix} \Bigg] \Bigg) \Bigg) \end{aligned} \tag{5.33}$$

and

$$\begin{aligned}\Lambda_{I_S^{agg}|t}(j\omega) &= \exp\Bigg(- \frac{2\pi\lambda_S j\omega P_S C_S}{t^{\alpha_S-2}(\alpha_S-2)} \frac{\delta_S^{\alpha_S-2}\Gamma\Big(2-\frac{2}{\alpha_S}\Big)}{\Gamma(1-\frac{2}{\alpha_S})} \\ &\quad \times G_{1,3}^{3,3}\Bigg[j\omega P_S C_S \delta_S^{\alpha_S} t^{-\alpha_S} \Bigg| \begin{matrix} 1, 0, \frac{2}{\alpha_S} \\ 0, -1, \frac{2}{\alpha_S}-1 \end{matrix} \Bigg] \Bigg), \end{aligned} \tag{5.34}$$

Proof: Following the same steps of proving (5.30) and (5.31) and considering that h_S follows the Rayleigh fading and the interferers antenna gain is constant, i.e., no

beamforming is employed, the expressions of $\Lambda_{S_S^{agg}|t}(j\omega)$ and $\Lambda_{I_S^{agg}|t}(j\omega)$ are written as in (5.33) and (5.34), respectively.

To realize the efficiency of the proposed dynamic user-centric cooperation, we introduce a non-cooperative transmission scheme, where the user is connected to only one BS. The SINR and rate coverage performances of the non-cooperative transmission can be easily obtained from the provided SINR and rate coverage expressions of the user-centric cooperation by letting $\delta_T = \delta_M = \delta_S = 1$.

5.5 Numerical Results

Table 5.1: Network Parameters for Numerical Computation

Parameter	THz Tier	mmWave Tier	sub-6GHz Tier
Operating frequency	$f_T = 0.8$ THz	$f_M = 73$ GHz	$f_S = 2.4$ GHz
Bandwidth	$B_T = 500$ MHz	$B_M = 100$ MHz	$B_S = 20$ MHz
BS density	$\lambda_T = 10^{-3}$ TBSs/m^2	$\lambda_M = 10^{-4}$ MBSs/m^2	$\lambda_M = 10^{-6}$ SBSs/m^2
Pathloss exponent	$\alpha_T = 3$	$\alpha_M = 2.5$	$\alpha_S = 2.1$
Transmit power	$P_T = 30$ dBm	$P_M = 30$ dBm	$P_S = 40$ dBm
Clustering Parameter (if fixed)	$\delta_T = 0.5$, 0.6, and 1	$\delta_M = 0.5$, 0.6, and 1	$\delta_S = 0.2$, 0.5, 0.8, and 1
Antenna array parameters	$N_T = 8$	$N_M = 8$	$N_S = 1$
SINR and rate thresholds (if fixed)	$\gamma_{th} = 10$ dB and $\mathcal{R}_{th} = 800$ Mpbs		

In this section, we provide numerical results for the SINR and rate coverage performances of the proposed use-centric hybrid networks under dynamic BS clustering. The provided analytical expressions in this chapter are validated using Monte Carlo simulations. For the SINR CCDF expression in (5.28), $\mathcal{F}_T(x)$, it is observed that

the summation over $\widetilde{n}$ converges fast where the first 10 terms can sufficiently match well with the simulation. The system parameters are given in Table 5.1. Note that the values of G_v^{max}, G_v^{min}, and θ_v are computed using (5.2)-(5.4) at $N_T = N_M = 8$ for the THz and mmWave tiers and at $N_S = 1$ for the sub-6GHz teir. The LOS range is $R_L = 225$ meter, which is equivalent to the rectangle Boolean model with $\beta = 0.0063$ [66]. Finally, for THz channel, the absorption coefficient, if fixed, is assumed as $k_a(f_T) = 0.03$. This value corresponds to the operating frequency, $f_T = 0.8$ THz, as stated in [94], [128] which mimics practical data measured for water vapor molecules at humidity 36.78%.

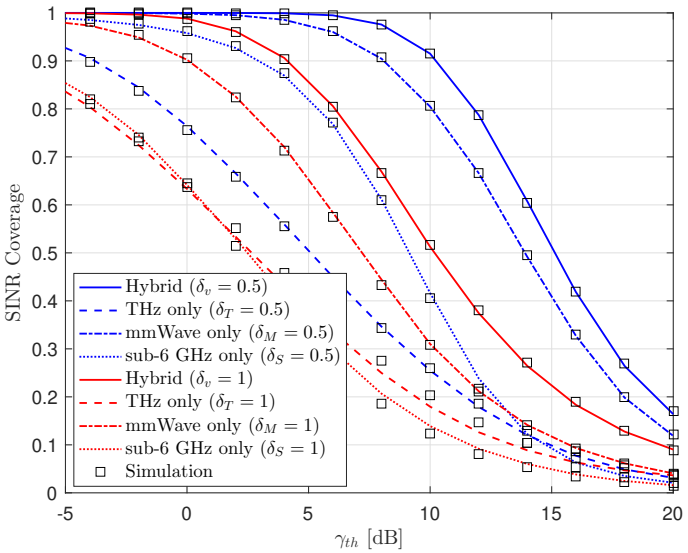

Figure 5.3: SINR coverage versus the threshold γ_{th} for the proposed user-centric cooperation of different networks under the MSCS scheme for $\delta_v = 0.5$, $v \in \{T,\ M,\ S\}$ compared to the non-cooperative transmission scheme, i.e. $\delta_v = 1$.

Fig. 5.3 demonstrates the SINR coverage as a function of the threshold γ_{th} for the considered user-centric hybrid network under the MSCS scheme with comparison to the SINR coverage of the stand-alone networks with clustering parameters $\delta_T = \delta_M = \delta_S = 0.5$. This figure shows that under MSCS scheme, hybrid user-centric cooperation can effectively improve the system performance in terms of SINR coverage. It also demonstrates that the proposed dynamic BS clustering enhances the system performance compared to the non-cooperative transmission,

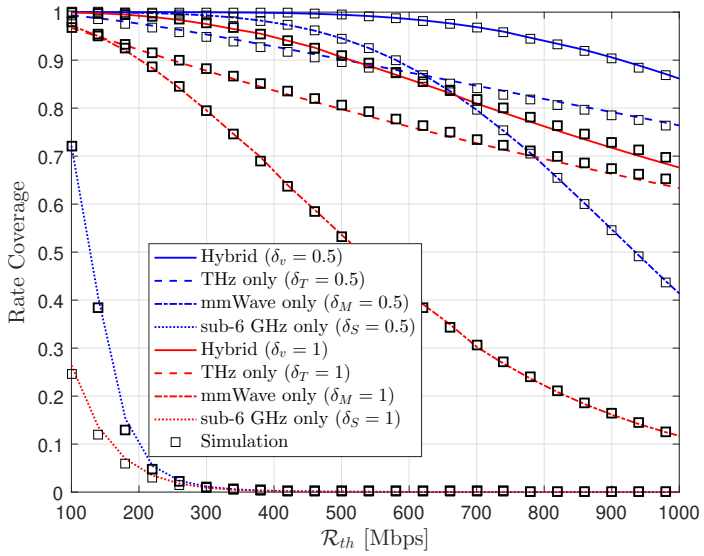

Figure 5.4: Rate coverage versus the threshold $\mathcal{R}_{th}$ for the proposed user-centric cooperation of different networks under the MRCS scheme for $\delta_v = 0.5$, $v \in \{T,\ M,\ S\}$ compared to the non-cooperative transmission scheme, i.e. $\delta_v = 1$.

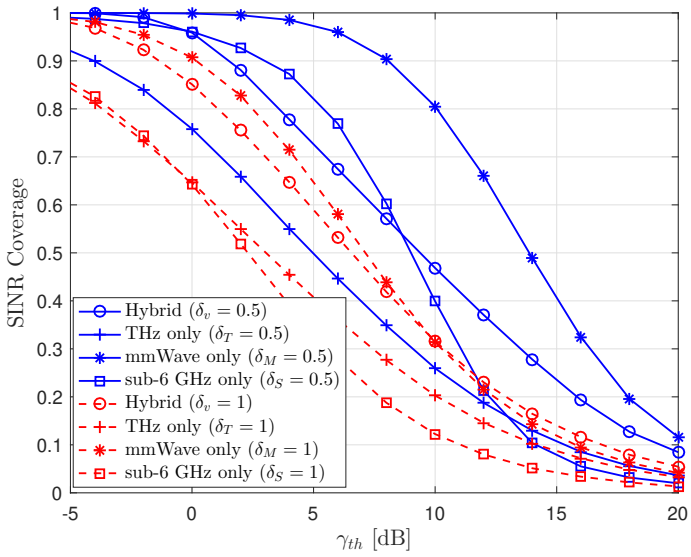

Figure 5.5: SINR coverage versus the threshold γ_{th} for the proposed user-centric cooperation of different networks under the MRCS scheme for $\delta_v = 0.5$, $v \in \{T,\ M,\ S\}$ compared to the non-cooperative transmission scheme, i.e. $\delta_v = 1$.

i.e, $\delta_T = \delta_M = \delta_S = 1$, when the user is served by only one BS. In addition, Fig. 5.3 illustrates that the THz-only tier provides lower SINR coverage performance, espe-

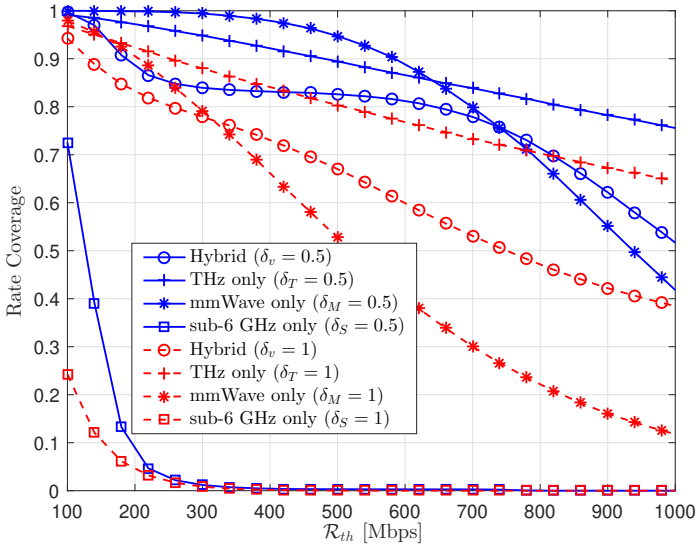

Figure 5.6: Rate coverage versus the threshold $\mathcal{R}_{th}$ for the proposed user-centric cooperation of different networks under the MSCS scheme for $\delta_v = 0.5$, $v \in \{T,\ M,\ S\}$ compared to the non-cooperative transmission scheme, i.e. $\delta_v = 1$.

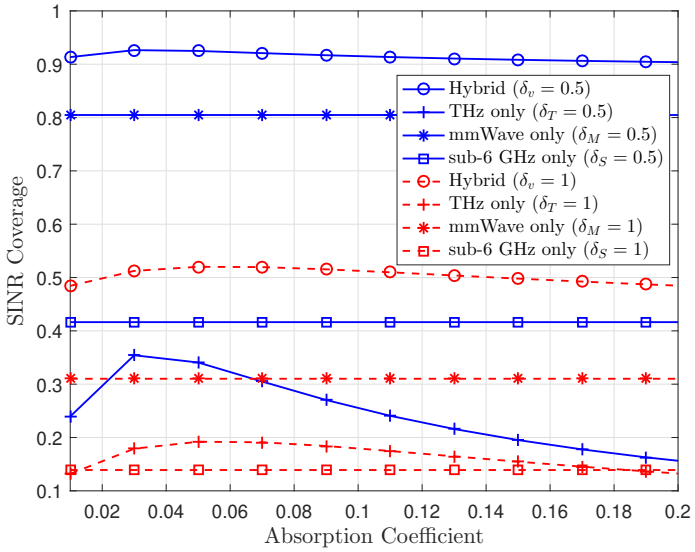

Figure 5.7: SINR coverage versus the absorption coefficient for the proposed user-centric cooperation of different networks under the MSCS scheme for $\delta_v = 0.5$ and $\delta_v = 1$, $v \in \{T,\ M,\ S\}$ at $\gamma_{th} = 10$ dB and $\mathcal{R}_{th} = 800$ Mbps.

cially for $\delta_v = 0.5$. This is due to the effect of the molecular absorption which limits the travel distance of the THz signal. The curves in Fig. 5.3 also show that the

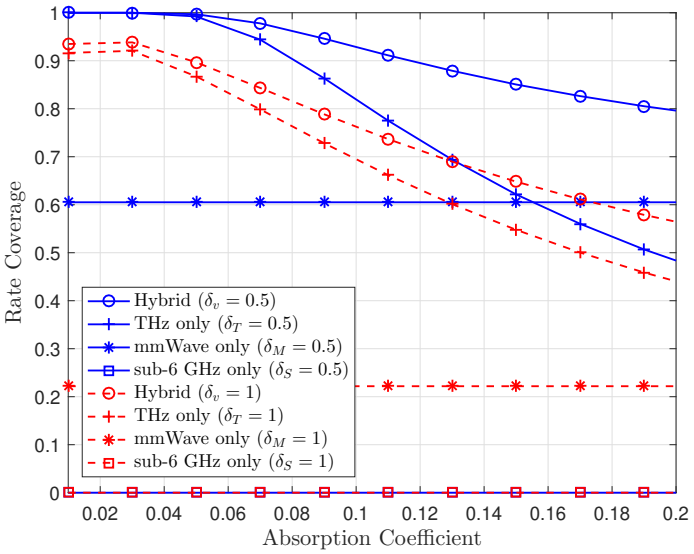

Figure 5.8: Rate coverage versus the absorption coefficient for the proposed user-centric cooperation of different networks under the MRCS scheme for $\delta_v = 0.5$ and $\delta_v = 1$, $v \in \{T,\ M,\ S\}$ at $\gamma_{th} = 10$ dB and $\mathcal{R}_{th} = 800$ Mbps.

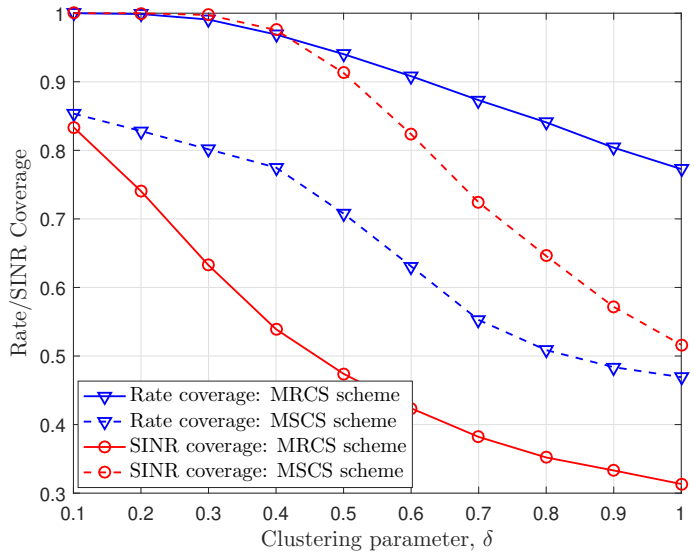

Figure 5.9: Rate and SINR coverage versus the clustering parameter δ_v for the proposed hybrid user-centric network. Comparison of MRCS and MSCS schemes at $\gamma_{th} = 10$ dB and $\mathcal{R}_{th} = 800$ Mbps.

analytical results match well with simulation which validates the provided analytical expressions of the SINR coverage in (5.19), (5.28), (5.29), and (5.32).

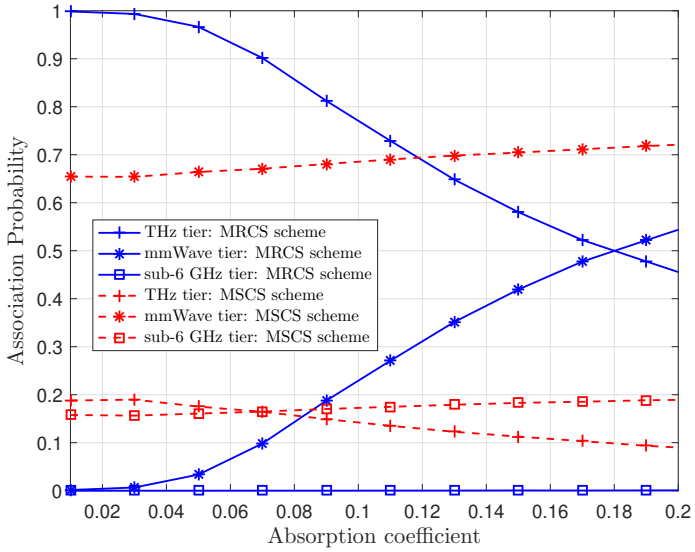

Figure 5.10: Probability of user association to different tiers as a function of the absorption coefficient under both MRCS and MSCS schemes.

The numerical results in Fig. 5.4 shows the rate coverage versus the threshold $\mathcal{R}_{th}$ ranging from 200 Mbps to 1000 Mbps. In this figure, the MRCS scheme is applied to the proposed hybrid user-centric network. It is clear that MRCS scheme can enhance the rate coverage performance of the hybrid user-centric networks compared to the single-tier user-centric networks. This figure shows that although THz signal suffers from deep large-scale fading due to the molecular absorption effect, it provides better rate coverage performance compared to both mmWave and sub-6GHz networks, thanks to the huge bandwidth provided in the THz bands. Again, Fig. 5.4 validates the provided analytical expression of the rate coverage as it matches well with simulations.

In Figs. 5.5 and 5.6, we plot the SINR coverage and rate coverage under MRCS and MSCS schemes, respectively. It is clear that in the considered hybrid user-centric network, MSCS scheme can maximize the SINR coverage. However, it may not be able to maximize the user link rate. On the contrary, the MRCS scheme can maximize the link rate but it may degrade the SINR coverage. This implies that it is not possible to find an association scheme that provides maximum rate and maximum SINR coverage at the same time in hybrid networks when different tiers

have different available spectrum bandwidth. Therefore, there should be a trade-off between link rate and SINR coverage.

Figs. 5.7 and 5.8, respectively, illustrate the effect of the absorption coefficient on the SINR coverage at a threshold $\gamma_{th} = 10$ dB, and the rate coverage, at a threshold $\mathcal{R}_{th} = 800$ Mpbs, for the two transmission cases, i.e, user-centric BS cooperation ($\delta_v = 0.5$) and non-cooperative transmission ($\delta_v = 0.5$), $v \in \{T,\ M,\ S\}$. Here, we consider the practical data of the absorption coefficient provided in [94, Table 4] where the absorption coefficient is measured at different values of the humidity. These two figures also demonstrate that since the molecular absorption effect is negligible in mmWave and sub-6GHz links, their coverage probability performances remain as horizontal lines w.r.t the absorption coefficient $k_a(f_T)$. From Fig. 5.7, it is clear that for the THz tier, and hence for the hybrid networks, the SINR coverage probability increases with the absorption coefficient to a maximum value and then gradually decreases. This can be interpreted in dense THz networks as follows: increasing $k_a(f_T)$ would decrease the interference power relative to the useful signal power and hence would improve the received SINR while, after a certain value of $k_a(f_T)$, the received signal power degrades as well and the performance starts decaying. Fig. 5.8 shows that for large values of the absorption coefficient, the rate coverage of mmWave tier may be better than that of THz tier while the hybrid network outperforms both. It can be seen that the rate coverage of sub-6GHz tier is close to zero, because the rate threshold is set to $\mathcal{R}_{th} = 800$ Mbps in this figure. However, the rate coverage of sub-6GHz tier under the MRCS scheme can reach 0.7 at lower rate thresholds as shown in Fig. 5.4.

The performance of MSCS and MRCS schemes is also illustrated in Fig. 5.9 where the SINR and rate coverages are both shown under the two association schemes as a function of the clustering parameter δ. Note that in this figure, clustering parameters are set as $\delta_T = \delta_M = \delta_S = \delta$. This figure clearly shows that for given clustering parameters, neither MSCS nor MRCS can maximize both the SINR and rate coverages, simultaneously. In addition, Fig. 5.9 shows that the system performance improves with decreasing δ. This is because decreasing δ increases the

size of user's serving cluster which in turn enhances the received power signal.

In Fig. 5.10, the association probability of the typical user to different network tiers is given under both MSCS and MSRS schemes as a function of the absorption coefficient. Again, the results in Fig. 5.10 are shown for SINR and rate thresholds, $\gamma_{th} = 10$ dB and $\mathcal{R}_{th} = 800$ Mbps, respectively. For the MSCS scheme, the user is associated to the mmWave tier with higher probability than to the THz tier, due to the absorption effect in THz band, and higher than its association to the sub-6GHz tiers, due to the long distance between the user and SBSs. For the MRCS scheme, at small values of the absorption coefficient, the association probability to the THz tier is very high due to the available huge bandwidth. It is clear that the probability of user association to the THz tier decreases with the absorption coefficient which in turn increases the association probability to the mmWave tier. Again, it can be seen from this figure that the user association probability to the sub-6GHz tier is close to zero since the rate threshold is $\mathcal{R}_{th} = 800$ Mbbps. However, the user may be associated to the sub-6GHz tier under the MRCS scheme at lower rate thresholds as shown in Fig. 5.4.

In all previous figures, equal clustering parameters are assumed for the three different tiers, i.e, $\delta_S = \delta_M = \delta_T$. Figs. 5.11 and 5.12, respectively, investigate the SINR and rate coverage of the considered user-centric hybrid network under both MSCS and MRCS schemes when different values of the clustering parameters are assumed. In particular, two scenarios are considered: Scenario 1$\rightarrow$ ($\delta_S = 0.2, \delta_M = 0.5,$ and $\delta_T = 0.6$) and Scenario 2$\rightarrow$ ($\delta_S = 0.8, \delta_M = 0.6,$ and $\delta_T = 0.5$). Recall that the size of the serving cluster from tier v is inversely related to the clustering parameter δ_v. We can observe that, the sub-6 GHz cluster size in Scenario 1 is largely greater than that in Scenario 2. As a result, under the MSCS, we can see a significant enhancement of the SINR coverage (as shown in Fig. 5.11) and a significant deterioration of the rate coverage (as shown in Fig. 5.12) for Scenario 1 compared to that for Scenario 2. On the other hand, a small change in the coverage performance is obtained between Scenarios 1 and 2 under the MRCS scheme because both mmWave and THz cluster sizes in Scenarios 1 and 2 are comparable.

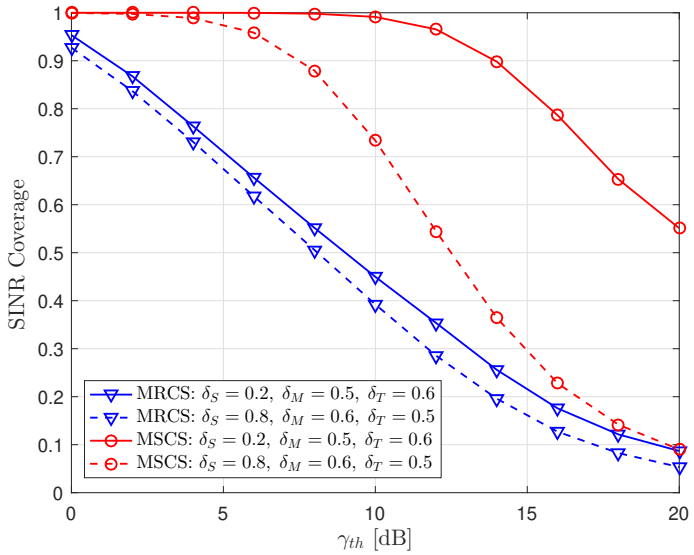

Figure 5.11: SINR coverage versus the threshold γ_{th} when different tiers are assigned different values of the clustering parameters. Two scenarios are assumed, i.e, Scenario 1→ $(\delta_S = 0.2, \delta_M = 0.5,$ and $\delta_T = 0.6)$ and Scenario 2→ $(\delta_S = 0.8, \delta_M = 0.6,$ and $\delta_T = 0.5)$.

5.6 Summary

In this chapter, a new dynamic BS clustering model is proposed to enable user-centric BS cooperation in a hybrid network composed of three types of BSs, namely, TBSs, MBSs, and SBSs. The BSs of the three tiers are spatially distributed according to independent homogeneous PPPs with different densities. In the proposed user-centric model, each user first forms three candidate clusters of BSs, each belonging to a different tier. Then, one of the candidate clusters is selected to serve the user based on one of two proposed selection schemes, namely, MSCS and MRCS. We exploited stochastic geometry to provide analytical framework for computing the SINR and rate coverage probabilities of the considered hybrid user-centric networks. It is shown that for such a hybrid network, it is not possible to find an association scheme that maximizes both rate and SINR coverage performances at the same time, raising an interesting issue for further investigation on a trade-off between rate and SINR coverages. As compared to the single-tier user-centric network, numerical

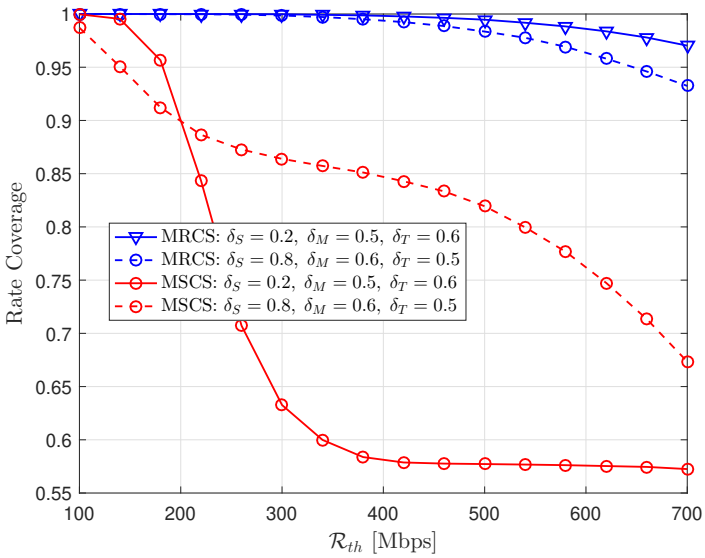

Figure 5.12: Rate coverage versus the threshold $_{th}$ when different tiers are assigned different values of the clustering parameters. Two scenarios are assumed, i.e, Scenario 1$\rightarrow$ ($\delta_S = 0.2, \delta_M = 0.5,$ and $\delta_T = 0.6$) and Scenario 2$\rightarrow$ ($\delta_S = 0.8, \delta_M = 0.6,$ and $\delta_T = 0.5$).

results show that the proposed user-centric hybrid network improves the system performance in terms of both SINR and rate coverage performances provided that a suitable cluster selection scheme is implemented.

This work permits many extensions. For example, both MSCS and MRCS schemes can be biased in order to encourage the user to be associated with a specific tier and to avoid the under-utilization of given tiers. This enables optimizing the overall system performance in hybrid networks. Also, incorporating the correlation between the spatial distributions of BSs from different tiers in hybrid networks is an interesting research point that can be considered in future.

5.7 Appendices

5.7.1 Proof of Lemma 5.4.1

Recall that the aggregated THz interference is expressed as $I_T^{agg} = \sum_{j\in\Phi_T\setminus\widetilde{\Phi}_T} P_T G_{T,j} C_T r_j^{-\alpha_T} \exp\big(-k_a(f_T)r_j\big)$. Also, the ultra-dense deployment of the THz BSs insures that $a_T < R_L$. Then, the characteristic function of I_T^{agg} for a given cluster radius a_T is obtained as

$$\begin{aligned}
\Lambda_{I_T^{agg}|a_T}(j\omega) &= \mathbb{E}_{G_T,\widetilde{\Phi}_T}\left[\left\{\exp -j\omega \sum_{j\in\Phi_T\setminus\widetilde{\Phi}_T} P_T G_{T,j} C_T r_j^{-\alpha_T} \exp\big(-k_a(f_T)r_j\big)\right\}\right] \\
&\overset{(a)}{=} \exp\left\{-2\pi\lambda_T \sum_{G_M} p_{G_M} \int_{a_T}^{R_L} \big(1-\exp\big(-j\omega P_T G_T t^{-\alpha_T} e^{-k_a(f_T)t}\big)tdt\big)\right\} \\
&\overset{(b)}{=} \exp\left\{-2\pi\lambda_T \sum_{G_T} p_{G_T} \int_{a_T}^{R_L} \sum_{q=1}^{\infty} \frac{(-j\omega P_T G_T C_T)^q t^{-q\alpha_T+1} e^{-qk_a(f_T)t}}{k!} dt\right\} \\
&\overset{(c)}{=} \exp\left\{-2\pi\lambda_T \sum_{G_T}\sum_{n=1}^{\infty}\left(\frac{p_{G_T}(-j\omega P_T C_T G_T)^n \Gamma(2-\alpha_T n, nk_a(f_T)a_T}{q!(nk_a(f_T))^{2-\alpha_T n}}\right.\right. \\
&\left.\left. -\frac{p_{G_T}(-j\omega P_T C_T G_T)^n \Gamma(2-\alpha_T n, nk_a(f_T)R_L}{q!(nk_a(f_T))^{2-\alpha_T n}}\right)\right\},
\end{aligned} \tag{5.35}$$

where (a) results from averaging over the interferers antenna gain, G_T, and then applying the probability generating functional of a PPP [63], and (b) follows from expanding the inner exponential function. Then, the expression in (c) results from using $\int_z^\infty t^{a-1}e^{-t}dt = \Gamma(a,z)$ [63].

5.7.2 Proof of Proposition 5.4.2

For a given cluster radius a_T, the THz aggregated received signal power can be written as $S_T^{agg} = P_T G_T^{max} C_T (\delta_T a_T)^{-\alpha_T} e^{-k_a(f_T)\delta_T a_T} + \sum_{k\in\widetilde{\Phi}_T\setminus(0,a_T\delta_T)} P_T G_T^{max} C_T r_k^{-\alpha_T} \exp\big(-k_a(f_T)r_k\big)$, where the first term is the received signal power from the nearest TBS in $\widetilde{\Phi}_T$ while the second term is the aggregated received signal powers from the other TBSs in $\widetilde{\Phi}_T$. Since the TBSs are distributed according to a PPP, each distance r_k in the second term is uniformly distributed in $[\delta_T a_T,\ a_T]$ with the following PDF

$$f_{r_k}(t) = \frac{2t}{a_T^2 - (\delta_T a_T)^2}, \qquad \delta_T a_T < t \leq a_T. \tag{5.36}$$

Assume there are n TBSs in $\widetilde{\Phi}_T \setminus (0, \delta_T a_T)$ and let $\widetilde{P}_T = P_T G_T^{max} C_T$, the average aggregated received signal power from $\widetilde{\Phi}_T$ is

$$\begin{aligned} S_T^{agg}|n &= \widetilde{P}_T(\delta_T a_T)^{-\alpha_T} e^{-k_a(f_T)\delta_T a_T} + n\widetilde{P}_T \int_{\delta_T a_T}^{a_T} (\delta_T a_T)^{-\alpha_T} e^{-k_a(f_T)\delta_T a_T} f_{r_k}(t)dt \\ &= \widetilde{P}_T(\delta_T a_T)^{-\alpha_T} e^{-k_a(f_T)\delta_T a_T} + 2n\widetilde{P}_T k_a(f_T)^{-\alpha_T+2}(\delta_T a_T)^{-\alpha_T}(\delta_T^{-2}-1)^{-1} \\ &\times \Big(\Gamma\big(2-\alpha_T, k_a(f_T)\delta_T a_T\big) - \Gamma\big(2-\alpha_T, k_a(f_T)a_T\big)\Big). \end{aligned} \tag{5.37}$$

Again, as the TBSs are distributed according to a PPP, the variable n in (5.37) is modeled as a Poisson random variable with a mean $\pi\lambda_T(\delta_T a_T)^2(\delta_T^{-2}-1)$ and a probability mass function given by

$$\Pr[n = \widetilde{n}] = \exp\Big(-\pi\lambda_T(\delta_T a_T)^2(\delta_T^{-2}-1)\Big)\frac{\big(\pi\lambda_T(\delta_T a_T)^2(\delta_T^{-2}-1)\big)^{\widetilde{n}}}{\widetilde{n}!}. \tag{5.38}$$

From (5.21) and (5.23), the SINR CCDF given $\phi = \widetilde{\Phi}_T$ for a cluster radius a_T at a threshold x is given by

$$\begin{aligned} \mathcal{F}_T(x) &= \mathbb{E}_{S_T^{agg}, a_T}\left[\widetilde{F}_{I_T^{agg}|a_T}\left(\frac{S_T^{agg}}{x} - \sigma_T^2\right)\right] \\ &\overset{(a)}{=} \frac{1}{2}\mathbb{E}_{S_T^{agg}, a_T}\left[1 + \mathrm{erf}\left(\frac{\frac{S_T^{agg}}{x} - \sigma_T^2 - \mu_{I_T^{agg}}(a_T)}{\sqrt{2\mathcal{V}_{I_T^{agg}}(a_T)}}\right)\right], \end{aligned} \tag{5.39}$$

where $\mu_{I_T^{agg}}(a_T)$ and $\mathcal{V}_{I_T^{agg}}(a_T)$ are given in (5.24) and (5.25), respectively. Plugging (5.37) in (5.39) and averaging over n using (5.38) and then averaging over a_T using (5.12), the SINR CCDF, given $\phi = \widetilde{\Phi}_T$, is expressed as in (5.28).

5.7.3 Proof of Lemma 5.4.2

For a given mmWave cluster radius a_M, the characteristic function of the aggregated signal, S_M^{agg}, is written as

$$\Lambda_{S_M^{agg}|a_M}(j\omega) = \Lambda_1(j\omega, a_M)\Lambda_2(j\omega, a_M), \tag{5.40}$$

where $\Lambda_1(j\omega, a_M)$ and $\Lambda_2(j\omega, a_M)$ are, respectively, the characteristic function of the maximum received signal and the characteristic function of the aggregated signals received from the mmWave serving cluster, except the maximum one, for a given cluster radius a_M. The expression of $\Lambda_1(j\omega, a_M)$ can be obtained as

$$\begin{aligned}\Lambda_1(j\omega, a_M) &= \mathbb{E}_{h_M}\left[\exp\left(-j\omega P_M G_M^{max} C_M h_M (a_M \delta_M)^{-\alpha_M}\right)\right] \\ &\overset{(a)}{=} \left(1 + \frac{j\omega P_M G_M^{max} C_M (a_M\delta_M)^{-\alpha_M}}{m}\right)^{-m}, \end{aligned} \tag{5.41}$$

where (a) results from applying the moment generation function of the Gamma random variable, h_M with parameters m and $1/m$. For $\Lambda_2(j\omega, a_M)$, it is computed as

$$\begin{aligned}\Lambda_2(j\omega, a_M) &= \mathbb{E}_{h_M, \widetilde{\Phi}_M}\left[\exp\left(-j\omega \sum_{k\in\widetilde{\Phi}_M \setminus B(0, a_M\delta_M)} P_M G_M^{max} C_M h_M r_k^{-\alpha_L}\right)\right] \\ &\overset{(b)}{=} \exp\left(-2\pi\lambda_M \mathbb{E}_{h_M}\left(\int_{a_M\delta_M}^{a_M}\left(1 - e^{-j\omega\widetilde{P}_M h_M t^{-\alpha_M}}\right) t dt\right)\right), \\ &\overset{(c)}{=} \exp\Bigg(-2\pi\lambda_M \Gamma(2)\mathbb{E}_{h_M}\Bigg(\int_{a_M\delta_M}^{a_M}\Bigg(j\omega\widetilde{P}_M h_M t^{-\alpha_M} \\ &\quad \times e^{-j\omega\widetilde{P}_M h_M t^{-\alpha_M}} G_{1,2}^{1,1}\left[-j\omega\widetilde{P}_M h_M t^{-\alpha_M}\middle| \begin{matrix} 0 \\ 0, -1 \end{matrix}\right]\Bigg) t dt\Bigg)\Bigg), \end{aligned} \tag{5.42}$$

where (b) follows from using the Campbell's theorem and letting $\widetilde{P}_M = P_M G_M^{max} C_M$, (c) results from applying $1 - e^{-x} = \Gamma(2) x e^{-x} G_{1,2}^{1,1}\left[-x\middle| \begin{matrix} 0 \\ 0, -1 \end{matrix}\right]$, where $\mathrm{G}_{p,q}^{m,n}(\cdot)$ is the Meijer's G function [62]. Integrating over t and averaging over the small-scale fading h_M using (5.7), $\Lambda_2(j\omega, a_M)$ can be expressed as

$$\begin{aligned}\Lambda_2(j\omega, a_M) &= \exp\Bigg\{\frac{-2\pi j\omega\lambda_M\Gamma(2)\widetilde{P}_M}{\alpha_M - 1}\frac{\Gamma(m+1)\Gamma(1-\frac{2}{\alpha_M})}{\Gamma(2)\Gamma(2-\frac{2}{\alpha_M})} \\ &\quad \times\Bigg((a_M\delta_M)^{2-\alpha_M} G_{3,3}^{1,3}\left[-j\omega\widetilde{P}_M(a_M\delta_M)^{-\alpha_M}\middle| \begin{matrix} -m,\ 0,\ \frac{2}{\alpha_M} \\ -1, \frac{2}{\alpha_M} - 1 \end{matrix}\right]\end{aligned}$$

$$-a_M^{2-\alpha_M} G_{3,3}^{1,3}\left[-j\omega \widetilde{P}_M a_M \middle| \begin{matrix} -m,\ 0,\ \frac{2}{\alpha_M} \\ -1, \frac{2}{\alpha_M} - 1 \end{matrix} \right] \Bigg) \Bigg\} \tag{5.43}$$

Then, substituting $\widetilde{P}_M$ by $P_M G_M^{max} C_M$ and plugging (5.41) and (5.43) in (5.40), we get the expression of $\Lambda_{S_M^{agg}|a_M}(j\omega)$ as in (5.30). The characteristic function of the aggregate interference can be written as

$$\Lambda_{I_M^{agg}|a_M}(j\omega) \;=\; \mathbb{E}_{G_M, h_M, \widetilde{\Phi}_M}\left[\exp\left(-j\omega \sum_{j \in \Phi_M \setminus \widetilde{\Phi}_M} P_M G_{M,j} C_M h_{M,j} r_j^{-\alpha_M} \right) \right], \tag{5.44}$$

Following the same steps of deriving $\Lambda_{S_M^{agg}|a_M}(j\omega)$ and then averaging over the interferer antenna gain G_M, $\Lambda_{I_M^{agg}|a_M}(j\omega)$ is obtained as in (5.31).

Chapter 6

Performance Characterization of SWIPT-enabled User-Centric mmWave Networks

6.1 Introduction

6.1.1 Background

As an emerging technology, low power devices, such as the nodes of internet of things (IoT), are predicted to be widely used and densely deployed in future communication networks [129]. They are usually powered by batteries with a limited capacity [130]. In order to extend the lifetime of these devices and guarantee sustainable wireless services, simultaneous wireless information and power transfer (SWIPT) technique is introduced as a flexible power source [131]. Mainly, SWIPT provides a guaranteed level of energy that can be harvested from radio frequency (RF) signals instead of costly conventional power sources [131]. Therefore, to enhance the energy efficiency of modern wireless communication systems, SWIPT has been considered as one of the most promising solutions [132]. In the literature, many operating modes are proposed to separate the received wireless information and harvested power, such as time switching, power splitting, and antenna allocation [131], [133]. This

implies the existence of a trade-off between the amount of wireless harvested energy and the achievable data rate [134]. Therefore, compromising techniques are highly recommended to enhance the efficiency of SWIPT-enabled wireless networks [135].

Millimeter wave (mmWave) technology has been featured as part of the 5G revolution to overcome the shortage of the available spectrum at microwave bands and hence to meet the fast growing demands of future wireless services [136]. Unfortunately, the signal transmitted at mmWave is more sensitive to blockages and suffers from a large penetration loss which reduces the coverage area of base stations (BSs) operating at these bands [36]. While, increasing the density of deployed BSs can improve the coverage of mmWave communication networks, it increases the amount of aggregated interferences a user may receive from close neighboring BSs. This leads to a negative effect of network densification since the system performance starts degrading when the BS density goes beyond a critical point [37], [66]. To enhance the communication reliability and effectively mitigate the aggregated interference, the system can enable multi-connectivity through BS cooperation [38], [40], [41]. As a promising technique, user-centric BS cooperating allows each user to be served by a set of carefully selected BSs, namely, user's serving cluster which can be adapted to its environment and quality-of-service (QoS) requirements [113].

6.1.2 Related Works

The performance of cellular networks with wireless power transfer has been studied in [126], [137]–[146] using stochastic geometry tools. In [126], SWIPT-enabled cellular networks were modeled and a new mathematical framework for system-level analysis and optimization was provided. The authors of [137] studied the receiver diversity of cellular systems with wireless power transfer and showed that the receiver diversity can effectively enhance the system performance in terms of received information rate and harvested energy. In [138], a methodology to analyze a real-time SWIPT-enabled mobile computing system is proposed. The performance of RF-powered IoT devices was investigated in [139] by taking into account the coupling between the locations of the devices and the RF sources. In particular, the

locations of RF-powered devices are modeled using Poisson cluster process with each cluster being centered by an IoT gateway. Considering the void cell phenomenon, the authors in [140] proposed an analytical model for the downlink and uplink user's rates in a SWIPT-enabled cellular system and characterized the amount of energy harvested by the user. In [141], a model named Poisson disk process is proposed to address the energy correlation issue in large-scale wirelessly powered networks. In this model, wireless-powered device is assumed to harvest enough energy only if there is at least one energy transmitting node within a given distance. Furthermore, the authors of [142] introduced the energy correlation coefficient to analyze the effect of energy correlation in RF-powered systems with energy beamforming. In [143], an antenna switching technique is used to separate the information and energy where a subset of antennas are allocated for data and the remaining are allocated for energy harvesting. The impact of the beamforming error, due to the imperfect beam alignment, on the wireless powered systems at mmWave frequencies was studied in [144]. The beam error between the receiver and the associated transmitter is modeled as truncated Gaussian distribution while the beam error between the receiver and the non-associated transmitter is assumed to follow a uniform distribution. In [145], the authors developed new analytical results for the performance of SWIPT-enabled users by taking into account the spatial interference correlation. The energy efficiency of a SWIPT-enabled wireless system with mode selection in devise-to-device (D2D) communications was studied in [146]. The analysis of SWIPT-enabled cellular system with a more realistic nonlinear energy harvester is investigated in [147], [148]. Specifically, in [147], the joint optimization scheme for beamforming and power splitting in wideband mmWave SWIPT-enabled cellular systems with nonlinear energy harvester under a limited channel state information and hybrid beamforming structure was proposed. The effects of channel fading on the coverage probability of a SWIPT-enabled wireless communication system assisted by unmanned aerial vehicles (UAV) with nonlinear energy harvesting receivers was investigated in [148].

The performance of mmWave networks under BS cooperation was investigated

in [53]–[55], [57]. The authors in [53] assumed that the user is cooperatively served by a cluster of a given number of BSs and studied the network coverage performance. They showed that the BS cooperation technique effectively improves the performance when the BS density is large. In [54], the user performs two steps to select its serving BS in a multi-tier wireless network. In the first step, a set of BSs, called candidates BSs, are preselected from different tiers while in the second step, one candidate is selected to transmit data to the user based on the highest achievable signal-to-interference-plus-noise ratio (SINR). With the aid of stochastic geometry tools, the work in [55] investigated the coverage and rate performances of mmWave networks under user-centric BS cooperation. In [57], two methods of BS clustering are considered, where the user's serving cluster is incorporated either with a fixed number of BSs or with a fixed region. Then, the system performance in terms of outage probability and downlink data rate is studied for the two BS cooperation methods. It is worth noting that in [53]–[55], [57], only static BS clustering was considered, where the user's serving cluster has either a fixed number of serving BSs or fixed radius. In [120], it is shown that the user-centric BS cooperation with adaptive BS clustering significantly outperforms that using fixed clustering in terms of coverage probability, spectral efficiency, and energy efficiency performances. In adaptive clustering, the user forms its own serving cluster based on the quality-of-service (QoS) requirements and channel conditions. Hence, the serving clusters of different users may have different sizes and can be adapted to the users' locations

6.1.3 Motivations and Contributions

Due to its large bandwidth, the mmWave communication is leveraged to meet the multi-Gigabit data transmission requirement. Moreover, it is shown in [34] that wireless power transfer at mmWave outperforms that at lower frequency bands. This implies that SWIPT-enabled mmWave systems are feasible and suitable for energy efficient communication networks. Furthermore, in addition to improving the downlink data rate, user-centric BS cooperation in mmWave networks is expected to further enhance the wireless power transfer due to the fact that the mmWave

transmitters/receivers are equipped with highly directive antennas, and thus the amount of energy that can be harvested from a useful signal is larger than that harvested from the interfering signal.

It is noteworthy that in the aforementioned works [34], [144] on the performance of SWIPT-enabled mmWave communication systems, the user is only associated to one BS, i.e, no BS cooperation was considered. To the best of our knowledge, the performance analysis for SWIPT-enabled user-centric networks in mmWave bands is still an open issue. To fill this gap, in this chapter, we use stochastic geometry to investigate the performance of SWIPT-enabled mmWave user-centric networks under adaptive BS clustering. In particular, the main contributions of our work are summarized as follows:

- We adopt the adaptive BS clustering for the SWIPT-enabled user-centic mmWave networks. The information and power at the user side are acquired using the time switching technique [130]. The user selects its serving BSs based on its channel condition, where a single parameter is introduced to control the size of the user's serving cluster. For the energy harvesting at the user side, both linear and non-linear energy harvesting models are considered in this work.

- Two cooperative transmission schemes are considered to transmit data to the user, namely, joint transmission (JT) scheme and optimal BS selection (OBS) scheme. In addition, The performance of JT and OBS schemes is compared to the non-cooperative (NC) scheme in which the user is associated to only a single BS.

- Using concepts from stochastic geometry, we provide an analytical framework to study the system performance of the considered SWIPT-enabled user-centric mmWave network in terms of rate coverage, energy coverage, and joint rate and energy coverage.

- Under reasonable assumptions, we develop a simplified mathematical expression of the joint rate and energy coverage and then an optimization framework

of the time switching coefficient to maximize the system performance for given system parameters.

- We provide numerical and simulation results to illustrate the performance of the considered SWIPT-enabled system and to validate the derived analytical expressions.

The rest of this chapter is organized as follows. In Section 6.2, we discuss the system model. Section 6.3 is dedicated to the system performance analysis under linear energy harvesting. In Section 6.4, a simplified analytical expression of the joint rate and energy coverage is provided. In section 6.5, we characterize the system performance under non-linear energy harvesting model. Numerical and simulation results along with necessary discussions are given in Section 6.6. Finally, we conclude this work in Section 6.7.

Notations: Im{x} denotes the imaginary part of x. $\Gamma(a,x) = \int_a^\infty t^{x-1}e^{-t}dt$ is the incomplete gamma function [62] where $\Gamma(x) = \Gamma(0,x)$. ${}_2F_1(.)$ is the Gauss hypergeometric function and $E_v(z) = \int_1^\infty \frac{e^{-zt}}{t^v}dt$ is the generalized exponential integral function [62]. Pr[A] denote ta the probability of event A. $\Psi_Z(jw)$ is the characteristic function of the random variable z, and $\mathbb{E}_X[\cdot]$ refers to the expectation over X.

6.2 System Model

6.2.1 Spatial Distribution and Propagation Models

Consider a user-centric SWIPT-enabled wireless network serving single-antenna wirelessly powered users in the downlink. The network BSs operate at mmWave band and are equipped with highly directional beamforming antenna array. It is assumed that the users are low power devices with no permanent power supply, and solely rely on the harvested energy from the ambient mmWave radio. The locations of the cellular network BSs and the users are modeled by two independent homogeneous Poisson point processes (PPPs) Φ_b and Φ_u with densities λ_b and

λ_u, respectively. The analysis is performed for a typical user located at the origin $(0,0) \in \mathbb{R}^2$ [63].

In mmWave, line-of-sight (LOS) and non-LOS (NLOS) channels have different propagation characteristics since the mmWave signal suffers from high penetration losses and hence it is more sensitive to blockages [36], [37]. Therefore, for the typical user, BSs can be, classified into two independent non-homogeneous PPPs, denoted here as Φ_b^L and Φ_b^N and refereed to as LOS and NLOS BSs, respectively. Both Φ_b^L and Φ_b^N are thinned processes of Φ_b with densities $\lambda_b P_{\text{LOS}}(r_k)$ and $\lambda_b\big(1-P_{\text{LOS}}(r_k)\big)$, respectively, where r_k is the distance from the typical user to the k-th BS in Φ_b and $P_{\text{LOS}}(r_k)$ is the probability of the k-th BS being in LOS to the typical user. For the k-th BS, the path loss for LOS and NLOS links can be expressed as [71]

$$\mathcal{L}(r_k) = \begin{cases} \mathcal{L}_L(r_k) = C_L r_k^{\alpha_L}, & \text{for LOS} \\ \\ \mathcal{L}_N(r_k) = C_N r_k^{\alpha_N}, & \text{for NLOS} \end{cases} \tag{6.1}$$

where α_L and α_N are the LOS and NLOS path loss exponents, respectively, and C_L and C_N are the intercepts of the LOS and NLOS path loss formulas [37]. Note that according to [149] C_L and C_N are equal for a short reference distance.

Moreover, the small-scale fading of mmWave channel links between the typical user and all BSs are modeled as independent Nakagami-m random variables, where m is the Nakagami parameter that describes the degree of fading severity. As such, the LOS and NLOS links have different Nakagami parameters denoted by m_L and m_N, respectively, where $m_L > m_N$ [37]. Therefore, the small-scale channel gain, denoted by h, is a normalized independent and identically distributed (i.i.d.) Gamma random variable with $h \sim \Gamma\left(m_v, 1/m_v\right)$, where $v \in \{L, N\}$, refers to the LOS or NLOS links, and $\Gamma(.,.)$ is the incomplete Gamma function. Accordingly, the probability density function (PDF) of the power fading, h, for LOS and NLOS links is given by

$$f_{|\zeta_k|^2}(x) = \frac{m_v^{m_v}}{\Gamma(m_v)} x^{m_v-1} e^{-m_v x}, \quad x > 0 \tag{6.2}$$

where $\Gamma(\cdot)$ is the Gamma function.

6.2.2 Antenna Array Radiation Patterns

The high attenuation of the transmitted mmWave signal is more harmful in SWIPT-enabled systems since it degrades the received SINR and it reduces the amount of harvested energy for a given time duration. To compensate for such high attenuation in mmWave bands and to mitigate the effect of co-channel interference, all BSs are supported with highly directional beamforming antenna arrays. For the sake of analysis tractability, we consider a sectored antenna model to describe the gain patterns of the BSs antenna arrays [68], [69], [126]. This model defines the array pattern using three parameters, G_m and G_s, θ_w for the main-lobe and all back and side-lobes, and the antenna beamwidth, respectively. In this chapter, the scheme in [125] is used to obtain the parameters G_m, G_s, and θ_w, which are related to the number of elements in the antenna array and the array geometry. As such, for a uniform linear antenna array with space between elements equal to half the operating wavelength, the array gain $G(\theta)$ in any arbitrary direction can be formulated as

$$G(\theta) = \begin{cases} G_m = \dfrac{2\pi N_t^2 \sin\left(\frac{3\pi}{2N_t}\right)}{\theta_w N_t^2 \sin\left(\frac{3\pi}{2N_t}\right) + (2\pi - \theta_w)}, & |\theta| \leq \frac{\theta_w}{2} \\ \\ G_s = \dfrac{2\pi}{\theta_w N_t^2 \sin\left(\frac{3\pi}{2N_t}\right) + (2\pi - \theta_w)}, & \text{otherwise} \end{cases} \tag{6.3}$$

where $\theta_w = 2 \arcsin\left(\frac{2.782}{\pi N_t}\right)$ is the antenna beamwidth, θ is the angle of the boresight direction which is modeled as a uniform random variable distributed in $[-\pi,\ \pi]$ and N_t is the number of antennas in the array. Note that in mmWave, to serve multiple users, BSs are equipped with large antenna arrays which consist of subsets of smaller antenna arrays known as subarrays. These subarrays can direct different beams to multiple users at different locations. In this case, N_t corresponds to the number of antennas in each subarray. The user is equipped with a single unity gain omnidirctional antenna and thus is able to simultaneously receive multiple beams from different directions. Therefore, the total antenna gain of a link between the user and an interfering BS is a random variable defined as $G = \{G_m,\ G_s\}$ with probability $p_G = \{\frac{\theta_w}{2\pi},\ \frac{2\pi - \theta_w}{2\pi}\}$. We assume that perfectly channel state information

is available at all BSs and thus they are capable of adjusting the antenna orientations to achieve the maximum directivity gain between a serving BS and the user [56], [66], [70].

6.2.3 Base Station Clustering and Data-Power Switching Models

In our SWIPT-enabled user-centric mmWave network, each user is served or powered by a cluster of carefully selected BSs, denoted as $\Phi_b^S \in \Phi_b$. For the SWIPT setup, a time switching protocol is considered. Specifically, in each downlink transmission time slot, each user first uses a fraction μ of the time slot for harvesting energy from all the received mmWave signals, and $1-\mu$ of time for receiving and decoding data from the serving cluster Φ_b^S, where $\mu \in [0,\ 1]$ is the time switching coefficient. It is also assumed that each user is battery-less and utilizes only the instantaneously harvested RF energy to supply its operation.

Information Transfer Phase

During this phase, all BSs in Φ_b^S cooperate to jointly serve the typical user within $1-\mu$ of time. In order to select a proper BS set Φ_b^S, the user employs a large-scale path-loss based clustering approach, which can be mathematically expressed as

$$\Phi_b^S \triangleq \{y_k \in \Phi_b :\ \mathcal{E}_{\Phi_b}(r_k, \delta) = 1\}, \tag{6.4}$$

where $y_k \in \mathbb{R}^2$ is the location of the k-th BS in Φ_b, $r_k = || y_k ||$ is the distance from the typical user to the k-th BS, $\mathcal{E}_{\Phi_b}(r_k, \delta) = \mathbb{1}(\delta \mathcal{L}(r_k) \leq \mathcal{L}(r))$ is an indicator function with $\delta \in [0, 1]$ being the clustering parameter and r being the distance between the typical user and the BS with the minimum path loss, namely, the user's reference BS denoted by ϕ. The case when $\delta = 1$ is known as the conventional single-serving BS, which is also referred in this chapter to as the non-cooperative (NC) scheme. The clustering approach in (6.4) means that a BS joins the serving cluster Φ_b^S if and only if its path-loss based received power at the typical user exceeds the path loss of ϕ scaled by δ. In contrast to the static clustering approaches reported in [55],

[56], (6.4) enables adaptive selection of BSs according to network configurations and the user's channel condition (i.e., path loss). Indeed, as will be discussed in Section 6.4, δ can be tuned according to the system status such as users' and BSs' densities, path loss exponents, and maximum load. Furthermore, a BS can joint multiple clusters with avoiding interference from BSs within the serving cluster by assigning orthogonal resources to different users.

Energy Harvesting Phase

We consider a practical energy harvesting model that depends on the locations of the nearby RF transmitters and the channel gain including small-scale fading and the associated array gains due to the use of directional antenna arrays. Specifically, during μ of time, a typical user harvests energy from all BSs in Φ_b^S with beam pointing toward its direction. It also harvests energy from the interference received from BSs in $\Phi_b \setminus \Phi_b^S$ with beams pointing towards and away from its direction.

Using field measurements and stochastic blockage models, the probability that the k-th BS at a distance r_k from the typical user is LOS can be modeled as $P_{\text{LOS}}(r_k) = e^{-\beta r_k}$, where β is a parameter dependent on the blockages sizes and density. For the analysis tractability, we use the model in [66], [70], [72], [120] which approximate the LOS probability function by a step function. In particular, $P_{\text{LOS}}(r_k)$ is one for $r_k \leq R_L$ and zero otherwise, where R_L is the LOS range. This model is proved to be tractable yet accurate enough to account for the effect of blockage in mmWave bands when R_L is carefully determined. According to [66], for accurate results, the LOS range is calculated such that $R_L = \sqrt{2}/\beta$.

From (6.4), it is clear that for a given BS density, the size of the user's serving cluster depends on the clustering parameter δ, the type of the reference BS ϕ, i.e, either LOS or NLOS, and the distance r. Note that based on the considered blockage model, the PDF of r is $f_r(t) = 2\pi\lambda_b t \exp\left(\pi\lambda_b t^2\right), \quad 0 \leq t < \infty$ [79]. As a result, there are three cases of the user's serving cluster, Φ_b^S, which can be defined as follows:

Case 1, $\Phi_b^S \subsetneq \Phi_b^L$

In this case, the user's serving cluster contains only LOS BSs. This case may dominate in ultra-dense deployments and/or when the average size of the user's serving cluster is small.

Case 2, $\Phi_b^S \subsetneq \Phi_b^N$

Here, the user's serving cluster contains only NLOS BSs. This case may dominate in low density networks.

Case 3, $\Phi_b^S \subsetneq \{\Phi_b^L,\ \Phi_b^N\}$

In this scenario, the user's serving cluster contains both LOS and NLOS BSs. This case occurs in moderate BS density and/or when the average cluster size is large.

6.3 Joint Rate and Energy Coverage Analysis

In this section, we study the performance of the SWIPT-enabled user-centric mmWave networks in terms of the rate coverage, energy coverage, and joint rate and energy coverage under linear energy harvesting. In particular, two cooperative transmission schemes are considered, namely, the JT and the OBS schemes. For the JT scheme, all BSs within the serving cluster transmit the same data to the user. On the other hand, the OBS scheme selects only the BS with the maximum average received power to send data to the user while the other BSs within Φ_b^S keep silent. Note that however those BSs keeping silent with the resource assigned to the typical user, they can serve other users using other orthogonal resources. This implies that OBS may degrade the system performance compared to the JT scheme but it can reduce the coordination cost since the user data is required to be available at only one BS. For the sake of comparison, we also introduce the NC transmission scheme. In the following, we first focus on the performance analysis of the system under the JT scheme and then obtain the performance of both OBS and NC schemes as special cases of the JT scheme.

6.3.1 User-Centric Rate and Energy

For the typical user, the power received from the k-th serving BS in Φ_b^S located at a distance r_k is $P_t G_m h_k (\mathcal{L}(r_k))^{-1}$, where P_t is the BS transmit power which is assumed the same for all BSs, G_m is the main-lobe gain , h_k is the small-scale fading channel gain between the user and the k-th BS in Φ_b^S. On the other hand, the power received by the typical user from the i-th interfering BS is $P_t G_i h_i (\mathcal{L}(r_i))^{-1}$, where G_i is defined in (6.3). The downlink received SINR, denoted as γ, under the JT scheme can be expressed as

$$\gamma = \frac{S_{agg}}{I_{agg} + \sigma^2}, \tag{6.5}$$

where σ^2 is the thermal noise and S_{agg} and I_{agg} are the aggregated useful signal received from all BSs in Φ_b^S and the aggregated interference recieved from all BSs in $\Phi_b \setminus \Phi_b^S$ which are, respectively, expressed as

$$\begin{aligned} S_{agg} &= \sum_{k \in \Phi_b^S} P_t G_m h_k (\mathcal{L}(r_k))^{-1} \\ &= \underbrace{\sum_{k \in \Phi_b^S \cap \Phi_b^L} P_t G_m h_k (\mathcal{L}_L(r_k))^{-1}}_{\text{LOS signals}} + \underbrace{\sum_{\hat{k} \in \Phi_b^S \cap \Phi_b^N} P_t G_m h_{\hat{k}} (\mathcal{L}_N(r_{\hat{k}}))^{-1}}_{\text{NLOS signals}} \end{aligned} \tag{6.6}$$

and

$$\begin{aligned} I_{agg} &= \sum_{i \in \Phi_b^L \setminus \Phi_b} P_t G_i h_i (\mathcal{L}(r_i))^{-1} \\ &= \underbrace{\sum_{i \in \Phi_b^L \setminus \Phi_b^S \cap \Phi_b^L} P_t G_i h_i (\mathcal{L}_L(r_i))^{-1}}_{\text{LOS interference}} + \underbrace{\sum_{j \in \Phi_b^N \setminus \Phi_b^S \cap \Phi_b^N} P_t G_j h_j (\mathcal{L}_N(r_j))^{-1}}_{\text{NLOS interference}} \end{aligned} \tag{6.7}$$

The downlink rate (normalized by the system bandwidth) and the linearly harvested energy (normalized by the time), respectively, denoted as $\mathcal{R}$ and $\mathcal{H}$, are given by

$$\mathcal{R} = (1 - \mu) \log_2 \big(1 + \gamma\big), \tag{6.8}$$

and

$$\mathcal{H} = \eta \mu \Big(S_{agg} + I_{agg} \Big), \tag{6.9}$$

where η is the efficiency of the energy conversion at the receiver. Note that since $\mathcal{R}$ in (6.8) is normalized by the bandwidth and $\mathcal{H}$ in (6.9) is normalized by the transmission time, thus they are expressed in bit/s/Hz and watts, respectively. It is clear from (6.5), (6.8), and (6.9) that $\mathcal{R}$ and $\mathcal{H}$ are correlated. This will be taken into consideration when computing the joint rate and energy coverage as follows.

6.3.2 Joint Rate and Energy Coverage Probability

In this subsection, we provide mathematical expressions for the coverage probabilities. First we focus on the joint rate and energy coverage denoted as $F_{\mathcal{R},\mathcal{H}}\big(\mathcal{R}_{th},\ \mathcal{H}_{th}\big)$ which is the joint complimentary cumulative distribution function (CCDF) of $\mathcal{R}$ and $\mathcal{H}$. Then, the individual rate and energy coverage probabilities can be obtained as marginal CCDFs of $F_{\mathcal{R},\mathcal{H}}\big(\mathcal{R}_{th},\ \mathcal{H}_{th}\big)$. The joint rate and energy coverage probability or in short the joint coverage probability, is expressed as

$$F_{\mathcal{R},\mathcal{H}}\big(\mathcal{R}_{th},\ \mathcal{H}_{th}\big) = \Pr\big[\mathcal{R} \geq \mathcal{R}_{th},\ \mathcal{H} \geq \mathcal{H}_{th}\big], \tag{6.10}$$

where $\mathcal{R}_{th}$ and $\mathcal{H}_{th}$ are the reliability thresholds of the rate and harvested power. Using (6.5)-(6.9) into (6.10), the joint coverage probability can be expressed as

$$F_{\mathcal{R},\mathcal{H}}\big(\mathcal{R}_{th},\ \mathcal{H}_{th}\big) \ = \ \Pr\left[I_{agg} \leq \frac{S_{agg}}{2^{\frac{\mathcal{R}_{th}}{(1-\mu)}}-1} - \sigma^2, I_{agg} \geq \frac{\mathcal{H}_{th}}{\eta\mu} - S_{agg}\right]. \tag{6.11}$$

By letting $\widetilde{\mathcal{R}}_{th} = 2^{\frac{\mathcal{R}_{th}}{(1-\mu)}} - 1$ and $\widetilde{\mathcal{H}}_{th} = \frac{\mathcal{H}_{th}}{\eta\mu}$, (11) can be arranged as

$$\begin{aligned} F_{\mathcal{R},\mathcal{H}}\big(\mathcal{R}_{th},\ \mathcal{H}_{th}\big) \ &= \ \Pr\left[\widetilde{\mathcal{H}}_{th} - S_{agg} \leq I_{agg} \leq \frac{S_{agg}}{\widetilde{\mathcal{R}}_{th}} - \sigma^2\right] \\ &\overset{(a)}{=} F_{I_{agg}}\left(\frac{S_{agg}}{\widetilde{\mathcal{R}}_{th}} - \sigma^2\right) - F_{I_{agg}}\left(\widetilde{\mathcal{H}}_{th} - S_{agg}\right), \end{aligned} \tag{6.12}$$

where (a) holds for

$$S_{agg} > \left(\widetilde{\mathcal{H}}_{th} + \sigma^2\right)\left(\frac{1}{\widetilde{\mathcal{R}}_{th}} + 1\right), \tag{6.13}$$

and $F_{I_{agg}}(x) = \Pr[I_{agg} \leq x]$ denotes the aggregated interference cumulative distribution function (CDF). From (6.12), it is clear that to calculate the joint coverage

probability, the distributions of both I_{agg} and S_{agg} must be computed. $F_{I_{agg}}(.)$ is calculated by resorting to the Gil–Pelaez inversion theorem [91], [127] as

$$F_{I_{agg}}(x) = \frac{1}{2} - \frac{1}{\pi}\int_0^{\infty} \frac{\mathrm{Im}\Big\{\exp(-j\omega x)\Psi_{I_{agg}}(j\omega)\Big\}}{\omega} d\omega \tag{6.14}$$

where $j = \sqrt{-1}$, Im{x} denotes the imaginary part of x, and $\Psi_{I_{agg}}(j\omega)$ is the interference characteristic function which can be computed for different clustering cases using the following lemma.

Lemma 6.3.1 *For a given distance r to the reference BS ϕ and a clustering parameter δ, the characteristic functions of the aggregated interference for the three clustering cases, $\Psi^{(a)}_{I_{agg}}(jw)$, $a \in \{1,\ 2,\ 3\}$, are written as*

$$\begin{aligned}
\Psi^{(1)}_{I_{agg}}(r, jw) \ = \ & \\
& \exp\Bigg\{ -\pi\lambda_b \sum_G p_G \Bigg[R_L^2 \Bigg(1 - {}_2F_1\Bigg(m_L, -\frac{2}{\alpha_L}; \frac{\alpha_L - 2}{\alpha_L}; -\frac{jwGC_L P_t R_L^{-\alpha_L}}{m_L}\Bigg)\Bigg) \\
& -r^2\delta^{\frac{-2}{\alpha_L}} \Bigg(1 - {}_2F_1\Bigg(m_L, -\frac{2}{\alpha_L}; \frac{\alpha_L - 2}{\alpha_L}; -\frac{jwGC_L P_t \delta r^{-\alpha_L}}{m_L}\Bigg)\Bigg) \\
& -R_L^2 \Bigg(1 - {}_2F_1\Bigg(m_N, -\frac{2}{\alpha_N}; \frac{\alpha_N - 2}{\alpha_N}; -\frac{jwGC_N P_t R_L^{-\alpha_N}}{m_N}\Bigg)\Bigg)\Bigg]\Bigg\},
\end{aligned} \tag{6.15}$$

$$\begin{aligned}
\Psi^{(2)}_{I_{agg}}(r, jw) \ = \ & \exp\Bigg\{ -\pi\lambda_b \sum_G p_G \Bigg[r^2\delta^{\frac{-2}{\alpha_L}} \Bigg(1 \\
& -{}_2F_1\Bigg(m_N, -\frac{2}{\alpha_N}; \frac{\alpha_N - 2}{\alpha_N}; -\frac{jwGC_N P_t r^{-\alpha_N}\delta^{\frac{\alpha_N}{\alpha_L}}}{m_N}\Bigg)\Bigg)\Bigg]\Bigg\},
\end{aligned} \tag{6.16}$$

and

$$\begin{aligned}
\Psi^{(3)}_{I_{agg}}(r, jw) \ = \ & \exp\Bigg\{ -\pi\lambda_b \sum_G p_G \Bigg[r^2\delta^{\frac{-2}{\alpha_N}} \Bigg(1 \\
& -{}_2F_1\Bigg(m_N, -\frac{2}{\alpha_N}; \frac{\alpha_N - 2}{\alpha_N}; -\frac{jwGC_N P_t \delta r^{-\alpha_N}}{m_N}\Bigg)\Bigg)\Bigg]\Bigg\}
\end{aligned} \tag{6.17}$$

where ${}_2F_1(a, b; c; z)$ is the Gauss hypergeometric function [62].

Proof: see Appendix 6.8.1

To proceed, the PDF of the aggregated signal $S_{agg}^{(a)}$ is obtained using the following lemma.

Lemma 6.3.2 *For a given distance r to ϕ and a clustering parameter δ, the PDF of the aggregated signal $S_{agg}^{(a)}|r$, $a \in \{1,2,3\}$, is given as*

$$\begin{aligned} f_{S_{agg}^{(a)}|r}(x) &= \frac{d}{dx} Pr\big[S_{agg}^{(a)} \leq x|r\big] \\ &\approx \frac{m_g^{m_g}}{\mathcal{A}^{(a)}(r)\Gamma(m_g)} \Big(x\mathcal{A}^{(a)}(r)\Big)^{m_g-1} \exp\Big(-m_g\mathcal{A}^{(a)}(r)x\Big) \end{aligned} \tag{6.18}$$

where $g = L$ for $a = 1,\ 2$ and $g = N$ for $a = 3$. $\mathcal{A}^{(1)}(r)$, $\mathcal{A}^{(2)}(r)$, and $\mathcal{A}^{(3)}(r)$ are given as

$$\mathcal{A}^{(1)}(r) = \Big(P_t C_L G_m\Big)^{-1} \Bigg(r^{-\alpha_L} + 2\pi\lambda_b r^{2-\alpha_L}\Big(\frac{\delta^{-\frac{2-\alpha_L}{\alpha_L}} - 1}{2-\alpha_L}\Big)\Bigg)^{-1}. \tag{6.19}$$

$$\mathcal{A}^{(2)}(r) = \Big(P_t C_L G_m\Big)^{-1} \Bigg(r^{-\alpha_L} + 2\pi\lambda_b\Big(\frac{R_L^{2-\alpha_L} - r^{2-\alpha_L}}{2-\alpha_L}\Big)\Bigg)^{-1} \tag{6.20}$$

and

$$\mathcal{A}^{(3)}(r) = \Big(P_t C_N G_m\Big)^{-1} \Bigg(r^{-\alpha_N} + 2\pi\lambda_b r^{2-\alpha_N}\Big(\frac{\delta^{-\frac{2-\alpha_N}{\alpha_N}} - 1}{2-\alpha_N}\Big)\Bigg)^{-1}. \tag{6.21}$$

Proof: see Appendix 6.8.2.

Now, we are in a position to formalize the joint coverage probability at the typical user as presented in the following proposition.

Proposition 6.3.1 *The joint coverage probability of the SWIPT-enabled user-centric mmWave network under adaptive BS clustering can be given by*

$$F_{\mathcal{R},\mathcal{H}}\big(\mathcal{R}_{th},\ \mathcal{H}_{th}\big) = \sum_{a\in\{1,\,2,\,3\}} \Lambda^{(a)} F_{\mathcal{R},\mathcal{H}}^{(a)}\big(\mathcal{R}_{th},\ \mathcal{H}_{th}\big), \tag{6.22}$$

where $F_{\mathcal{R},\mathcal{H}}^{(a)}\big(\mathcal{R}_{th},\ \mathcal{H}_{th}\big)$ is the joint coverage probability in Case a, $a \in \{1,\ 2,\ 3\}$, which is expressed as

$$F_{\mathcal{R},\mathcal{H}}^{(a)}\big(\mathcal{R}_{th},\ \mathcal{H}_{th}\big) = \frac{m_g^{m_g}}{\Gamma(m_g)\pi}\Bigg(\int_{r\in I_a}\int_0^\infty \frac{1}{\omega} Im\Bigg\{e^{-jw\sigma^2}\Psi_{I_{agg}}^{(a)}(r, j\omega)\Bigg(\frac{\mathcal{T}}{\mathcal{A}^{(a)}(r)}\Bigg)^{m_g}$$

$$\times E_{1-m_g}\left(\frac{m_g\mathcal{T}}{\mathcal{A}^{(a)}(r)}-\frac{jw\mathcal{T}}{\widetilde{\mathcal{R}}_{th}}\right)\Bigg\}f_r(r)d\omega dr-\int_{r\in I_a}\int_0^{\infty}\frac{1}{\omega}Im\Bigg\{e^{jw\widetilde{\mathcal{H}}_{th}}$$

$$\times\Psi^{(a)}_{I_{agg}}(r,j\omega)\left(\frac{\mathcal{T}}{\mathcal{A}^{(a)}(r)}\right)^{m_g}E_{1-m_g}\left(\frac{m_g\mathcal{T}}{\mathcal{A}^{(a)}(r)}+jw\mathcal{T}\right)\Bigg\}f_r(r)dwdr\Bigg)\Bigg] \quad (6.23)$$

with $E_g(z)=\int_1^{\infty}\frac{e^{-zt}}{t^g}dt$ *being the generalized exponential integral function [62] and* $I_1=[0,\ R_L\delta^{\frac{2}{\alpha_L}}]$, $I_2=[R_L\delta^{\frac{2}{\alpha_L}},\ R_L]$, *and* $I_3=[R_L,\ \infty]$ *are the ranges of* r *corresponding to Case 1, 2, and 3, respectively. In (6.22),* $\Lambda^{(a)}$ *is the probability of Case* a *which can be written as*

$$\Lambda^{(1)}=1-\exp\big(-\pi\lambda_b R_L^2\delta^{\frac{2}{\alpha_L}}\big), \quad (6.24)$$

$$\Lambda^{(2)}=\exp\big(-\pi\lambda_b R_L\delta^{\frac{2}{\alpha_L}}\big)-\exp\big(-\pi\lambda_b R_L^2\big), \quad (6.25)$$

and

$$\Lambda^{(3)}=\exp\big(-\pi\lambda_b R_L^2\big) \quad (6.26)$$

Proof: Applying (6.14) in (6.12) for Case $a\in\{1,\ 2,\ 3\}$, the joint coverage probability $F^{(a)}_{\mathcal{R},\mathcal{H}}\big(\mathcal{R}_{th},\ \mathcal{H}_{th}\big)$ can be written as

$$F^{(a)}_{\mathcal{R},\mathcal{H}}\big(\mathcal{R}_{th},\ \mathcal{H}_{th}\big) \ =$$

$$\mathbb{E}_{S^{(a)}_{agg},r\in I_a}\Bigg[\frac{1}{\pi}\Bigg(\int_0^{\infty}\frac{\mathrm{Im}\Big\{\exp\Big(-j\omega\Big(\frac{S^{(a)}_{agg}|r}{\widetilde{\mathcal{R}}_{th}}-\sigma^2\Big)\Big)\Psi^{(a)}_{I_{agg}}(r,j\omega)\Big\}}{\omega}d\omega$$

$$-\int_0^{\infty}\frac{\mathrm{Im}\Big\{\exp\Big(-j\omega\Big(\widetilde{\mathcal{H}}_{th}-S^{(a)}_{agg}|r\Big)\Big)\Psi^{(a)}_{I_{agg}}(r,j\omega)\Big\}}{\omega}\Bigg)dw\Bigg] \quad (6.27)$$

Then, averaging (6.27) over $S^{(a)}_{agg}$ for the given distance r using its PDF in (6.18) and considering the condition in (6.13), $F^{(a)}_{\mathcal{R},\mathcal{H}}\big(\mathcal{R}_{th},\ \mathcal{H}_{th}\big)$ can be expressed as in (6.23), where $\mathcal{T}=\frac{\mathcal{H}_{th}+\mu\sigma^2}{\mu}\Big(1-2^{-\frac{\mathcal{R}_{th}}{(1-\mu)}}\Big)$. Moreover, from the clustering model in (6.4) it is clear that the radius of the user's serving cluster depends on its distance to ϕ, r. Therefore, the probability of the serving cluster falling in Case 1, 2, and 3 is equivalent to the probability of $r\in[0,\ R_L\delta^{\frac{2}{\alpha_L}}]$, $r\in[R_L\delta^{\frac{2}{\alpha_L}},\ R_L]$, and $r\in[R_L,\ \infty]$,

respectively. Since the PDF of r is $f_r(t) = 2\pi\lambda_b t \exp\left(\pi\lambda_b t^2\right), \quad 0 \leq t < \infty$, its CDF is given as $F_r(t) = \Pr[r \leq t] = 1 - \exp\left(\pi\lambda_b t^2\right)$. Therefore $\Lambda^{(1)}$, $\Lambda^{(2)}$, and $\Lambda^{(3)}$ can be easily computed as given in (6.24), (6.25), and (6.26), respectively.

Corollary 6.3.1 *Given the joint coverage probability of the SWIPT-enabled use-centric mmWave network, $F_{\mathcal{R},\mathcal{H}}\big(\mathcal{R}_{th},\ \mathcal{H}_{th}\big)$, the individual rate coverage probability, denoted as $F_{\mathcal{R}}\big(\mathcal{R}_{th}\big)$ and energy coverage probability, denoted as $F_{\mathcal{H}}\big(\mathcal{H}_{th}\big)$, can be obtained as follows*

$$F_{\mathcal{R}}\big(\mathcal{R}_{th}\big) = \lim_{\mathcal{H}_{th}\to 0} F_{\mathcal{R},\mathcal{H}}\big(\mathcal{R}_{th},\ \mathcal{H}_{th}\big), \tag{6.28}$$

and

$$F_{\mathcal{H}}\big(\mathcal{H}_{th}\big) = \lim_{\mathcal{R}_{th}\to 0} F_{\mathcal{R},\mathcal{H}}\big(\mathcal{R}_{th},\ \mathcal{H}_{th}\big). \tag{6.29}$$

The CCDFs in (6.23), (6.28), and (6.29) are all obtained under the JT scheme. For the OBS and the NC schemes, the joint coverage and the individual rate coverage and energy coverage probabilities can be provided using the following corollary.

Corollary 6.3.2 *Given the joint coverage probability $F_{\mathcal{R},\mathcal{H}}\big(\mathcal{R}_{th},\ \mathcal{H}_{th}\big)$ of the SWIPT-enabled use-centric mmWave network under the JT scheme, the joint coverage probability under the OBS scheme, denoted as $\widetilde{F}_{\mathcal{R},\mathcal{H}}\big(\mathcal{R}_{th},\ \mathcal{H}_{th}\big)$, can be obtained as follows*

$$\widetilde{F}_{\mathcal{R},\mathcal{H}}\big(\mathcal{R}_{th},\ \mathcal{H}_{th}\big) = \sum_{a\in\{1,\,2,\,3\}} \Lambda^{(a)}\, \widetilde{F}^{(a)}_{\mathcal{R},\mathcal{H}}\big(\mathcal{R}_{th},\ \mathcal{H}_{th}\big), \tag{6.30}$$

with

$$\widetilde{F}^{(a)}_{\mathcal{R},\mathcal{H}}\big(\mathcal{R}_{th},\ \mathcal{H}_{th}\big) = F^{(a)}_{\mathcal{R},\mathcal{H}}\big(\mathcal{R}_{th},\ \mathcal{H}_{th}\big)_{\left(\mathcal{A}^{(a)}(r)\to\widetilde{\mathcal{A}}^{(a)}(r)\right)}, \tag{6.31}$$

where $\widetilde{\mathcal{A}}^{(1)}(r) = \widetilde{\mathcal{A}}^{(2)}(r) = P_t G_m C_L r^{-\alpha_L}$ and $\widetilde{\mathcal{A}}^{(2)}(r) = P_t G_m C_N r^{-\alpha_N}$. For the NC scheme, the joint coverage probability, denoted as $\widehat{F}_{\mathcal{R},\mathcal{H}}\big(\mathcal{R}_{th},\ \mathcal{H}_{th}\big)$, is provided as a special case of the joint coverage probability under the JT scheme as follows,

$$\widehat{F}_{\mathcal{R},\mathcal{H}}\big(\mathcal{R}_{th},\ \mathcal{H}_{th}\big) = F_{\mathcal{R},\mathcal{H}}\big(\mathcal{R}_{th},\ \mathcal{H}_{th}\big)_{\delta\to 1}. \tag{6.32}$$

Similar to (6.28) and (6.29), the individual rate coverage and energy coverage probabilities under the OBS and the NC schemes can be obtained as a marginal CCDFs of $\widetilde{F}_{\mathcal{R},\mathcal{H}}\big(\mathcal{R}_{th},\ \mathcal{H}_{th}\big)$ and $\widehat{F}_{\mathcal{R},\mathcal{H}}\big(\mathcal{R}_{th},\ \mathcal{H}_{th}\big)$, respectively.

Remark 6.3.1 ***(Effect of BS Load)*** *According to (6.15)-(6.22), and as will be shown in the numerical results section, the coverage performance improves with increasing the cluster size, i.e, decreasing δ. This is because all BSs are assumed to have enough orthogonal resources to serve all associated users without incurring the interference from BSs within the user's serving cluster. In fact, the cluster size can not increase to infinity and BSs can only assign orthogonal resources to a limited number of users. Hence, the minimum value of the clustering parameter $\delta_{\min}$, which returns the maximum cluster size, should be selected such that the number of users associated to a BS is less than or equal to its maximum load. Let $\mathcal{N}_u(\delta)$ be the average number of users associated to a BS for a given δ which is computed as $\mathcal{N}_u(\delta) = \frac{\lambda_u}{\lambda_b}\left(\delta^{\frac{-2}{\alpha_L}}\left(1-e^{-\pi\lambda_b R_L^2}\left(1+\pi\lambda_b R_L^2\right)\right)+e^{-\pi\lambda_b R_L^2}\delta^{\frac{-2}{\alpha_N}}\left(1+\pi\lambda_b R_L^2\right)\right)$. Then $\delta_{\min}$ is obtained such that $\delta_{\min} = \min\{\delta \in [0,1];\ \mathcal{N}_u(\delta) \leq \psi\}$, where ψ is the maximum BS load. This means that for $\psi \to \infty$, then $\delta_{\min} \to 0$. Accordingly, the network controller determines the value of δ and then broadcast this value to all users.*

6.4 Joint Rate and Energy Coverage Optimization under Network Densification

MmWave networks are expected to be designed with ultra-dense BS deployments in order to reduce the signal blockage probability. This enables each user to observe multiple LOS BSs in its vicinity. However, network densification increases the aggregated interference at the user, and thus user-centric BS cooperation can be employed to mitigate the interference effect [120]. In this section, we consider a highly dense mmWave network, where both the aggregated signal S_{agg}, and the aggregated interference, I_{agg} are dominated by LOS components. Therefore, the problem is simplified by neglecting the effect of NLOS components. In this case, $S_{agg} = \sum_{k\in\Phi_b^S\cap\Phi_b^L} P_t G_m h_k(\mathcal{L}_L(r_k))^{-1}$ and $I_{agg} = \sum_{i\in\Phi_b^L\setminus\Phi_b^S\cap\Phi_b^L} P_t G_i h_i(\mathcal{L}_L(r_i))^{-1}$. Accordingly, the interference characteristic function, $\Psi_{I_{agg}}$, can be interestingly approximated using the following lemma.

Lemma 6.4.1 *For a user-centric mmWave network with highly dense BS deployments and large cluster size, the characteristic function of the aggregated LOS interference, given the distance r to ϕ, can be approximated as*

$$\Psi_{I_{agg}}(r, jw) \approx \exp\left\{-2\pi\lambda_b \frac{C_L G_{av} P_t(jw)}{\alpha_L - 2}\left(\delta^{\frac{\alpha_L-2}{\alpha_L}} r^{2-\alpha_L} - R_L^{2-\alpha_L}\right)\right\}, \quad (6.33)$$

where $G_{av} = \sum_G p_G G$ is the average gain.

Proof: see Appendix 6.8.3

Using (6.33) into (6.27), the joint coverage probability in highly dense networks can be written as

$$\begin{aligned} F_{\mathcal{R},\mathcal{H}}\big(\mathcal{R}_{th},\, \mathcal{H}_{th}\big) &\overset{(a)}{=} \mathbb{E}_{S_{agg},r}\Bigg[\frac{-1}{\pi}\Bigg(\int_0^\infty \frac{\sin\Big(\omega\Big(\frac{S_{agg}|r}{\widetilde{\mathcal{R}}_{th}} - \sigma^2 - \mathcal{B}(r)\Big)\Big)}{\omega} d\omega \\ &\quad - \int_0^\infty \frac{\sin\Big(\omega\Big(\widetilde{\mathcal{H}}_{th} - S_{agg}|r - \mathcal{B}(r)\Big)\Big)}{\omega} dw\Bigg)\Bigg], \\ &\overset{(b)}{=} \mathbb{E}_{S_{agg},r}\Bigg[\mathrm{sgn}\Big(\widetilde{\mathcal{H}}_{th} - S_{agg}|r - \mathcal{B}(r)\Big) \\ &\quad - \mathrm{sgn}\Bigg(\frac{S_{agg}|r}{\widetilde{\mathcal{R}}_{th}} - \sigma^2 - \mathcal{B}(r)\Bigg)\Bigg], \end{aligned} \quad (6.34)$$

where (a) follows from the fact that $\mathrm{Im}\big(\exp(-jx)\big) = -\sin(x)$ for $x \in \mathbb{R}/0$ together with the following substitution

$$\mathcal{B}(r) = 2\pi\lambda_b \frac{C_L G_{av} P_t}{\alpha_L - 2}\left(\delta^{\frac{\alpha_L-2}{\alpha_L}} r^{2-\alpha_L} - R_L^{2-\alpha_L}\right), \quad (6.35)$$

and (b) follows from the equality $\int_0^\infty \frac{\sin(ax)}{x} dx = \frac{\pi}{2}\mathrm{sgn}(a)$, where $\mathrm{sgn}(a)$ returns the sign of a if $a \neq 0$ and $\mathrm{sgn}(0) = 0$. Averaging (6.34) over $S_{agg}^{(1)}|r$ using (6.18), the joint coverage probability can be expressed as

$$\begin{aligned} F_{\mathcal{R},\mathcal{H}}\big(\mathcal{R}_{th},\, \mathcal{H}_{th}\big) &= \mathbb{E}_{r\in I_1}\Bigg[\frac{1}{\Gamma(m_L)}\Bigg\{\Gamma\Bigg(m_L, \frac{m_L\big(\widetilde{\mathcal{H}}_{th} + \mathcal{B}(r)\big)}{\mathcal{A}(r)}\Bigg) + \Bigg(\Gamma\Bigg(m_L, \frac{m_L\mathcal{T}}{\mathcal{A}(r)}\Bigg) \\ &\quad - \Gamma\Bigg(m_L, \frac{m_L\big(\widetilde{\mathcal{H}}_{th} + \mathcal{B}(r)\big)}{\mathcal{A}(r)}\Bigg)\Bigg)\mathcal{U}\Big(\mathcal{T} - \widetilde{\mathcal{H}}_{th} - \mathcal{B}(r)\Big) - \Bigg(\Gamma\Bigg(m_L, \frac{m_L\mathcal{T}}{\mathcal{A}(r)}\Bigg) \end{aligned}$$

$$-\Gamma\bigg(m_L, \frac{m_L\widetilde{\mathcal{R}}_{th}\big(\sigma^2-\mathcal{B}(r)\big)}{\mathcal{A}(r)}\bigg)\bigg)\mathcal{U}\Big(\widetilde{\mathcal{R}}_{th}\sigma^2-\mathcal{T}-\widetilde{\mathcal{R}}_{th}\mathcal{B}(r)\Big)\bigg\}\bigg], \quad (6.36)$$

where $\mathcal{U}(.)$ represents the unit step function. Then, by averaging (6.36) over the distance r and performing mathematical manipulations, we can obtain the joint coverage probability as stated in the following proposition.

Proposition 6.4.1 *The joint coverage probability of the SWIPT-enabled user-centric mmWave network under adaptive BS clustering and highly-dense BS deployments can be approximated as*

$$F_{\mathcal{R},\mathcal{H}}\big(\mathcal{R}_{th},\ \mathcal{H}_{th}\big) \ \approx\ \chi_1 H_1\big(\mathcal{R}_{th},\mathcal{H}_{th}\big)+\chi_1 H_2\big(\mathcal{R}_{th},\mathcal{H}_{th}\big)+\chi_1 H_3\big(\mathcal{R}_{th},\mathcal{H}_{th}\big) \quad (6.37)$$

where $\chi_1 = 1-\exp\left(-\pi\lambda_b\mathcal{M}_1^2\right)$, $\chi_2 = \exp\left(-\pi\lambda_b\mathcal{M}_2^2\right)-\exp\left(-\pi\lambda_b\mathcal{M}_1^2\right)$, $\chi_3 = \exp\left(-\pi\lambda_b R_L^2\delta^{\frac{2}{\alpha_L}}-\exp\left(-\pi\lambda_b\mathcal{M}_1^2\right)\right.$, *and* $H_1\big(\mathcal{R}_{th},\mathcal{H}_{th}\big)$, $H_2\big(\mathcal{R}_{th},\mathcal{H}_{th}\big)$, *and* $H_3\big(\mathcal{R}_{th},\mathcal{H}_{th}\big)$ *are, respectively, expressed as*

$$H_1\big(\mathcal{R}_{th},\ \mathcal{H}_{th}\big) \ =\ \frac{2\pi\lambda_b}{\Gamma(m_L)}\bigg\{\int_0^{\mathcal{M}_1} re^{-\pi\lambda_b r^2}\Gamma\bigg(m_L, \frac{m_L\big(\widetilde{\mathcal{H}}_{th}+\mathcal{B}(r)\big)}{\mathcal{A}(r)}\bigg)dr\bigg\}, \quad (6.38)$$

$$\begin{aligned} H_2\big(\mathcal{R}_{th},\ \mathcal{H}_{th}\big) \ =\ &\frac{2\pi\lambda_b}{\Gamma(m_L)}\bigg\{\int_{\mathcal{M}_1}^{\mathcal{M}_2} re^{-\pi\lambda_b r^2}\bigg(\Gamma\bigg(m_L, \frac{m_L\big(\widetilde{\mathcal{H}}_{th}+\mathcal{B}(r)\big)}{\mathcal{A}(r)}\bigg)dr \\ &-\Gamma\bigg(m_L, \frac{m_L\mathcal{T}}{\mathcal{A}(r)}\bigg)-\Gamma\bigg(m_L, \frac{m_L\widetilde{\mathcal{R}}_{th}\big(\sigma^2-\mathcal{B}(r)\big)}{\mathcal{A}(r)}\bigg)\bigg)dr\bigg\}, \end{aligned} \quad (6.39)$$

and

$$\begin{aligned} H_3\big(\mathcal{R}_{th},\ \mathcal{H}_{th}\big) \ =\ &\frac{2\pi\lambda_b}{\Gamma(m_L)}\bigg\{\int_{\mathcal{M}_2}^{R_L\delta^{\frac{1}{\alpha_L}}} re^{-\pi\lambda_b r^2} \\ &\times\Gamma\bigg(m_L, \frac{m_L\widetilde{\mathcal{R}}_{th}\big(\sigma^2-\mathcal{B}(r)\big)}{\mathcal{A}(r)}\bigg)dr\bigg\}, \end{aligned} \quad (6.40)$$

with $\mathcal{M}_1$ *and* $\mathcal{M}_2$ *being given as*

$$\mathcal{M}_1 \ =\ \bigg(\delta^{\frac{2}{\alpha_L}-1}\bigg(R_L^{2-\alpha_L}-\frac{\widetilde{\mathcal{R}}_{th}-\mathcal{T}}{\widetilde{\mathcal{R}}_{th}}\Big(\frac{\alpha_L-2}{2\pi\lambda_b P_t C_L G_{av}}\Big)\bigg)\bigg)^{\frac{1}{2-\alpha_L}}, \quad (6.41)$$

and

$$\mathcal{M}_2 \;=\; \left(\delta^{\frac{2}{\alpha_L}-1}\left(R_L^{2-\alpha_L}-\left(\mathcal{T}-\widetilde{\mathcal{H}}_{th}\right)\left(\frac{\alpha_L-2}{2\pi\lambda_b P_t C_L G_{av}}\right)\right)\right)^{\frac{1}{2-\alpha_L}}, \qquad (6.42)$$

Note that the expression in (6.37) needs the computation of only one integral making it more tractable for system design and analysis. Although (6.37) provides a tractable approximation of the joint coverage probability, it is still difficult to see its insight and implication about the system behaviour due to the long and complex expressions involved. As a spacial case, here we consider the fact that ultra-dense mmWave networks are interference-limited, where the noise effect can be neglected, i.e, $\sigma^2 = 0$. By using the expressions of $\widetilde{\mathcal{R}}_{th}$, $\widetilde{\mathcal{H}}_{th}$, $\mathcal{T}$, $\mathcal{B}(r)$, and $\mathcal{A}(r)$ into (6.36) and setting $\sigma^2 = 0$, the joint coverage for a given distance $r = \hat{r}$ can be simplified as

$$F_{\mathcal{R},\mathcal{H}}\big(\mathcal{R}_{th},\,\mathcal{H}_{th}\big)_{r=\hat{r}} \;=\; \frac{1}{\Gamma(m_L)}$$

$$\times\begin{cases}\Gamma\left[m_L,\,\dfrac{2\pi\lambda_b m_L G_{av}\left(2^{\frac{\mathcal{R}_{th}}{1-\mu}}-1\right)\left(\hat{r}^2\delta-R_L^{2-\alpha_L}\hat{r}^{\alpha_L}\delta^{\frac{2}{\alpha_L}}\right)}{G_m\delta^{\frac{2}{\alpha_L}}(2\pi\lambda_b\hat{r}^2+\alpha_L-2)-2\pi\delta\lambda_b\hat{r}^2}\right], & \mathcal{Q}(\mu)\le 0\\[2ex] \Gamma\left[m_L,\,\dfrac{2\pi\lambda_b m_L P_t C_L G_{av}\mu\left(R_L^{2-\alpha_L}\hat{r}^{\alpha_L}\delta^{\frac{2}{\alpha_L}}-\hat{r}^2\delta\right)+m_L\mathcal{H}_{th}\hat{r}^{\alpha_L}\delta^{\frac{2}{\alpha}L}(\alpha_L-2)}{P_t G_m C_L\mu\left(\delta^{\frac{2}{\alpha_L}}\left(\alpha_L-2+2\pi\lambda_b\hat{r}^2\right)-2\pi\lambda_b\delta\hat{r}^2\right)}\right], & \mathcal{Q}(\mu)>0\end{cases} \qquad (6.43)$$

where $\mathcal{Q}(\mu)$ is given as

$$\mathcal{Q}(\mu) \;=\; \frac{2^{-\frac{\mathcal{R}_{th}}{1-\mu}}\mathcal{H}_{th}}{\eta\mu}-\frac{2\pi P_t C_L G_{av}\left(2^{\alpha_L-2}\lambda_b^{\frac{\alpha_L}{2}}\delta^{\frac{\alpha_L-2}{\alpha_L}}-\lambda_b R_L^{2-\alpha_L}\right)}{\alpha_L-2}. \qquad (6.44)$$

Since $\Gamma(m_L, x)$ is a decreasing function for $x > 0$, by analyzing the relationship between the argument x and the variable μ in (6.43) and considering all other parameters in x as constant (for given system parameters), one can find that the first part in the right side of (6.43) decreases with μ while the second part increases with μ. This implies that, with respect to μ, (6.43) always increases for $\mathcal{Q}(\mu) > 0$ and always decreases for $\mathcal{Q}(\mu) \le 0$. Moreover, as will be shown in the numerical results section, the provided expression of the approximated joint coverage probability is a continuous function of μ for given system parameters which means that the two

parts in the right side of (6.43) are equal at $\mathcal{Q}(\mu) = 0$. As such, the optimum value of the time switching coefficient μ_{opt} that provides the maximum joint coverage performance for given system parameters can be determined from

$$\mu_{\text{opt}} = \big\{\mu,\ \mathcal{Q}(\mu) = 0,\ \ \text{s.t.}\ \ 0 < \mu < 1\big\}, \tag{6.45}$$

which can be computed with the aid of numerical tools. For (6.45) to hold and provide a unique solution, $\mathcal{Q}(\mu)$ should be a monotonically decreasing function of μ with a zero crossing point. This can be verified by calculating the first derivative of $\mathcal{Q}(\mu)$, namely $\frac{d\mathcal{Q}(\mu)}{d\mu} = -\frac{\mathcal{H}_{th}}{\eta\mu^2} 2^{-\frac{\mathcal{R}_{th}}{1-\mu}} \Big(1+\mu(1-\mu)^{-2}\ln(2)\mathcal{R}_{th}\Big)$ which is always negative. This proves that $\mathcal{Q}(\mu)$ is a strictly monotonically decreasing function of μ for any given rate and energy thresholds. Fig. 6.1 also shows that for a given δ, $\mathcal{Q}(\mu)$ monotonically decreases with μ and crosses the μ-axis at a specific point which corresponds to the optimal value of μ as indicated by the vertical dotted line. Note that all system parameters used to plot the curves in Fig. 6.1 are provided in Section 6.6, where the behaviour of the system performance is discussed in more details. From (6.44) and (6.45), it can be observed that the optimum value of

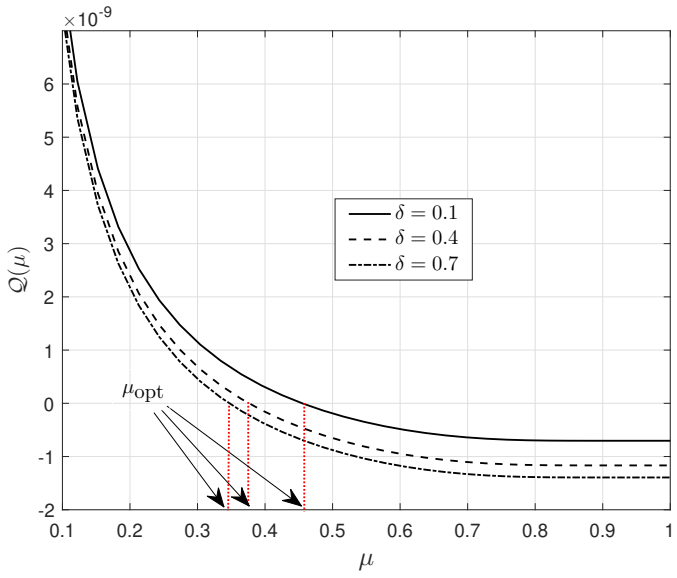

Figure 6.1: Plot of the function $\mathcal{Q}(\mu)$ versus μ. This figure shows that $\mathcal{Q}(\mu)$ is a one-to-one function (a strictly monotonic decreasing function) which provides a unique solution of (6.45).

μ depends on the channel and system parameters including the rate and energy

threshold requirements, transmitted power, beamforming antenna arrays parameter, BS density, blockage effect, channel large-scale fading, and serving cluster size.

6.5 Performance Characterization under Non-linear Energy Harvesting

In this section, we consider a non-linear energy harvesting model. In fact, energy harvesting circuit usually results in a non-linear wireless power conversion. As such, we adopt the model proposed in [150] which gives the following normalized non-linearly harvested energy

$$\mathcal{H}^{NL} = \mu \frac{\frac{D}{1+\exp\left(-a_1\left(S_{agg}+I_{agg}-a_2\right)\right)} - \frac{D}{1+\exp\left(a_1 a_2\right)}}{1 - \frac{1}{1+\exp\left(a_1 a_2\right)}}, \tag{6.46}$$

where S_{agg} and I_{agg} are expressed in (6.6) and (6.7), respectively, a_1 and a_2 are constants related to the specifications of the energy harvesting circuit and D is a constant denoting the maximum harvested power at saturation [150]. For a high enough value of D, the joint coverage probability in the case of non-linear energy harvesting is expressed as

$$F^{NL}_{\mathcal{R},\mathcal{H}^{NL}}\big(\mathcal{R}_{th},\ \mathcal{H}_{th}\big) = \Pr\big[\mathcal{R} \geq \mathcal{R}_{th},\ \mathcal{H}^{NL} \geq \mathcal{H}_{th}\big], \tag{6.47}$$

From (6.8) and (6.46), the joint coverage probability in (6.47) can be expressed, after some arrangements, as

$$F^{NL}_{\mathcal{R},\mathcal{H}^{NL}}\big(\mathcal{R}_{th},\ \mathcal{H}_{th}\big) = F_{I_{agg}}\left(\frac{S_{agg}}{\widetilde{\mathcal{R}}_{th}} - \sigma^2\right) - F_{I_{agg}}\left(\widetilde{\mathcal{H}}^{NL}_{th} - S_{agg}\right), \tag{6.48}$$

where $\widetilde{\mathcal{R}}_{th}$ is defined as in (6.12) and $\widetilde{\mathcal{H}}^{NL}_{th}$ is given as

$$\begin{aligned}\widetilde{\mathcal{H}}^{NL}_{th} \ &= \ -\frac{1}{a_1}\ln\Bigg\{\Bigg(\frac{\mathcal{H}_{th}}{D\mu}\Big(1 - \frac{1}{1+\exp(a_1 a_2)}\Big) \\ &\qquad + \frac{1}{1+\exp(a_1 a_2)}\Bigg)^{-1} - 1\Bigg\} + a_2.\end{aligned} \tag{6.49}$$

Similar to the discussion in (6.12), the joint coverage probability in (6.48) holds for

$$S_{agg} > \left(\widetilde{\mathcal{H}}_{th}^{NL} + \sigma^2\right)\left(\frac{1}{\widetilde{\mathcal{R}}_{th}} + 1\right), \tag{6.50}$$

From (6.48) and (6.50), it is clear that the expression of the joint coverage probability with non-linear energy harvesting can be obtained from that of the joint coverage probability in the case of linear harvesting by replacing $\widetilde{\mathcal{H}}_{th}$ with $\widetilde{\mathcal{H}}_{th}^{NL}$, i.e.,

$$F_{\mathcal{R},\mathcal{H}^{NL}}^{NL}\big(\mathcal{R}_{th},\ \mathcal{H}_{th}\big) = F_{\mathcal{R},\mathcal{H}}\big(\mathcal{R}_{th},\ \mathcal{H}_{th}\big)_{\widetilde{\mathcal{H}}_{th}\to\widetilde{\mathcal{H}}_{th}^{NL}}. \tag{6.51}$$

Similarly, the joint coverage probabilities for OBS and NC transmissions schemes in the case of non-linear energy harvesting are, respectively, obtained as $\widetilde{F}_{\mathcal{R},\mathcal{H}^{NL}}^{NL}\big(\mathcal{R}_{th},\ \mathcal{H}_{th}\big) = \widetilde{F}_{\mathcal{R},\mathcal{H}}\big(\mathcal{R}_{th},\ \mathcal{H}_{th}\big)_{\widetilde{\mathcal{H}}_{th}\to\widetilde{\mathcal{H}}_{th}^{NL}}$ and $\widehat{F}_{\mathcal{R},\mathcal{H}^{NL}}^{NL}\big(\mathcal{R}_{th},\ \mathcal{H}_{th}\big) = \widehat{F}_{\mathcal{R},\mathcal{H}}\big(\mathcal{R}_{th},\ \mathcal{H}_{th}\big)_{\widetilde{\mathcal{H}}_{th}\to\widetilde{\mathcal{H}}_{th}^{NL}}$.

6.6 Numerical Results

In this section, we provide numerical results to illustrate the performance of the considered system and to validate the mathematical framework developed in this chapter. Unless otherwise specified, the details of the system setup are as follows. The system operates at frequency of 28 GHz and the number of elements in each antenna array is $N_t = 8$. The Nakagami-m channel parameters for LOS and NLOS are, respectively, set as $m_L = 3$, $m_N = 2$ and the path loss exponents for LOS and NLOS links are $\alpha_L = 2.5$ and $\alpha_N = 4$. The BS transmit power is set to $P_t = 30$ dBm and the noise power is $\sigma^2 = -94$ dBm. The energy conversion efficiency is assumed as $\eta = 0.8$. If fixed, the BS density is set to $\lambda_b = 10^{-3}$ BS/m^2, the normalized rate threshold is $\mathcal{R}_{th} = 2$ bps/Hz (bit/s/Hz), and the normalized energy threshold is $\mathcal{H}_{th} = -55$ dBm. The LOS range is assumed to be 150 meters and the user density is $\lambda_u = 2 \times 10^{-3}$ users/m^2.

Figs. 6.2 and 6.3 show, respectively, the downlink rate coverage probability and energy coverage probability at the typical user versus the time switching coefficient, μ, for different values of the system clustering parameter, δ. As expected, Fig. 6.2 demonstrates that the rate coverage probability for the three transmission schemes (JT, OBS, and NC) degrades with increasing μ since the time slot for receiving

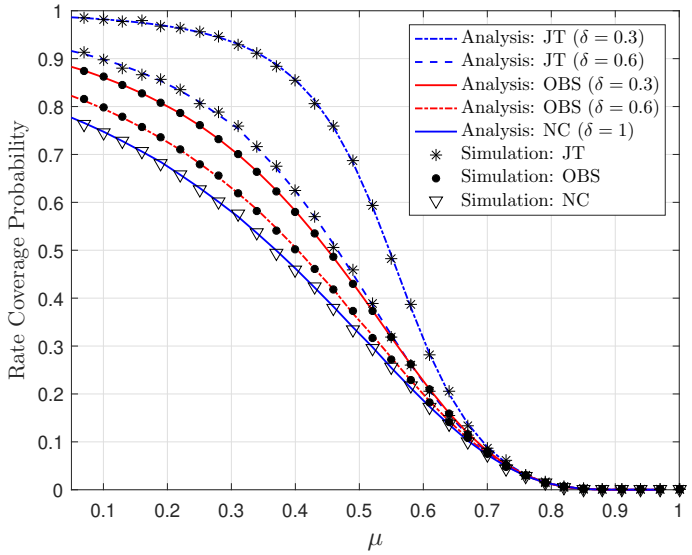

Figure 6.2: Rate coverage probability as a function of the time switching coefficient, μ, for different transmission schemes and different values of the clustering parameter δ with $\mathcal{R}_{th} = 2$ bps/Hz.

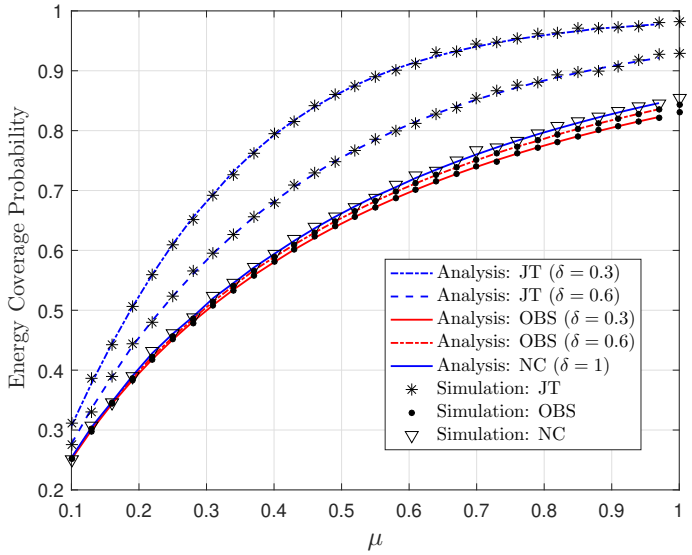

Figure 6.3: Energy coverage probability as a function of the time switching coefficient, μ, for different transmission schemes and different values of the clustering parameter δ with $\mathcal{H}_{th} = -55$ dBm.

.

data decreases with μ. On the other hand, the energy coverage probability at the typical user for the three schemes increases with increasing μ as shown in Fig. 6.3. This is because the time slot for harvesting energy increases with μ. In addition, these two figures show that the JT scheme, with $\delta = 0.3$ and 0.6, outperforms both the OBS and NC schemes in terms of rate and energy coverages and also show that the performance of the JT significantly improves with decreasing the clustering parameter, δ. This results from the fact that the number of BSs joining the user's serving cluster increases with decreasing δ and hence this increases the amount of received power used either for data symbol detection or for energy harvesting. Moreover, we also note that the OBS transmission scheme outperforms the NC scheme in terms of rate coverage, as shown in Fig. 6.2, but it provides lower energy coverage, as shown in Fig. 6.3. Such performance behaviour arises because, when applying the OBS scheme, only one BS in the serving cluster is selected to serve the user while the others keep silent. This reduces the interference at the typical user which enhances the received SINR but decreases the amount of harvested energy since the user harvests energy from both received useful signal and interference according to (6.9).

In Fig. 6.4, we plot the joint coverage probability against the time switching coefficient μ. As shown in the figure, both JT and OBS schemes outperform the NC scheme. Furthermore, Fig. 6.4 demonstrate that for a given transmission scheme and a given value of the clustering parameter δ, there is an optimal value of the time switching coefficient μ at which the joint rate and energy coverage performance is maximum. This optimal behaviour of the joint coverage performance happens due to the fact that when μ increases, the rate coverage decreases while the energy coverage increases and vice-versa. Clearly, the optimal value of μ depends on the applied transmission scheme and on the clustering parameter, δ.

In Figs. 6.5 and 6.6, we illustrate, respectively, the rate and energy coverage probabilities against the clustering parameter δ under the JT and OBS schemes for different values of μ. As shown in the two figures, for the JT scheme, both rate and energy coverage probability performances dramatically degrade with δ while for

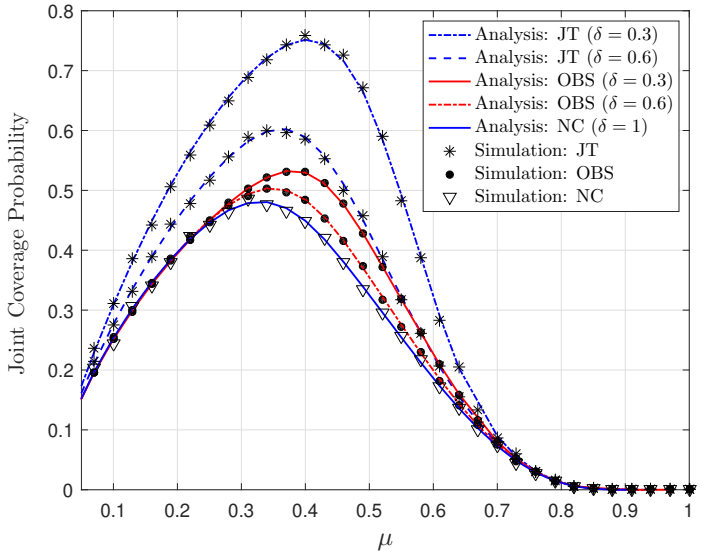

Figure 6.4: Joint coverage probability as a function of the time switching coefficient, μ, for different transmission schemes and different values of the clustering parameter δ with $\mathcal{R}_{th} = 2$ bps/Hz and $\mathcal{H}_{th} = -55$ dBm.

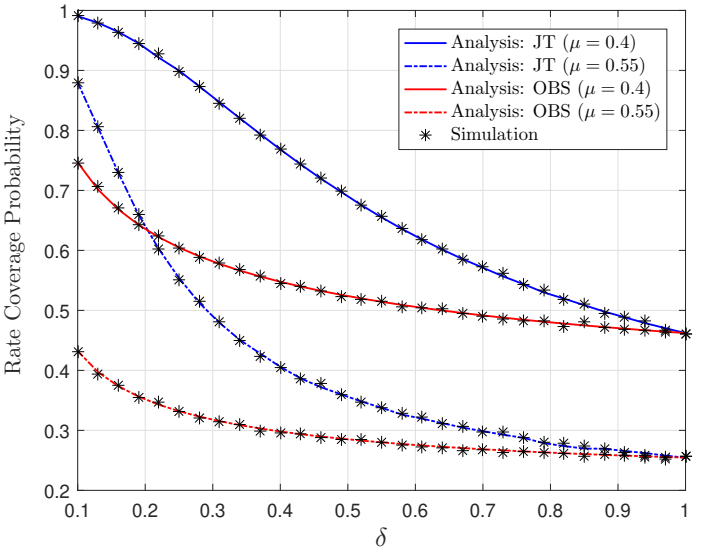

Figure 6.5: Rate coverage as a function of the system BS clustering parameter, δ with $\mathcal{R}_{th} = 2$ bps/Hz.

.

the OBS, the rate coverage probability gradually decreases and the energy coverage probability gradually increases with δ. The reason is that for the JT scheme, the in-

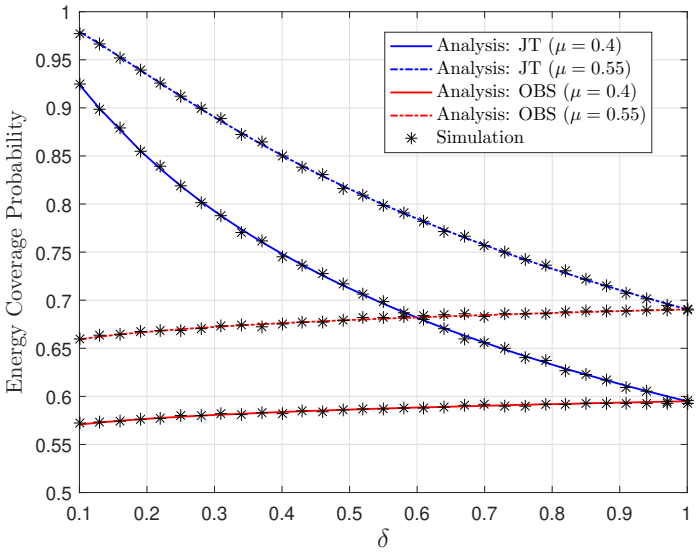

Figure 6.6: Energy coverage probability as a function of the system BS clustering parameter, δ with $\mathcal{H}_{th} = -55$ dBm.

.

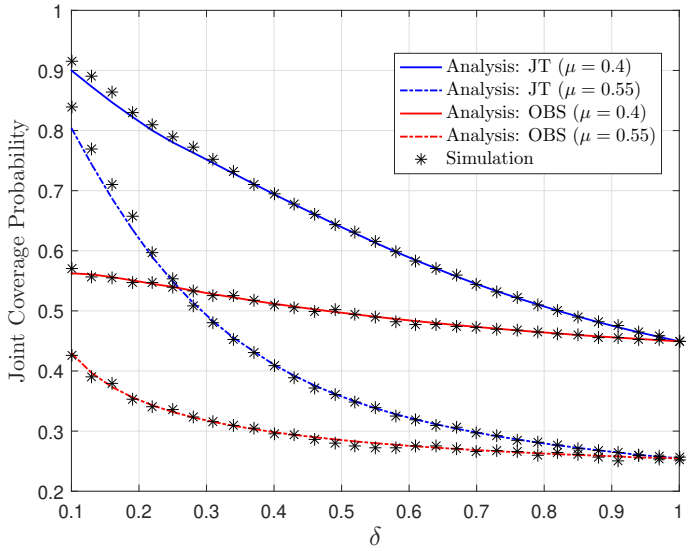

Figure 6.7: Joint coverage probability as a function of the system BS clustering parameter, δ with $\mathcal{R}_{th} = 2$ bps/Hz and $\mathcal{H}_{th} = -55$ dBm.

.

terfering signals are transformed to useful signals which largely increases the amount of useful received power for user symbol detection and energy harvesting. On the

other hand, for the OBS scheme, all BSs in the cluster keep silent except that the BS with the highest average received power serves the user. Therefore, decreasing the size of the user's serving cluster, i.e, increasing δ, largely affects the performance of the JT compared to that of the OBS. Similar to the rate coverage probability, the joint coverage probability decreases with increasing δ as shown in Fig. 6.7. Figs. 6.5, 6.6, 6.7 show that the performances of both JT and OBS schemes match at $\delta = 1$ where they return to a NC scheme which also validates our mathematical derivations in Section 6.3.

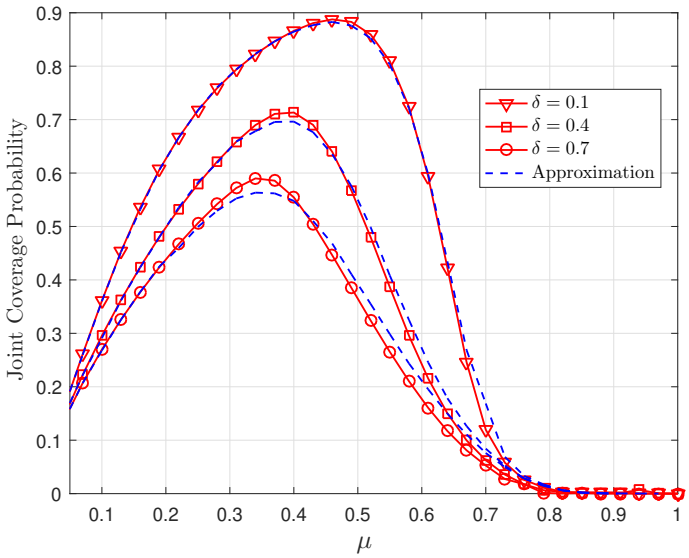

Figure 6.8: Joint coverage probability of the JT scheme along with the approximation provided in (6.37) as a function of the time switching coefficient, μ, for different values of the clustering parameter δ with $\mathcal{R}_{th} = 2$ bps/Hz and $\mathcal{H}_{th} = -55$ dBm.

Fig. 6.8 depicts the joint coverage probability of the JT scheme for different values of δ, along with the approximate joint CCDF calculated using (6.37), as a function of the time switching coefficient, μ. It can be observed that the approximate mathematical expression in (6.37) shows accurate results especially for small δ, i.e., large cluster sizes. Therefore, this simplified expression can be effectively used for the system design without compromising its performance.

In Fig. 6.9 we illustrate the performance of the JT scheme in terms of the joint coverage against the BS density for different values of μ and δ. The figure shows that

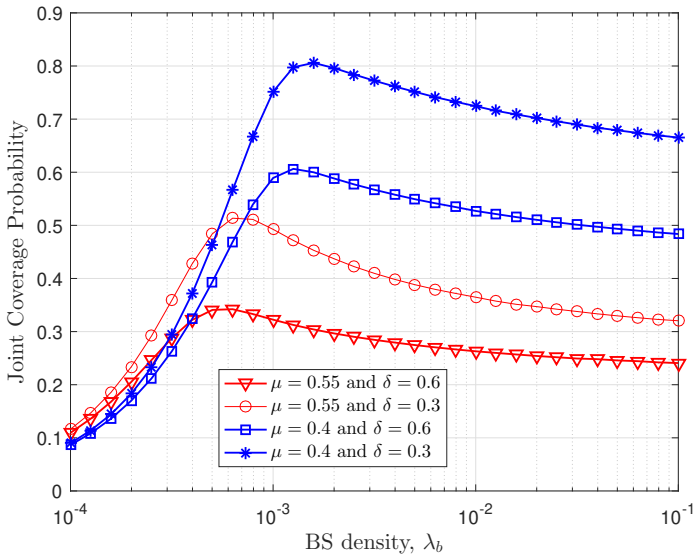

Figure 6.9: Joint coverage probability as a function of the BS density, λ_b, for the JT scheme and for different values of the time switching coefficient, μ, and the system BS clustering parameter δ with $\mathcal{R}_{th} = 2$ bps/Hz and $\mathcal{H}_{th} = -55$ dBm.

for given μ and δ, the performance increases with the BS density to a specific value and starts decaying afterwards. This means that there is an optimal BS density which provides maximum performance and this optimal value depends on both the time switching coefficient, μ, and the system clustering parameter, δ.

Previous figures show the system performances when there is enough orthogonal resources at each BS such that all its associated users are assigned different resources to avoid the interference from BSs within the serving cluster [73]. In Fig. 6.10, we consider that a BS has a limited number of orthogonal resources and to achieve the maximum performance while avoiding the cluster-overlap, the value of the clustering parameter δ is selected such that the average number of users equals the maximum BS load ψ, i.e, the number of available resources. As expected, the results in Fig. 6.10 illustrate that the joint coverage probability under the JT scheme increases with the BS load.

The optimization framework provided in (6.45) is validated in Fig. 6.11, where the optimum time switching coefficient, μ_{opt}, is plotted as a function of the system clustering parameter δ. As shown in the previous figures, under larger size of the

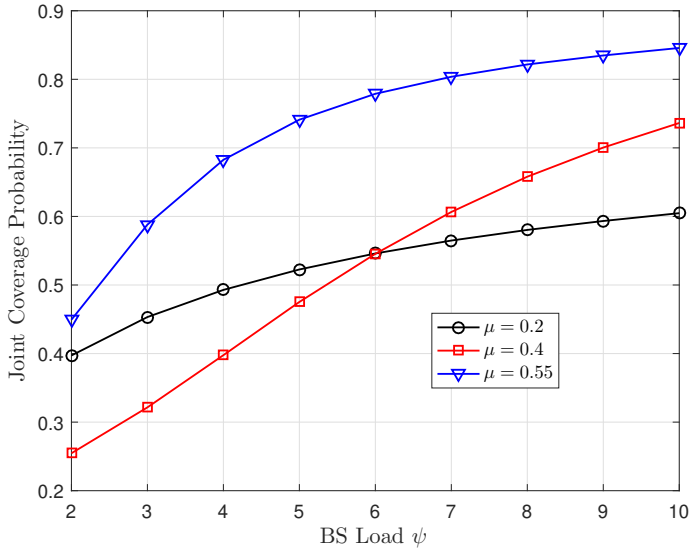

Figure 6.10: Joint coverage probability of a load-constraint system as a function of the BS load, for the JT scheme and for different values of the time switching coefficient, μ with $\mathcal{R}_{th} = 2$ bps/Hz and $\mathcal{H}_{th} = -55$ dBm.

.

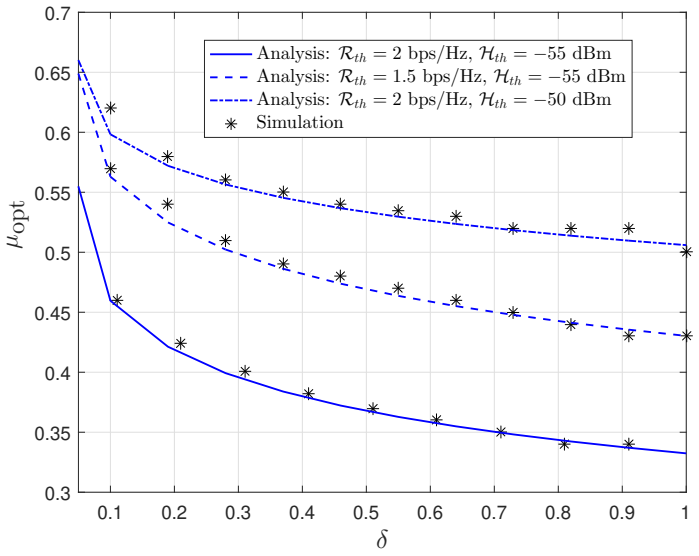

Figure 6.11: Optimum value of the time switching coefficient μ_{opt} of the JT scheme versus the clustering parameter δ for different values of the rate and energy thresholds. The analytical curves of μ_{opt} are provided by solving (6.45) numerically.

user's serving cluster, which corresponds to smaller δ, the rate coverage and energy coverage improves. However, the effect of δ on the rate coverage is greater than its effect on the energy coverage as shown in Figs. 6.5 and 6.6. As a result, Fig. 6.11 demonstrates a decrease of μ_{opt} with δ for given rate and energy thresholds. Furthermore, Fig. 6.11 shows that μ_{opt} changes with the required rate and energy reliability thresholds. In particular, μ_{opt} increases with either decreasing $\mathcal{R}_{th}$ or increasing $\mathcal{H}_{th}$. This is expected since μ represents the fraction of the time during which the receiver harvests energy from the received RF signal.

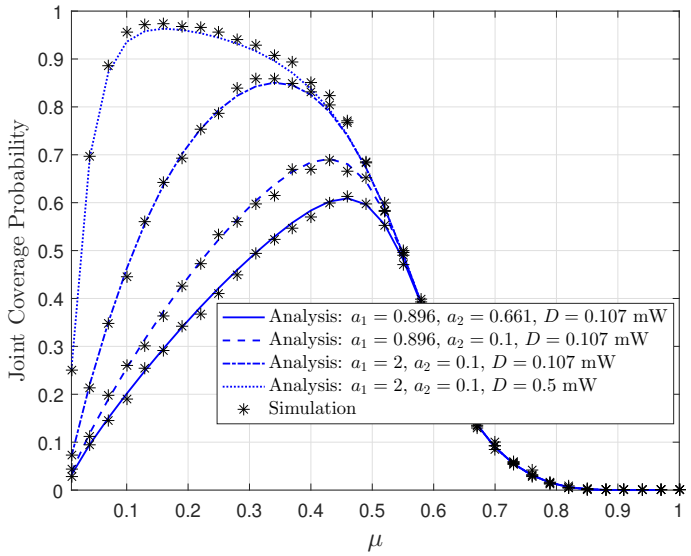

Figure 6.12: Joint coverage probability of the JT scheme as a function of the time switching coefficient, μ, for a non-linear energy harvesting receiver with different values of the non-linear energy harvesting circuit parameters, a_1, a_2 and D when $\delta = 0.3$, $\mathcal{R}_{th} = 2$ bps/Hz and $\mathcal{H}_{th} = -35$ dBm.

Now, we investigate an example of the non-linear energy harvesting receiver. Fig. 6.12 shows the the joint coverage probability under the JT scheme for the non-linear energy harvester. For, the solid line curve, the values of the non-linear energy harvesting circuit parameters a_1, a_2, and D are taken from [130], where a standard curve fitting algorithm was applied to experimental data of a given energy harvesting hardware circuit. As shown in the figure, the joint coverage performance depends on the parameters a_1, a_2 and D. In particular, since a_1 represents the

nonlinear charging rate with regard to the input power, a_2 controls the minimum turn-on power required to harvest energy, and D is the maximum harvested power at saturation [130], [150], the system performance is improved with increasing a_1, decreasing a_2 and/or increasing D.

6.7 Summary

In this work, mmWave and user-centric BS cooperation are integrated to enhance the performance of SWIPT-enabled wireless networks. Time switching protocol is assumed to separate the signal for energy harvesting and data symbols decoding, where both linear and non-linear energy harvesting models are considered. With the aid of stochastic geometry tools, we have analyzed the system performance in terms of the joint rate and energy coverage as well as the individual coverage performances. A pathloss-based BS clustering model is applied which enables each user to select its serving cluster of BSs according to the large-scale channel condition. Two cooperative transmission schemes, namely, JT and OBS, are implemented to transmit the user data and energy. Mathematical formulas of the coverage probabilities of the SWIPT-enabled mmWave user-centric network are provided, where the effect of the serving cluster size, time switching coefficient, and BS density is demonstrated. Furthermore, we discussed how the BS loading capability limits the size of the user's serving cluster. In addition, a more tractable expression for the joint coverage probability in networks with highly dense BS deployments is provided and then followed by an optimization framework of the time swatch coefficient to maximize the system performance. Numerical results have shown that adaptive user-centric BS clustering can largely improve the coverage performance of SWIPT-enabled mmWave systems.

6.8 Appendices

6.8.1 Proof of Lemma 6.3.1

Using the probability generating functional (p.g.fl.) of a PPP, the characteristic function of the aggregated interference I_{agg} for Case 1, which contains LOS and NLOS components, can be computed as

$$\begin{aligned}
\Psi^{(1)}_{I_{agg}}(r, jw) &= \mathbb{E}_{I_{agg}}\Big[\exp\big(jwI_{agg}\big)\Big] \\
&\overset{(a)}{=} \mathbb{E}_{\{\Phi_b^L\setminus\Phi_b^S\cap\Phi_b^L\},G,h}\left[\exp\left(jw\sum_{i\in\Phi_b^L\setminus\Phi_b^S\cap\Phi_b^L} P_tC_LG_ih_ir_i^{-\alpha_L}\right)\right] \\
&\times\mathbb{E}_{\{\Phi_b^N\setminus\Phi_b^S\cap\Phi_b^N\},G,h}\left[\exp\left(jw\sum_{j\in\Phi_b^N\setminus\Phi_b^S\cap\Phi_b^N} P_tC_NG_jh_jr_j^{-\alpha_N}\right)\right] \\
&\overset{(b)}{=} \mathbb{E}_{Q_L|r}\left[\left(\mathbb{E}_{G,z_L}\left[\left(\frac{m_L}{m_L - jwP_tGC_Lz_L^{-\alpha_L}}\right)^{m_L}\right]\right)^{Q_L}\right] \\
&\times\mathbb{E}_{Q_N|r}\left[\left(\mathbb{E}_{G,z_N}\left[\left(\frac{m_N}{m_N - jwP_tGC_Nz_N^{-\alpha_N}}\right)^{m_N}\right]\right)^{Q_N}\right] \\
&\overset{(c)}{=} \Psi^{(1)}_L(r, jw)\Psi^{(1)}_N(r, jw),
\end{aligned} \tag{6.52}$$

where (a) follows from the assumption that LOS and NLOS interference are independent, (b) results from applying the characteristic function of a summation of Q_L and Q_N gamma distributed random variables, i.e, h_i and h_j, and (c) follows from letting $\Psi^{(1)}_L(r, jw) = \mathbb{E}_{Q_L|r}\Big[\mathbb{E}_{G,z_L}\big[\big(1 - \frac{jwP_tGC_Lz_L^{-\alpha_L}}{m_L}\big)^{-m_L}\big]\Big]$ and $\Psi^{(1)}_N(r, jw) = \mathbb{E}_{Q_N|r}\Big[\mathbb{E}_{G,z_N}\big[\big(1 - \frac{jwP_tGC_Nz_N^{-\alpha_N}}{m_N}\big)^{-m_N}\big]\Big]$, which represent the characteristic functions of the LOS and NLOS interferences, respectively. In the following, we will derive the expression of $\Psi^{(1)}_L(r, jw)$, while $\Psi^{(1)}_N(r, jw)$ can be computed by following the same steps. In (6.52), Q_L and Q_N are discrete random variables which represent the number of LOS and NLOS interfering BSs, respectively, and follow a Poisson distribution. Therefore, $\Psi^{(1)}_L(r, jw)$ can be written as

$$\Psi^{(1)}_L(r, jw) = \sum_{q=0}^{\infty}\left(\mathbb{E}_{G,z_L}\left[\left(1 - \frac{jwP_tC_Lz_L^{-\alpha_L}}{m_L}\right)^{-m_L}\right]\right)^q f_{Q_L|r}(q), \tag{6.53}$$

where $f_{Q_L|r}(q)$ is the PMF of the Poisson random variable Q_L which returns the number of BSs with distances $z_L \in [r\delta^{-\frac{1}{\alpha_L}},\ R_L]$. Then $f_{Q_L|r}(q)$ can be expressed as

$$\begin{aligned} f_{Q|r}(q) &= \mathbb{P}\big[\mathcal{N}\big(\mathcal{B}\big(r\delta^{-\frac{1}{\alpha}}, R_L\big)\big) = q\big] \\ &= \frac{\big(-\int_{\mathcal{B}(r\delta^{-\frac{1}{\alpha}}, R_L)} \widetilde{\lambda}_b(x)dx\big)^q}{q!} e^{-\int_{\mathcal{B}\left(r\delta^{-\frac{1}{\alpha}}, R_L\right)} \widetilde{\lambda}_b(x)dx}, \end{aligned} \tag{6.54}$$

where $\mathcal{B}\big(r\delta^{-\frac{1}{\alpha}}, R_L\big)$ is the area of a disc with inner radius $r\delta^{-\frac{1}{\alpha}}$ and outer radius R_L and $\mathcal{N}\big(\mathcal{B}\big)$ defines the number of points located in area $\mathcal{B}$. Using the mapping theorem of PPPs [79] which maps the 2-D PPP to a 1-D PPP such that $\widetilde{\lambda}_b(x) = 2\pi\lambda_b x$, $f_{Q|r}(q)$ can be expressed as

$$f_{Q|r}(q) = e^{-2\pi\lambda_b\left(R_L^2 - r^2\delta^{\frac{-r}{\alpha_L}}\right)} \frac{\left(2\pi\lambda_b\left(R_L^2 - r^2\delta^{\frac{-3}{\alpha_L}}\right)\right)^q}{q!}. \tag{6.55}$$

Substituting (6.55) in (6.53) gives

$$\begin{aligned} \Psi_L(r, jw) &= \sum_{q=0}^{\infty} e^{-2\pi\lambda_b\left(R_L^2 - r^2\delta^{\frac{-r}{\alpha_L}}\right)} \Bigg(\mathbb{E}_{G,z_L}\Bigg[\\ &\left(1 - \frac{jwP_tGC_Lz_L^{-\alpha_L}}{m_L}\right)^{-m_L}\Bigg]\Bigg)^q \frac{\left(2\pi\lambda_b\left(R_L^2 - r^2\delta^{\frac{-2}{\alpha_L}}\right)\right)^q}{q!}, \end{aligned} \tag{6.56}$$

Since BSs are distributed according to a PPP, the distance z_L to a random point in $[r\delta^{\frac{-1}{\alpha_L}},\ R_L]$, is uniformly distributed with a PDF $f_{z_L}(t)$ given as [79]

$$f_{z_L}(t) = \frac{2t}{R_L^2 - r^2\delta^{\frac{-2}{\alpha_L}}}, \quad t \in [r\delta^{\frac{-1}{\alpha_L}},\ R_L], \tag{6.57}$$

Let $\mathcal{O}(r, jw) = \mathbb{E}_{z_L}\left[\left(1 - \frac{jwP_tGC_Lz_L^{-\alpha_L}}{m_L}\right)^{-m_L}\right]$ and using (6.57), we get

$$\begin{aligned} \mathcal{O}(r, jw) &= \frac{2}{R_L^2 - r^2\delta^{\frac{-2}{\alpha_L}}} \int_{r\delta^{\frac{-1}{\alpha_L}}}^{R_L} \left(1 - \frac{jwP_tGC_Lt^{-\alpha_L}}{m_L}\right)^{-m_L} tdt \\ &= \frac{2R_L^2 {}_2\mathrm{F}_1\left(m_L, -\frac{2}{\alpha_L}; \frac{\alpha_L - 2}{\alpha_L}; \frac{jwGC_LP_tR_L^{-\alpha_L}}{m_L}\right)}{R_L^2 - r^2\delta^{\frac{-2}{\alpha_L}}} \end{aligned}$$

$$-\frac{2r^2\delta^{\frac{-2}{\alpha_L}}{}_2\mathrm{F}_1\left(m_L,-\frac{2}{\alpha_L};\frac{\alpha_L-2}{\alpha_L};\frac{jwGC_LP_t\delta r^{-\alpha_L}}{m_L}\right)}{R_L^2-r^2\delta^{\frac{-2}{\alpha_L}}}. \tag{6.58}$$

Plugging (6.58) into (6.56) and averaging over the gain G using (6.3), $\widetilde{\Psi}_L(r,jw)$ can be written as

$$\widetilde{\Psi}_L(r,jw) \;=\; \exp\left\{\pi\lambda_b\sum_G p_G\left[R_L^2\left(1-{}_2\mathrm{F}_1\left(m_L,-\frac{2}{\alpha_L};\frac{\alpha_L-2}{\alpha_L};-\frac{jwGC_LP_tR_L^{-\alpha_L}}{m_L}\right)\right)\right.\right.$$
$$\left.\left.-r^2\delta^{\frac{-2}{\alpha_L}}\left(1-{}_2\mathrm{F}_1\left(m_L,-\frac{2}{\alpha_L};\frac{\alpha_L-2}{\alpha_L};\frac{jwGC_LP_t\delta r^{-\alpha_L}}{m_L}\right)\right)\right]\right\} \tag{6.59}$$

Similarly, $\widetilde{\Psi}_N(r,jw)$ can be written as

$$\widetilde{\Psi}_N(r,jw) \;=\; \exp\left\{\pi\lambda_b\sum_G p_G R_L^2\left(1-\right.\right.$$
$$\left.\left.{}_2\mathrm{F}_1\left(m_N,-\frac{2}{\alpha_N};\frac{\alpha_N-2}{\alpha_N};\frac{jwGC_NP_tR_L^{-\alpha_N}}{m_N}\right)\right)\right\}. \tag{6.60}$$

Plugging (6.59) and (6.60) into (6.52) gives the result in (6.15). Likewise, by following the same steps, $\Psi^{(2)}_{I_{agg}}(r,jw)$ and $\Psi^{(3)}_{I_{agg}}(r,jw)$ can be obtained as given in (6.16) and (6.17), receptively.

6.8.2 Proof of Lemma 6.3.2

For Case 1, the total amount of the aggregated signal for a given distance r to the nearest BS can be accurately written as

$$S^{(1)}_{agg}|r{=}P_tC_LG_mhr^{-\alpha_L}+\mathbb{E}_{\Phi_b^S}\left[\sum_{j\in\Phi_b^S\setminus B(0,r)}P_tC_LG_mh_jr_j^{\alpha_L}\right]. \tag{6.61}$$

Let $S^{(1)}_{agg}|r=U(r)+D(r)$, where $U(r)=P_tC_Lhr^{-\alpha_L}$ is the maximum average power received from ϕ at a distance r and $D(r)=\mathbb{E}_{\Phi_b^S}[\sum_{j\in\Phi_b^S\setminus B(0,r)}P_tC_Lh_jr_j^{\alpha_L}]$ is the aggregated power from the other BSs in the user's serving cluster. To find $D(r)$,

we first find the Laplace transform of $\widetilde{D}(r) = \sum_{j\in\Phi_b^S\setminus B(0,r)} P_t C_L h_j r_j^{\alpha_L}$, denoted by $\Xi_{\widetilde{D}(r)}(s)$ and computed as

$$\begin{aligned}
\Xi_{\widetilde{D}(r)}(s) &= \mathbb{E}_{\Phi_b^S}\left[e^{-sD(r)}\right] \\
&= \mathbb{E}_{\Phi_b^S}\left[e^{-s\sum_{j\in\Phi_b^S\setminus B(0,r)} P_t G_m C_L h_j r_j^{\alpha_L}}\right] \\
&\overset{(a)}{=} \exp\left(-2\pi\lambda_b \int_r^{r\delta^{\frac{-1}{\alpha_L}}} \left(1-e^{-sC_L G_m h t^{-\alpha_L}}\right) t dt\right) \\
&= \exp\left\{-2\pi\lambda_b\left(\frac{r^2\left(\delta^{\frac{-2}{\alpha_L}}-1\right)}{2} + \frac{2}{\alpha_L}\left(r^2\delta^{\frac{-2}{\alpha_L}} E_{\frac{2+\alpha_L}{\alpha_L}}\left(sP_tC_LG_mhr^{-\alpha_L}\delta\right)\right.\right.\right. \\
&\quad \left.\left.\left. -r^2 E_{\frac{2+\alpha_L}{\alpha_L}}\left(sP_tC_LG_mhr^{-\alpha_L}\right)\right)\right)\right\}, \qquad (6.62)
\end{aligned}$$

where (a) results from applying the Campbell's theorem and the mapping theorem of PPPs [79] and $E_v(z) = \int_1^\infty \frac{e^{-zt}}{t^v} dt$ is the generalized exponential integral function [62]. Then $D(r)$ can be obtained such that $D(r) = -\frac{d\Xi_{\widetilde{D}(r)}(s)}{ds}\big|_{s=0}$ which can be written as,

$$D(r) = \frac{2\pi\lambda_b p_t C_L G_m h r^{-\alpha_L+2}\left(\delta^{-\frac{2-\alpha_L}{\alpha_L}}-1\right)}{\alpha-2}. \qquad (6.63)$$

Using this into (6.62) and recalling that h follows a gamma distribution, the PDF of $S_{agg}^{(1)}|r$ is expressed as in (6.18). Following the same steps, the PDFs of $S_{agg}^{(2)}|r$ and $S_{agg}^{(3)}|r$ can be obtained as well.

6.8.3 Proof of Lemma 6.4.1

In ultra dense deployments where the LOS interfering signals are dominant, the aggregated interference is given by $I_{agg} = \sum_{i\in\Phi_b^L\setminus\Phi_b^S} P_t C_L G_i h_i r_i^{-\alpha_L}$ and its characteristic function is expressed as

$$\Psi(r, jw) = \mathbb{E}_{\Phi_b^S}\left[e^{jw\sum_{i\in\Phi_b^L\setminus\Phi_b^S} P_t C_L G_i h_i r_i^{-\alpha_L}}\right]$$

$$= \exp\left(2\pi\lambda_b \int_{r\delta^{\frac{-1}{\alpha_L}}}^{R_L} \left(1 - e^{jwC_L G h t^{-\alpha_L}}\right) t dt\right)$$

$$\overset{(a)}{\approx} \exp\left(2\pi\lambda_b \int_{r\delta^{\frac{-1}{\alpha_L}}}^{R_L} jwC_L G h t^{-\alpha_L+1} dt\right) \tag{6.64}$$

where (a) results from using $1 - e^{-x} \approx x$ for small x. This indeed holds for small δ, i.e, large serving cluster size. Conducting the integral in (6.64) and averaging over the gain G and small-scale fading h complete the proof of the results in Lemma 6.4.1.

Chapter 7

Conclusions and Future Research Directions

In this chapter, we conclude the thesis and point out a number of potential future research directions

7.1 Conclusions

In this thesis, we first proposed a novel user-centric BS clustering scheme for mmWave networks in which a user selects a set of serving BSs dynamically based on its channel condition and network configurations. In the proposed BS clustering model, the size of the serving cluster is controlled using a single clustering parameter, leading to a low computational complexity since only a single parameter needs to be optimized and broadcasted to all users. Unlike existing clustering schemes in literature, where the serving cluster has either a fixed radius or a fixed number of serving BSs, the proposed clustering model allows a dynamic selection of BSs. This implies that different users can form their own serving clusters with different sizes. With the aid of stochastic geometry, we investigate the coverage probability and average spectral efficiency using the proposed dynamic clustering model under the BS-load and resources limitation considerations. The performance of the new clustering model is studied under two different BS cooperation schemes namely dynamic JT and dy-

namic OPS and compared with that of the static clustering and single-BS selection schemes. We also developed an optimization framework for computing the clustering parameter to maximize the system performance in terms of average spectral efficiency. In this chapter, we showed analytically and by simulations that the proposed clustering technique considerably outperforms the existing static clustering schemes in terms of the coverage probability and spectral efficiency.

Aiming to reduce the interference in THz networks and enhance user's coverage performance, we adopted the user-centric BS clustering for THz networks. In particular, we presented both dynamic and static clustering schemes to form user's serving BS cluster. Although both schemes have been investigated for mmWave and sub-6 GHz networks, the performance of user-centric THz networks was unexplored before this work. It is worthy to mention that the analytical approaches proposed in literature for user-centric mmWave/sub-6 GHz networks are not applicable to user-centric networks operating in THz bands. This is because the THz propagation model is different due to the fact that the transmitted signal power in THz band suffers from a severe attenuation caused by the molecular absorption. Using stochastic geometry, we characterized the distribution of the aggregated interference in dense THz networks by leveraging the CLT. Then, we proposed an analytically tractable framework to study the coverage probability of user-centric THz networks under both static and dynamic clustering. Numerical computation and Monte Carlo simulation with different network and channel configurations and clustering parameters have been carried out to validate the provided theoretical finding and demonstrated the superiority of the proposed dynamic as well as static clustering schemes to the single BS association in the THz networks.

Providing solutions to increase the application range of UAV communication systems has been one of the main objectives of researchers from both academia and industry. As such, we have been motivated to consider a UAV-to-UAV communication system in this thesis. In this regard, we extended the proposed 2D clustering model to a 3D clustering model to design an energy efficient user-centric air-to-air network where an AUE is cooperatively served by a cluster of carefully selected

ABSs according to its operation conditions. Then, we derived analytical expressions for the spectral efficiency and energy efficiency under the proposed clustering model. Considering that the high energy consumption of UAVs for flying/hovering is one of the main drawbacks of UAV systems, we developed an efficient and tractable optimization framework for the clustering parameter to provide maximum energy efficiency in dense large-scale spatial UAVs networks.

The THz waves with enormous bandwidth can be used along with the existing sub-6 GHz and millimeter wave (mmWave) bands to achieve the ever evolving ecosystem of applications that need to be supported by the modern wireless networks. As such, we investigated in this thesis a user-centric dynamic BS clustering design for a hybrid network where THz, mmWave, and sub6-GHz BSs coexist. Invoking the proposed clustering model, the BS cooperation within each band is made possible by considering long term channel variations and all the surrounding BSs within a cluster with tunable size. A typical user is associated with the best BS cluster, from either a sub6-GHz, mmWave or THz tier based on the maximum SINR criterion or the maximum rate criterion. Using tools from stochastic geometry, we assessed the performance of the proposed user-centric hybrid system in terms of SINR and rate coverage performances, while accounting for: band specific propagation models, directional beamfroming, and BSs random locations. The obtained results recognize a clear coverage/rate trade-off where a high fraction of THz BSs improves the rate significantly but may degrade the coverage performance. Thus, with carefully planned networks, enabling user-centric BS cooperation for hybrid wireless systems can achieve ultra-high rates while maintaining sufficient coverage in sixth-generation (6G) networks.

In this thesis, we also considered a user-centric SWIPT-enabled mmWave system, where a time switching protocol is employed at users to support both energy harvesting and information decoding. To enable user-centric BS cooperation, adaptive BS clustering is used to adapt the user's serving cluster to the channel condition. Both linear and non-linear energy harvesting models are considered. For this setup, we characterized the joint coverage, namely, the probability that the user can harvest

sufficient energy in a given time slot and receive the required minimum data from a given serving cluster. The analysis is challenging because of the random serving clusters as well as the correlation between the amount of harvested energy and the information rate. A tractable tight approximation of the joint coverage probability was also derived for ultra-dense networks. Then, a mathematical optimization model for the time switching coefficient was developed to maximize the system joint rate and energy coverage performance. All analytical results are corroborated by simulations which showed that the proposed analytical models are accurate and efficient in the design and deployment of user-centric-SWIPT mmWave systems.

7.2 Future Research Directions

Although we addressed several research issues related to enabling the user-centric technique for future wireless systems, there are still many open questions that need to be addressed. In particular, some of these questions which could be investigated in the immediate future work are as follows.

- **RIS-assisted user-centric network:** reconfigurable intelligent surfaces (RISs) has been considered as a promising technology to enhance the coverage of beyond 5G and 6G future wireless networks. Specifically, as a passive element, RIS is a low-cost and low-complexity technology capable of producing strong beams in any desired direction by intelligently adjusting the scattering properties of its reflecting elements. Future networks are supposed to move to higher frequency bands (such as mmWave and THz bands) to provides a communication with higher bandwidth and hence higher data rate. Due to the fact that communication links in such higher frequency bands are suffering from a high path losses, the NLOS users may be blocked. One potential use of RIS technology is providing indirect LOS links between users and base BSs when the direct link is blocked. As such, to compose highly efficient communication networks, the integration of mmWave/THz communications and RISs is a promising solution. Recently, this technology has gained some attention [151],

[152]. However, none of these works has considered the combined configuration where RIS-assisted mmWave/THz systems are used together with other emerging beyond 5G technologies such as user-centric networking in particular.

- **Resource allocation:** considering that the users are randomly distributed and the selection of serving BSs for a user depends on the user's channel condition, the serving clusters of different users may overlap, i.e. a BS may join two or more clusters. It should be pointed out that this overlap will create inter-cluster interference even though it is advantageous in removing the cell-edge effect in user-centric networks. In this work, we considered a straightforward resource allocation scheme in which the overlapped clusters are assigned to different orthogonal resources and thus the maximum number of clusters a BS can join depends on the available orthogonal resources. To this end, efficient resource allocation is needed to mediate the computational complexity and network performances.

- **Channel state information:** in this thesis, we assumed that the user has perfect knowledge of the downlink channel of all BSs in its serving cluster. In this case, the pilot sequence required in the downlink will be related to the number of serving BSs, and this is a problem in highly-dense deployments where the number of serving BSs is very large. A novel and efficient ideas that can solve or mitigate the impact of this problem are in strong demand.

- **SWIPT-enabled 3D User-centric network:** in Chapter 6, we have investigated the performance of SWIPT-enabled mmWave user-centric networks under dynamic BS clustering and developed an optimization framework of the time-splitting coefficient in order to maximize the system joint rate and energy coverage performance. It is shown that in addition to improving the downlink data rate, user-centric BS cooperation in mmWave networks can further enhance the wireless power transfer due to the fact that the mmWave transmitters/receivers are equipped with highly directive antennas, and thus the amount of energy that can be harvested from a useful signal is larger than

that harvested from the interfering signal. This idea can be extended by integrating both aerial and terrestrial networks to provide massive (a large number of users) connectivity. In this case, a new 3D dynamic BS clustering model is needed where the user serving cluster can contain both UAV and ground BSs. This is expected to improve both rate and energy coverage for all users in the network.

Publications

Throughout the course of this thesis research, the following peer-reviewed journal and conference papers have been published/submitted:

1. Khaled Humadi, I. Trigui, Wei-Ping Zhu, and W. Ajib, "THz user-centric cluster design in the presence of beam alignment error," *IEEE Transactions on Communications* (to be submitted).

2. Khaled Humadi, I. Trigui, Wei-Ping Zhu, and W. Ajib, "Simultaneous wireless information and power transfer in mmWave networks under user-centric base station clustering," *IEEE Transactions on Wireless Communications* (under 2nd round of review).

3. Khaled Humadi, I. Trigui, Wei-Ping Zhu, and W. Ajib, "User-centric cluster design and analysis for hybrid sub-6GHz-mmWave-THz dense networks," *IEEE Transactions on Vehicular Technology* (published online), April 2022.

4. Khaled Humadi, I. Trigui, Wei-Ping Zhu, and W. Ajib, "Coverage analysis of user-centric terahertz networks," *IEEE Communication Letters*, vol. 25, no. 9, pp. 2864– 2868, Sept. 2021.

5. Khaled Humadi, I. Trigui, Wei-Ping Zhu, and W. Ajib, "Dynamic base station clustering in user-centric millimeter wave networks: Performance analysis and optimization," *IEEE Transactions on Communications*, vol. 69, no. 7, pp. 4847–4861, Apr. 2021.

6. Khaled Humadi, I. Trigui, Wei-Ping Zhu, and W. Ajib,"Energy-efficient cluster sizing for user-centric air-to-air networks," *IEEE Communications Letters*, vol.

25, no. 4, pp. 1308—1312 , Dec. 2020.

7. Khaled Humadi, I. Trigui, Wei-Ping Zhu, and W. Ajib, "Joint rate and energy coverage performance of user-centric mmWave networks with simultaneous wireless information and power transfer," in Proc. *IEEE International Conference on Communications (IEEE ICC 2022)*, Seoul, South Korea, 16-20 May 2022 (accepted).

8. Khaled Humadi, I. Trigui, Wei-Ping Zhu, and W. Ajib, "hybrid mmWave-THz networks with user-centric clustering," in Proc. *IEEE Global Communications Conference (IEEE GLOBECOM 2021)*, Madrid, Spain, 7-11 December 2021.

9. Khaled Humadi, I. Trigui, Wei-Ping Zhu, and W. Ajib, "Coverage analysis of user-centric millimeter wave networks under dynamic base station clustering,"in Proc. *IEEE International Conference on Communications (IEEE ICC 2021)*, Montreal, QC, Canada, 14-23 June 2021.

10. Khaled Humadi, Wei-Ping Zhu, and W. Ajib, "Performance analysis of adaptive modulation for millimeter wave cellular systems," in Proc. *2020 IEEE 91st Vehicular Technology Conference (VTC2020-Spring)*, 2020, pp. 1-5.

References

[1] H. Tataria, M. Shafi, A. F. Molisch, *et al.*, "6G wireless systems: Vision, requirements, challenges, insights, and opportunities," *Proceedings of the IEEE*, vol. 109, no. 7, pp. 1166–1199, 2021.

[2] I. Union, "Imt traffic estimates for the years 2020 to 2030," *Report ITU*, vol. 2370, 2015.

[3] M. Alsabah, M. A. Naser, B. M. Mahmmod, *et al.*, "6g wireless communications networks: A comprehensive survey," *IEEE Access*, vol. 9, pp. 148 191–148 243, Nov. 2021.

[4] A. Al-Fuqaha, M. Guizani, M. Mohammadi, M. Aledhari, and M. Ayyash, "Internet of things: A survey on enabling technologies, protocols, and applications," *IEEE commun. surveys tuts.*, vol. 17, no. 4, pp. 2347–2376, Jun. 2015.

[5] K.-H. Chang, "Bluetooth: A viable solution for iot?[industry perspectives]," *IEEE Wireless Commun.*, vol. 21, no. 6, pp. 6–7, Dec. 2014.

[6] S. R. Pokhrel and C. Williamson, "Modeling compound tcp over wifi for iot," *IEEE/ACM trans. netw.*, vol. 26, no. 2, pp. 864–878, Mar. 2018.

[7] X. Chen, D. W. K. Ng, W. Yu, *et al.*, "Massive access for 5g and beyond," *IEEE J. Sel. Areas Commun.*, vol. 39, no. 3, pp. 615–637, 2020.

[8] H. Q. Ngo, E. G. Larsson, and T. L. Marzetta, "Energy and spectral efficiency of very large multiuser mimo systems," *IEEE Trans. Commun.*, vol. 61, no. 4, pp. 1436–1449, Feb. 2013.

[9] Y. Han, B. D. Rao, and J. Lee, "Massive uncoordinated access with massive mimo: A dictionary learning approach," *IEEE Trans. Wireless Commun.*, vol. 19, no. 2, pp. 1320–1332, Nov. 2019.

[10] M. Shirvanimoghaddam, M. Condoluci, M. Dohler, and S. J. Johnson, "On the fundamental limits of random non-orthogonal multiple access in cellular massive iot," *IEEE J. Sel. Areas Commun.*, vol. 35, no. 10, pp. 2238–2252, Jul. 2017.

[11] S. R. Islam, N. Avazov, O. A. Dobre, and K.-S. Kwak, "Power-domain non-orthogonal multiple access (noma) in 5g systems: Potentials and challenges," *IEEE Commun. Surveys Tuts.*, vol. 19, no. 2, pp. 721–742, Oct. 2016.

[12] M. Shafi, A. F. Molisch, P. J. Smith, *et al.*, "5g: A tutorial overview of standards, trials, challenges, deployment, and practice," *IEEE j. sel. areas commun.*, vol. 35, no. 6, pp. 1201–1221, Apr. 2017.

[13] S. Verma, S. Kaur, M. A. Khan, and P. S. Sehdev, "Toward green communication in 6g-enabled massive internet of things," *IEEE Internet Things J.*, vol. 8, no. 7, pp. 5408–5415, Nov. 2020.

[14] T. D. P. Perera, D. N. K. Jayakody, S. K. Sharma, S. Chatzinotas, and J. Li, "Simultaneous wireless information and power transfer (swipt): Recent advances and future challenges," *IEEE Commun. Surveys Tuts.*, vol. 20, no. 1, pp. 264–302, Jan. 2018.

[15] I. Krikidis, S. Timotheou, S. Nikolaou, *et al.*, "Simultaneous wireless information and power transfer in modern communication systems," *IEEE Commun. Mag.*, vol. 52, no. 11, pp. 104–110, Nov. 2014.

[16] W. Lu, P. Si, G. Huang, *et al.*, "Swipt cooperative spectrum sharing for 6g-enabled cognitive iot network," *IEEE Internet Things J.*, vol. 8, no. 20, pp. 15 070–15 080, Sep. 2020.

[17] A. El Shafie, N. Al-Dhahir, and R. Hamila, "Cooperative access schemes for efficient swipt transmissions in cognitive radio networks," in *2015 IEEE Globecom Workshops (GC Wkshps)*, IEEE, Dec. 2015, pp. 1–6.

[18] M. S. J. Solaija, H. Salman, A. B. Kihero, M. İ. Sağlam, and H. Arslan, "Generalized coordinated multipoint framework for 5g and beyond," *IEEE Access*, vol. 9, pp. 72 499–72 515, May 2021.

[19] Ö. Tuğfe Demir, E. Björnson, and L. Sanguinetti, "Foundations of user-centric cell-free massive mimo," *arXiv e-prints*, arXiv–2108, 2021.

[20] H. Q. Ngo, A. Ashikhmin, H. Yang, E. G. Larsson, and T. L. Marzetta, "Cell-free massive MIMO versus small cells," *IEEE Trans. Wireless Commun.*, vol. 16, no. 3, pp. 1834–1850, Jan. 2017.

[21] E. Björnson and L. Sanguinetti, "Making cell-free massive mimo competitive with mmse processing and centralized implementation," *IEEE Trans. Wireless Commun.*, vol. 19, no. 1, pp. 77–90, Sep. 2019.

[22] E. Nayebi, A. Ashikhmin, T. L. Marzetta, H. Yang, and B. D. Rao, "Precoding and power optimization in cell-free massive mimo systems," *IEEE Trans. Wireless Commun.*, vol. 16, no. 7, pp. 4445–4459, May 2017.

[23] P. Liu, K. Luo, D. Chen, and T. Jiang, "Spectral efficiency analysis of cell-free massive MIMO systems with zero-forcing detector," *IEEE Trans. Wireless Commun.*, vol. 19, no. 2, pp. 795–807, Oct. 2019.

[24] A. Papazafeiropoulos, P. Kourtessis, M. Di Renzo, S. Chatzinotas, and J. M. Senior, "Performance analysis of cell-free massive MIMO systems: A stochastic geometry approach," *IEEE Trans. Veh. Technol.*, vol. 69, no. 4, pp. 3523–3537, Jan. 2020.

[25] S. Buzzi and C. D'Andrea, "Cell-free massive mimo: User-centric approach," *IEEE Wireless Commun. Lett.*, vol. 6, no. 6, pp. 706–709, Aug. 2017.

[26] S. Buzzi, C. D'Andrea, A. Zappone, and C. D'Elia, "User-centric 5g cellular networks: Resource allocation and comparison with the cell-free massive mimo approach," *EEE Trans. Wireless Commun.*, Nov. 2019.

[27] H. A. Ammar, R. Adve, S. Shahbazpanahi, G. Boudreau, and K. V. Srinivas, "User-centric cell-free massive mimo networks: A survey of opportunities, challenges and solutions," *IEEE Communications Surveys & Tutorials*, Dec. 2021.

[28] J. Zhang, S. Chen, Y. Lin, *et al.*, "Cell-free massive mimo: A new next-generation paradigm," *IEEE Access*, vol. 7, pp. 99 878–99 888, Jul. 2019.

[29] A. Papazafeiropoulos, H. Q. Ngo, P. Kourtessis, S. Chatzinotas, and J. M. Senior, "Towards optimal energy efficiency in cell-free massive mimo systems," *IEEE Transactions on Green Communications and Networking*, vol. 5, no. 2, pp. 816–831, Feb. 2021.

[30] L. Wang and Q. Liang, "Optimization for user centric massive mimo cell free networks via large system analysis," in *2016 IEEE Global Communications Conference (GLOBECOM)*, IEEE, 2016, pp. 1–1.

[31] M. Kamel, W. Hamouda, and A. Youssef, "Ultra-dense networks: A survey," *IEEE Commun. Surveys Tuts.*, vol. 18, no. 4, pp. 2522–2545, May 2016.

[32] H. Yang and T. L. Marzetta, "Energy efficiency of massive mimo: Cell-free vs. cellular," in *2018 IEEE 87th Vehicular Technology Conference (VTC Spring)*, IEEE, 2018, pp. 1–5.

[33] U. S. Hashmi, "Novel user-centric architectures for future generation cellular networks: Design, analysis and performance optimization," 2019.

[34] T. A. Khan, A. Alkhateeb, and R. W. Heath, "Millimeter wave energy harvesting," *IEEE Transactions on Wireless Communications*, vol. 15, no. 9, pp. 6048–6062, 2016.

[35] H. ElSawy, E. Hossain, and M. Haenggi, "Stochastic geometry for modeling, analysis, and design of multi-tier and cognitive cellular wireless networks: A survey," *IEEE Commun. Surveys Tuts.*, vol. 15, no. 3, pp. 996–1019, Jun. 2013.

[36] T. S. Rappaport, S. Sun, R. Mayzus, *et al.*, "Millimeter wave mobile communications for 5G cellular: It will work!" *IEEE access*, vol. 1, pp. 335–349, May. 2013.

[37] J. G. Andrews, T. Bai, M. N. Kulkarni, *et al.*, "Modeling and analyzing millimeter wave cellular systems," *IEEE Trans. Commun.*, vol. 65, no. 1, pp. 403–430, Jan. 2017.

[38] G. Yu, R. Liu, Q. Chen, and Z. Tang, "A hierarchical SDN architecture for ultra-dense millimeter-wave cellular networks," *IEEE Commun. Mag.*, vol. 56, no. 6, pp. 79–85, Jan. 2018.

[39] 3GPP TR 36.819, "Coordinated multi-point operation for LTE physical layer aspects," 3rd Generation Partnership Project, Tech. Rep. V11.2.0, Sep. 2013 [Online]. Available: http://www.3gpp.org/dynareport/36819.h.

[40] G. Nigam, P. Minero, and M. Haenggi, "Coordinated multipoint joint transmission in heterogeneous networks," *IEEE Trans. Commun.*, vol. 62, no. 11, pp. 4134–4146, Oct. 2014.

[41] R. Tanbourgi, S. Singh, J. G. Andrews, and F. K. Jondral, "A tractable model for noncoherent joint-transmission base station cooperation," *IEEE Trans. Wireless Commun.*, vol. 13, no. 9, pp. 4959–4973, Jul. 2014.

[42] Y. Li, M. Xia, and S. Aıssa, "Coordinated multi-point transmission: A poisson-delaunay triangulation based approach," *IEEE Trans. Wireless Commun.*, vol. 19, no. 5, pp. 2946–2959, Jan. 2020.

[43] N. Lee, D. Morales-Jimenez, A. Lozano, and R. W. Heath, "Spectral efficiency of dynamic coordinated beamforming: A stochastic geometry approach," *IEEE Trans. Wireless Commun.*, vol. 14, no. 1, pp. 230–241, Jul. 2014.

[44] G. Chen, L. Qiu, and Y. Li, "Stochastic geometry analysis of coordinated beamforming small cell networks with CSI delay," *IEEE Commun. Lett.*, vol. 22, no. 5, pp. 1066–1069, Mar. 2018.

[45] V. Garcia, Y. Zhou, and J. Shi, "Coordinated multipoint transmission in dense cellular networks with user-centric adaptive clustering," *IEEE Trans. Wireless Commun.*, vol. 13, no. 8, pp. 4297–4308, Apr. 2014.

[46] C. Li, J. Zhang, M. Haenggi, and K. B. Letaief, "User-centric intercell interference nulling for downlink small cell networks," *IEEE Trans. Commun.*, vol. 63, no. 4, pp. 1419–1431, Feb. 2015.

[47] S. Bassoy, H. Farooq, M. A. Imran, and A. Imran, "Coordinated multi-point clustering schemes: A survey," *IEEE Commun. Surveys Tuts.*, vol. 19, no. 2, pp. 743–764, Feb. 2017.

[48] Y. Zhang and Y. J. Zhang, "User-centric virtual cell design for cloud radio access networks," in *IEEE Int. Workshop on Signal Process. Adv. in Wireless Commun.*, Jun. 2014, pp. 249–253.

[49] W. Nie, F.-C. Zheng, X. Wang, W. Zhang, and S. Jin, "User-centric cross-tier base station clustering and cooperation in heterogeneous networks: Rate improvement and energy saving," *IEEE J. Sel. Areas Commun.*, vol. 34, no. 5, pp. 1192–1206, Apr. 2016.

[50] H. Zhang, Z. Yang, Y. Liu, and X. Zhang, "Power control for 5G user-centric network: Performance analysis and design insight," *IEEE Access*, vol. 4, pp. 7347–7355, Oct. 2016.

[51] W. Bao and B. Liang, "Optimizing cluster size through handoff analysis in user-centric cooperative wireless networks," *IEEE Trans. Wireless Commun.*, vol. 17, no. 2, pp. 766–778, Nov. 2017.

[52] U. S. Hashmi, S. A. R. Zaidi, and A. Imran, "User-centric cloud ran: An analytical framework for optimizing area spectral and energy efficiency," *IEEE Access*, vol. 6, pp. 19 859–19 875, Apr. 2018.

[53] D. Maamari, N. Devroye, and D. Tuninetti, "Coverage in mmwave cellular networks with base station co-operation," *IEEE trans. Wireless Commun.*, vol. 15, no. 4, pp. 2981–2994, Jan. 2016.

[54] C. Skouroumounis, C. Psomas, and I. Krikidis, "Low-complexity base station selection scheme in mmwave cellular networks," *IEEE Trans. Commun.*, vol. 65, no. 9, pp. 4049–4064, Jun. 2017.

[55] J. Shi, C. Pan, W. Zhang, and M. Chen, "Performance analysis for user-centric dense networks with mmwave," *IEEE Access*, vol. 7, pp. 14 537–14 548, Jan. 2019.

[56] L. Yang, J. Zhao, and Y. Gong, "Modeling and analysis of user-centric collaborative millimeter-wave cellular networks," in *2019 IEEE Int. Conf. Commun. Workshops (ICC Workshops)*, May 2019, pp. 1–6.

[57] H.-M. Wang, K.-W. Huang, and T. A. Tsiftsis, "Base station cooperation in millimeter wave cellular networks: Performance enhancement of cell-edge users," *IEEE Trans. Commun.*, vol. 66, no. 11, pp. 5124–5139, Jun. 2018.

[58] S. Zaidi, O. B. Smida, S. Affes, *et al.*, "User-centric base-station wireless access virtualization for future 5G networks," *IEEE Trans. Commun.*, vol. 67, no. 7, pp. 5190–5202, Apr. 2019.

[59] A. Maaref, J. Ma, M. Salem, H. Baligh, and K. Zarin, "Device-centric radio access virtualization for 5G networks," in *Proc. IEEE GLOBECOM'2014*, Austin, TX, USA, Dec. 2014, pp. 887–893.

[60] Z. Zhang, N. Wang, J. Zhang, and X. Mu, "Dynamic user-centric clustering for uplink cooperation in multi-cell wireless networks," *IEEE Access*, vol. 6, pp. 8526–8538, Jan. 2018.

[61] Q. Liu, S. Sun, and H. Gao, "Joint user-centric clustering and frequency allocation in ultra-dense C-RAN," in *IEEE (WCNC)*, IEEE, May 2020, pp. 1–6.

[62] I. S. Gradshteyn and I. M. Ryzhik, *Table of integrals, series, and products.* 5th ed. New York, NY, USA: Academic, 1994.

[63] F. Baccelli and B. Blaszczyszyn, *Stochastic Geometry and Wireless Networks, Volume I—Theory.* Delft, The Netherlands: Now Publishers, 2009.

[64] A. I. Sulyman, H. Seleem, A. Alwarafy, K. M. Humadi, and A. Alsanie, "Effects of solar radio emissions on outdoor propagation path loss models at 60 GHz bands for access/backhaul links and D2D communications," *IEEE Trans. Antennas Propag.*, vol. 65, no. 12, pp. 6624–6635, Oct. 2017.

[65] I. Trigui, P. D. Diamantoulakis, S. Affes, and G. K. Karagiannidis, "Shadowed FSO/mmwave systems with interference," *IEEE Trans. Commun.*, vol. 67, no. 9, pp. 6256–6267, Jan. 2019.

[66] T. Bai and R. W. Heath, "Coverage and rate analysis for millimeter-wave cellular networks," *IEEE Trans. Wireless Commun.*, vol. 14, no. 2, pp. 1100–1114, Jan. 2015.

[67] X. Wu, C.-X. Wang, J. Sun, *et al.*, "60-GHz millimeter-wave channel measurements and modeling for indoor office environments," *" IEEE Trans. Antennas Propag.*, vol. 65, no. 4, pp. 1912–1924, Feb. 2017.

[68] M. Di Renzo, "Stochastic geometry modeling and analysis of multi-tier millimeter wave cellular networks," *IEEE Trans. Wireless Commun.*, vol. 14, no. 9, pp. 5038–5057, May. 2015.

[69] S. Kusaladharma, W.-P. Zhu, and W. Ajib, "Stochastic geometry-based modeling and analysis of massive MIMO-enabled millimeter wave cellular networks," *IEEE Trans. Commun.*, vol. 67, no. 1, pp. 288–301, Sep. 2018.

[70] E. Turgut and M. C. Gursoy, "Uplink performance analysis in D2D-enabled millimeter-wave cellular networks with clustered users," *IEEE Trans. Wireless Commun.*, vol. 18, no. 2, pp. 1085–1100, Jan. 2019.

[71] G. R. MacCartney, J. Zhang, S. Nie, and T. S. Rappaport, "Path loss models for 5G millimeter wave propagation channels in urban microcells," in *IEEE GLOBECOM*, Dec. 2013, pp. 3948–3953.

[72] S. Singh, M. N. Kulkarni, A. Ghosh, and J. G. Andrews, "Tractable model for rate in self-backhauled millimeter wave cellular networks," *IEEE J. Sel. Areas Commun.*, vol. 33, no. 10, pp. 2196–2211, Oct., 2015.

[73] Y. Lin, R. Zhang, C. Li, L. Yang, and L. Hanzo, "Graph-based joint user-centric overlapped clustering and resource allocation in ultradense networks," *IEEE Trans. Veh. Technol.*, vol. 67, no. 5, pp. 4440–4453, Dec. 2017.

[74] R. Tanbourgi, S. Singh, J. G. Andrews, and F. K. Jondral, "Analysis of non-coherent joint-transmission cooperation in heterogeneous cellular networks," in *IEEE International Conference on Communications (ICC)*, IEEE, Jun. 2014, pp. 5160–5165.

[75] K. A. Hamdi, "A useful lemma for capacity analysis of fading interference channels," *IEEE Trans. Commun.*, vol. 58, no. 2, pp. 411–416, Feb. 2010.

[76] S. N. Chiu, D. Stoyan, W. S. Kendall, and J. Mecke, *Stochastic geometry and its applications*. John Wiley & Sons, 2013.

[77] T. Bai, R. Vaze, and R. W. Heath, "Analysis of blockage effects on urban cellular networks," *IEEE Trans. Wireless Commun.*, vol. 13, no. 9, pp. 5070–5083, Jun. 2014.

[78] 3GPP, "Study on channel model for frequencies from 0.5 to 100 GHz(version 14.3.0 release 14)," 2018, URL: https://www.etsi.org/deliver/etsi_tr/138900_138999/138901 14.03.00_60/tr_138901v140300p.pdf.

[79] J. F. Kingman, *Poisson Processes*. Oxford University Press, 1993.

[80] C. Tellambura, A. Annamalai, and V. K. Bhargava, "Closed form and infinite series solutions for the MGF of a dual-diversity selection combiner output in bivariate nakagami fading," *IEEE Trans. Commun.*, vol. 51, no. 4, pp. 539–542, May 2003.

[81] I. Trigui and S. Affes, "Unified analysis and optimization of D2D communications in cellular networks over fading channels," *IEEE Trans. Commun.*, vol. 67, no. 1, pp. 724–736, Jul. 2018.

[82] F. Baccelli, B. Blaszczyszyn, and P. Muhlethaler, "Stochastic analysis of spatial and opportunistic aloha," *IEEE J. Sel. Areas Commun.*, vol. 27, no. 7, pp. 1105–1119, Sep. 2009.

[83] H. Elayan, O. Amin, R. M. Shubair, and M.-S. Alouini, "Terahertz communication: The opportunities of wireless technology beyond 5G," in *Proc. IEEE Int. Conf. Adv. Commun. Technol. Netw.*, Apr. 2018, pp. 1–5.

[84] H. Elayan, O. Amin, B. Shihada, R. M. Shubair, and M.-S. Alouini, "Terahertz band: The last piece of RF spectrum puzzle for communication systems," *IEEE Open J. Commun. Soc.*, vol. 1, pp. 1–32, Nov. 2019.

[85] J. Kokkoniemi, J. Lehtomäki, and M. Juntti, "Stochastic geometry analysis for mean interference power and outage probability in THz networks," *IEEE Trans. Wireless Commun.*, vol. 16, no. 5, pp. 3017–3028, Mar. 2017.

[86] Z. Hossain, C. N. Mollica, J. F. Federici, and J. M. Jornet, "Stochastic interference modeling and experimental validation for pulse-based terahertz communication," *IEEE Trans. Wireless Commun.*, vol. 18, no. 8, pp. 4103–4115, Jun. 2019.

[87] J. Sayehvand and H. Tabassum, "Interference and coverage analysis in coexisting RF and dense terahertz wireless networks," *IEEE Wireless Commun. Lett.*, vol. 9, no. 10, pp. 1738–1742, Oct. 2020.

[88] Y. Wu, J. Kokkoniemi, C. Han, and M. Juntti, "Interference and coverage analysis for terahertz networks with indoor blockage effects and line-of-sight access point association," *IEEE Trans. Wireless Commun.*, Mar. 2021.

[89] K. Humadi, I. Trigui, W.-P. Zhu, and W. Ajib, "Energy-efficient cluster sizing for user-centric air-to-air networks," *IEEE Commun. Lett.*, vol. 25, no. 4, pp. 1308–1312, Dec. 2020.

[90] S. Mumtaz, J. M. Jornet, J. Aulin, *et al.*, "Terahertz communication for vehicular networks," *IEEE Trans Veh. Technol.*, vol. 66, no. 7, Jul. 2017.

[91] M. Di Renzo and P. Guan, "Stochastic geometry modeling of coverage and rate of cellular networks using the gil-pelaez inversion theorem," *IEEE Commun. Lett.*, vol. 18, no. 9, pp. 1575–1578, Jul. 2014.

[92] H. ElSawy, A. Sultan-Salem, M.-S. Alouini, and M. Z. Win, "Modeling and analysis of cellular networks using stochastic geometry: A tutorial," *IEEE Commun. Surveys Tuts.*, vol. 19, no. 1, pp. 167–203, Nov. 2016.

[93] M. Aljuaid and H. Yanikomeroglu, "Investigating the gaussian convergence of the distribution of the aggregate interference power in large wireless networks," *IEEE Trans. Veh. Technol.*, vol. 59, no. 9, pp. 4418–4424, Nov. 2010.

[94] D. M. Slocum, E. J. Slingerland, R. H. Giles, and T. M. Goyette, "Atmospheric absorption of terahertz radiation and water vapor continuum effects," *J. Quant. Spectrosc. Radiat. Transf.*, vol. 127, pp. 49–63, Sep. 2013.

[95] M. Mozaffari *et al.*, "A tutorial on uavs for wireless networks: Applications, challenges, and open problems," *IEEE Commun. Surveys Tuts.*, vol. 21, no. 3, pp. 2334–2360, Mar. 2019.

[96] Y. Zeng and R. Zhang, "Energy-efficient uav communication with trajectory optimization," *IEEE Trans. Wireless Commun.*, vol. 16, no. 6, pp. 3747–3760, Mar. 2017.

[97] S. Yang, Y. Deng, X. Tang, Y. Ding, and J. Zhou, "Energy efficiency optimization for uav-assisted backscatter communications," *IEEE Commun. Lett.*, vol. 23, no. 11, pp. 2041–2045, Jul. 2019.

[98] S. Ahmed, M. Z. Chowdhury, and Y. M. Jang, "Energy-efficient uav relaying communications to serve ground nodes," *IEEE Commun. Lett.*, vol. 24, no. 4, pp. 849–852, Jan. 2020.

[99] S. T. Muntaha, S. A. Hassan, H. Jung, and M. S. Hossain, "Energy efficiency and hover time optimization in uav-based hetnets," *IEEE Trans. Intell. Transp. Syst.*, Aug. 2020.

[100] S. Ahmed, M. Z. Chowdhury, and Y. M. Jang, "Energy-efficient uav-to-user scheduling to maximize throughput in wireless networks," *IEEE Access*, vol. 8, pp. 21 215–21 225, Jan. 2020.

[101] M. M. Azari, G. Geraci, A. Garcia-Rodriguez, and S. Pollin, "Uav-to-uav communications in cellular networks," *IEEE Trans. Wireless Commun.*, vol. 19, no. 9, pp. 6130–6144, Sep. 2020.

[102] L. Liu, S. Zhang, and R. Zhang, "Multi-beam uav communication in cellular uplink: Cooperative interference cancellation and sum-rate maximization," *IEEE Trans. Wireless Commun.*, vol. 18, no. 10, pp. 4679–4691, Jan. 2019.

[103] Y. Li *et al.*, "Air-to-air communications beyond 5g: A novel 3d comp transmission scheme," *IEEE Trans. Wireless Commun.*, vol. 19, no. 11, pp. 7324–7338, Nov. 2020.

[104] A. A. Khuwaja, Y. Chen, N. Zhao, M.-S. Alouini, and P. Dobbins, "A survey of channel modeling for uav communications," *IEEE Commun. Surveys Tuts.*, vol. 20, no. 4, pp. 2804–2821, Jul. 2018.

[105] Y. Zeng, J. Xu, and R. Zhang, "Energy minimization for wireless communication with rotary-wing uav," *IEEE Trans. Wireless Commun.*, vol. 18, no. 4, pp. 2329–2345, Mar. 2019.

[106] M. R. Akdeniz, Y. Liu, M. K. Samimi, *et al.*, "Millimeter wave channel modeling and cellular capacity evaluation," *IEEE J. Sel. Areas Commun.*, vol. 32, no. 6, pp. 1164–1179, Jun. 2014.

[107] T. S. Rappaport, Y. Xing, O. Kanhere, *et al.*, "Wireless communications and applications above 100 ghz: Opportunities and challenges for 6G and beyond," *IEEE access*, vol. 7, pp. 78 729–78 757, Jun. 2019.

[108] Z. Zhang, Y. Xiao, Z. Ma, *et al.*, "6G wireless networks: Vision, requirements, architecture, and key technologies," *IEEE Veh. Technol. Mag.*, vol. 14, no. 3, pp. 28–41, Jul. 2019.

[109] M. Giordani, M. Polese, M. Mezzavilla, S. Rangan, and M. Zorzi, "Toward 6G networks: Use cases and technologies," *IEEE Commun. Mag.*, vol. 58, no. 3, pp. 55–61, Mar. 2020.

[110] H. Sarieddeen, M.-S. Alouini, and T. Y. Al-Naffouri, "An overview of signal processing techniques for terahertz communications," *Proceedings of the IEEE*, Aug. 2021.

[111] C. Saha, M. Afshang, and H. S. Dhillon, "Enriched K-tier hetnet model to enable the analysis of user-centric small cell deployments," *IEEE Trans. Wireless Commun.*, vol. 16, no. 3, pp. 1593–1608, Jan. 2017.

[112] S. M. Azimi-Abarghouyi, M. Nasiri-Kenari, and M. Debbah, "Stochastic design and analysis of user-centric wireless cloud caching networks," *IEEE Trans. Wireless Commun.*, vol. 19, no. 7, pp. 4978–4993, Apr. 2020.

[113] K. Humadi, I. Trigui, W.-P. Zhu, and W. Ajib, "Coverage analysis of user-centric millimeter wave networks under dynamic base station clustering," in *IEEE Int. Conf. Commun (ICC)*, Jun. 2021, pp. 1–6.

[114] O. Semiari, W. Saad, M. Bennis, and M. Debbah, "Integrated millimeter wave and sub-6 ghz wireless networks: A roadmap for joint mobile broadband and ultra-reliable low-latency communications," *IEEE Wireless Commun.*, vol. 26, no. 2, pp. 109–115, Feb. 2019.

[115] W. Sui, X. Chen, S. Zhang, Z. Jiang, and S. Xu, "Energy-efficient resource allocation with flexible frame structure for hybrid embb and urllc services," *IEEE Trans. Green Commun. Netw.*, vol. 5, no. 1, pp. 72–83, Oct. 2020.

[116] H. Elshaer, M. N. Kulkarni, F. Boccardi, J. G. Andrews, and M. Dohler, "Downlink and uplink cell association with traditional macrocells and millimeter wave small cells," *IEEE Tran. Wireless Commun.*, vol. 15, no. 9, pp. 6244–6258, Jun. 2016.

[117] C.-H. Liu, "Coverage-rate tradeoff analysis in mmwave heterogeneous cellular networks," *IEEE Tran. Commun.*, vol. 67, no. 2, pp. 1720–1736, Nov. 2018.

[118] A. A. Raja, H. Pervaiz, S. A. Hassan, *et al.*, "Coverage analysis of mmwave and THz-enabled aerial and terrestrial heterogeneous networks," *IEEE Trans. Intell. Transp. Syst.*, Jun. 2021.

[119] J. Zhao, L. Yang, M. Xia, and M. Motani, "Unified analysis of coordinated multi-point transmissions in mmwave cellular networks," *IEEE Internet Things J.*, Dec. 2021.

[120] K. Humadi, I. Trigui, W.-P. Zhu, and W. Ajib, "Dynamic base station clustering in user-centric mmwave networks: Performance analysis and optimization," *IEEE Trans. Commun.*, vol. 69, no. 7, pp. 4847–4861, Apr. 2021.

[121] Q. Cui, X. Yu, Y. Wang, and M. Haenggi, "The sir meta distribution in poisson cellular networks with base station cooperation," *IEEE Trans. Commun.*, vol. 66, no. 3, pp. 1234–1249, Nov. 2017.

[122] K. Feng and M. Haenggi, "A location-dependent base station cooperation scheme for cellular networks," *IEEE Trans. Commun.*, vol. 67, no. 9, pp. 6415–6426, May. 2019.

[123] L. Yang, T. J. Lim, J. Zhao, and M. Motani, "Modeling and analysis of hetnets with interference management using poisson cluster process," *IEEE Transactions on Vehicular Technology*, vol. 70, no. 11, pp. 12 039–12 054, 2021.

[124] K. Humadi, I. Trigui, W.-.-P. Zhu, and W. Ajib, "Hybrid mmWave-THz networks with user-centric clustering," in *Proc. IEEE GLOBECOM'2021*, IEEE, Dec. 2021, pp. 01–06.

[125] B. R. Mahafza, *Radar signal analysis and processing using MATLAB*. Boca Raton, FL, USA, Chapman and Hall/CRC, 2016.

[126] M. Di Renzo and W. Lu, "System-level analysis and optimization of cellular networks with simultaneous wireless information and power transfer: Stochastic geometry modeling," *IEEE Trans. Veh. Technol.*, vol. 66, no. 3, pp. 2251–2275, Jun. 2016.

[127] J. Gil-Pelaez, "Note on the inversion theorem," *Biometrika*, vol. 38, no. 3-4, pp. 481–482, 1951.

[128] J. M. Jornet and I. F. Akyildiz, "Channel modeling and capacity analysis for electromagnetic wireless nanonetworks in the terahertz band," *IEEE Trans. Wireless Commun.*, vol. 10, no. 10, pp. 3211–3221, Aug. 2011.

[129] C. Bockelmann, N. Pratas, H. Nikopour, *et al.*, "Massive machine-type communications in 5g: Physical and mac-layer solutions," *IEEE Commun. Mag.*, vol. 54, no. 9, pp. 59–65, Sep. 2016.

[130] B. Clerckx, R. Zhang, R. Schober, *et al.*, "Fundamentals of wireless information and power transfer: From RF energy harvester models to signal and system designs," *IEEE J. Sel. Areas Commun.*, vol. 37, no. 1, pp. 4–33, Jan. 2019.

[131] X. Lu, P. Wang, D. Niyato, D. I. Kim, and Z. Han, "Wireless networks with RF energy harvesting: A contemporary survey," *IEEE Commun. Surveys Tut.*, vol. 17, no. 2, pp. 757–789, Nov. 2014.

[132] L.-T. Tu and M. Di Renzo, "Analysis of millimeter wave cellular networks with simultaneous wireless information and power transfer," in *IEEE Int. Conf. Recent Adv. Signal Process., Telecommun. Comput. (SigTelCom)*, Jan. 2017, pp. 39–43.

[133] Y. Al-Eryani, M. Akrout, and E. Hossain, "Antenna clustering for simultaneous wireless information and power transfer in a mimo full-duplex system: A deep reinforcement learning-based design," *IEEE Transactions on Communications*, vol. 69, no. 4, pp. 2331–2345, Jan. 2021.

[134] X. Zhou, R. Zhang, and C. K. Ho, "Wireless information and power transfer: Architecture design and rate-energy tradeoff," *IEEE Trans. commun.*, vol. 61, no. 11, pp. 4754–4767, Oct. 2013.

[135] D. Kudathanthirige, R. Shrestha, and G. A. A. Baduge, "Max–min fairness optimal rate-energy trade-off of swipt for massive mimo downlink," *IEEE Communications Letters*, vol. 23, no. 4, pp. 688–691, Jan. 2019.

[136] F. Boccardi, R. W. Heath, A. Lozano, T. L. Marzetta, and P. Popovski, "Five disruptive technology directions for 5g," *IEEE Commun. Mag.*, vol. 52, no. 2, pp. 74–80, Feb.2014.

[137] T. L. Thanh, M. Di Renzo, and J. P. Coon, "Stochastic geometry analysis of receiver diversity in cellular networks with swipt," in *IEEE 19th International Workshop on Signal Processing Advances in Wireless Communications (SPAWC)*, Jun. 2018, pp. 1–5.

[138] A. I. Akin, N. Janatian, I. Stupia, and L. Vandendorpe, "Swipt-based real-time mobile computing systems: A stochastic geometry perspective," in *IEEE Wireless Communications and Networking Conference (WCNC)*, Apr. 2019, pp. 1–7.

[139] M. A. Abd-Elmagid, M. A. Kishk, and H. S. Dhillon, "Joint energy and sinr coverage in spatially clustered rf-powered iot network," *IEEE Trans. Green Commun. Netw.*, vol. 3, no. 1, pp. 132–146, Nov. 2018.

[140] C.-H. Liu, "Energy efficiency optimization of heterogeneous networks with swipt: A cell-load perspective," in *IEEE 90th Vehicular Technology Conference (VTC2019-Fall)*, Sept. 2019, pp. 1–6.

[141] N. Deng and M. Haenggi, "A tractable model for wirelessly powered networks with energy correlation," *IEEE Trans. Wireless Commun.*, vol. 19, no. 9, pp. 5765–5778, Jun. 2020.

[142] ——, "The energy correlation coefficient and its key role in wirelessly powered networks," *IEEE Trans. Wireless Commun.*, Jun. 2021.

[143] Y. Guo, C. Skouroumounis, and I. Krikidis, "Threshold-based pair switching scheme in swipt-enabled wireless downlink system," in *IEEE 93rd Vehicular Technology Conference (VTC2021-Spring)*, Apr. 2021, pp. 1–7.

[144] M. Wang, C. Zhang, X. Chen, and S. Tang, "Performance analysis of millimeter wave wireless power transfer with imperfect beam alignment," *IEEE Trans. Veh. Technol.*, vol. 70, no. 3, pp. 2605–2618, Feb. 2021.

[145] Y. Guo, C. Skouroumounis, and I. Krikidis, "Joint information and energy transfer of swipt-enabled mobile users in wireless networks," *IEEE Trans. Green Commun. Net.*, Dec. 2021.

[146] J. Huang, J. Cui, C.-C. Xing, and H. Gharavi, "Energy-efficient swipt-empowered d2d mode selection," *IEEE Trans. Veh. Technol.*, vol. 69, no. 4, pp. 3903–3915, Jan. 2020.

[147] G. Kwon, H. Park, and M. Win, "Joint beamforming and power splitting for wideband millimeter wave swipt systems," *IEEE J. Sel. Top. Signal Process.*, Jun. 2021.

[148] R. Jiang, K. Xiong, H.-C. Yang, *et al.*, "On the coverage of uav-assisted swipt networks with nonlinear eh model," *IEEE Trans. Wireless Commun.*, Dec. 2021.

[149] T. S. Rappaport, G. R. MacCartney, M. K. Samimi, and S. Sun, "Wideband millimeter-wave propagation measurements and channel models for future wireless communication system design," *IEEE trans. Commun.*, vol. 63, no. 9, pp. 3029–3056, May. 2015.

[150] E. Boshkovska, D. W. K. Ng, N. Zlatanov, and R. Schober, "Practical non-linear energy harvesting model and resource allocation for swipt systems," *IEEE Commun. Lett.*, vol. 19, no. 12, pp. 2082–2085, Sep. 2015.

[151] H. Du, J. Zhang, J. Cheng, and B. Ai, "Millimeter wave communications with reconfigurable intelligent surfaces: Performance analysis and optimization," *IEEE Trans. Commun.*, vol. 69, no. 4, pp. 2752–2768, Jan. 2021.

[152] Y. Pan, K. Wang, C. Pan, H. Zhu, and J. Wang, "Sum-rate maximization for intelligent reflecting surface assisted terahertz communications," *IEEE Trans. Veh. Technol.*, pp. 1–1, 2022. DOI: 10.1109/TVT.2022.3140869.